



The
University
Of
Sheffield.

**Improvement of sulphur dioxide yield from the sulphuric acid
thermal decomposition process by membrane separation**

Ian Atkin

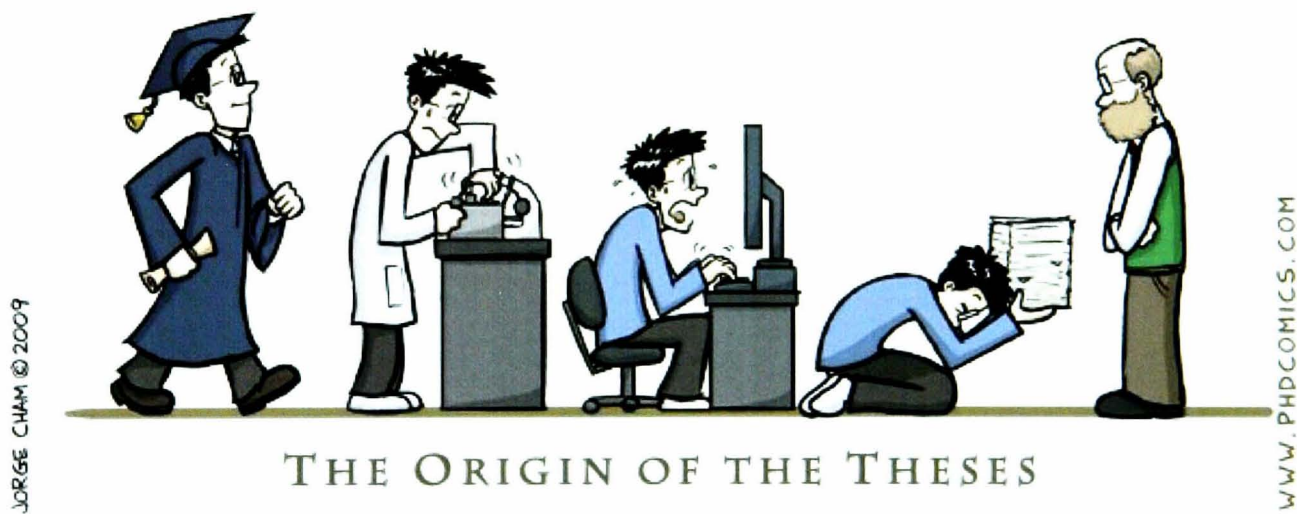
Submitted for the degree of Doctor of Philosophy

Department of Chemical and Process Engineering

October 2009

Supervisor: Prof RWK Allen

I dedicate this work to my parents, David and June Atkin, and the rest of my family, for their unwavering support throughout my undeniably lengthy studies.



THE ORIGIN OF THE THESES

"Piled Higher and Deeper" by Jorge Cham

www.phdcomics.com

ACKNOWLEDGEMENTS

I would like to thank my supervisor Prof Ray Allen and the members of staff who have assisted me, including Dr Geof Priestman and Prof Derek Sinclair.

I have been ably assisted by many friends and colleagues including Andrew Donovan, Dr Rachael Elder, Jamil Khan, Dr Ana Parracho, Moises Romero, Dr Andrew Shaw, Robert Sochon, Alison Whalen and especially Marie Taylor, without whose Parafilming skills many of the experiments would not have happened!

I would also like to thank the Engineering and Physical Sciences Research Council (EPSRC) and the HycycleS consortium for funding my postgraduate studies.

ABSTRACT

This work investigates the feasibility of applying high temperature oxygen separation to the sulphuric acid decomposition process, a step used in large scale hydrogen production processes currently under development. Porous and dense membranes are both considered. Equilibrium calculations show yttria-stabilised zirconia (YSZ), combined with platinum electrodes, to be a candidate membrane. Process simulations show the potential sulphur dioxide yield increases that could be achieved through the use of a high temperature oxygen separation membrane in two different configurations. Bespoke experimental apparatus was designed, procured and assembled in order to investigate the oxygen flux through YSZ membranes in the presence of sulphur dioxide, during external voltage application. Experiments were performed in the 700 – 900°C temperature range. Results show that oxygen permeation through YSZ membranes occurs under these conditions. A decrease in oxygen permeation with time was observed and attributed to sulphur dioxide adsorption on to the platinum electrodes. Future work would concentrate on using variable applied voltages to reduce this performance decrease.

Contents

1	Introduction	1
1.1	Summary and outline	1
1.2	The “hydrogen economy”	2
1.3	Current hydrogen production processes	3
1.3.1	Steam methane reforming	3
1.3.2	Electrolysis	4
1.3.3	Comparison of electricity generation processes	5
1.4	Other hydrogen production processes	6
1.5	The Sulphur-Iodine Cycle	7
1.5.1	Cycle steps	7
1.5.2	Recent SI cycle experimental work	8
1.6	The Hybrid Sulphur cycle	9
2	Sulphuric acid thermal decomposition	10
2.1	Process flowsheets	10
2.2	Decomposer literature designs	12
2.3	Catalyst selection	13
2.4	Materials of construction	15
2.5	Process heat sources	16
2.6	Equilibrium calculation validation	17
2.6.1	Comparison to literature SO ₃ decomposition data	18

2.6.2	Comparison to literature H ₂ SO ₄ decomposition data	19
2.7	SO ₃ /H ₂ SO ₄ equilibrium calculations	20
2.7.1	Aim	20
2.7.2	Method	20
2.7.3	Results	20
2.8	SO ₂ /H ₂ SO ₄ equilibrium calculations	21
2.8.1	Aim	21
2.8.2	Method	21
2.8.3	Results	21
2.9	Conclusions	23
3	Proposed membrane process: introduction and simulations	24
3.1	Downstream membrane separation	25
3.2	Catalytic membrane reactor	26
3.3	Membrane sealing and other issues	27
3.4	Introduction to process simulations	28
3.5	Validation of ProSimPlus simulations against literature data	29
3.5.1	Aim	29
3.5.2	Literature data	29
3.5.3	Method	29
3.5.4	Results	30
3.6	General method of novel simulations	32
3.7	CMR simulations	32
3.7.1	Aim	32
3.7.2	Method	33
3.7.3	Results	33
3.7.4	Conclusions	36
3.8	Downstream membrane simulations	37
3.8.1	Aim	37

3.8.2	Method	37
3.8.3	Results	38
3.8.4	Conclusions	43
3.9	Overall conclusions	43
4	Porous membranes for sulphuric acid thermal decomposition	44
4.1	Recent research into materials and fabrication techniques	44
4.2	Experimental membrane permeance	46
4.3	Separation factors	47
4.4	Determination of molecular diameters	49
4.4.1	Literature values	49
4.4.2	Calculated values	49
4.4.3	Conclusions	51
4.5	Conclusions of porous membrane material investigations	51
5	Dense oxygen separation membranes for sulphuric acid thermal decomposition	53
5.1	Ion conducting dense membranes	54
5.2	Mixed ion/electron conducting dense membranes	64
5.3	Dense membrane sulphation calculations	67
5.3.1	Aim	67
5.3.2	Method	67
5.3.3	Results	68
5.3.4	Conclusions of metal oxide equilibrium simulations	73
5.4	Conclusions of dense membrane materials investigations	74
6	Experimental work: description and design	75
6.1	Aims	75
6.2	Background	75
6.3	Dense membrane procurement, specification and fabrication	76

6.4	Membrane exposure/permeance apparatus	78
6.4.1	Description and schematic	78
6.4.2	Tubular furnace	79
6.4.3	High temperature membrane holder	81
6.4.4	Sealing	86
6.4.5	Membrane electrical connection	86
6.4.6	Membrane holder support and stand	87
6.4.7	Post-furnace cooling	90
6.4.8	Gas analysis	90
6.4.9	Gas venting	90
6.4.10	Instrumentation	90
6.4.11	Low temperature pipework	91
6.5	Surface analysis	91
6.5.1	X-ray diffraction (XRD)	91
6.5.2	X-ray photoelectron spectroscopy (XPS)	92
6.5.3	Scanning electron microscopy (SEM)	93
6.5.4	Impedance spectroscopy (IS)	93
6.6	FLUENT simulations of high temperature membrane holder	93
6.6.1	Data collection	95
6.6.2	Results and discussion	97
7	Experimental work: commissioning	106
7.1	Furnace temperature calibration	106
7.2	Metalwork electrical resistance	107
7.3	Passive oxygen flux prediction	108
7.3.1	YSZ membrane resistance	109
7.3.2	Current and oxygen flow prediction	109
7.4	Graphite seal lifespan testing	111
7.4.1	Method	111

7.4.2	Results	111
7.5	O ₂ permeation through prototype membrane from He/O ₂ mixtures . .	112
7.5.1	750°C	112
7.5.2	700°C	115
7.5.3	Variation of circuit resistance with temperature	120
7.6	O ₂ permeation through prototype membrane from He/O ₂ /SO ₂ mixtures	121
7.7	XRD analysis of prototype membrane	125
7.8	Graphite seal coating testing	127
7.8.1	Aim	127
7.8.2	Gasket types	127
7.8.3	Method	129
7.8.4	Results	130
7.8.5	Conclusions	132
7.9	Gold foil/membrane sealing	133
7.9.1	Aim	133
7.9.2	Method	133
7.9.3	Results	133
7.10	Alumina adhesive testing	134
7.10.1	Aim	134
7.10.2	Method	134
7.10.3	Results	134
7.10.4	Conclusions	136
7.11	Conclusions of commissioning work	136
8	Experimental work: results	137
8.1	SO ₂ exposure at 900°C	137
8.1.1	Aims	138
8.1.2	Method	138
8.1.3	Results	140

8.1.4	Implications for experimental programme	149
8.1.5	Conclusions	150
8.2	Recovery test at 900°C	150
8.2.1	Aim	151
8.2.2	Method	151
8.2.3	Results	151
8.2.4	Conclusions	156
8.3	SO ₂ exposure at 800°C (Pt and Au electrodes)	156
8.3.1	Aim	156
8.3.2	Method	158
8.3.3	Results	158
8.3.4	Conclusions	172
8.4	SO ₂ exposure at 800°C (replacement of Pt electrode)	173
8.4.1	Aim	173
8.4.2	Method	173
8.4.3	Results	174
8.4.4	Conclusions	177
8.5	SO ₂ exposure at 850°C (Metalor Pt ink)	177
8.5.1	Aim	178
8.5.2	Method	178
8.5.3	Results	179
8.5.4	Conclusions	191
8.6	SO ₂ exposure at 850°C (GEM Pt ink)	193
8.6.1	Aim	193
8.6.2	Method	193
8.6.3	Results	194
8.6.4	Conclusions	202
8.7	SO ₂ exposure at 850°C (varying applied potential)	204

8.7.1	Aim	204
8.7.2	Method	204
8.7.3	Results	204
8.7.4	Conclusions	207
8.8	Overall conclusions of experimental programme	208
9	Overall conclusions and future work	209
9.1	Future work	210
9.1.1	Membrane performance recovery	210
9.1.2	Progression from pure gas feeds to in-situ acid decomposition . .	211
9.1.3	Thin supported membranes	213
	References	213
A	Process simulation tables	224
B	Metal oxide/sulphate equilibrium calculations	230

List of Figures

1.1	CO ₂ produced by various electricity generation systems (WEC 2004) . . .	6
2.1	Sulphuric acid decomposition flowsheet (Huang 2005)	11
2.2	National Hydrogen Initiative Silicon Carbide Integrated Decomposer (Nagarajan 2008)	12
2.3	Variation in SO ₃ equilibrium conversion with temperature at 0.1 bara . .	19
2.4	SO ₂ yield calculations from <i>HSC Chemistry</i> and Brutti (2007)	20
2.5	Variation in SO ₃ equilibrium yield from H ₂ SO ₄ at 1 bara	21
2.6	Equilibrium SO ₂ yield from H ₂ SO ₄ at 600-1200°C, 0.1-20 bara and 92.7wt% acid feed	22
2.7	Equilibrium SO ₂ yield from H ₂ SO ₄ at 850°C, 0.1-20 bara and 92.7wt% acid feed	22
3.1	Schematic of downstream membrane separation process	26
3.2	Schematic of catalytic membrane reactor	27
3.3	<i>ProSimPlus</i> simulation diagram for a CMR with six theoretical stages . .	30
3.4	<i>ProSimPlus</i> simulation diagram for a CMR with four theoretical stages .	33
3.5	<i>ProSimPlus</i> CMR simulation at 1000K and 1 atm	34
3.6	<i>ProSimPlus</i> CMR simulation at 1 atm with 6 stages	35
3.7	<i>ProSimPlus</i> CMR simulation at 1 atm with 2 stages	35
3.8	<i>ProSimPlus</i> CMR simulation at 1000K with 2 stages	36
3.9	<i>ProSimPlus</i> simulation diagram for separate membrane separation . . .	38

3.10	<i>ProSimPlus</i> downstream membrane simulation at 1000K, 1 atm, 75% membrane efficiency, 80% retentate recycle	39
3.11	<i>ProSimPlus</i> downstream membrane simulation at 1 atm, 75% membrane efficiency, 80% retentate recycle	40
3.12	<i>ProSimPlus</i> membrane simulations at 1 atm, 1000K, F=100 - configuration comparison	40
3.13	<i>ProSimPlus</i> downstream membrane simulation at 1000K, 75% membrane efficiency, 80% retentate recycle	41
3.14	<i>ProSimPlus</i> downstream membrane simulation at 1 atm, 75% membrane efficiency, F=100	42
3.15	<i>ProSimPlus</i> downstream membrane simulation at 30 bara, 75% membrane efficiency, F=100	42
4.1	Molecular diameters calculated from <i>ProSim</i> viscosities	50
5.1	Electroded dense oxygen separation membrane process schematic	54
5.2	Open circuit voltage across oxygen separation membrane at 850°C	56
5.3	Zirconia unit cell (Moulson and Herbert 1990)	57
5.4	YSZ total conductivity vs. sintering temperature (He et al. 2002)	58
5.5	Calculated variation of ionic current density with temperature and oxygen partial pressure for YSZ-Pt SOFC cathode (Lau 2008)	59
5.6	Calculated variation of ionic current density with applied voltage for YSZ-Pt SOFC cathode (Lau 2008)	60
5.7	Reaction pathway for Pt-YSZ-O ₂ system (Mitterdorfer 1999)	61
5.8	SO ₄ molecular structure on Pt(111) surface (Lin et al. 2004)	62
5.9	Oxide conductivity of La _{0.9} Sr _{0.1} Ga _{0.8} Mg _{0.2} O ₃ compared to other materials (Ishihara et al. 1994)	63
5.10	Oxide conductivity of Sm _{0.8} Ca _{0.2} AlO _{2.9} compared to other materials (Yamamura et al. 2003)	64
5.11	Non-electroded dense oxygen separation membrane process schematic	65
5.12	Equilibrium calculation of SiO ₂ stability at 1 bara	69
5.13	Equilibrium calculation of SiO ₂ stability at 20 bara	69

5.14	Equilibrium calculation of Al_2O_3 stability at 1 bara	70
5.15	Equilibrium calculation of Al_2O_3 stability at 20 bara	70
5.16	Equilibrium calculation of Pt stability at 1 bara	71
5.17	Equilibrium calculation of Pt stability at 20 bara	71
5.18	Equilibrium calculation of Y_2O_3 stability at 1 bara	72
5.19	Equilibrium calculation of Y_2O_3 stability at 20 bara	72
5.20	Equilibrium calculation of ZrO_2 stability at 1 bara	73
5.21	Equilibrium calculation of ZrO_2 stability at 20 bara	73
6.1	Photo mosaic of platinum electrode application process	78
6.2	Photograph of experimental apparatus in situ	79
6.3	Schematic diagram of experimental apparatus	80
6.4	Furnace and rotameters	81
6.5	Schematic diagram of quartz membrane holder	84
6.6	Quartz membrane holder	85
6.7	Schematic diagram of membrane holder stand	88
6.8	Schematic diagram of membrane holder support	89
6.9	Outline of flow domain for <i>FLUENT</i> simulations	94
6.10	Flow domain for <i>FLUENT</i> simulations showing data collection lines	96
6.11	Flow domain for <i>FLUENT</i> simulations showing data collection plane	96
6.12	Simulated membrane holder gas velocity contours at 2.087 m/s	97
6.13	Simulated membrane holder gas velocity contours at 4.175 m/s	98
6.14	Simulated membrane holder gas velocity contours at 6.262 m/s	98
6.15	Simulated membrane holder gas velocity contours at 8.350 m/s	99
6.16	Membrane holder full width simulated velocity magnitude profiles from 0.5mm below centreline	99
6.17	Membrane holder partial width simulated velocity magnitude profiles from 0.5mm below centreline	100
6.18	Membrane holder full width simulated velocity magnitude profiles from 2.0mm below centreline	100

6.19	Membrane holder partial width simulated velocity magnitude profiles from 2.0mm below centreline	100
6.20	Membrane holder full width simulated velocity magnitude profiles from 0.5mm below transverse centreline	101
6.21	Membrane holder full width simulated velocity magnitude profiles from 2.0mm below transverse centreline	101
6.22	Simulated membrane holder path lines at 2.087 m/s (side view)	102
6.23	Simulated membrane holder path lines at 2.087 m/s (top view)	102
6.24	Simulated membrane holder path lines at 4.175 m/s (side view)	103
6.25	Simulated membrane holder path lines at 4.175 m/s (top view)	103
6.26	Simulated membrane holder path lines at 6.262 m/s (side view)	104
6.27	Simulated membrane holder path lines at 6.262 m/s (top view)	104
6.28	Simulated membrane holder path lines at 8.350 m/s (side view)	105
6.29	Simulated membrane holder path lines at 8.350 m/s (top view)	105
7.1	Furnace setpoint and centre temperature during warm-up	107
7.2	Furnace setpoint and centre temperature at steady state	107
7.3	Variation of apparatus external circuit resistance with temperature	108
7.4	Variation of YSZ conductivity with temperature (from West 1999)	109
7.5	Calculated resistance of whole electrical circuit	109
7.6	Calculated passive current	110
7.7	Calculated passive O ₂ permeate flow rate	110
7.8	Graphite gasket mass loss: 700°C, 15 min recording intervals	112
7.9	O ₂ permeation through membrane at 750°C with external voltage - 20% O ₂ feed	113
7.10	Electrical resistance at 750°C - 20% O ₂ feed	113
7.11	Graphite gaskets after run at 750°C, 20% O ₂ feed	114
7.12	Graphite gaskets after run at 750°C, 20% O ₂ feed	114
7.13	O ₂ permeation through membrane at 700°C with external voltage - 20% O ₂ feed	115

7.14	Electrical resistance at 700°C - 20% O ₂ feed	116
7.15	Graphite gaskets after run at 700°C, 20% O ₂ feed	117
7.16	Initial and equilibrium current at 700°C - 20% O ₂ feed	117
7.17	Membrane voltage drop schematic	119
7.18	Average circuit resistance at 700 – 850°C - 20% O ₂ feed	120
7.19	Results of first SO ₂ run with prototype membrane	123
7.20	Results of second SO ₂ run with prototype membrane	124
7.21	Results of third SO ₂ run with prototype membrane	125
7.22	XRD data for prototype membrane, post-exposure	126
7.23	Gold sputtered graphite gasket	128
7.24	Gold sputtered graphite gasket with some foil wrapping	128
7.25	Gold foil rings	129
7.26	Timed flow results for graphite/gold gasket tests	130
7.27	Timed flow results for gold foil gasket test 1 using bubble meter	131
7.28	Timed flow results for gold foil gasket test 2 using bubble meter	132
7.29	Broken quartz following baking with alumina adhesive	135
7.30	Broken quartz following baking with alumina adhesive	135
7.31	Broken quartz following baking with alumina adhesive	135
8.1	Current and permeate oxygen concentration vs. time for long 900°C test	141
8.2	YSZ membrane feed side after exposure to SO ₂ for 870 minutes at 900°C	142
8.3	YSZ membrane feed side after membrane feed side exposure to SO ₂ for 870 minutes at 900°C	142
8.4	YSZ phase diagram (West 1999)	144
8.5	Pre- and post-SO ₂ exposure XRD data for YSZ/Pt pellet, 900°C per- meate side	145
8.6	Pre- and post-SO ₂ exposure XRD data for YSZ/Pt pellet, 900°C feed side	146
8.7	Partial post-SO ₂ exposure XRD data for YSZ/Pt pellet, 900°C feed side	147
8.8	Summarised impedance spectroscopy for YSZ/Pt before/after 900°C SO ₂ exposure	148

8.9	Z^* plot for YSZ/Pt at 245°C after SO ₂ exposure at 900°C	149
8.10	Retest of YSZ/Pt pellet previously exposed to SO ₂ at 900°C with O ₂ - day 1 results	153
8.11	Retest of YSZ/Pt pellet previously exposed to SO ₂ at 900°C with O ₂ - day 2 results	154
8.12	Summarised impedance spectroscopy for YSZ/Pt before/after 900°C O ₂ "recovery" exposure	155
8.13	XRD data for unused YSZ/Pt membrane, after 900°C SO ₂ exposure and after 900°C O ₂ exposure	157
8.14	YSZ/Pt pellet exposed to SO ₂ and O ₂ at 800°C	160
8.15	YSZ/Au pellet exposed to SO ₂ and O ₂ at 800°C	161
8.16	Before and after XRD data for YSZ/Pt membrane, 800°C SO ₂ exposure	163
8.17	Before and after XRD data for YSZ/Au membrane, 800°C SO ₂ exposure	164
8.18	Summarised impedance spectroscopy for YSZ/Pt before/after 800°C SO ₂ exposure	165
8.19	Comparison of experimental YSZ conductivity with literature values . .	166
8.20	Z^* plot for unused YSZ/Pt at 293°C	167
8.21	Z^* plot for YSZ/Pt at 300°C after SO ₂ exposure at 800°C	167
8.22	Z^* plots for unused YSZ/Pt at 441°C	168
8.23	Z^* plots for YSZ/Pt at 451°C after SO ₂ exposure at 800°C	168
8.24	Summarised impedance spectroscopy for YSZ/Au before/after 800°C SO ₂ exposure	169
8.25	Z^* plot for unused YSZ/Au at 337°C	170
8.26	Z^* plots for YSZ/Au at 341°C after SO ₂ exposure at 800°C	170
8.27	Z^* plot for unused YSZ/Au at 444°C	171
8.28	Z^* plots for YSZ/Au at 449°C after SO ₂ exposure at 800°C	171
8.29	XRD data for YSZ/Pt membrane after initial 800°C SO ₂ exposure and during sanding	175
8.30	YSZ/Pt pellet re-exposed to SO ₂ and O ₂ at 800°C after electrode re- application	176

8.31 Comparison of O ₂ permeation during first and repeat exposure of YSZ/Pt pellet to SO ₂ and O ₂ at 800°C	177
8.32 YSZ/Pt pellet exposed to SO ₂ and O ₂ at 850°C	181
8.33 XPS wide scan of unelectroded YSZ pellet	182
8.34 XPS wide scan of unused YSZ/Pt pellet - thin electrode point	183
8.35 XPS wide scan of unused YSZ/Pt pellet - thick electrode point	184
8.36 XPS wide scan of used YSZ/Pt pellet - thin electrode point	185
8.37 XPS wide scan of used YSZ/Pt pellet - thick electrode point	186
8.38 SEM image of unelectroded YSZ pellet, 3000x magnification	187
8.39 SEM image of electroded YSZ pellet, 3000x magnification	188
8.40 SEM image of electroded YSZ pellet, 10000x magnification	188
8.41 SEM image of electroded YSZ pellet, 1500x magnification	189
8.42 SEM image of SO ₂ exposed YSZ pellet, 2000x magnification	190
8.43 SEM image of SO ₂ exposed YSZ pellet, 10000x magnification	190
8.44 Before and after XRD data for YSZ/Pt membrane, 850°C SO ₂ exposure	192
8.45 YSZ/Pt pellet exposed to SO ₂ and O ₂ at 850°C - comparison of permeate oxygen concentration with GEM and Metalor inks	194
8.46 SO ₂ poisoning of PEMFC cathode (Fu 2009)	195
8.47 YSZ/Pt pellet exposed to SO ₂ and O ₂ at 850°C - GEM ink	196
8.48 XPS wide scan of unused YSZ/Pt pellet (GEM ink)	197
8.49 XPS wide scan of 850°C SO ₂ exposed YSZPt pellet (GEM ink, platinum removed)	198
8.50 XPS wide scan of 850°C SO ₂ exposed YSZ/Pt pellet (GEM ink, platinum in place)	199
8.51 SEM image of electroded YSZ pellet (GEM ink), 1500x magnification . .	200
8.52 SEM image of electroded YSZ pellet (GEM ink), 3000x magnification . .	200
8.53 SEM image of SO ₂ exposed YSZ pellet (GEM ink), 1500x magnification .	201
8.54 SEM image of SO ₂ exposed YSZ pellet (GEM ink), 3000x magnification .	201

8.55	Feed side XRD data for YSZ/Pt membranes with Metalor and GEM inks, 850°C SO ₂ exposure	203
8.56	YSZ/Pt pellet (GEM ink) exposed to SO ₂ and O ₂ at 850°C - comparison of current upon SO ₂ application at 1V and 2V applied potential	205
8.57	YSZ/Pt pellet exposed to SO ₂ and O ₂ at 850°C - GEM ink, variable voltage	206
9.1	Schematic of experimental rig extension to include in-situ acid decomposition	212
B.1	Equilibrium calculation of BaO ₂ stability	231
B.2	Equilibrium calculation of Bi ₂ O ₃ stability	231
B.3	Equilibrium calculation of CaO stability	231
B.4	Equilibrium calculation of CeO ₂ stability	232
B.5	Equilibrium calculation of CoO stability	232
B.6	Equilibrium calculation of Dy ₂ O ₃ stability	232
B.7	Equilibrium calculation of Eu ₂ O ₃ stability	233
B.8	Equilibrium calculation of Fe ₂ O ₃ stability	233
B.9	Equilibrium calculation of Gd ₂ O ₃ stability	233
B.10	Equilibrium calculation of La ₂ O ₃ stability	234
B.11	Equilibrium calculation of Nd ₂ O ₃ stability	234
B.12	Equilibrium calculation of Pr ₂ O ₃ stability	234
B.13	Equilibrium calculation of Rb ₂ O ₃ stability	235
B.14	Equilibrium calculation of Sm ₂ O ₃ stability	235
B.15	Equilibrium calculation of SrO stability	235

List of Tables

3.1	Comparison of <i>ProSimPlus</i> data with Forsberg data	31
4.1	Molecular diameters calculated from Van der Waal's constants	51
6.1	Gas velocities used in <i>FLUENT</i> simulations	95
7.1	Graphite gasket weights following He/O ₂ run	115
7.2	Graphite gasket weights following He/O ₂ run	116
7.3	Gold foil/YSZ membrane sealing test results	133
8.1	Comparison of key results at 800°C for YSZ membranes with platinum or gold electrodes	159
A.1	CMR process simulation results	225
A.2	Downstream separation process simulation results (20% recycle)	226
A.3	Downstream separation process simulation results (40% recycle)	227
A.4	Downstream separation process simulation results (60% recycle)	228
A.5	Downstream separation process simulation results (80% recycle)	229
B.1	Species used for <i>HSC Chemistry</i> metal oxide stability calculations: Al - Dy236	
B.2	Species used for <i>HSC Chemistry</i> metal oxide stability calculations: Eu - Pt 237	
B.3	Species used for <i>HSC Chemistry</i> metal oxide stability calculations: Rb - Zr 238	

Chapter 1

Introduction

1.1 Summary and outline

This thesis documents efforts to investigate the feasibility of improving the yield of sulphur dioxide (SO_2) from the sulphuric acid (H_2SO_4) thermal decomposition process by the use of membrane separation.

It is hypothesised that by utilising a membrane separation step, the yield of sulphur dioxide from the sulphuric acid thermal decomposition process could be increased beyond the thermodynamic equilibrium value at any given temperature. If this could be accomplished, it would permit the use of lower temperature heat sources with the sulphur-iodine and hybrid sulphur cycles, removing one of the primary barriers to the development of these processes. Alternatively, it would allow reactor throughput to be increased for a given heating duty.

As is discussed in Section 4.1, suitable membranes have yet to be developed for this process.

The objectives of the research were to:

- Carry out process simulations of the sulphuric acid decomposition process in order to quantify the potential benefits of the membrane separation step;
- Identify a membrane material that may be suitable for use with this process;
- Test the selected membrane material experimentally in order to assess its suitability for this process.

Chapter 1 introduces the topic, reviewing current hydrogen production technologies,

the drivers for change, and the new hydrogen production methods to which this research is relevant. It also introduces the H_2SO_4 thermal decomposition process itself.

Chapter 2 covers the H_2SO_4 thermal decomposition process in more detail and presents equilibrium calculations demonstrating the high temperatures required for high SO_2 yields. Chapter 3 discusses the proposed membrane separation step and how it might be implemented. Process simulations are presented that demonstrate the potential SO_2 yield increases from the use of membrane separation.

Chapter 4 discusses porous membranes that may be suitable for the H_2SO_4 thermal decomposition process, including potential separation factors. Chapter 5 covers dense oxygen transport membranes and presents equilibrium calculations that are used to select a candidate material for the membrane for this process.

Chapter 6 describes the experimental apparatus designed and built to test the candidate material, as well as the fabrication of the membranes themselves. It also describes the analysis techniques used and the *FLUENT* simulations used to determine the optimum flow rate to use in the apparatus.

Chapter 7 presents the tests carried out during commissioning of the experimental apparatus, whilst Chapter 8 presents the main body of experimental results obtained.

Finally, Chapter 9 presents the overall conclusions from the work and future work that could be carried out on the topic.

1.2 The “hydrogen economy”

Concerns have grown in recent years about the over-reliance of modern society on fossil fuels. These concerns include:

- decreased supply security;
- environmental impact of carbon dioxide emissions;
- rising fossil fuel costs.

Current trends suggests that the European Union (EU) will import 80% of its gas and 90% of its oil requirements from foreign sources by 2030 (Steenberghen & Lopez 2008). These foreign sources are often located in politically unstable regions, reducing their reliability. Unreliable energy supplies could seriously damage the EU’s economy in the future.

As of 2008, transport accounted for >30% of final energy consumption in the EU (Steenberghen & Lopez 2008). Although vehicles are becoming cleaner, the use of transport is growing at a sufficient rate to negate the benefits. This is threatening the meeting of Kyoto Protocol emissions targets.

As a result of these issues, renewed interest is being shown in the concept of migrating to a hydrogen-based economy in the coming years. This would involve the phasing out of fossil fuel-driven transportation like cars and buses, and their replacement with hydrogen-powered vehicles utilising either combustion engines or electrochemical fuel cells. If a significant proportion of transportation were to shift from fossil fuels to hydrogen, very large scale hydrogen production facilities would ultimately be required, along with the associated delivery infrastructure (Agrawal et al. 2005).

Unlike fossil fuels, hydrogen is not an energy source but an energy vector, a means of transporting energy. It must be manufactured in as efficient a manner as possible to minimise the losses of the primary heat and/or electrical power.

Steam methane reforming is used to produce most industrial hydrogen at present (see Section 1.3.1) but this uses fossil fuel as a feedstock. Future sustainable hydrogen generating processes must use alternative feeds such as water.

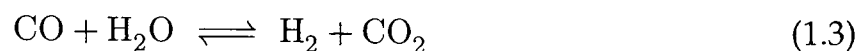
Generating the hydrogen is only one part of the implementation of a hydrogen economy. Where hydrogen is produced in large centralised facilities, it will be necessary to construct a transportation and storage network to transport it to the point of use. Steenberghen & Lopez (2008) estimate an EU-wide cost of 26 billion Euros to provide a filling station network with 20% of the stations of the current petrol filling network. They believe this to be a sufficiently numerous network to reach the critical mass required for widespread take-up of hydrogen as a transportation fuel.

1.3 Current hydrogen production processes

1.3.1 Steam methane reforming

96% of industrial hydrogen production today uses fossil fuels, with steam methane reforming (SMR) being the most common process (Ewan & Allen 2005). Modern processes for steam reforming of natural gas operate at 600-900°C, 5-40 bar and use a catalyst of nickel oxide supported on alumina (El-Bousiffi & Gunn 2007). The follow-

ing reactions occur in an SMR process:



It can be seen that the SMR process produces carbon dioxide as a byproduct. Steenberghen & Lopez (2008) believe that the short and medium-term development of the use of hydrogen as a transportation fuel will have to rely on SMR, as it is an established technology which is still currently the cheapest method of mass scale hydrogen production. The Joint Research Council estimates a “well to wheel” CO_2 emission of 80-85g/km for an SMR-derived hydrogen fuel cell vehicle in 2010. This compares to a total CO_2 emission of around 100g/km for a diesel hybrid vehicle. If these figures are accurate, they demonstrate that whilst SMR may need to be used as the primary hydrogen source for early adopters of hydrogen fuel cell vehicles, hydrogen production methods that do not use fossil fuel feedstocks will need to be employed eventually if the potential environmental benefits of a hydrogen economy are to be realised.

CO_2 sequestration can be used to reduce the greenhouse gas emissions to the atmosphere of a process. Research is ongoing into various methods of CO_2 sequestration, for example the injection of CO_2 into depleting oil wells in order to enhance oil recovery (Song 2006). Whilst CO_2 sequestration may reduce the carbon footprint of the SMR process, it will also increase the cost of the hydrogen produced. There is also a finite number of suitable oil wells, therefore CO_2 sequestration is not a long term solution.

1.3.2 Electrolysis

Water electrolysis is an established, proven technology for producing hydrogen. The standard process uses nickel electrodes with an electrolyte of approximately 30wt% KOH in water (Stojic et al. 2003). Electrolysers themselves are generally highly efficient. The efficiency of the electricity production process to a great extent defines the efficiency of the electrolysis process using that power. In the case of typical large power plant, this would limit an electrolytic process' efficiency to <40%. High temperature electrolysis is also in development (see Section 1.4).

1.3.3 Comparison of electricity generation processes

“Renewable” energy sources such as wind, solar and hydroelectric are generally considered to be more sustainable than fossil fuelled generation processes that overtly emit carbon dioxide. Nuclear energy is also promoted as a CO₂-free electricity generator.

Contrary to popular belief, nuclear power generation is not completely CO₂-free. Ailleret’s (2004) World Energy Council report detailed life cycle analyses of the environmental impact of a variety of energy generation systems. Their report states that the greenhouse gas emissions from a nuclear fuel cycle arise from the fossil fuel-based energy and electricity needed to mine and process uranium and for the fabrication of fuel cycle facilities, with most of the energy being consumed by uranium enrichment. The report goes on to state that uranium enrichment by gas diffusion consumes about 40 times more electricity than the gas centrifuge method. A chart from the report, presented as Figure 1.1, gives a lower and higher value for the CO₂ emissions arising from a nuclear fuel cycle. The higher value is based on uranium enrichment by the gas diffusion method, where the current US electricity production mix (65% fossil fuel-based) is used to generate the required electrical power for the enrichment. The lower limit refers to uranium enrichment either by the centrifuge method (as used in the UK) or by gas diffusion in a French facility where the electricity is produced by nuclear power.

Similarly, renewable energy sources are responsible for some CO₂ emissions during construction, etc. It can be seen that, on a whole life cycle analysis, nuclear power is comparable on CO₂ emissions with wind power and may even produce fewer CO₂ emissions than hydroelectric or photovoltaics.

A key consideration with electricity production is the process “energy density”. Renewable sources exhibit very low “energy density” (power output per unit land area required) in comparison to traditional large scale power stations. Vast amounts of land would be required to generate the power required for a large scale electrolytic hydrogen production facility. In contrast, nuclear power benefits from both high “energy density” and zero CO₂ operational emissions and would be a more suitable electricity generation technology for processes such as electrolytic hydrogen production.

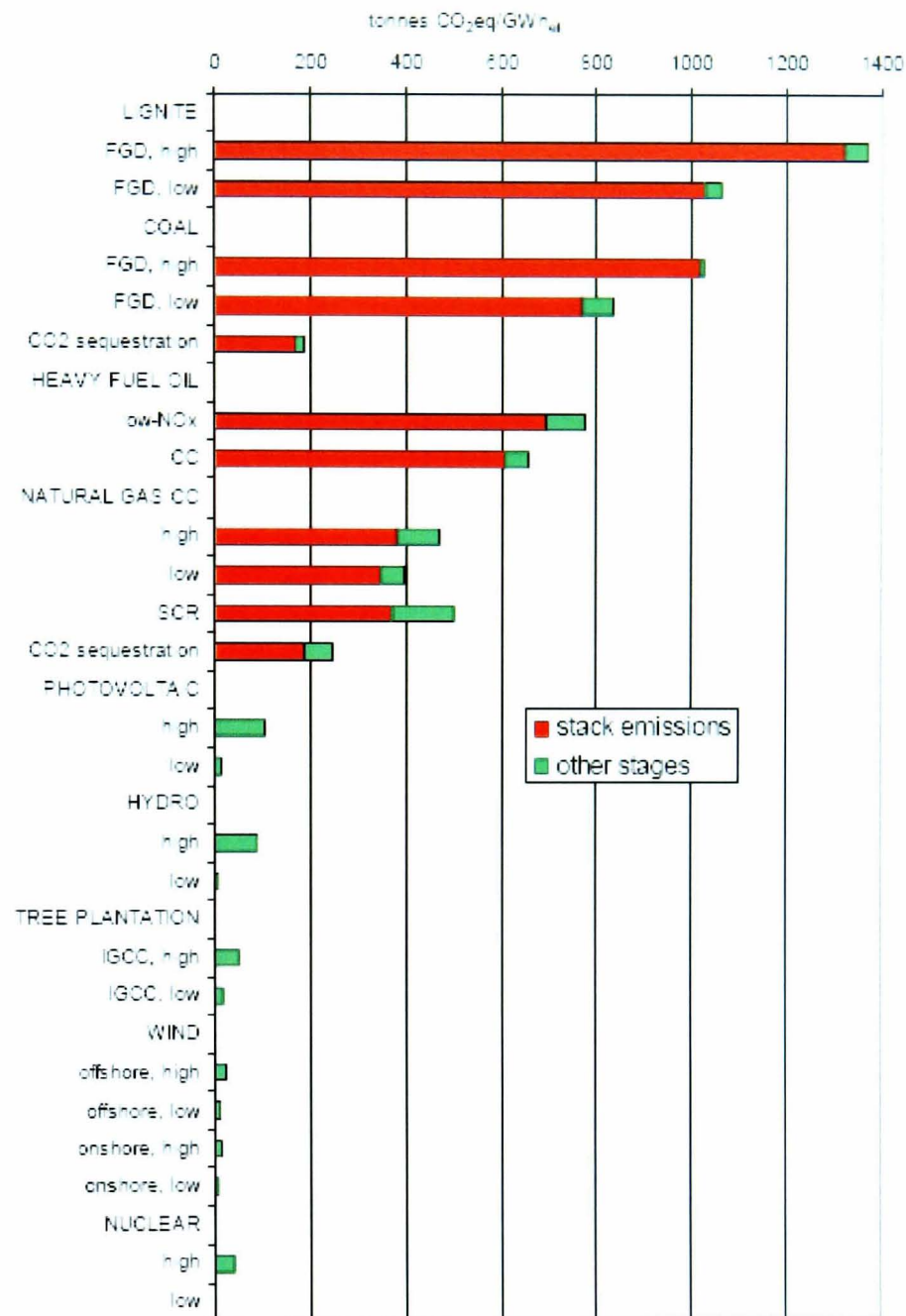


Figure 1.1: CO₂ produced by various electricity generation systems (Ailleret 2004)

1.4 Other hydrogen production processes

There is currently a great deal of research effort worldwide into new hydrogen production processes that are more environmentally friendly than SMR. Momirlan & Veziroglu's (2002) review covers electrochemical, thermochemical and photochemical/catalytic/electrochemical/biological processes. The main electrochemical (electrolytic) processes are alkaline electrolysis, polymer membrane electrolysis and ceramic oxide membrane (high temperature) electrolysis. The photo- processes include direct catalysed photochemical reduction of water, decomposition of water us-

ing light-activated semiconductor layers (i.e. solar energy storage by chemical means), and photosynthesis of hydrogen from substrates such as sugar cane juice using photosynthetic bacteria.

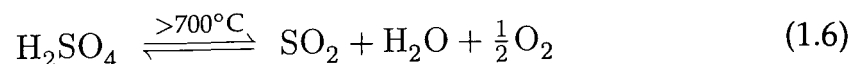
Thermochemical and hybrid thermochemical/electrochemical cycles are massive scale processes producing hydrogen and oxygen, utilising water as the only feedstock and producing no waste streams. They are discussed in a National Research Council (2004) report into hydrogen production. The report indicates that, in the future, a thermochemical process utilising high temperature nuclear heat may have the lowest unit cost of the non fossil-fuelled centralised production processes. Others requiring natural gas and coal (with and without CO₂ sequestration) have lower predicted unit costs. The calculated unit cost takes into account both the cost of production in a large scale centralised plant and the cost of transportation and storage of the hydrogen.

There are many hundreds of possible hydrogen-producing thermochemical cycles, however very few of these cycles have been investigated intensively for viability, both technical and economic (Abanades et al. 2006). One such cycle is the sulphur-iodine cycle.

1.5 The Sulphur-Iodine Cycle

1.5.1 Cycle steps

The most heavily developed pure thermochemical hydrogen production cycle to date is the sulphur-iodine (SI) cycle, originally developed by General Atomics in the 1970s. It is considered to be one of the most promising near-term options for hydrogen production from solar energy (Perkins & Weimer 2004). The SI cycle uses a closed cycle of three reactions to achieve the overall result of decomposing water to hydrogen and oxygen:



The “Bunsen reaction” (equation 1.4) is a liquid phase reaction carried out at around 130°C. The hydriodic acid produced is decomposed, producing the hydrogen product and iodine which is recycled to the Bunsen reaction. Similarly, the sulphuric acid produced by the Bunsen reaction is decomposed at >700°C, producing the oxygen

product and sulphur dioxide and water which are recycled. The iodine and sulphur based inventory therefore exists in a closed loop. Make-up water is the only reactant added during normal operation.

The theoretical maximum efficiency with which the SI cycle can operate is 51%, with a realistic efficiency of 36%, based on current flowsheets (Goldstein et al. 2005). Combined hydrogen/electricity producing plants operating an SI cycle linked to a high temperature nuclear reactor could have efficiencies of up to 60% (Forsberg 2003a). The equilibrium for H_2SO_4 decomposition lies strongly to the left as written in equation 1.6 at low temperatures, hence the high temperatures required. This is described in greater detail in Chapter 2.

1.5.2 Recent SI cycle experimental work

Funk (2001) describes in great detail the process by which thermochemical cycles were selected for consideration during the first period of interest in the 1970s and early 1980s. He notes that the SI cycle was developed in that first period to the point of construction of a preliminary bench scale experimental rig.

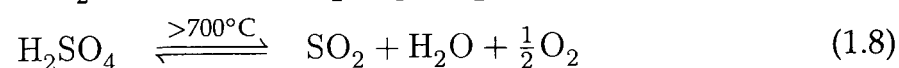
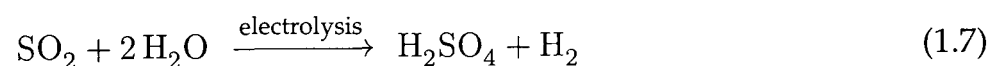
The Japanese have been the most active in recent years in their development of the SI cycle. The Japan Atomic Energy Agency (JAEA) has demonstrated operation of a completely closed loop, small scale SI cycle (Kubo et al. 2004). The cycle operated with good stability for 20 hours. The test demonstrated that closed loop operation is possible, however the apparatus used was only suitable for laboratory use. The materials of construction were quartz, glass and Teflon (Wu & Onuki 2005) and therefore the entire cycle had to be operated at atmospheric pressure. In order to reduce plant size and hydrogen transport costs, a commercial plant is likely to operate at a minimum of 10 bar pressure, which is impractical for glass components. Additionally, the heat required for the sulphuric acid and hydriodic acid sections was provided by electrical heaters, which would be unacceptably inefficient for large scale use. Pilot scale studies currently underway are using electrically heated helium as the heat source for the SI cycle. Engineering materials are also being tested. In parallel, design work is underway for the HTTR-IS process whereby an SI cycle will be linked, via an intermediate heat exchanger, to the high temperature engineering test nuclear reactor (HTTR) (Sakaba et al. 2007). The basic design of the HTTR-IS system is hoped to be completed in 2010.

The International Nuclear Energy Research Initiative (INERI) project, a collaboration between Sandia National Laboratory, General Atomics and the French nuclear energy agency (CEA), is currently constructing an integrated lab scale (ILS) demon-

stration SI cycle capable of producing 100-200 l/hr of H₂ (Russ et al. 2008). Each step in the cycle has been constructed in a modular unit or “skid” by the partners. There are four skids in total: sulphuric acid decomposition, hydriodic acid decomposition, Bunsen reaction, and an interface skid. These modular units are now located at General Atomics. Personal communication with a member of this research group indicates that there have been difficulties with the Bunsen reaction section, in that the amount of H₂SO₄ present in the HI phase produced is too high and subsequent scrubbing is required before passing the phase to the hydriodic acid decomposition section (Buckingham 2009). Funding to progress this project is currently uncertain.

1.6 The Hybrid Sulphur cycle

The hybrid sulphur (HyS) cycle, originally developed by Westinghouse in the late 1970s, shares the sulphuric acid decomposition step with the SI cycle. The HyS cycle is a two step hybrid process. Instead of reacting the SO₂ with iodine, as in the SI cycle, it is electrolysed in the presence of water, producing hydrogen directly and regenerating the sulphuric acid.



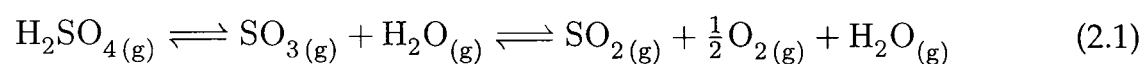
The theoretical voltage required to electrolyse SO₂ (0.17V) is significantly lower than that of traditional water electrolysis (1.23V) (Jeong & Kazimi 2007). Because of this, the electrolyser power required per unit of hydrogen production is much lower.

Chapter 2

Sulphuric acid thermal decomposition

The thermal decomposition of sulphuric acid is a process step common to two hydrogen production processes which are currently receiving worldwide attention, the sulphur-iodine (SI) and hybrid sulphur (HyS) cycles.

The overall reaction involves the decomposition of sulphuric acid (H_2SO_4) to sulphur dioxide (SO_2), oxygen (O_2) and water (H_2O). An intermediate step exists, whereby the sulphuric acid is first decomposed to sulphur trioxide (SO_3) and water.



For the first stage of the decomposition (to SO_3), $\Delta G=0$ at $\approx 670\text{K}$, at which temperature $\Delta H \approx +95\text{kJ/mol}$. Similarly, for the decomposition of SO_3 to SO_2 , $\Delta G=0$ at $\approx 970\text{K}$, at which temperature $\Delta H \approx +97\text{kJ/mol}$ (Goldstein et al. 2005). The high temperature required for negative free energy change in each step of the process indicates the high temperatures required in order to obtain meaningful equilibrium SO_2 yields. Simulations have been carried out to quantify the equilibrium yields from the two reactions taking place.

2.1 Process flowsheets

A flowsheet for the sulphuric acid thermal decomposition section of the SI cycle was produced by Ozturk et al. (1995). The paper claims that, providing the rest of the cycle is as originally designed, this new sulphuric acid decomposition section increases the

2.2 Decomposer literature designs

Kim et al. (2008) present an acid decomposer design consisting of two shell and tube decomposers, the first for H_2SO_4 decomposition to SO_3 and the second for SO_3 decomposition to SO_2 . Their design is heated by an intermediate helium heating loop from a Very High Temperature Nuclear Reactor (VHTR) and achieves an SO_3 decomposition conversion of 66% at a nominal outlet temperature of 850°C , and 7 bar pressure.

As part of the USA National Hydrogen Initiative (NHI), a silicon carbide integrated decomposer (SID) has been designed (Nagarajan et al. 2008) that combines a sulphuric acid boiler, superheater, decomposer and heat recuperator into a single unit (Figure 2.2). The parametric study carried out on the design yielded a wide range of SO_3 conversions, but a general value of 30-60% is quoted.

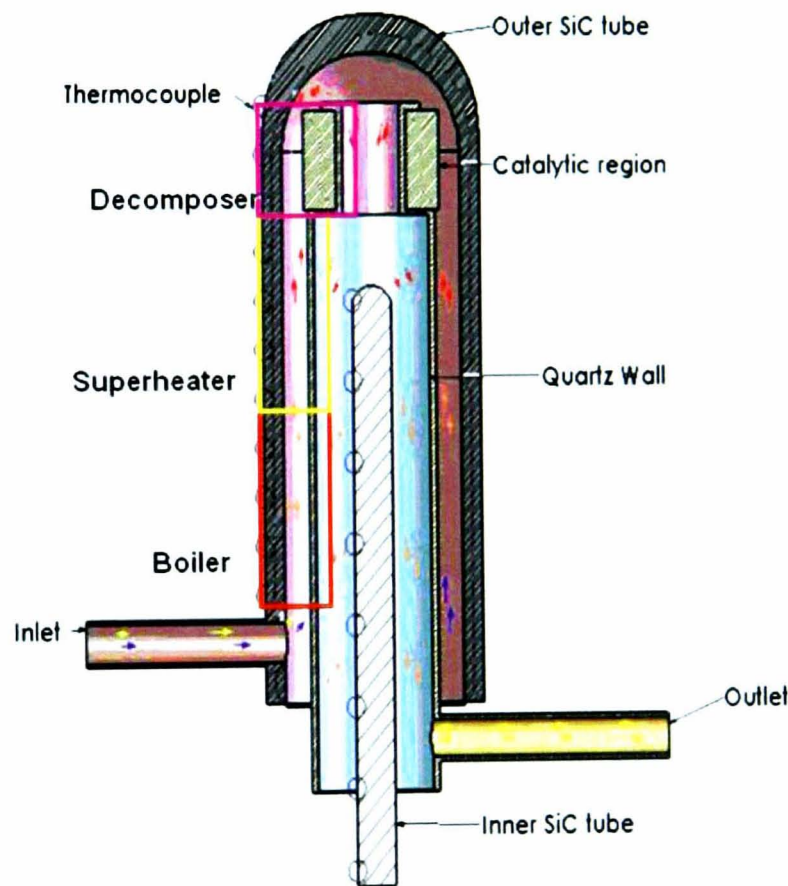


Figure 2.2: *National Hydrogen Initiative Silicon Carbide Integrated Decomposer (Nagarajan 2008)*

Kuchi et al. (2008) present a similar tranche of modelling work on a more conventional shell and tube decomposer unit. They quote SO_3 conversion of up to 93% at 1 bara and a hot side helium feed temperature of 950°C , which would appear to be simply

the equilibrium composition (see Section 2.8) and hence may be an over-estimate of the SO_3 conversion that would be seen in practice with such a unit.

2.3 Catalyst selection

The sulphuric acid decomposition process usually employs a heterogeneous catalysed bed reactor. The extreme operating conditions of the process place great demands on the catalyst.

Some of the earlier work on sulphur trioxide decomposition was carried out by Brittain & Hildenbrand (1983) as an extension of work carried out on catalysts for magnesium sulphate decomposition. The conditions used were temperatures of 600-1000K and an SO_3 initial partial pressure of around 1×10^{-6} atm. The temperatures used are lower than those expected to be used in the SI cycle, and the SO_3 partial pressure is a tiny fraction of that to be used in the SI process and hence the catalyst longevity estimated in this study could not be applied directly to the SI cycle. The study found that platinum and ruthenium catalysed SO_3 at the lowest temperatures, with detectable decomposition occurring at 593K. Metal oxides which were found to catalyse the reaction were V_2O_4 , Cr_2O_3 , Fe_2O_3 , NiO , Mn_3O_4 , CoO and ZnO . Tests with SO_3 initial partial pressures of up to 88×10^{-6} atm demonstrated that the temperature at the onset of decomposition increases with increasing pressure.

Tagawa & Endo (1989) expanded this work, with specific focus on suitable catalysts for sulphuric acid thermal decomposition. Aqueous sulphuric acid at 67wt% was evaporated at 550°C , which is closer to the conditions likely to be found in a commercial SI cycle. However, a nitrogen carrier stream was used to carry the acid into the reactor, reducing the acid concentration to 4-12 mol%, which is unrealistically low for an integrated SI cycle. This work acknowledges that platinum is the reference catalyst for this process, producing near equilibrium conversion of SO_3 to SO_2 at temperatures above 600°C . Fe_2O_3 catalyst was found to produce conversion comparable to platinum at temperatures above 820°C , whilst Cr_2O_3 was found to produce conversion comparable to platinum at temperatures above 700°C . For each of the catalysts tested, individual plots of space velocity versus SO_3 conversion for different temperatures are presented. However, the values on the overall comparison graph do not match with the individual plots, which reduces confidence in the conclusions presented. Tagawa proposes that the higher the instability of a metal sulphate, the more catalytically active the corresponding metal oxide. Iron and chromium have the most unstable sulphates of the metals investigated, which results in the high conversions

stated earlier.

Barbarossa et al. (2006) carried out bench scale sulphuric acid thermal decomposition using an iron (III) oxide catalyst and a silver palladium intermetallic alloy. The Ag-Pd catalyst was in the form of 5mm diameter rings. Barbarossa proposed that the catalytically active species was PdO. The Fe_2O_3 catalyst was in the form of nanometric particles on quartz wool. Whilst this form facilitates a very high surface area to volume ratio, it is not a preparation technique that is transferable to large scale processes. Of the two catalysts, Ag-Pd appeared to produce higher conversions at lower temperatures ($\leq 873\text{K}$), with Fe_2O_3 producing higher conversions at $> 873\text{K}$.

Ginosar et al. (2005) from Idaho National Laboratory presented the most realistic catalyst study to date for sulphuric acid decomposition. Platinum, on a number of support materials, was used as the catalyst. Concentrated sulphuric acid was vaporised and fed to the catalyst bed, creating similar conditions to those found in the SI cycle sulphuric acid decomposition section. Information on the experimental apparatus and procedure used by Ginosar will prove particularly useful if full sulphuric acid decomposition is carried out in the future (see Section 9.1.2). Most of the catalysts were severely structurally degraded with less than six hours of operation at 800°C . However the platinum on a TiO_2 support did not show such degradation and was subsequently found to demonstrate a high level of catalytic activity for 200 hours of continuous operation. Whilst this is encouraging, the high cost of the catalyst means that continuous operation for much longer than 200 hours will be required to make the process economically viable.

Ginosar et al. (2007) reported on studies of 0.1-0.2% platinum catalyst supported on alumina, titania and zirconia. These studies were carried out under process conditions representative of those that would be encountered in an atmospheric pressure industrial sulphuric acid decomposition process, i.e. $800\text{-}850^\circ\text{C}$ and 96wt% sulphuric acid feed. Previous studies have used more idealised conditions, with dilute acid feeds. Initial SO_2 yields at 850°C were 45% for Pt/ ZrO_2 , 25% for Pt/ TiO_2 and 50% for Pt/ Al_2O_3 . A long term test was performed using the Pt/ TiO_2 catalyst, with the 850°C SO_2 yield increasing to $\approx 32\%$ after 10 hours on stream, followed by a roughly linear decrease to $\approx 23\%$ after 240 hours on stream. After 6 hours the catalyst had not lost an appreciable amount of platinum, but after 200 hours it had suffered a 30wt% platinum loss. None of the catalysts investigated showed new sulphurous phases under x-ray diffraction (XRD).

Petkovic et al. (2008) continued the work described above and attempted to find the causes of the platinum loss and deactivation of the Pt/ TiO_2 catalyst. A further long

term (548 hour) test was carried out on a 1% Pt/TiO₂ catalyst at 850°C and atmospheric pressure. It was found that the deposited platinum was sintered and oxidised and some was lost by volatilisation. The catalyst activity decreased for the first 66 hours on stream, recovered until 102 hours had elapsed, then decreased slowly for the remainder of the run. Petkovic states that "the activity profile suggested that a complex dynamical situation involving platinum sintering, oxidation and sublimation, along with TiO₂ morphological changes, affected catalyst activity in a non-monotonic way."

2.4 Materials of construction

Ginosar et al. (2007) and Petkovic et al.'s (2008) experimental apparatus was constructed from Teflon tubing, glass, and a quartz reactor. Whilst these are suitable materials for a bench scale experiment, they are not suitable for a large scale plant. Finding engineering materials suitable for this process is an area of research in itself. Savitsky et al. (1982) first tested the corrosion resistance of a number of alloys in both boiling 94% sulphuric acid, testing for liquid corrosion, and, in "an atmosphere of SO₂, SO₃, O₂ and H₂O", tested for gas corrosion. The composition of the gaseous atmosphere was not explicitly stated, though presumably it was specified to represent the atmosphere expected within a sulphuric acid decomposition reactor. The most corrosion resistant material in the boiling liquid was the alloy CrNi45Al, with a sound metal loss equivalent to 4.23mm per year. This is a large corrosion loss and is almost certainly unacceptable for a large scale, continuous production environment. The most resistant material in the gaseous test environment was the alloy B1950.

A series of three papers was published in the 1980s by the Ispra research centre on the results of corrosion resistance studies for Ispra's CRISTINA thermochemical cycle for hydrogen production (Coen Porisini 1983, Coen Porisini 1985, Coen Porisini 1989). The CRISTINA process decomposes sulphuric acid using air as an energy vector, hence the conditions are much less corrosive than those found in an SI cycle sulphuric acid decomposition section. The results still provide useful information on potential materials candidates, however.

For the high temperature section, carrying gases at 400-900°C, stainless steel AISI 310 was found to be suitable at temperatures up to 700°C, with Incoloy 800 suitable at up to 900°C. Tubes fabricated from these alloys operated as tubular decomposers for 8500 hours at 1 bar pressure, using the readily formed iron oxide layer as the catalyst. The sound metal loss was of the order of 0.5mm per year, which is much more

acceptable than those values found by Savitsky. Coen Porisini noted that maximum corrosion occurred where surfaces were exposed to an SO_3 rich atmosphere at a relatively low temperature. This indicates that maintaining a high wall temperature is important where there is a significant proportion of SO_3 present. The earlier papers comment that the silicon and chromium content of an alloy are important factors in corrosion resistance under the type of conditions found in a sulphuric acid decomposer. Silicon content of around 1wt% is suggested to be optimum, with chromium content of greater than 18wt% deemed to be necessary.

Design work such as that reported by Ponyavin et al. (2008) and that currently underway as part of the European Union HycycleS project is concentrating on the use of silicon carbide (SiC) as an engineering material for solar-heated decomposition of sulphuric acid. SiC has been shown to be chemically resistant to the conditions required for sulphuric acid decomposition.

2.5 Process heat sources

The National Research Council (2004) comments that only future high temperature gas cooled nuclear reactors could supply the necessary temperatures for these hydrogen-producing thermochemical processes. The Department of Energy in the USA is conducting research into these so-called "Generation IV" reactor types and the NRC supports nuclear hydrogen generation research as "a small incremental effort to the nuclear-to-power program".

Amongst the nuclear reactor types that could be employed for hydrogen generation is the South African designed pebble bed modular reactor, or PBMR. The PBMR employs a helium coolant which enters the reactor at 500°C and exits the reactor at 900°C (Koster et al. 2003). This temperature is suitable for use with thermochemical hydrogen generation cycles, although higher temperatures would be ideal. The design is both passively safe and close to commercialisation, with a demonstration reactor currently under consideration in South Africa. PBMR, in partnership with Westinghouse, have studied a number of heat transfer configurations for the purpose of linking the PBMR to the HyS cycle (Elder & Allen 2009). Initial estimates suggest that hydrogen could be produced from such a system at a cost of \$2-3/kg along with electricity at an efficiency of approximately 38%.

The required heat could also be provided by concentrated solar energy, as described by Huang & T-Raissi's (2005) flowsheets. The higher temperatures ($< 1200^\circ\text{C}$) available from a solar heat source allow higher SO_3 conversions to be achieved (see Section 2.8),

however the lower energy density of concentrated solar power means the available heat duty may be less than that available from a nuclear reactor.

Kodama & Gokon (2007) present a comprehensive review of thermochemical cycles utilising high temperature solar heat. Of the various types of large scale solar collectors, the parabolic trough is the only type not suitable for thermochemical hydrogen production, as their low concentration ratio only allows a maximum fluid temperature of 400°C, too low for these cycles. All of the other types (heliostat field with central tower, parabolic dish, and double concentrator) have maximum temperatures above 1300°C and hence are suitable. The absorption efficiency of a solar collector at very high temperatures is limited by radiative losses. Consequently, the optimum operation temperature for a solar collector of concentration ratio 5000 is calculated to be 1200°C, when the collector is assumed to be a black body radiator.

Kodama & Gokon (2007) discusses the design of a solar-powered CRISTINA process in the 1980s for H₂SO₄ thermal decomposition. This contacted superheated air (heated by solar power) with liquid H₂SO₄ in adiabatic reactors to perform the heating and decomposition steps. It was envisaged that the plant would be run in reverse overnight, reacting some of the SO₂ produced during the day with oxygen from the air to maintain the process temperature and prevent thermal cycling issues. The requirement for very expensive materials such as Incoloy for the heat recuperators is noted as a challenge to this process.

Kodama & Gokon (2007) also discusses the solar thermal decomposition process investigated by the EU HYTHEC consortium, the predecessor of the HycycleS project with which this work is associated. The HYTHEC program investigated the use of a solar tower performing H₂SO₄ decomposition at 1200°C. The German aerospace centre (DLR), in their work for HYTHEC, developed a porous silicon carbide (SiC) solar receiver into which liquid sulphuric acid could be introduced. The solar energy would pass through a quartz window into the reactor, decomposing the H₂SO₄ without catalyst, because of the very high temperature employed.

2.6 Equilibrium calculation validation

The *HSC Chemistry* software package was used to calculate equilibrium compositions relevant to sulphuric acid decomposition. Firstly, results from *HSC Chemistry* simulations were compared to values from literature in order to confirm the validity of the data produced.

Results obtained here using *HSC Chemistry* are compared to other calculations in the

literature. The results are not being compared to experimental data. For a catalysed process such as this it is expected that experimental yields may be lower than at equilibrium for certain temperatures. For example, although platinum has been reported to give near-equilibrium conversions above 600°C, iron and chromium oxides only exhibit near-equilibrium performance at 820°C and 700°C respectively (Tagawa & Endo 1989). Section 2.3 covers other literature on possible catalysts for the process.

2.6.1 Comparison to literature SO₃ decomposition data

This set of simulations was carried out using *HSC Chemistry* to predict the equilibrium composition of the products of SO₃ decomposition at temperatures between 600-1400K and 0.1 bara. The predictions were based on the Gibbs free energy minimisation technique. The starting composition of the mixture was taken to be 100 kmol SO₃, zero SO₂ and zero O₂.

Barbarossa et al. (2006) published the results of similar equilibrium calculations using *Thermocalc* at a pressure of 0.1 bara. Barbarossa quotes a large number of minor species and complexes to be considered when conducting equilibrium calculations for this system, over and above the major species of SO₃, SO₂, O₂ and H₂O. These minor species and complexes were SO, H₂S, H, HO, HSO, SOH, HO₂, HS, H₂, H₂SO, HSOH, H₂O₂, H₂S₂, O, O₃, S, S₂, S₃, S₄, S₅, S₆, S₇, S₈, SO₃-H₂O, SO₃-2H₂O, SO₃-3H₂O, H₂SO₄-H₂O, and H₂SO₄-2H₂O.

In order to assess the effect of these minor species, a further *HSC Chemistry* simulation was run at a pressure of 0.1 bara using all of the minor species available from the *HSC Chemistry* database. The system was defined with a starting composition of 100 kmol SO₃ and zero of each of the following gaseous species: SO₂, O₂, SO, H₂S, H⁺, HO, HO²⁻, HS, H₂, H₂O₂, H₂S₂, O⁻, O₃, S, S₂, S₃, S₄, S₅, S₆, S₇, and S₈.

Results

The output from the simulations, along with the Barbarossa results, are presented in Figure 2.3.

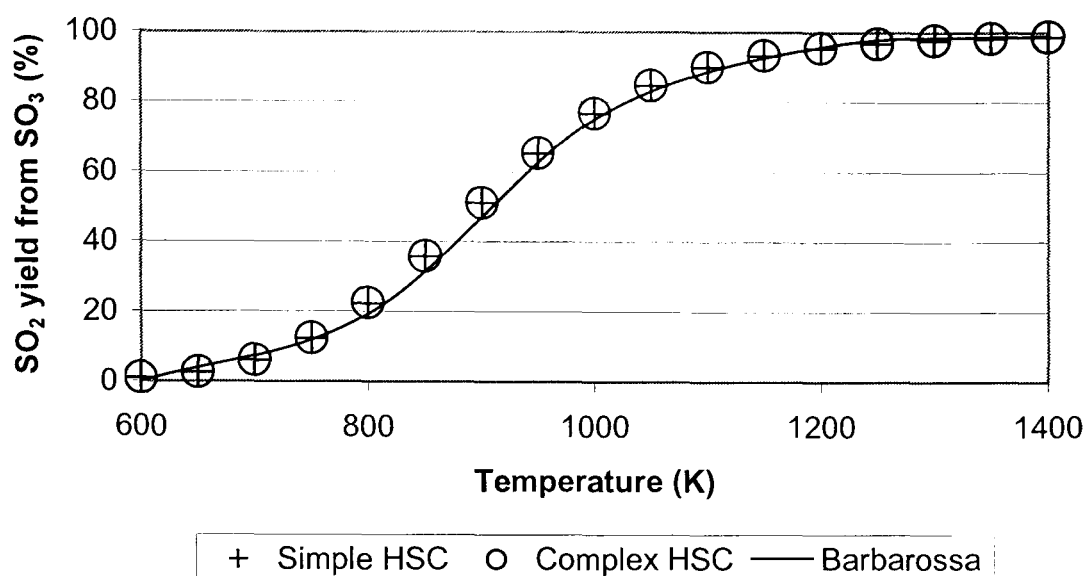


Figure 2.3: Variation in SO_3 equilibrium conversion to SO_2 with temperature at 0.1 bara, as calculated by HSC Chemistry and Barbarossa (using Thermocalc)

The HSC Chemistry values at 0.1 bara exhibit a variation in SO_2 yield between the complex and simple simulations of $<0.5\%$ over the temperature range 700-1600K. Because of the magnitude of this variation, it was not considered necessary to apply the minor species to future work.

2.6.2 Comparison to literature H_2SO_4 decomposition data

Brutti et al. (2007) also quotes the results of equilibrium calculations for this process as part of an experimental investigation. The calculations were made using Thermocalc with a feed of 1 mol of pure H_2SO_4 at 0.61 bara and 800-1300K. These conditions were entered into HSC Chemistry and the results compared.

Results

Figure 2.4 shows the comparison between the literature data and that calculated by HSC Chemistry. It can be clearly seen that the two sets of data are in very good agreement and hence the equilibrium data produced by the HSC Chemistry package is further validated.

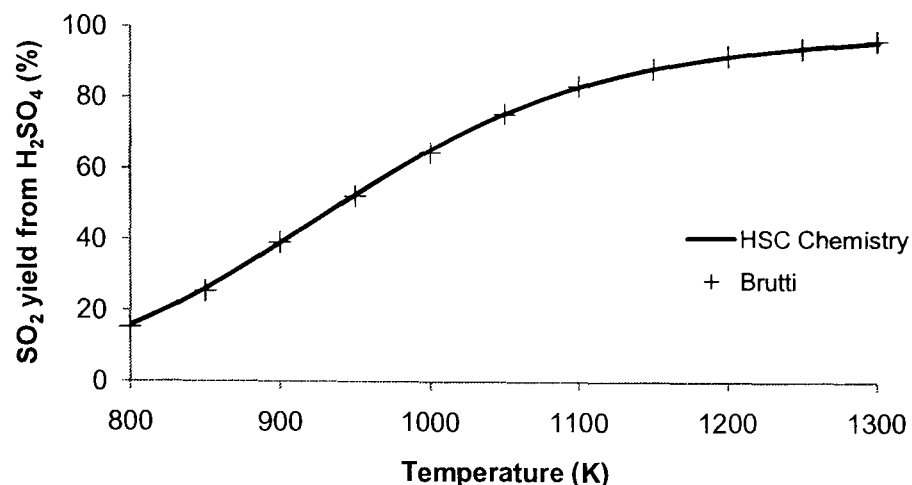


Figure 2.4: Comparison of SO₂ equilibrium yield calculations from HSC Chemistry and Brutti (2007). Feed of 1 mol pure H₂SO₄ at 0.61 bara.

2.7 SO₃/H₂SO₄ equilibrium calculations

2.7.1 Aim

The aim of these simulations was to calculate the equilibrium yield of sulphur trioxide from sulphuric acid at a range of temperatures. This data, in conjunction with subsequent simulations of sulphur dioxide production yields, aims to show that the decomposition of H₂SO₄ to SO₃ is not the yield limiting step in the process.

2.7.2 Method

The simulations were carried out using the *HSC Chemistry* software package. Given a list of components present, this calculates the equilibrium composition of the components using the Gibbs free energy minimisation technique.

The species modelled as taking part in this equilibrium system were H₂SO₄, H₂O and SO₃, i.e. those species participating in the first reaction of the decomposition process.

The starting composition of the gas was taken to be 100 kmol H₂SO₄, zero SO₃ and zero H₂O. The pressure was set at 1 bara.

2.7.3 Results

Figure 2.5 shows the results of the equilibrium calculations over the temperature range of interest. The equilibrium yield of SO₃ was calculated as 90% at 734K, 95% at 773K

and 99% at 880K. As the following work will show, SO₃ decomposition only proceeds meaningfully at temperatures in excess of 900K and consequently it can be assumed for future calculations that complete decomposition of H₂SO₄ to SO₃ and H₂O has occurred in the SO₃ decomposition process operating temperature range.

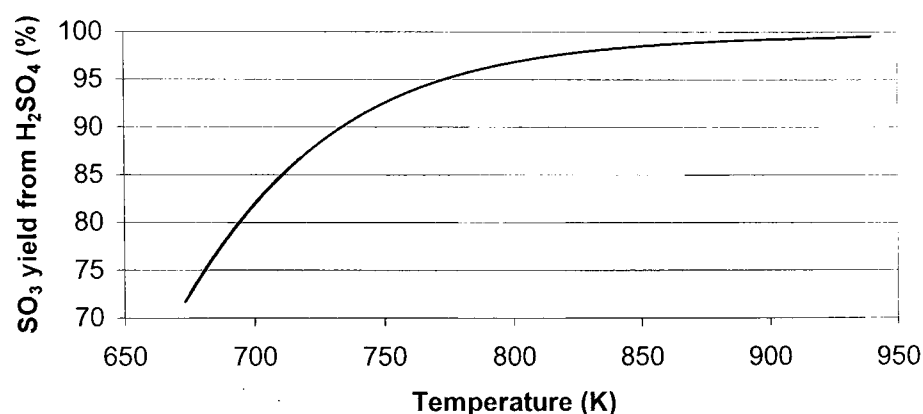


Figure 2.5: Variation in SO₃ equilibrium yield from H₂SO₄ at 1 bara, as calculated by HSC Chemistry

2.8 SO₂/H₂SO₄ equilibrium calculations

2.8.1 Aim

These simulations aim to show the equilibrium yield of sulphur dioxide attainable from an aqueous sulphuric acid feed as used in literature process flowsheets.

2.8.2 Method

HSC Chemistry was programmed with a feed of 100 kmol of H₂SO₄ and 42.86 kmol of H₂O, the same acid concentration (92.7wt%) fed to the decomposer in the General Atomics SI cycle flowsheet (Ozturk et al. 1995). Other components made available were SO₃, SO₂ and O₂, all in the gaseous phase. The equilibrium composition was calculated at 600-1200°C and at pressures of 0.1, 1, 10 and 20 bara.

2.8.3 Results

The SO₂ yields calculated by HSC Chemistry are shown in Figure 2.6. It can be seen that there is a steep decrease in SO₂ yield with increasing pressure in the lower pressure range, with the decrease less pronounced at higher pressures. Figure 2.7 demonstrates this at 850°C.

These results can be used to provide some context to the SO₃ decomposer design proposed by Kim et al. (2008) that achieved 66% SO₃ conversion at a nominal outlet temperature of 850°C, pressure of 7.09 bara, and a feed of 80% SO₃ with trace H₂SO₄ and balance water. Comparison with the equilibrium calculations performed here would suggest that this decomposer design is producing near-equilibrium SO₂ yields. This is however a relatively low yield considering the very high temperatures employed.

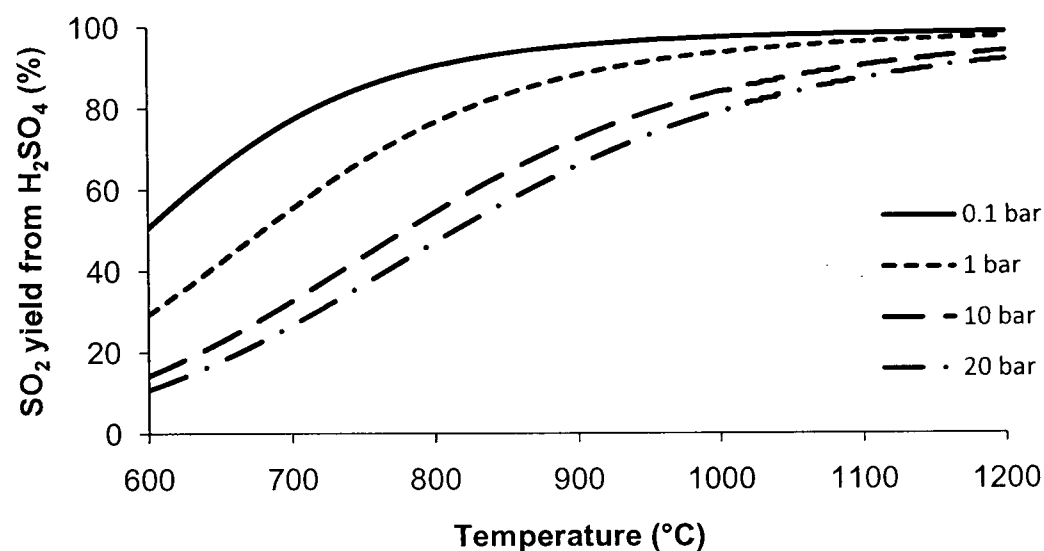


Figure 2.6: Equilibrium SO₂ yield from H₂SO₄ at 600-1200°C, 0.1-20 bara and 92.7wt% acid feed. Calculated by HSC Chemistry. The initial composition was 100 kmol H₂SO₄, 42.86 kmol H₂O and zero SO₃, SO₂ and O₂.

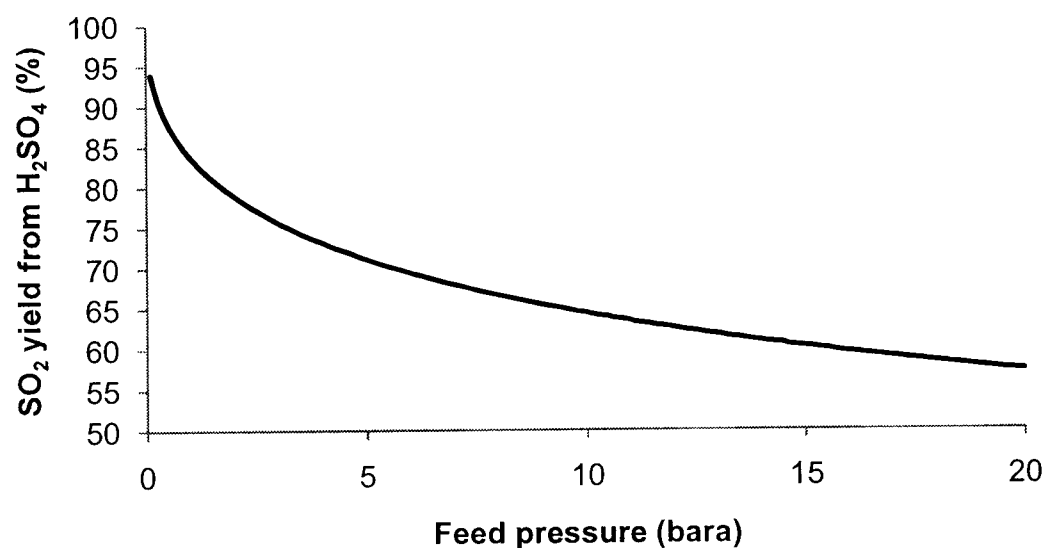


Figure 2.7: Equilibrium SO₂ yield from H₂SO₄ at 850°C, 0.1-20 bara and 92.7wt% acid feed. Calculated by HSC Chemistry. The initial composition was 100 kmol H₂SO₄, 42.86 kmol H₂O and zero SO₃, SO₂ and O₂.

2.9 Conclusions

The equilibrium compositions calculated in Section 2.6 show the large change in SO_2 yield with temperature over the temperature range 800-1250K. It can be seen that there is an opportunity to significantly increase conversion beyond equilibrium values in this temperature range. The following chapter presents the proposed membrane separation, intended to increase SO_2 yield at lower temperatures.

Chapter 3

Proposed membrane process: introduction and simulations

The equilibrium data presented in Section 2.8 illustrated the low sulphur dioxide yields that can be achieved using a standard equilibrium catalytic reactor. If the process SO_2 yield could be increased at relatively low temperatures, it would enable the use of a more diverse range of heat sources.

It is proposed that by adding a membrane separation step to the H_2SO_4 decomposition process, the yield of SO_2 at a given temperature may be increased (Zaman & Chakma 1994).

Once a gaseous reaction has reached its equilibrium composition, selective removal of one or more of the species present will cause the new mixture to come to a new equilibrium. Examination of the sulphur trioxide decomposition reaction



indicates that, according to Le Chatelier's Principle, removal of a proportion of the SO_2 and/or O_2 should cause the equilibrium to move to the right as written, causing a greater proportion of the SO_3 to decompose than would be the case for a simple equilibrium process at that temperature. Removal of water from the process could have a similar effect.

The membrane separation could take two forms:

- Standard catalytic reactor, with a membrane separator downstream and re-tentate recycling;

- Use of a catalytic membrane reactor (CMR) in lieu of the standard catalytic reactor.

At the present time, peer-reviewed literature does not exist for a high temperature membrane process associated with sulphuric acid thermal decomposition. Forsberg (2003b) presented the ongoing porous membrane research of the Oak Ridge National Laboratory in the USA at the 2003 American Nuclear Society Winter Meeting. The presentation reiterated the potential benefits of using a membrane separation in this process, suggesting that the process peak temperature could be reduced to 650-750°C. A graph showing the variation of SO₂ conversion with temperature for various pressures was presented. The values correspond to those calculated in Chapter 3 using process simulation software such as *Prosim* and *HSC Chemistry*. Forsberg speculates that the permeance of a 'nanoporous' membrane increases with temperature, rather than decreasing, as would be the case with a mesoporous membrane exhibiting Knudsen flow behaviour. A nanoporous membrane is defined as having nominal pore diameters of less than 2nm. This unusual correlation is attributed by Forsberg to "thermally activated diffusion", with data for the separation of He and SF₆ presented as proof. This is discussed further in Section 4.3.

3.1 Downstream membrane separation

A separation membrane placed downstream of the equilibrium reactor could permit a stream of non-equilibrium composition to be removed from the process. A fraction of the retentate is then recycled to the reactor feed, with the remaining retentate removed as the process product. A notional process of this type is illustrated in Figure 3.1.

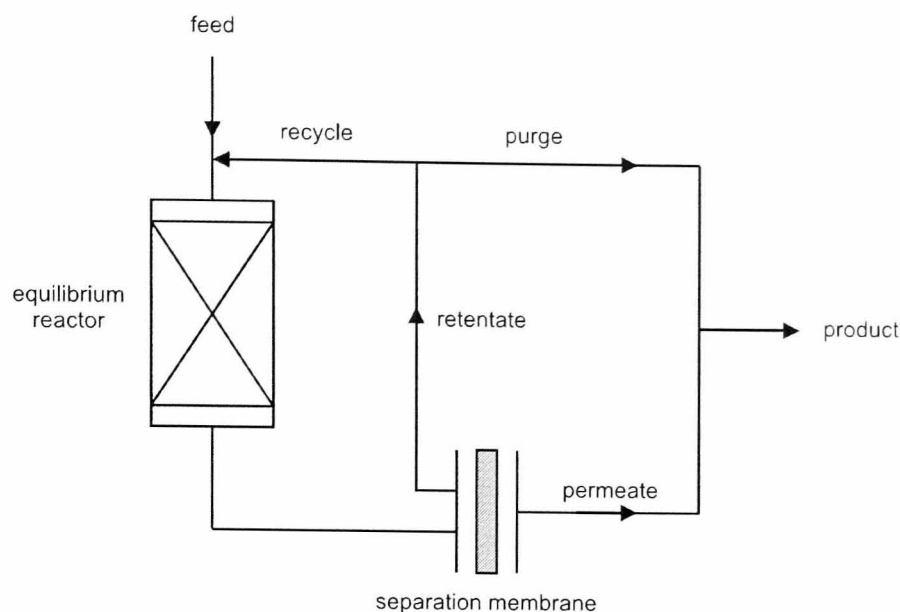


Figure 3.1: Schematic of downstream membrane separation of products of a H_2SO_4 thermal decomposition equilibrium reactor.

Given that the process shown in Figure 3.1 would operate at very high temperature, flow around the recycle loop could not be easily achieved by a conventional compressor. An ejector could be employed at the mixing junction between the feed and recycle streams, with the process feed as the primary flow and the recycle stream as the secondary flow. By pressurising the feed stream at a point in the process where conditions are less severe, the problem of pumping the high temperature streams may be avoided.

The purge and permeate streams do not necessarily have to be combined. It may be that the permeate from some membranes is a saleable product in its own right.

3.2 Catalytic membrane reactor

A catalytic membrane reactor (CMR) would replace the normal equilibrium reactor. One form of the CMR, as depicted in Figure 3.2, employs a number of tubular membranes inserted into a catalyst bed. The membranes selectively allow some products to permeate out of the catalyst bed, continuously shifting the reaction equilibrium in the manner described in Section 3.1 and therefore potentially allowing a much greater yield of SO_2 than would be possible using a single equilibrium reactor. This is an application of the “extractor” operating mode described by Julbe et al. (2001).

Strictly speaking, the type of reactor described above could be known as an inert membrane packed bed reactor (IMPBR) or, if the membrane surface is catalytic, a packed

bed catalytic membrane reactor (PBCMR) (Zaman & Chakma 1994). However for simplicity it will be referred to generically as a CMR throughout this work.

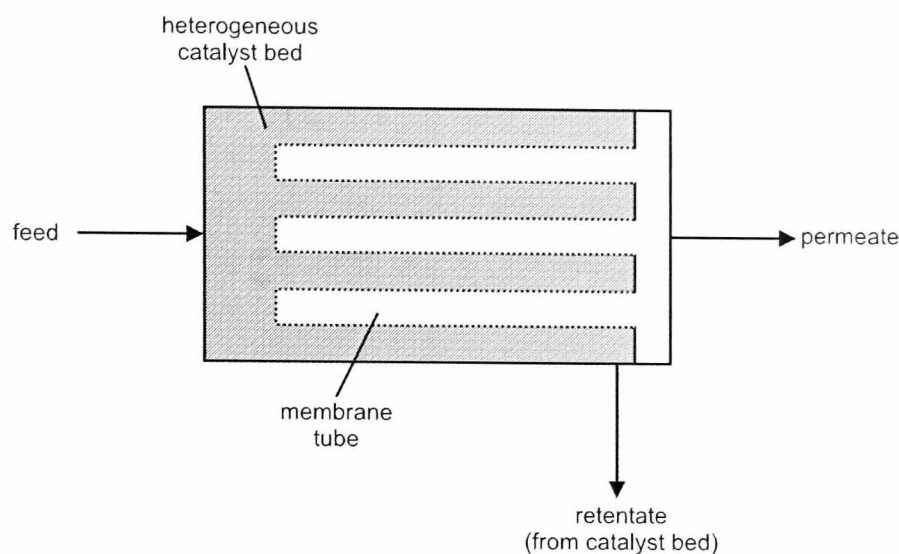


Figure 3.2: Schematic of catalytic membrane reactor

Armor (1998) presents a review of the potential uses for CMRs in petrochemical processes. They note that the traditional approach to a CMR is to apply a thin film of the membrane material to a mesoporous support tube constructed from a material such as alumina.

In recent work, a CMR consisting of gold catalyst deposited on a titania/silica support tube has been shown to increase propylene oxide yield during propylene oxidation by up to 200% compared to standard conditions (Oyama et al. 2008). Dong et al. (2008) has demonstrated the use of a CMR employing an $\text{La}_2\text{NiO}_{4+\delta}$ (LNO) support and $\text{La}_2\text{Ni}_{0.9}\text{Co}_{0.1}\text{O}_{4+\delta}$ (LNCO) mixed ion electron conducting (MIEC) membrane material. This has proved successful in allowing the use of air as a feedstock for the partial oxidation of methane, combining oxygen separation and methane oxidation processes into a single unit. As described in similar work by Zhang et al. (2007), using a CMR to perform the oxygen separation removes the need for a separate costly cryogenic separation step to separate oxygen from air.

3.3 Membrane sealing and other issues

If the proposed membrane separation process is to be industrially successful, it may be necessary to seal a ceramic membrane against a metallic surface at temperatures higher than those that standard rubber or metal O rings can withstand. In their work on coal gasification, Weil et al. (2006) at the Pacific Northwest National Laboratory

investigated the use of a braze as a sealant for ceramic membrane to metal interfaces. They found that the two conventional commercially available active metal brazes produced an oxide layer at the membrane interface when heated to 800°C, making the seal ineffective. The proposed alternative involves “air brazing”, where the brazing takes place in a normal atmosphere, rather than under an inert atmosphere. This type of braze did not exhibit oxidation or loss of hermeticity following 1000 hours of exposure to 800°C. Although still a proprietary, experimental technique, this work demonstrates the diverse challenges present in engineering a process to take advantage of the increased conversion permitted by a catalytic membrane reactor.

In their pursuit of on-line monitoring of the sulphuric acid decomposition process, researchers at Sandia National Laboratory have also recognised the need to find suitable gasket materials (Rivera 2005). Their work only involves relatively low temperatures and low concentrations of the corrosive species SO₂ and SO₃ and hence does not have direct relevance to an operating decomposer. They state that soft metals such as gold can be used as gaskets at this temperature range and under oxidising conditions, however they tend to alloy into materials such as hastelloy, causing them to become permanently bonded. A suggested alternative is a graphite foil known commercially as Grafoil. However this is only rated to 525°C and hence it is probably not suitable for long term usage in the environments under consideration. Both graphite and gold were evaluated for use in this work (see Section 7.8).

The issues associated with sealing were identified by Saracco et al.’s (1994) review of high temperature membrane reactor technology. The other primary issues to be overcome are:

- high cost;
- low membrane permeability;
- difficulties with producing defect free critical membrane layers;
- chemical/physical instability of both membrane and reactor.

3.4 Introduction to process simulations

In order to quantify the potential benefits of a membrane separation step, a series of process simulations have been carried out to investigate both the CMR and downstream separation processes. Both dense oxygen separation membranes and Knudsen

regime porous membranes have been simulated, with each process using the *ProSimPlus* package. Before proceeding to novel simulations, the *ProSimPlus* package is validated against literature data.

3.5 Validation of ProSimPlus simulations against literature data

3.5.1 Aim

The aim of this work was to validate the *ProSimPlus* process simulation package by comparing simulations of a catalytic membrane reactor to literature data.

3.5.2 Literature data

Forsberg et al.'s (2004) conference paper discusses the possibility of using membranes in the sulphuric acid decomposition process and presents simulation data in support of the proposal. His simulations take a 100 mol sulphur trioxide feed at 1 atm pressure and 700°C and 850°C and pass the feed through a train of six theoretical reactor/separator stages that are intended to model the continuous product removal of a CMR. Each theoretical reactor performs a Gibbs free energy minimisation, in the same way as the *HSC Chemistry* package, to calculate the equilibrium composition at each stage. The separators are modelled as perfect component splitters, removing the specified components and passing the "retentate" to the next equilibrium reactor. The quantity of SO₃, SO₂ and O₂ present at the outlet of each equilibrium reactor stage was recorded.

3.5.3 Method

Forsberg's CMR simulation used up to six theoretical equilibrium stages. This is modelled in *ProSimPlus* by a train of reactor/separator stages, the layout of which is shown in Figure 3.3. The same conditions were used as for the literature simulation, namely a feed of 100 mol of pure SO₃ at atmospheric pressure and the specified temperature.

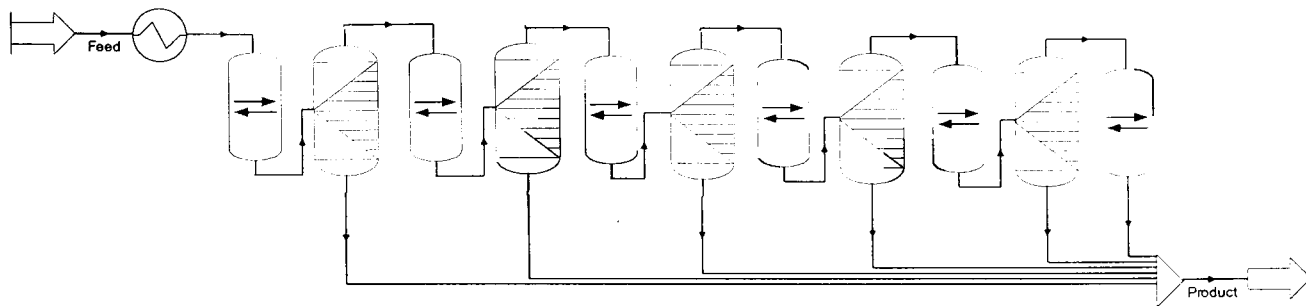


Figure 3.3: *ProSimPlus* simulation diagram for a catalytic membrane reactor (CMR) with six theoretical equilibrium reactor/separator stages, as used by Forsberg (2004).

The composition of the stream leaving each equilibrium reactor was recorded. The component splitters remove all of the O_2 in the stream, or the O_2 and SO_2 , depending on the configuration.

3.5.4 Results

Table 3.1 shows the resulting *ProSimPlus* data alongside the Forsberg data.

Comparing the *ProSimPlus* data and Forsberg's data, it can be seen that the maximum variation in amount of any species predicted to be present following any given stage was 0.5 mol. On the basis of these small variations, the work presented here using the *ProSimPlus* package can be considered equivalent to that produced by Forsberg and *ProSimPlus* can be considered reliable for use with the novel simulations presented in later sections.

The following sections will show further simulations extending Forsberg's work.

	Stage	ProSimPlus			Forsberg		
		SO ₃	SO ₂	O ₂	SO ₃	SO ₂	O ₂
O ₂ removal 700°C	0	100.0	0.0	0.0	100.0	0.0	0.0
	1	52.1	47.9	24.0	52.5	47.6	23.8
	2	38.4	61.6	6.8	38.9	61.2	6.8
	3	31.3	68.7	3.5	31.8	68.2	3.5
	4	26.8	73.2	2.3	27.2	72.8	2.3
	5	23.6	76.4	1.6	24.0	76.0	1.6
	6	21.2	78.8	1.2	21.6	78.4	1.2
O ₂ removal 850°C	0	100.0	0.0	0.0	100.0	0.0	0.0
	1	20.8	79.2	39.6	21.1	78.9	39.4
	2	10.1	89.9	5.4	10.3	90.0	5.4
	3	6.3	93.7	1.9	6.5	93.6	1.9
	4	4.5	95.5	0.9	4.6	95.4	0.9
	5	3.4	96.6	0.5	3.5	96.5	0.5
	6	2.8	97.2	0.3	2.9	97.1	0.3
SO ₂ & O ₂ removal 700°C	0	100.0	0.0	0.0	100.0	0.0	0.0
	1	52.1	47.9	24.0	52.5	47.6	23.8
	2	27.1	25.0	12.5	27.5	24.9	12.5
	3	14.1	13.0	6.5	14.4	13.1	6.5
	4	7.3	6.8	3.4	7.6	6.9	3.4
	5	3.8	3.5	1.8	4.0	3.6	1.8
	6	2.0	1.8	0.9	2.1	1.9	0.9

Table 3.1: Comparison of ProSimPlus data with Forsberg data. Values indicate quantity of each component remaining after shown number of theoretical equilibrium reactors in a CMR. P=1 atm, 100% SO₃ feed, perfect separation at each stage

3.6 General method of novel simulations

Each of the proposed process configurations were modelled using *ProSimPlus*. The components used for the simulations were H_2SO_4 , H_2O , SO_2 , SO_3 and O_2 . A stream consisting of 92.7wt% H_2SO_4 and 7.3wt% H_2O enters the process, heated to the required temperature. This acid concentration mirrors that specified by the original General Atomics flowsheet for the SI cycle acid decomposition section feed (Ozturk et al. 1995). The simulations were carried out at temperatures in the range 900-1300K, in 100K steps, and pressures of 1 atm to 30 bara. As with the Forsberg comparison work, the reactor is modelled as a gas phase equilibrium reactor performing a Gibbs free energy minimisation at the specified process temperature.

The porous membranes were simulated as exhibiting Knudsen regime separation factors (see Section 4.3). The dense oxygen separation membranes were simulated as exhibiting separation factors F of 10, 100, 1000 and 10000 with respect to O_2 . The separation factor is the multiplier by which the ratio of oxygen concentration to the concentration of each other species changes across the membrane. For dense membranes, these separation factors represent cross membrane leakage, either as a result of membrane defects or poor sealing.

The overall yield of SO_2 was recorded for each simulation. Taking the system as a whole, the SO_2 yield is equal to:

$$\text{yield}(\%)_{\text{SO}_2} = 100 \times \frac{\text{mols of SO}_2 \text{ in product}}{\text{mols of H}_2\text{SO}_4 \text{ in feed}}$$

3.7 CMR simulations

3.7.1 Aim

The aim of these simulations was to extend the work on CMRs reported in literature by covering a wider range of process pressures and temperatures and membrane separation factors. In combination with subsequent simulations of the downstream separation membrane described in Section 3.1, these simulations aim to show that the sulphur dioxide yield from the sulphuric acid thermal decomposition process could be increased through the use of membrane separation.

3.7.2 Method

The process is identical to that employed for the Forsberg comparison simulations, except that the permeate streams from each stage are combined with the final retentate stream at the end of the train of stages in order to produce the final product.

Forsberg's simulations assumed that each theoretical separation stage was ideal, i.e. $F = \infty$. These simulations use the separation factors stated previously in Section 3.6 in order to mimic a "real" separation membrane.

Forsberg's CMR simulation used up to six theoretical equilibrium stages. To investigate the sensitivity of the SO_2 yield to the number of equilibrium stages, these simulations were carried out with two, four, six and eight stage trains of theoretical reactors/separators. By way of example, the *ProSimPlus* flowsheet for the four stage train is shown in Figure 3.4.

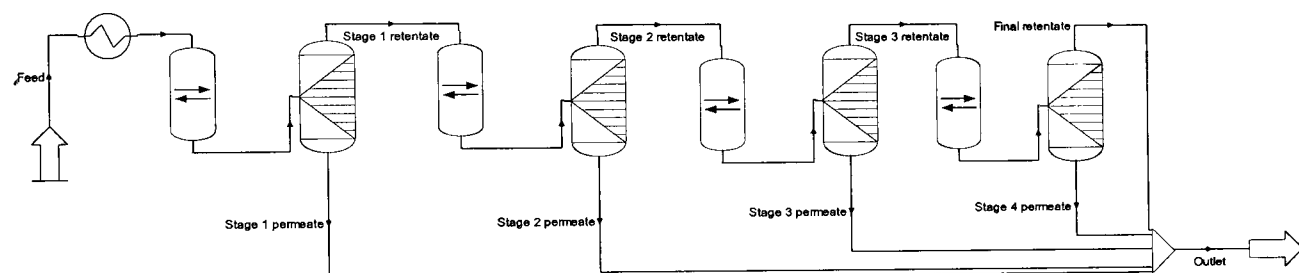


Figure 3.4: *ProSimPlus* simulation diagram for a catalytic membrane reactor (CMR) with four theoretical stages.

3.7.3 Results

In total, 420 simulations were carried out for this section (including the "control" simulations which provided the equilibrium line.) The full results table can be found in Appendix A.

Variation of yield with separation ratio and number of theoretical stages

Figure 3.5 shows the results at 1000K and 1 atm pressure. It can be seen that increasing the separation ratio of a dense membrane above $F = 100$ does not result in an appreciable increase in SO_2 yield. Examination of the full results table shows that this is the case at all temperatures and pressures simulated. Because of this result, yields for $F = 1000$ and $F = 10000$ will not be included in future graphs for the sake of clarity.

The addition of extra theoretical "stages" to the CMR produces a diminishing return

in terms of yield increase - in practical terms this demonstrates the compromise that must be made between membrane tube length and the degree of separation.

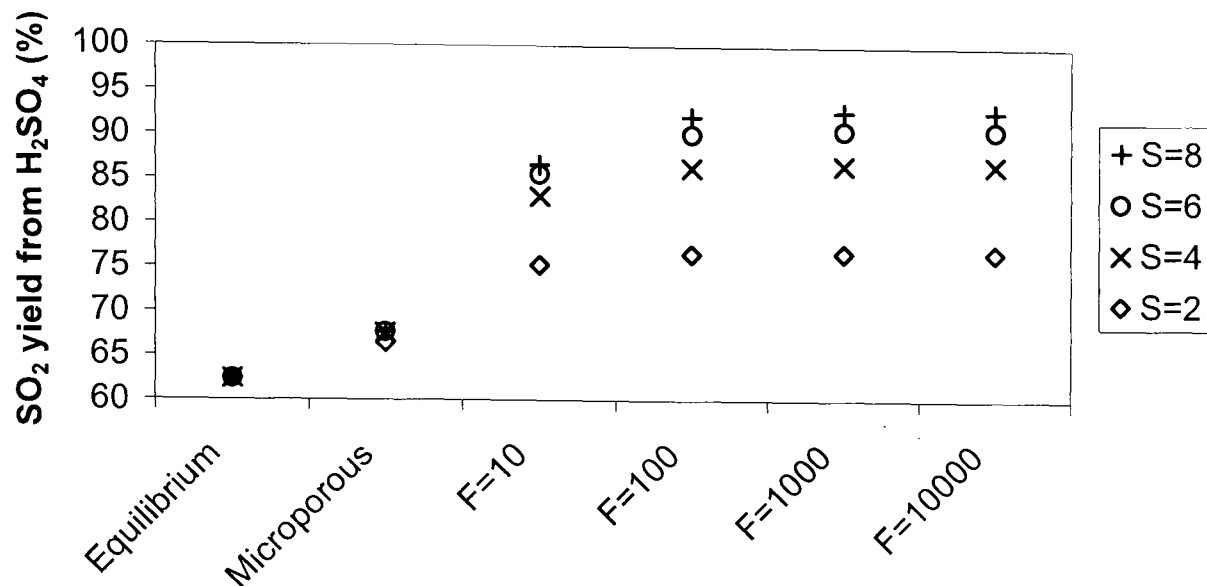


Figure 3.5: ProSimPlus CMR simulation at 1000K and 1 atm - microporous membranes were modelled as having Knudsen separation factors, whilst F (separation) values indicate dense oxygen separating membranes. S = number of theoretical stages.

Variation of yield with separation ratio and temperature

Figure 3.6 shows the variation of yield with temperature at 1 atm and using six theoretical stages. Because the equilibrium yield approaches 100% when a temperature of 1200K is approached, the potential for yield improvements through the CMR system decreases. We are interested at increasing yields at the lower end of the temperature range and it can be seen that large yield improvements can be made in the range 900-1100K. For example, at 1000K a dense oxygen removal membrane of $F = 100$ increases the process SO_2 yield from 62.3% to 90.1%. A microporous membrane (exhibiting Knudsen regime separation factors) only increases yield to 67.6% under the same conditions. Although this is still an appreciable increase, it is only a fraction of the increase that is possible using dense oxygen separation membranes.

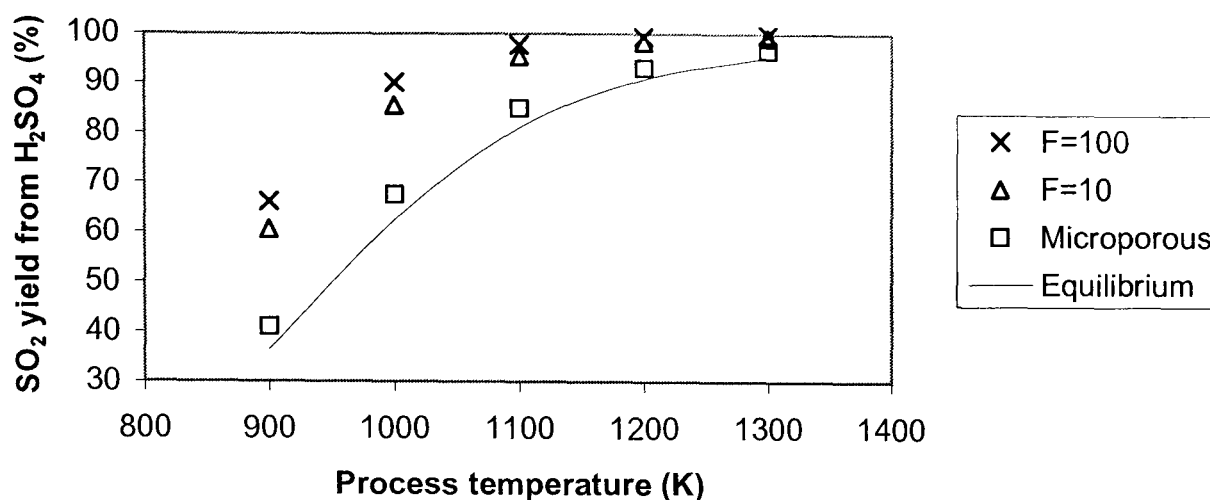


Figure 3.6: ProSimPlus CMR simulation at 1 atm with six theoretical stages - microporous membranes were modelled as having Knudsen separation factors, whilst F values indicate dense oxygen separating membranes.

Figure 3.7 shows the result of having a “short” membrane tube, modelled here by the use of only two theoretical stages. The yield increase for the microporous membrane is almost identical, but the yields for the dense membranes decrease compared to the six stage case. Additionally, the results for $F = 10$ and $F = 100$ are very similar, with <2% additional SO_2 yield for the higher separation ratio. This suggests that if a “short” reactor is to be used, the extra effort required to increase the unit’s separation ratio beyond approximately $F = 10$ would not be worthwhile.

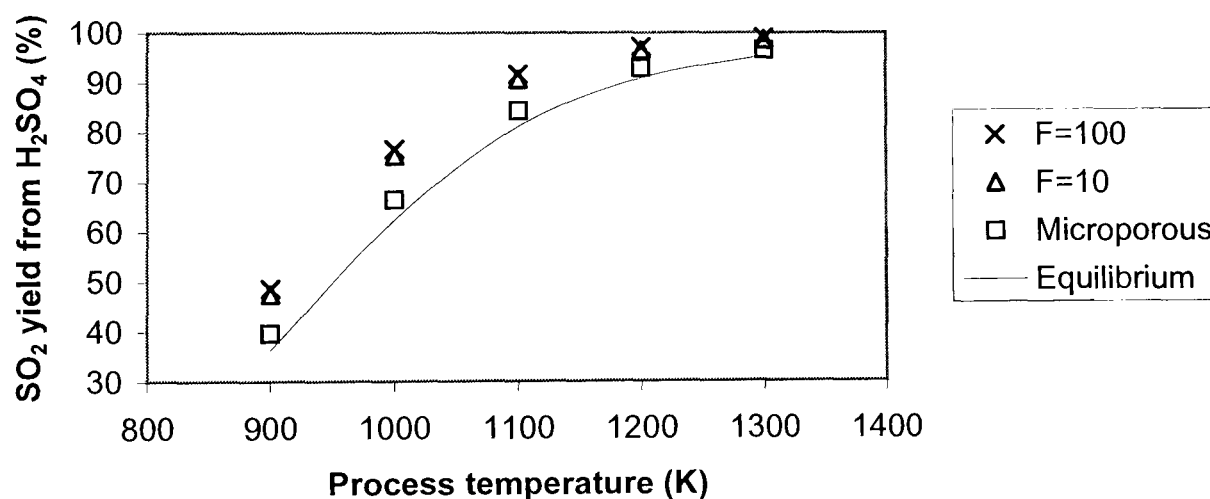


Figure 3.7: ProSimPlus CMR simulation at 1 atm with two theoretical stages - microporous membranes were modelled as having Knudsen separation factors, whilst F values indicate dense oxygen separating membranes.

Variation of yield with separation ratio and pressure

The result of varying pressure shows a similar pattern to that of varying temperature. Figure 3.8 illustrates the effect of varying pressure between atmospheric and 30 bara at 1000K. Again, the microporous membrane shows a small but appreciable increase in SO₂ yield over equilibrium, but the dense oxygen removal membranes show significantly greater yield increases. Given that an industrial process is likely to run at elevated pressures, showing that CMRs could increase SO₂ yield under these conditions is of great importance.

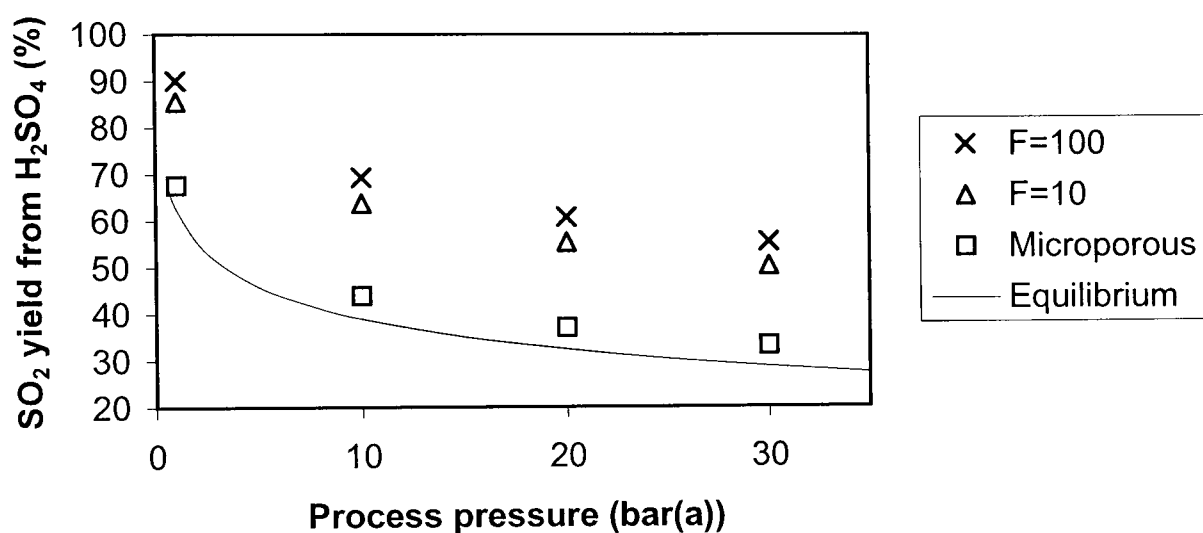


Figure 3.8: ProSimPlus CMR simulation at 1000K with six theoretical stages - microporous membranes were modelled as having Knudsen separation factors, whilst F values indicate dense oxygen separating membranes.

3.7.4 Conclusions

The simulation data presented above demonstrates that by replacing a standard equilibrium reactor with a CMR, the yield of SO₂ from the process can be increased at temperatures of 900-1300K and pressures from atmospheric to 30 bara. The greatest benefit is seen at temperatures below 1100K, as the high equilibrium yield at higher temperatures reduces the scope for yield improvements. The yield increases are significant at all pressures simulated. Although microporous membranes offer a small SO₂ yield increase, far greater increases can be achieved by the use of dense oxygen separation membranes. In the pressure and temperature parameter space simulated, increasing the separation factor above $F = 100$ did not improve the yield appreciably and therefore the extra effort required in, for example, sealing to achieve very high

separation ratios is not worthwhile.

3.8 Downstream membrane simulations

3.8.1 Aim

These simulations extend those carried out in the previous section by investigating the downstream separation process configuration described in Section 3.1. The aim is to show that this configuration can also increase SO_2 yield in the sulphuric acid thermal decomposition process above the equilibrium values.

3.8.2 Method

The *ProSimPlus* simulation replicates the process depicted in Figure 3.1. The resulting flowsheet is shown in Figure 3.9. The initial heated feed passes into the equilibrium reactor. A proportion of the reactor outlet stream passes through the membrane according to the membrane separation factor. A fraction of the membrane retentate is recycled and the remainder of the retentate is mixed with the membrane permeate to produce the process outlet stream. Recycle fractions of 20-80% (in 20% steps) were used. It is anticipated that increasing the recycle ratio will increase yield, but would require larger process plant in practice.

Simulations were carried out for 25%, 50%, 75% and 100% permeation through the membrane. The proportion of the feed that permeates through the membrane would depend on a number of factors in reality, including the membrane material, oxygen partial pressure gradient across the membrane faces, and the total membrane surface area available. As the ratio of maximum permeate to actual permeate tends to unity, so the actual membrane area required would tend to infinity. By modelling varying fractions of permeation, this mimics the effect of the available membrane area and feed residence time on the process.

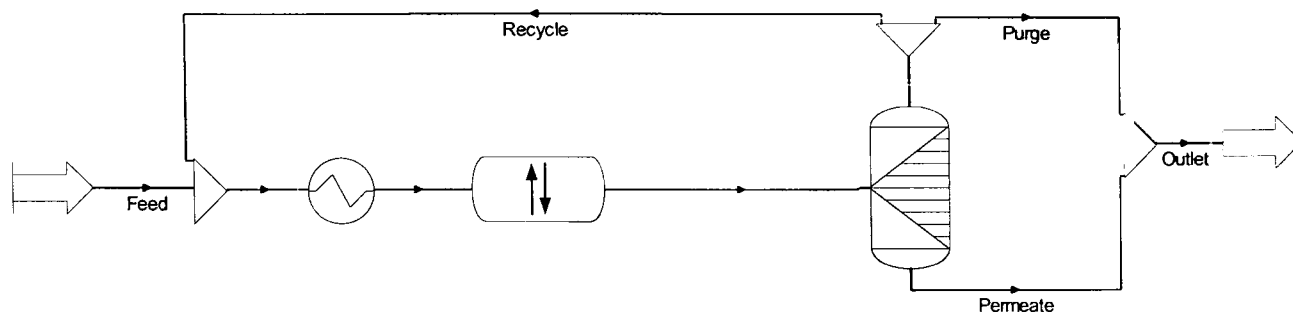


Figure 3.9: ProSimPlus simulation diagram for the use of a downstream membrane to separate the reaction products of H_2SO_4 thermal decomposition

3.8.3 Results

In total, 1620 simulations were carried out for this section (including the “control” simulations which provided the equilibrium line.) The full results tables can be found in Appendix A.

Variation of yield with separation ratio

Examination of a sample case shows that the relative performance of each of the membrane types simulated here is similar to the results of the CMR simulations. Figure 3.10 shows the SO_2 yield resulting at 1 atm and 1000K with 80% retentate recycling and 75% membrane efficiency. The now familiar pattern can be seen - the microporous membrane gives a small increase in yield over the equilibrium amount (64.0% compared to 62.4%) but the dense membranes with separation ratio $F = 10$ and $F = 100$ give much greater yield increases (to 72.2% and 74.2% respectively.) Also, it can be seen that increasing the separation ratio above 100 produces no appreciable increase in SO_2 yield and hence yields for $F = 1000$ and $F = 10000$ will not be presented be presented on further figures, for clarity.

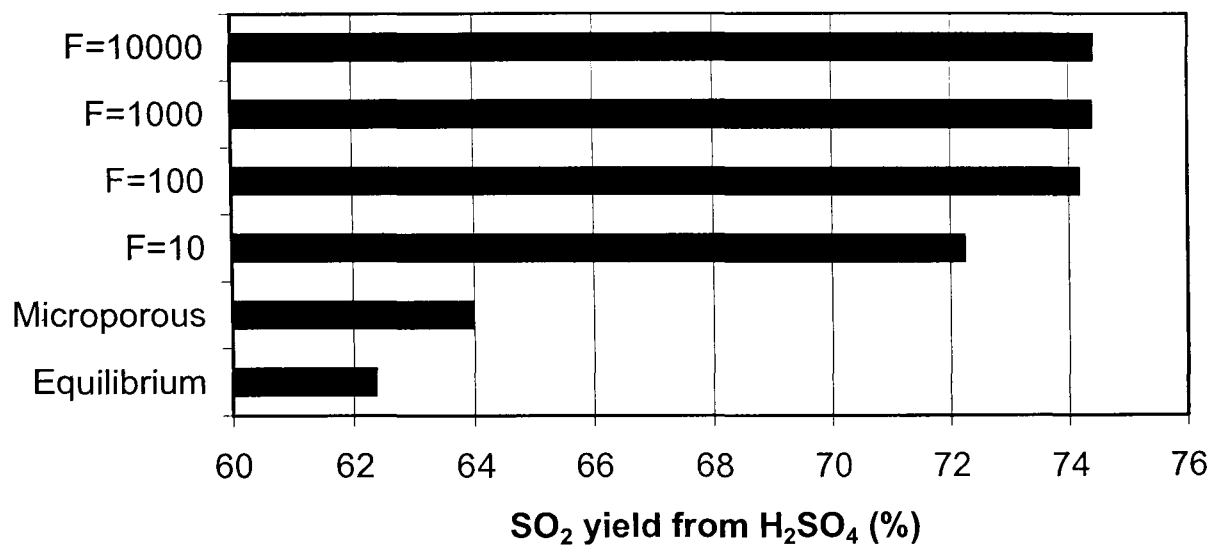


Figure 3.10: ProSimPlus downstream membrane simulation at 1000K, 1 atm, 75% membrane efficiency, 80% retentate recycle - microporous membranes were modelled as having Knudsen separation factors, whilst F values indicate dense oxygen separating membranes.

Variation of yield with separation ratio and temperature

As an extension of the above, Figure 3.11 illustrates the variation of the SO₂ yield with temperature and membrane separation factor. The membrane efficiency is fixed at 75% and the retentate recycle fraction is fixed at 80%. As will be shown later, these settings represent a best case scenario for this process configuration.

As with the CMR simulations, it can be seen that the membrane separation is most effective at lower temperatures. Above 1100K the SO₂ yield improvements are relatively small.

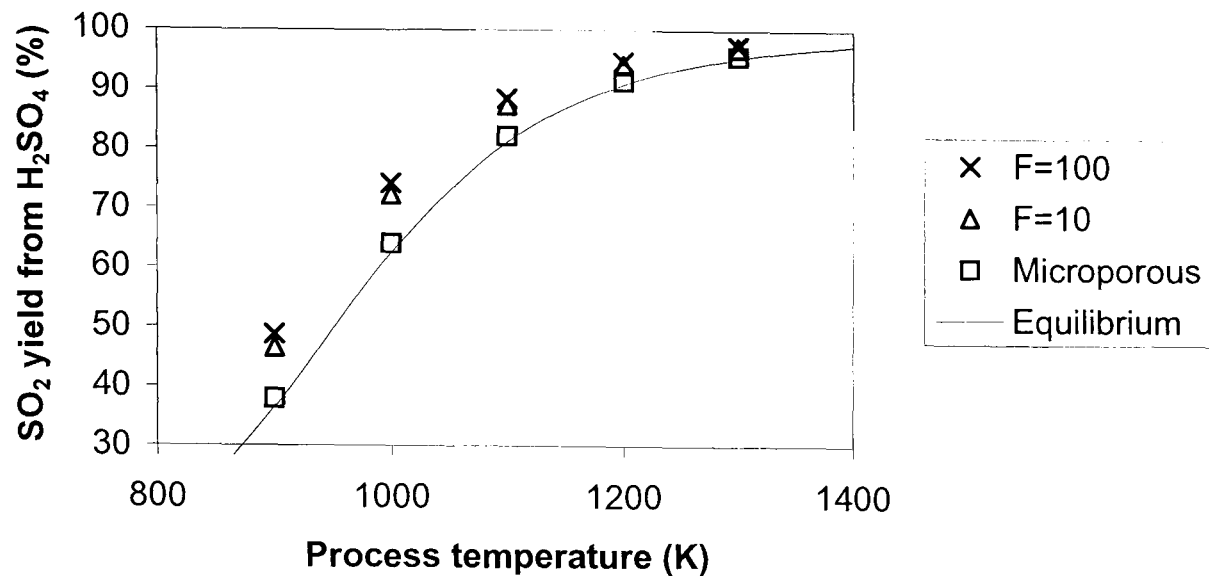


Figure 3.11: ProSimPlus downstream membrane simulation at 1 atm, 75% membrane efficiency, 80% retentate recycle - microporous membranes were modelled as having Knudsen separation factors, whilst F values indicate dense oxygen separating membranes.

Comparison with Figures 3.6 and 3.7 show that both the “long” and “short” CMRs produce greater SO_2 yield improvements than the downstream separation process. Figure 3.12 summarises this. Given this evidence, use of a CMR may seem preferable to using downstream separation. However, a CMR may be significantly more difficult to engineer in practice and hence the smaller SO_2 yield improvement offered by the downstream separation process may be more economic.

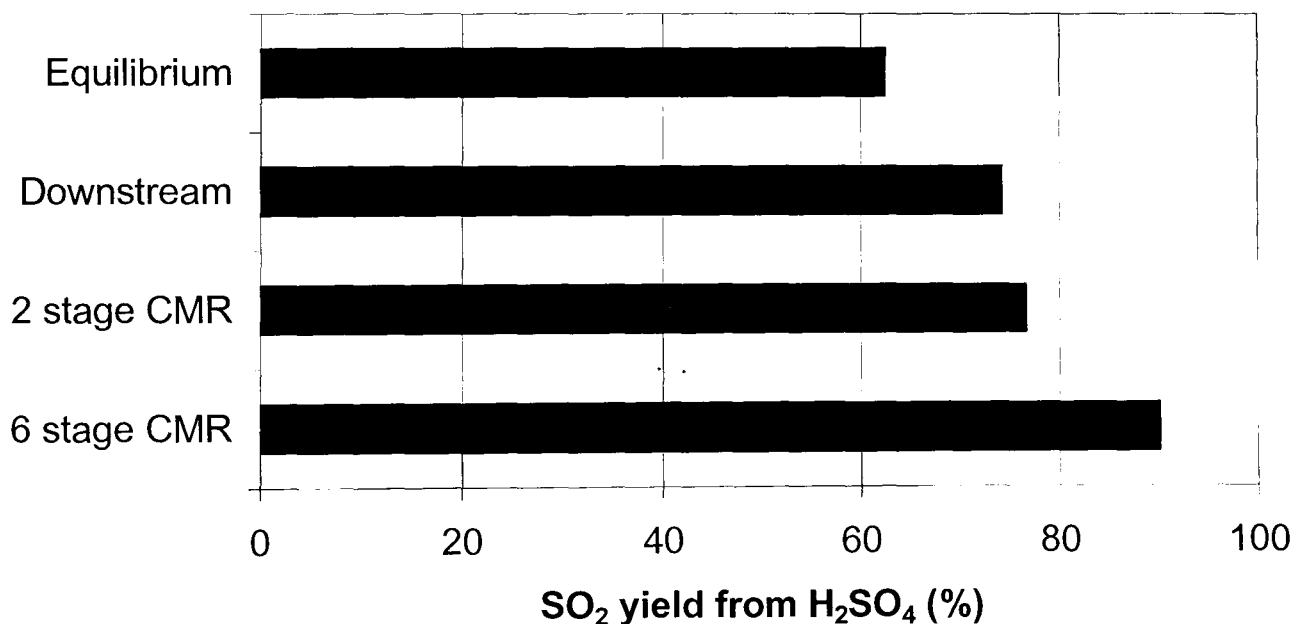


Figure 3.12: ProSimPlus membrane simulations at 1 atm, 1000K, $F=100$ - configuration comparison. Downstream separation has 75% membrane efficiency, 80% retentate recycle.

Variation of yield with separation ratio and pressure

The downstream separation process configuration produces a similar pressure-yield relationship to the CMR, as can be seen in Figure 3.13.

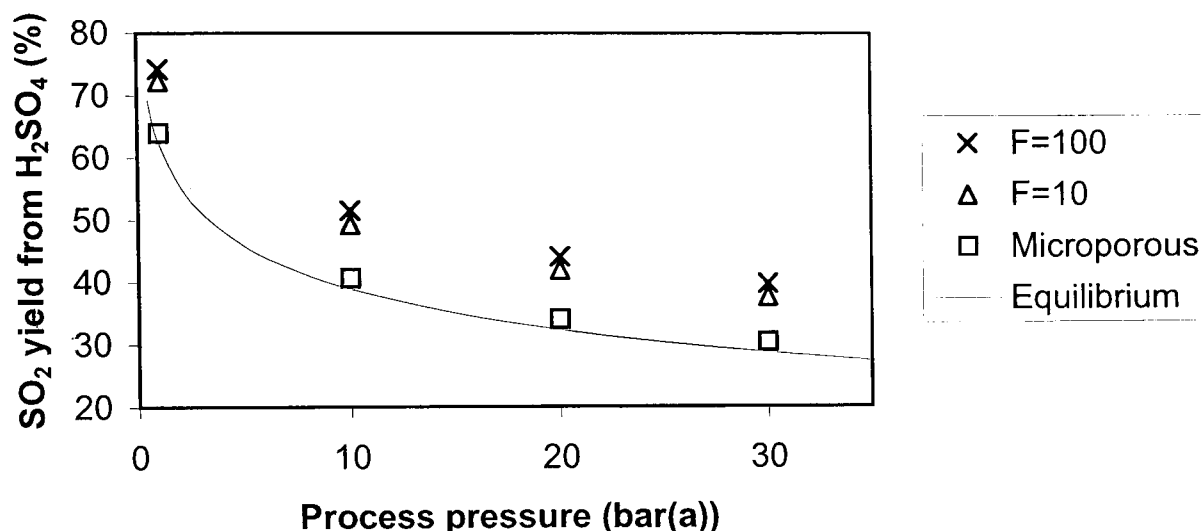


Figure 3.13: ProSimPlus downstream membrane simulation at 1000K, 75% membrane efficiency, 80% retentate recycle - microporous membranes were modelled as having Knudsen separation factors, whilst F values indicate dense oxygen separating membranes.

Variation of yield with retentate recycle ratio and membrane efficiency

These issues are specific to the downstream separation process configuration. As can be seen in Figure 3.14, SO₂ yield tends to the equilibrium value as the retentate recycle fraction tends to zero. This makes logical sense, as zero retentate recycling means all of the membrane permeate and all of the membrane retentate are mixed to form the product stream, negating the effect of the separation process.

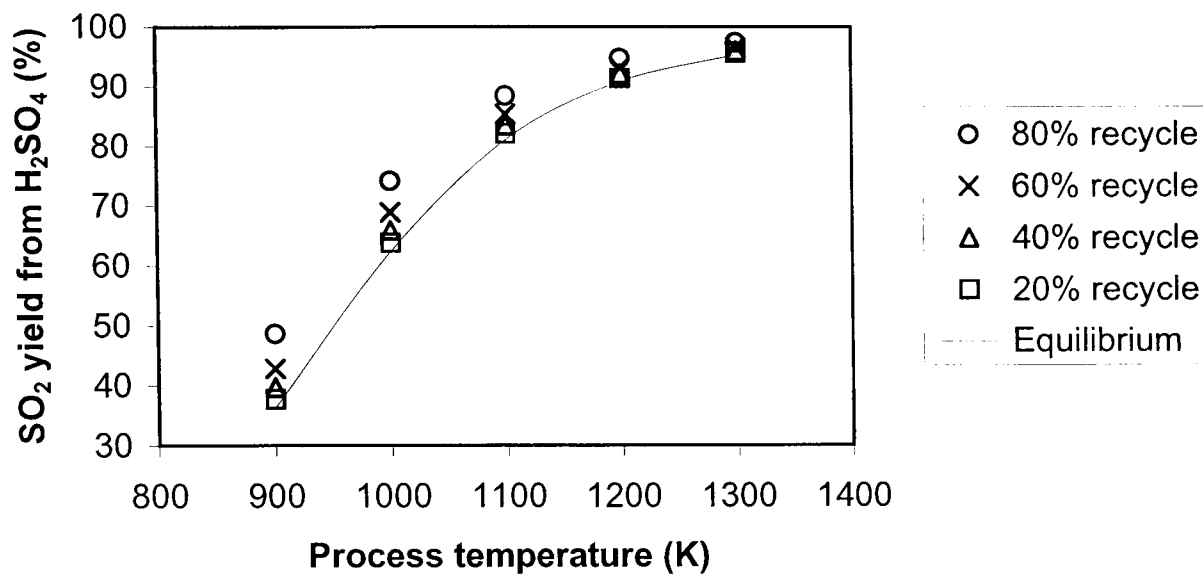


Figure 3.14: ProSimPlus downstream membrane simulation at 1 atm, 75% membrane efficiency, $F=100$.

Increasing the process pressure would decrease the physical size of the process plant for a given throughput. Therefore, a plant operating at 30 bar and 80% recycling may be of a similar size to a plant operating at 1 atm and 20% recycling. Figure 3.15 shows the achievable SO_2 yields at 30 bara.

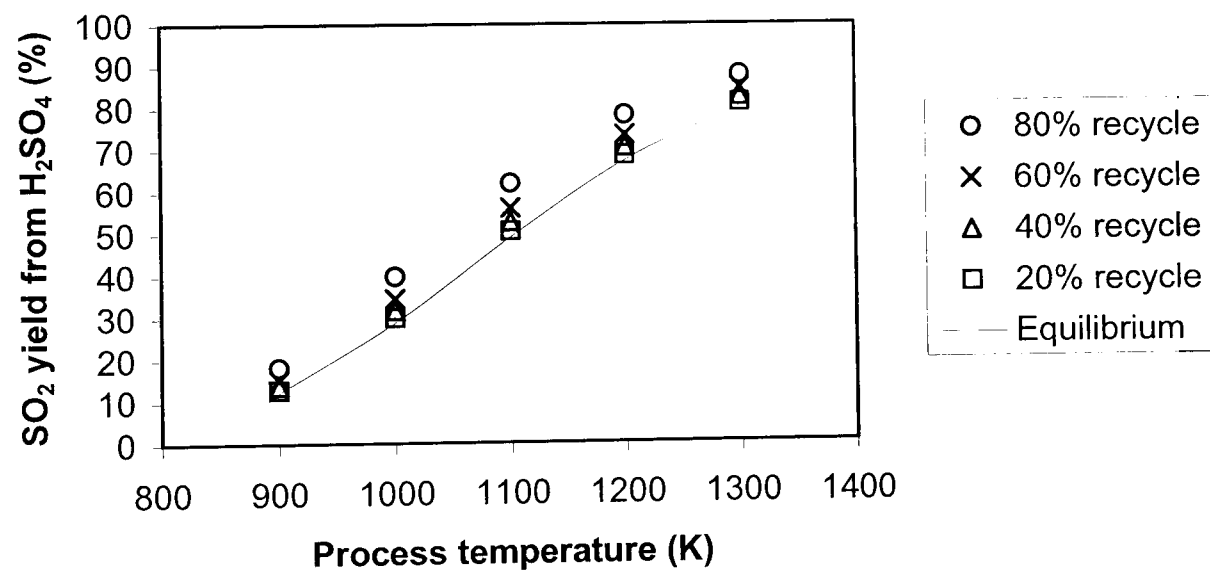


Figure 3.15: ProSimPlus downstream membrane simulation at 30 bara, 75% membrane efficiency, $F=100$.

3.8.4 Conclusions

Under the conditions simulated here, dense oxygen separation membranes are calculated to produce greater SO₂ yields than microporous membranes exhibiting Knudsen regime selectivities. Increasing the selectivity of dense membranes above 100 (with respect to oxygen) does not appreciably improve the SO₂ yield, therefore removing minute sources of trans-membrane leakage would not be a fruitful course of action. The largest yield increases are seen below 1100K. Increasing the recycle ratio increases the yield at a given temperature and selectivity. Downstream membrane separation produces smaller yield increases than the CMRs as modelled here.

3.9 Overall conclusions

Process simulations have demonstrated that the use of selective separation processes in the sulphuric acid thermal decomposition process can increase SO₂ yield at a given temperature. The yield increases have been shown to exist across the pressure range $1 \text{ atm} \leq P \leq 30 \text{ bara}$. Porous membranes which exhibit Knudsen separation produce a small yield improvement, however dense oxygen separation membranes produce significantly greater yield increases. Chapters 4 and 5 discuss the literature concerning possible porous and dense membrane materials respectively. Complex CMR processes may be more suitable when very high SO₂ yields are required, whereas comparatively simple downstream separation processes may be more suitable where modest yield improvements are sufficient.

The membrane process simulations described in Chapter 3 provided strong evidence that the use of a membrane separation could have the desired effect of reducing the process temperature required to achieve a given SO₂ yield.

Chapter 4

Porous membranes for sulphuric acid thermal decomposition

4.1 Recent research into materials and fabrication techniques

Lin's (2001) review paper covers recent developments in techniques for producing microporous silica (SiO_2) membranes. As later sulphation calculations will show (see Section 5.3), silica (and zirconia) are chemically stable under the process conditions expected here. They report that the use of higher quality support materials, with smaller pore diameters, and the use of clean room conditions allow the application of pinhole-free silica coatings down to 30nm thickness. These ultra-thin membranes exhibit higher gas permeance and separation factors than previously reported microporous membranes. Hollow fibre silica membranes are reported to have higher separation factors than sol-gel derived microporous membranes. However, since sol-gel derived layers exhibit gas permeance two orders of magnitude greater than hollow fibres, and have greater mechanical strength, they are considered to be the more industrially viable option. Lin also states that amorphous microporous SiO_2 membranes tend not to be stable at high temperatures, especially when H_2O is present. Doping the SiO_2 with ZrO_2 may improve high temperature stability, although it may also increase pore sizes.

Hydrophobic SiO_2 membranes have been produced by repeated dip coating of γ -alumina membranes with a sol prepared by acid-catalysed hydrolysis and condensation of tetra-ethylortho-silicate (TEOS) (de Vos et al. 1999). Adding methyl-tri-ethoxy-silane (MTES) to the sol gave the membrane its hydrophobic character. The final thickness and approximate pore size of the silica membrane was 60nm and 0.7nm respect-

ively.

Thin porous $\text{ZrO}_2\text{-SiO}_2$ membranes, supported by porous alumina, have been produced (Agoudjil et al. 2005). Pore diameters of 100nm were reported when a continuous $2\mu\text{m}$ membrane layer was applied to the alumina support and thermally treated at 600°C . McLeary & Jansen (2004) report a method for converting amorphous silica-based porous material into a crystalline state, providing the benefits of each type (surface continuity and high selectivity respectively).

The stability of $\alpha\text{-SiO}_2$ and $\gamma\text{-SiO}_2$ membranes produced by chemical vapour deposition (CVD) on to SiO_2 support tubes has been investigated for gaseous mixtures of steam and hydriodic acid (HI) as might be found in the SI cycle (Hwang et al. 2003). The $\alpha\text{-SiO}_2$ membrane was found to be more stable.

Lee & Oyama (2002) describe a CVD-deposited SiO_2 membrane supported on a porous Vycor glass support. The pores were found to be slit-shaped and had an average size of 3.6nm. Vycor is the trade name for a 96% silica glass produced by Corning.

Dual layer SiO_2 microporous membranes have been deposited on to a $\gamma\text{-Al}_2\text{O}_3$ support (Tsai et al. 2000). This approach resulted in a gradual pore size reduction, from 5nm (support) to 1.0-1.2nm (templated silica intermediate layer) to 0.3-0.4nm (30nm thick top layer). The intermediate layer prevented the top coating penetrating into the support's pores, increasing permeance.

Silicon carbide (SiC) is also a candidate engineering material for this process. Corrosion of porous SiC by high temperature steam has been investigated (Fukushima et al. 2008). It was found that corrosion was very low at 600°C (0.7% of the SiC converted to silica) but over an order of magnitude greater at 1000°C (95.7% SiC conversion). Also, the sample porosity decreased from an initial 37% to 36% with water vapour exposure at 600°C or 4% after 1000°C corrosion. The sample increased in volume by 17% at 1000°C . The densification of the sample at 1000°C would indicate that SiC is not a suitable porous material for the sulphuric acid decomposition process at the high end of the temperature range, but may be suitable at lower temperatures. Tests on SiC samples containing 4% alumina produced similar results.

Literature indicates that since SiC is not a sinterable material, sintering agents (such as carbon, boron and/or alumina) must be added, producing highly dense material (Suwanmethanond et al. 2000). They found that using boron carbide and phenolic resin as the sintering agents with pressureless sintering under an argon-inerted atmosphere produced the most promising porous SiC substrates.

Silicon carbide nanoporous membranes have been investigated for medical applic-

ations (Rosenbloom et al. 2004). The membranes in the study passed molecules of diameter 4.7nm and excluded those of diameter 5.0nm.

Elyassi et al. (2008) presented a new method of producing nanoporous SiC membranes. They applied alternate layers of polystyrene sacrificial interlayers and SiC pre-ceramic layers to SiC support tubes. They claimed that this method doubles or triples permeance compared to conventional preparation techniques, because the sacrificial interlayers prevent the SiC coating from blocking the pores of the support tube.

Other fabrication methods investigated by the same group were chemical vapour deposition (CVD) and chemical vapour infiltration (CVI) (Chen et al. 2008). Early work involved the deposition of SiC via a tri-isopropylsilane (TPS) precursor on to an alumina support. Current work involves the use of macroporous SiC supports in order to reduce the potential for mechanical failure resulting from differential thermal expansion. The supports, with an average pore diameter of 28nm, were produced by the method previously described by Suwanmethanon. The use of SiC support instead of alumina also increases the likelihood of chemical compatibility with the sulphuric acid decomposition process.

Based on this literature survey and the material stability calculations shown in Section 5.3, it would appear that SiC or SiO₂ membranes and supports operating at the lower end of the proposed temperature range (say 700 – 850°C) are most likely to be compatible with the sulphuric acid decomposition process.

4.2 Experimental membrane permeance

The only paper found in the literature with direct relevance to the sulphuric acid decomposition process is that presented by Forsberg et al. (2004) at the 2004 AIChE Spring Meeting. This built on his previous work, presenting data for pure SO₂, SO₃, and O₂ gas flows through a commercial inorganic membrane. Although SO₂ and O₂ permeance tests were carried out at a range of temperatures up to 133°C, SO₃ permeance tests were only carried out at 133°C. Because of this, the change in SO₃ permeance with temperature was not determined and hence the change in separation factor with temperature could not be determined. Problems with SO₃ adsorbing on to the membrane were noted. This work was of limited value, since it only dealt with relatively low temperatures. Tests would need to be carried out to validate the thermally activated diffusion transport model at the temperatures of interest, i.e. >700°C. However, the low temperature tests suggest that, for the particular membrane used, permeance did increase with temperature.

Forsberg et al. (2004) determined a permeance for an unspecified membrane of around $2 \times 10^{-10} \text{ mol/m}^2 \text{ s} \cdot \text{Pa}$ for SO_2 at 130°C and O_2 at 133°C . This compares favourably with values obtained elsewhere for sol gel templated silica membranes with pore sizes of around 3.5 \AA (Xomeritakis et al. 2003).

4.3 Separation factors

Porous membranes exhibit separation factors which can be predicted based on the flow regime present through the membrane pores. For the purposes of this work, there are three flow regimes to be considered:

- Knudsen diffusion;
- Activated surface diffusion;
- Molecular sieving.

Gilron & Soffer (2002) described each of these flow regimes.

For all three mechanisms, the molar flux through the pore is stated by Fick's Law:

$$J_i = -D_i \frac{\partial C}{\partial x}$$

The diffusion coefficient D_i is composed of a corrected diffusion coefficient, which varies for each transport mechanism, and a thermodynamic correction factor Γ .

The Knudsen flow regime applies where the membrane pore diameter is much smaller than the mean free path of the molecules passing through it, subject to a lower pore diameter limit of approximately 2 nm . Gilron gives the corrected diffusion coefficient as:

$$D_{K,c} = \frac{d_p}{3} \sqrt{\frac{8RT}{\pi M}}$$

Porous membranes operating in the Knudsen flow regime therefore have an ideal separation ratio equal to the square root of the ratio of the molecular weights of the components to be separated. Thus, the ideal separation factor between SO_3 and SO_2 is:

$$S_{\text{SO}_3/\text{SO}_2} = \sqrt{\frac{M_{\text{SO}_3}}{M_{\text{SO}_2}}} = \sqrt{\frac{80}{64}} = 1.118$$

Similarly, the separation factors for SO_3 / O_2 and $\text{SO}_3 / \text{H}_2\text{O}$ are:

$$S_{\text{SO}_3/\text{O}_2} = \sqrt{\frac{M_{\text{SO}_3}}{M_{\text{O}_2}}} = \sqrt{\frac{80}{32}} = 1.581$$

$$S_{\text{SO}_3/\text{H}_2\text{O}} = \sqrt{\frac{M_{\text{SO}_3}}{M_{\text{H}_2\text{O}}}} = \sqrt{\frac{80}{18}} = 2.108$$

It can be clearly seen that a single membrane with separation factors of this magnitude will not result in an appreciable conversion improvement.

Surface diffusion and molecular sieving are both activated processes (Gilron & Soffer 2002) and hence the corrected diffusion coefficients are given by Arrhenius-type expressions:

$$\text{Surface diffusion: } D_{S,c} = D_S^0 \exp\left(\frac{-E_{a,S}}{RT}\right)$$

$$\text{Molecular sieving: } D_{MS,c} = D_{MS}^0 \exp\left(\frac{-E_{a,MS}}{RT}\right)$$

The temperature dependency of the flux for each transport type is then also given:

$$\text{Knudsen diffusion: } F_k \approx (MRT)^{(-0.5)}$$

$$\text{Surface diffusion: } F_S \approx D_0(T) \exp\left(\frac{-E_{a,S} - E_{ads}}{RT}\right)$$

$$\text{Molecular sieving: } F_{MS} \approx D_0(T) \exp\left(\frac{-E_{a,MS} - E_{ads}}{RT}\right)$$

A clear difference in temperature dependence can be seen here. When Knudsen transport dominates, increasing temperature would be expected to decrease the flux. However, for the other two regimes, the dependence could be either positive or negative, depending on whether the transport activation energy E_a is greater or smaller than the heat of adsorption E_{ads} .

The variation in temperature dependence between transport regimes leads to a qualitative statement that if the flux through the membrane is observed to increase with increasing temperature, then Knudsen flow is not dominating and smaller pores must therefore be present.

4.4 Determination of molecular diameters

The simulation results presented in Chapter 3 showed the potential SO₂ yield improvements to the sulphuric acid thermal decomposition process through the use of a separation membrane. They also showed that the ideal separation factors of a Knudsen regime microporous membrane were not sufficiently high to produce yield improvements comparable to dense oxygen separation membranes. Separation factors an order of magnitude greater than those exhibited by Knudsen flow regime membranes would be required for a competitive porous membrane. This could be achieved by the use of molecular sieving.

Molecular sieving involves creating pores with sufficiently small diameters such that permeation through the membrane is dependent on whether the molecules are physically small enough to pass through the pore. Molecules that are larger than the pore diameter would be excluded from the membrane, resulting in high separation factors for these molecules.

Calculating a “molecular diameter” for the purposes of deciding the pore sizes needed for molecular sieving to occur is not a trivial task. There is no single definition of what constitutes the molecular diameter. Many values exist in the literature, calculated using different methods.

4.4.1 Literature values

One measure is the molecular size used as a force constant for Lennard Jones potential calculations. Values for this molecular size, as calculated from viscosity measurements, are presented below (Hirschfelder et al. 1954):

O₂: 3.541Å (300K < T < 1000K)

SO₂: 4.29Å (300K < T < 1000K)

H₂O: 2.606Å

4.4.2 Calculated values

The following equation has been proposed, linking the viscosity of a fluid and that fluid’s molecular diameter (Hildebrand 1976):

$$\eta = \frac{2(mkT)^{\frac{1}{2}}}{3\pi^{\frac{3}{2}}\sigma^2} \therefore \sigma = \sqrt{\frac{2(mkT)^{\frac{1}{2}}}{3\pi^{\frac{3}{2}}\eta}}$$

η = viscosity (Poise)

m = mass of one molecule (g)

k = Boltzmann constant

T = temperature (K)

Using the viscosity correlations from *Prosim's Component Plus* package, values for the molecular diameter were calculated over a range of temperatures.

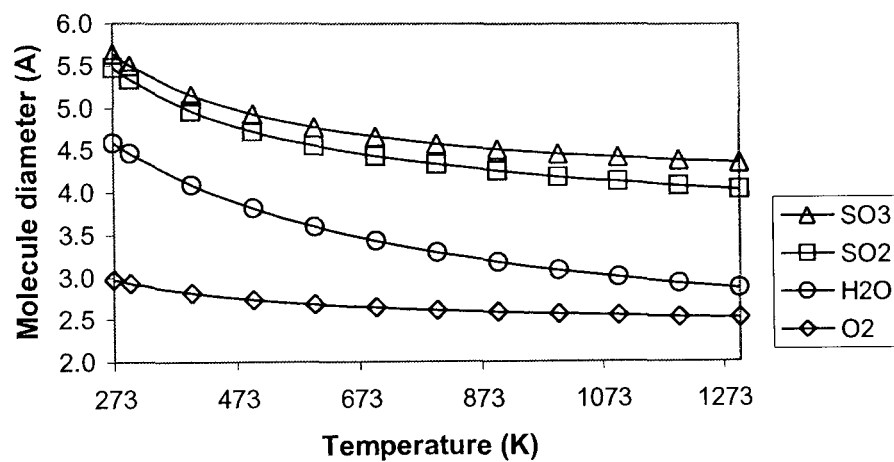


Figure 4.1: Molecular diameters calculated from ProSim viscosities using Hildebrand (1976)

The values in the graph above can be compared to those quoted by Bischoff et al. (2005) of 4.11Å, 3.47Å and 2.64Å for SO₂, O₂ and H₂O respectively. It can be seen that there are significant differences between these sets of values.

A further set of values can be calculated from Van der Waal's constants.

Van der Waal modified the ideal gas law by including two constants, a and b , to account for non-ideality:

$$\left(P + \frac{n^2a}{V^2}\right)(V - nb) = nRT$$

The constant b represents the difference in volume of the real gas compared to an ideal gas. One quarter of b represents the volume occupied solely by the molecules, assumed to be hard spheres. From this, the diameter of one molecule can be calculated (Dean 1999).

	b (l/mol)	d (Å)
SO ₃	0.06220	5.37
SO ₂	0.05636	5.20
O ₂	0.03186	4.30
H ₂ O	0.03052	4.24

Table 4.1: Van der Waal's constants and molecular diameters calculated from them as described by Dean (1999)

The values stated in Table 4.1 compare favourably with those presented in Figure 4.1 at room temperature, except for oxygen, whose diameter is calculated to be much lower using viscosity measurements in comparison to Van der Waal's constants.

4.4.3 Conclusions

Looking at the calculated values, it can be seen that the estimated molecular diameters of SO₂ and SO₃ are very similar. The values for O₂ and H₂O are also quite similar. This would seem to indicate that molecular sieving with the goal of separating SO₃ and SO₂ is likely to be difficult. Separation of O₂ and H₂O from the other reactants may however be possible using a nanoporous membrane exhibiting molecular sieving.

4.5 Conclusions of porous membrane material investigations

Silicon carbide and silica appear to be the most promising materials of construction for a porous membrane for this process, although the reaction of SiC with steam means that process temperatures would have to be limited to far below 1000°C. The lack of SiC steam corrosion information in the range 600 – 1000°C makes the potential longevity of the membrane uncertain without further experimental work.

Porous membranes were initially pursued because these had the potential to be used for SO₂ removal, whilst dense membranes are only suitable for O₂ removal.

The simulations presented in Section 4.3 demonstrated that porous membranes exhibiting Knudsen regime flow would give very poor separation of SO₃ from SO₂ and O₂. Microporous membranes would therefore be necessary in order to introduce a degree of molecular sieving. Molecular sieving may increase the membrane separation to a sufficiently high value to make their use feasible for O₂ separation, but the similar molecular diameters of SO₃ and SO₂ presented in Section 4.4 suggest that it is very

unlikely that a reasonable separation of SO_3 and SO_2 could be obtained even with molecular sieving.

Chapter 5

Dense oxygen separation membranes for sulphuric acid thermal decomposition

Dense oxygen separation membranes are a type of fast ion conducting electroceramic. These allow the transport of specific ions through a solid crystal lattice. In order for ions to move through the lattice, it must possess vacant sites into which the ions can move. There is usually only one mobile ion, which may be a cation or an anion. This is because only one ion possesses the correct charge and size to be accepted into the crystal lattice vacancy. When the lattice ions are in their normal positions they are in an electrostatic potential energy “well”. In order for an ion to move to an adjacent vacant site it must possess more energy than the activation energy required to escape the “well” and migrate to the new site (Moulson & Herbert 1990).

The basic requirements for a material for this process are:

- transports appreciable amounts of oxygen ions through its lattice structure at 700 – 1000°C;
- gas-tight (no pores connecting the membrane faces);
- chemically and physically stable under the required process conditions.

For most applications, e.g. solid oxide fuel cells, high oxygen ion flux at low temperatures is desirable. However, stable operation at high temperatures of $>700^{\circ}\text{C}$ is necessary for the acid decomposition process being studied here, since the reaction

equilibrium prohibits operation at lower temperatures. The reaction equilibrium is discussed further in Chapter 2.

Electroceramics can be broadly categorised according to their relative ionic and electronic conductivities. Since we are interested in oxygen transport, we only consider those materials that exhibit good ionic conductivity.

5.1 Ion conducting dense membranes

This category of membrane utilises materials that conduct oxygen ions when heated, but conduct electrons poorly. In order for ion conduction to occur, an external electron conduction path must be provided. This requirement is used to good effect in solid oxide fuel cells (SOFCs) in order to extract electrical power from an electrochemical cell using a material of this type as an electrolyte. If an oxygen partial pressure difference exists across the membrane, an electrical potential difference is set up across the membrane electrodes. Providing an electron conduction path under these circumstances would cause oxygen to be transported from high to low concentration and a current to flow externally. Similarly, an electrical potential can be applied across the membrane in order to drive the flow of oxygen ions. This can be used to “pump” oxygen from a low to a higher partial pressure, against the concentration gradient.

A schematic of such a membrane is shown in Figure 5.1.

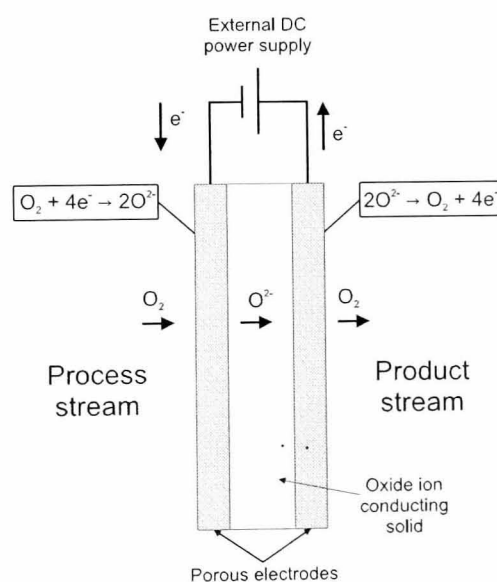


Figure 5.1: Schematic of a dense oxygen separation membrane. This membrane utilises an electrical potential to provide the driving force for the oxygen ion flux from process side to product side and hence can drive the flow against an oxygen partial pressure gradient.

Since the membrane is an electrochemical device, the electrical current flowing

through the external circuit is fixed by the oxygen permeation rate (and vice versa). As is indicated in Figure 5.1, the transmission of four moles of electrons is required for the transmission of one mole of molecular oxygen. The amount of oxygen permeating n_{O_2} (mol/s) can therefore be calculated from the current I (A) and Faraday's constant F (96485 C/s):

$$n_{O_2} = \frac{I}{4F}$$

For example, for a water splitting hydrogen production process where all of the oxygen produced passed through a membrane, the production of one mole per second of H_2 (and therefore half a mole per second of O_2) would require a current of 193kA.

The open circuit voltage E is the voltage present across the membrane electrodes when there is no current flowing, that is, there is an infinite load resistance. It is not fixed and can be calculated from the Nernst equation:

$$E = E^0 - \frac{RT}{nF} \ln \frac{P_{O_2, \text{process}}}{P_{O_2, \text{product}}} \quad (5.1)$$

For a concentration cell such as this, where the same half-reaction is occurring on both sides of the electrolytic cell, the standard electrode potential E^0 is equal to zero, therefore the Nernst equation reduces to:

$$E = \frac{RT}{2F} \ln \frac{P_{O_2, \text{process}}}{P_{O_2, \text{product}}} \quad (5.2)$$

Inspection of this equation indicates that the open circuit potential across the membrane is based on both the ratio of the oxygen partial pressures and the operating temperature of the membrane. Figure 5.2 shows the variation of open circuit voltage across the membrane at 850°C with the ratio of O_2 partial pressures, as calculated by the Nernst equation.

Application of an external electrical potential to an oxygen separation membrane would increase the energy requirements of the sulphuric acid decomposition section. It was previously shown that for 1 mol/s of H_2 production and separation of all of the associated O_2 a current of 192970A would be required. The electrical power requirement is therefore 193kJ/V.mol H_2 . If the electrical power was generated at e.g. 40% thermal efficiency, this would give a thermal power requirement for the separation process of 484kJ/V.mol H_2 . Given that 420kJ/mol H_2 is taken as a baseline energy requirement for the sulphuric acid decomposition process (Goldstein et al. 2004), the extra energy required by the separation process is significant. Minimising the applied voltage would be important in maximising the benefits from the oxygen separation.

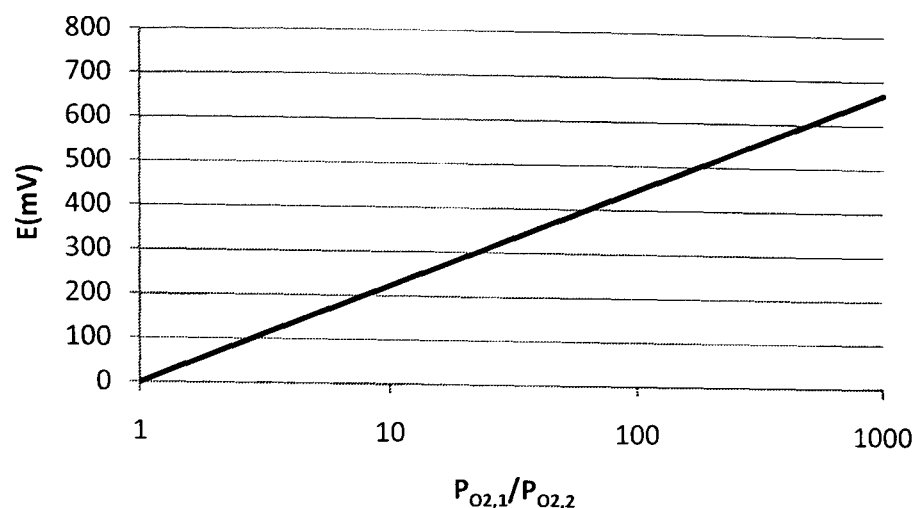


Figure 5.2: Variation of open circuit voltage across oxygen separation membrane at 850°C with the ratio of oxygen partial pressures across the membrane. Values calculated using the Nernst equation.

Despite the increased power requirements, an oxygen separation step based on a predominantly ion conducting material can still be of practical use, if it enables the operation of the process using a lower temperature heat source than would normally be considered, because of the low SO_2 yields that would normally result.

Badwal & Ciacchi's (2001) review of ceramic membrane technology comments on the properties of a number of dense oxygen separation membrane materials. Early work in the field concentrated on zirconia (ZrO_2) as an oxygen ion conductor. Yttria (Y_2O_3) stabilised zirconia, known as YSZ, is both a good conductor of oxygen ions and possesses good mechanical strength. Zirconia can exist in three phases - the highest temperature phase, the cubic phase, is conductive to oxide ions (Moulson & Herbert 1990). The addition of Y_2O_3 stabilises the cubic zirconia phase to lower temperatures. Figure 5.3, taken from Moulson & Herbert (1990), shows the fluorite structure of the zirconia unit cell and the oxide ion vacancy resulting from the addition of a dopant like yttrium. When Y^{3+} is added to the lattice, an oxide vacancy must be created in order to maintain charge neutrality in the crystal lattice. It is via these oxide vacancies that oxide ions transport through the lattice. Zirconia intrinsically exhibits an infinite separation ratio with respect to oxygen (Drioli et al. 2000) with any permeation of other species being via mechanical defects in the membrane. This may allow very oxygen rich permeates to be produced. YSZ is a proven solid electrolyte material for use in solid oxide fuel cells. Sintered YSZ components possess sufficient mechanical strength at both room temperature and the operating temperature of around 800°C (Badwal & Ciacchi 2001).

Electrochemical cells making use of YSZ have been used to create SO_x sensors (Kale et al. 2003). Production of YSZ tubes with a closed end by vacuum casting has been

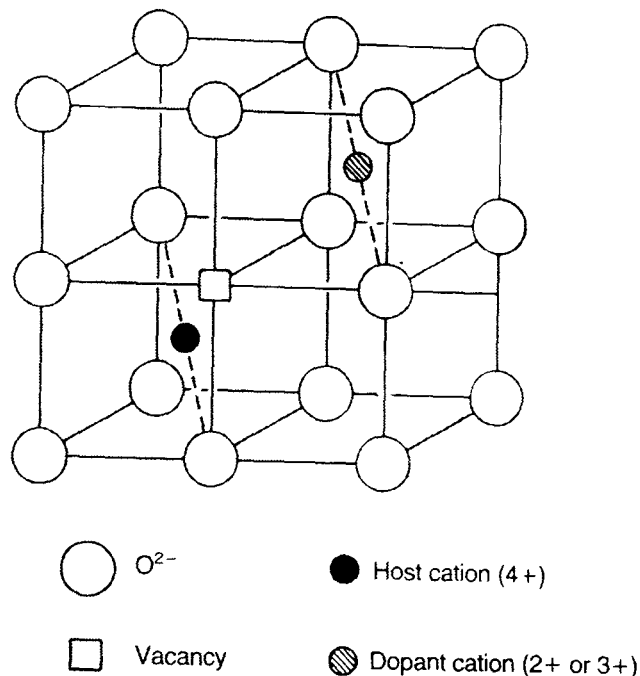


Figure 5.3: Schematic of zirconia unit cell (Moulson and Herbert 1990)

demonstrated (He et al. 2002). It is reported that this method can produce tubes of 98% density, 0.2mm thickness and 254mm length and is more cost effective than chemical deposition of YSZ films on to porous support tubes. The variation of total conductivity of the tubes with sintering temperature was measured using impedance spectroscopy (Figure 5.4) and 1600°C was found to give the highest conductivity.

Tu & Goto (2003) present data for the exposure of YSZ-coated Hastelloy to sulphur dioxide in argon ($P_{\text{SO}_2} = 10\text{kPa}$). They conclude that the YSZ film exhibits “excellent corrosion resistance” during exposure at 1273K. Furthermore, they note the development of a dense oxide layer between the YSZ film and the Hastelloy, which is attributed to oxygen diffusion through the YSZ film. This further strengthens the case for investigating the use of YSZ under high SO_2 concentration conditions. Tu only investigated the resistance of YSZ to SO_2 at one temperature, 1273K, so the resistance of the material to SO_2 at lower temperatures and at the concentrations typically found in thermochemical cycles for hydrogen production is still to be proven.

A common porous electrode material used with YSZ is platinum. These electrodes, as well as catalysing the dissociation of oxygen molecules at the ceramic surface, act as current distributors and are connected to the external electrical circuit. Adler’s (2004) extensive review of literature concerning oxygen reduction in SOFC cathodes provides relevant information for the membranes being discussed here. It is apparent from the review that there is much debate over the precise mechanism by which molecular gaseous O_2 is incorporated into a solid electrolyte such as YSZ via the porous surface electrode. There is also debate over which step is rate limiting. The general mechanism

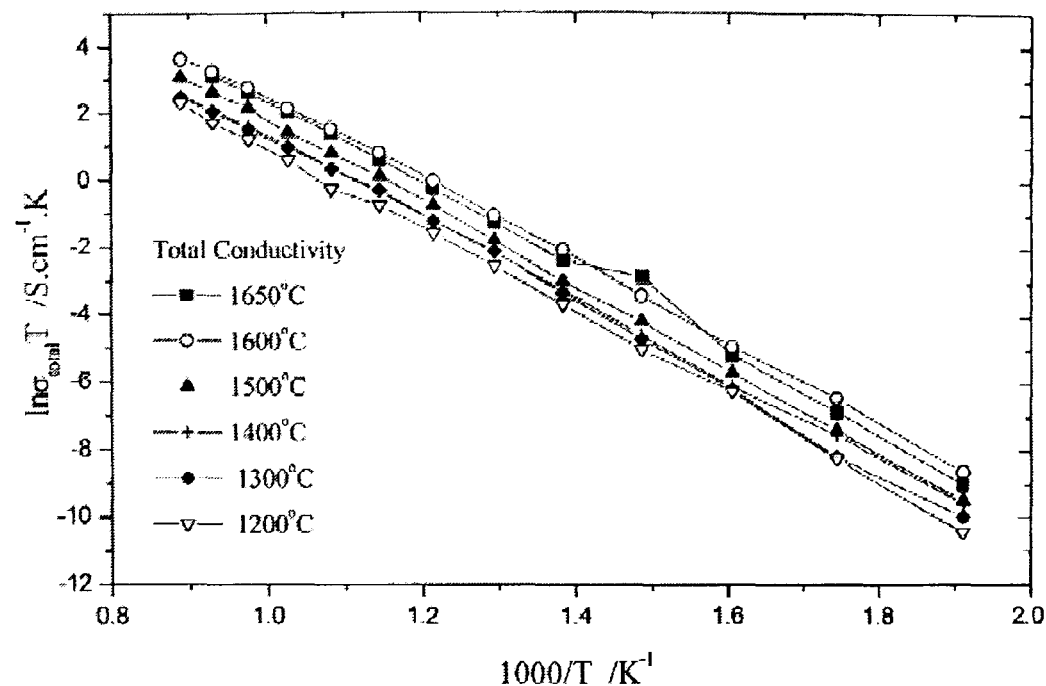


Figure 5.4: Variation of YSZ total conductivity with sintering temperature (He et al. 2002) Measured on tubes of 0.2mm thickness and 254mm length prepared by vacuum casting.

is:

- adsorption of molecular oxygen on to the bulk electrode surface;
- reduction of that molecular oxygen to O^{n-} ions;
- transport of the ions across the bulk electrode surface to the triple phase boundary (TPB) between the electrode, YSZ and gaseous phases;
- incorporation of the ions into the electrolytic YSZ bulk as O^{2-} ions.

According to the review, the important factors for the electrochemical kinetics of this system are not yet fully understood, with

chemical adsorption, surface transport, and interfacial electrochemical kinetics all playing a significant role (as well as other factors which are still not fully understood)

Although there is general consensus on the reaction pathways involved in these electrode-electrolyte-oxygen systems (see Figure 5.7), there is little knowledge of the actual mechanism. It is generally accepted that direct reaction of molecular oxygen with YSZ and solid state transport through Pt or Au electrodes does not occur (Mitterdorfer & Gauckler 1999). The manner in which oxygen interacts with a metallic platinum surface varies with temperature. Below 120K molecular adsorption occurs,

between 170-700K atomic adsorption dominates and in the range 800-1100K subsurface oxides predominate (Gland et al. 1980). The calculated phase diagram for oxygen adsorbed on to the Pt(111) surface indicates that at low and moderate temperatures ordered phases are to be expected, but no ordered phases are expected at temperatures greater than approximately 700K (Tang et al. 2004). Lau et al. (2008) presents a simplified Kinetic Monte Carlo simulation of a Pt-YSZ fuel cell cathode. Amongst the calculated data are investigations of varying the oxygen partial pressure (Figure 5.5) and the applied voltage (Figure 5.6). They found that, for this electrode system, the diffusion of adsorbed oxygen atoms across the platinum surface is the rate determining step for the conduction of oxygen through the YSZ electrolyte.

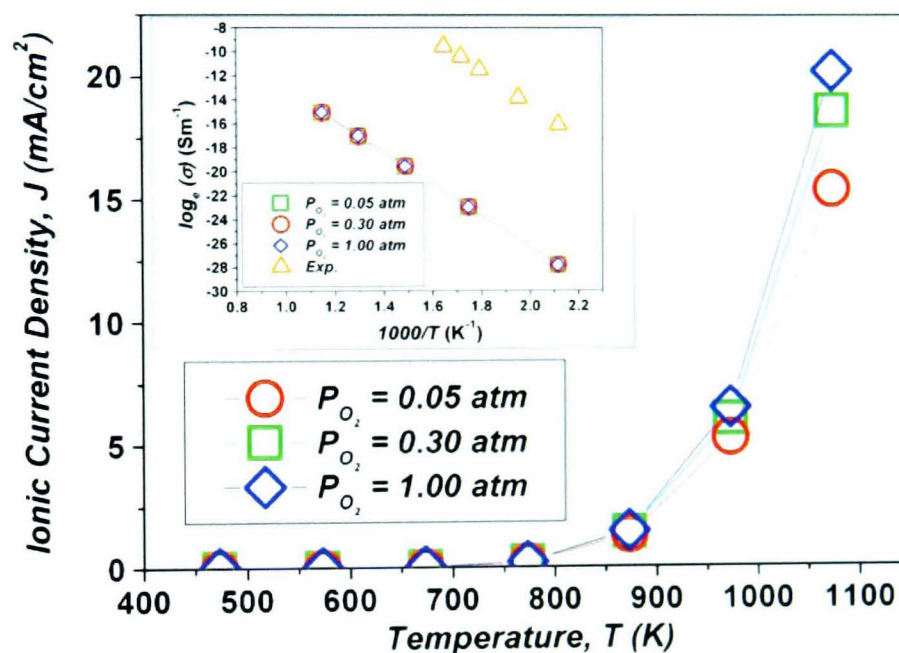


Figure 5.5: Calculated variation of ionic current density with temperature and oxygen partial pressure for YSZ-Pt SOFC cathode (Lau 2008)

Thick electrolytes exhibit high ohmic resistances (Joo & Choi 2008), therefore thin solid electrolyte films are often used in SOFCs to overcome this and increase the achievable current density at a given voltage. The use of thin electrolytes in this way may make the use of YSZ in a passive mode, i.e. with no externally applied voltage, more practical. The use of a thin electrolyte would require it to be applied as a backing layer to a porous support with a compatible rate of thermal expansion, in order for the membrane to possess sufficient mechanical strength.

It has been observed that:

at temperatures above 300K, SO_2 undergoes oxidation on [adsorbed atomic oxygen]-precovered Pt(111) to yield chemisorbed SO_4

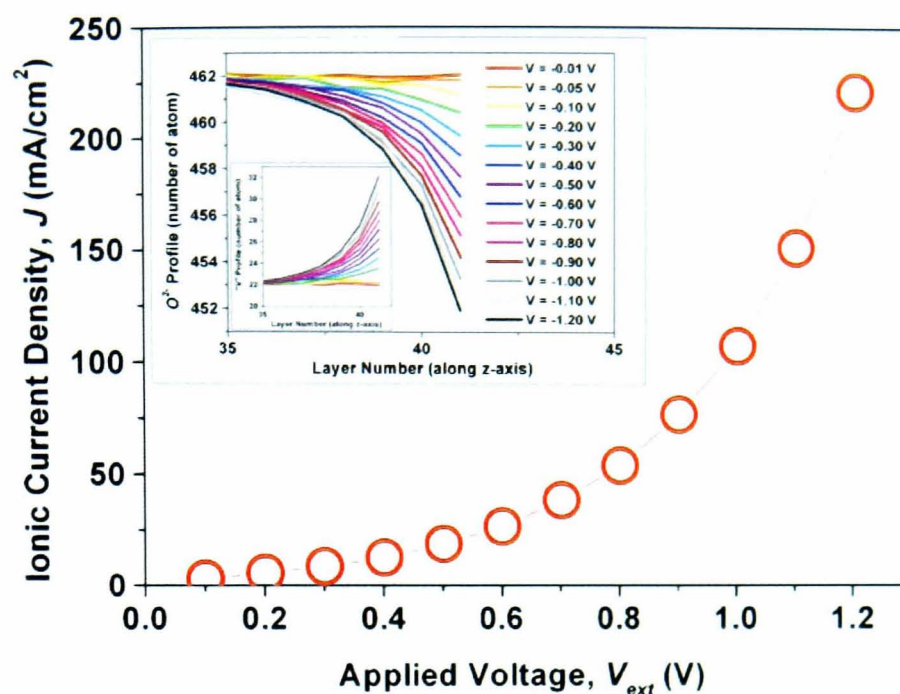


Figure 5.6: Calculated variation of ionic current density with applied voltage for YSZ-Pt SOFC cathode (Lau 2008). Values calculated at 1073K and oxygen partial pressure of 0.3 atm.

with SO_3 desorption observed at 550K (Wilson et al. 1997). The same study observed that at 450K the adsorption geometry of the adsorbed SO_4 changes from monodentate to bidentate, that is, the SO_4 bonds to the Pt through two sites rather than one. Although this is below the temperature range of interest, it does highlight a potential scenario by which the use of SO_2 could interfere with a platinum electroded oxygen pump as proposed here.

Computations are reported that consider the thermodynamics of the chemisorption of oxygen and the sulphur oxides on to Pt(111) surfaces (Lin et al. 2004). This study also showed that the most thermodynamically favourable sulphur oxide species chemisorbed on to a platinum surface is SO_4 , when the surface is pre-covered with both low and high coverages of adsorbed oxygen. The paper concludes,

SO_4 is not stable in the gas phase and thermal desorption from this species is expected to release SO_3 . SO_4 is thus a likely intermediate or spectator in the Pt-catalyzed oxidation of SO_2 to SO_3 .

Lin et al.'s (2004) paper also presents calculations of binding energies of sulphur oxides to Pt(111) surfaces. The most stable SO_4 configuration is SO_4 fcc $11^3\text{-O}_a\text{,O}_a\text{,O}_a$ (Figure 5.8), where the four oxygen atoms surround the sulphur atom in a tetrahedron and the molecule is bound to the surface through three oxygen atoms. These strongly bound SO_4 species have the potential to block O_2 adsorption and transport to the triple phase boundary with the YSZ electrolyte.

Evidence of SO_2 adsorption affecting the operation of a PEM fuel cell platinum electrode was found towards the close of this project (Fu et al. 2009). This indicates that surface coverage by sulphur oxide species can be sufficient to retard oxygen transport across the platinum surface to the triple phase boundary. This is further discussed in Section 8.6.3 and influences the direction of the proposed future work. Fu found that variation of the electrical potential at the electrode affects the relative kinetics of O_2 and SO_2 adsorption. This may enable the retardation of SO_2 adsorption on to the electrode surface, and removal of that SO_2 which does adsorb. The only other literature found also examined the effect of very low SO_2 concentrations (2.5-5ppm) on PEM cathodes (Mohtadi et al. 2004). The work was carried out at 70°C and hence is not directly applicable to the high temperature process being considered here. However, an important observation was that cell performance decreased markedly during SO_2 exposure, but could be recovered through the use of cyclic voltametry.

To the best of the author's knowledge, no literature exists on the effect on fuel cell electrodes of such high SO_2 concentrations as those used in this work.

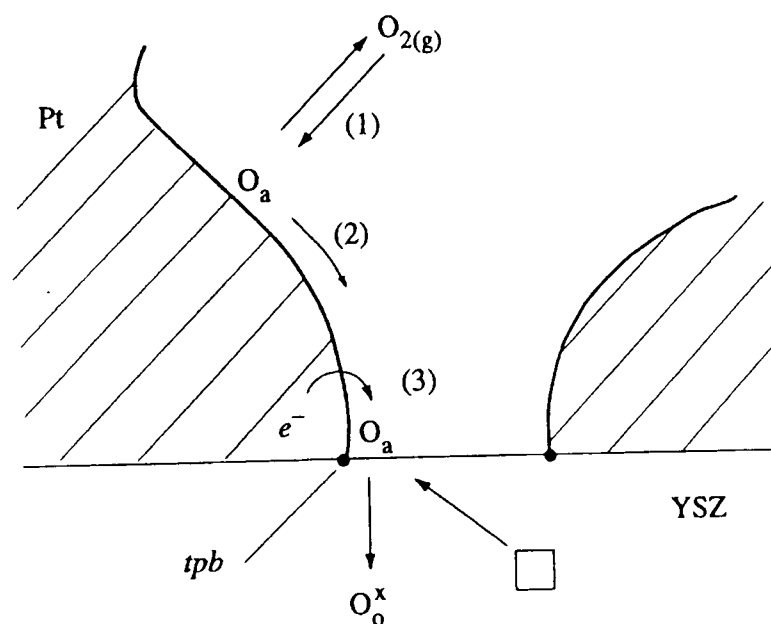


Figure 5.7: Reaction pathway for Pt-YSZ- O_2 system (Mitterdorfer 1999) showing (1) adsorption of molecular O_2 on to Pt surface followed by dissociation to atomic oxygen; (2) diffusion of the adsorbed oxygen to the triple phase boundary (TPB); (3) electronation of the adsorbed atomic oxygen and incorporation into the YSZ, filling a lattice vacancy.

As part of a study into SO_2 -poisoned ceria-zirconia mixed oxides, Luo & Gorte (2004) exposed 1wt% Pd on ZrO_2 to 1% SO_2 in 50% O_2 at 673K for 30 minutes. Based on weight change, they deduced that the sulphate coverage of the surface was "somewhat less" than would be expected for a total coverage monolayer. Additionally, when undergoing temperature programmed desorption (TPD) using a pure helium

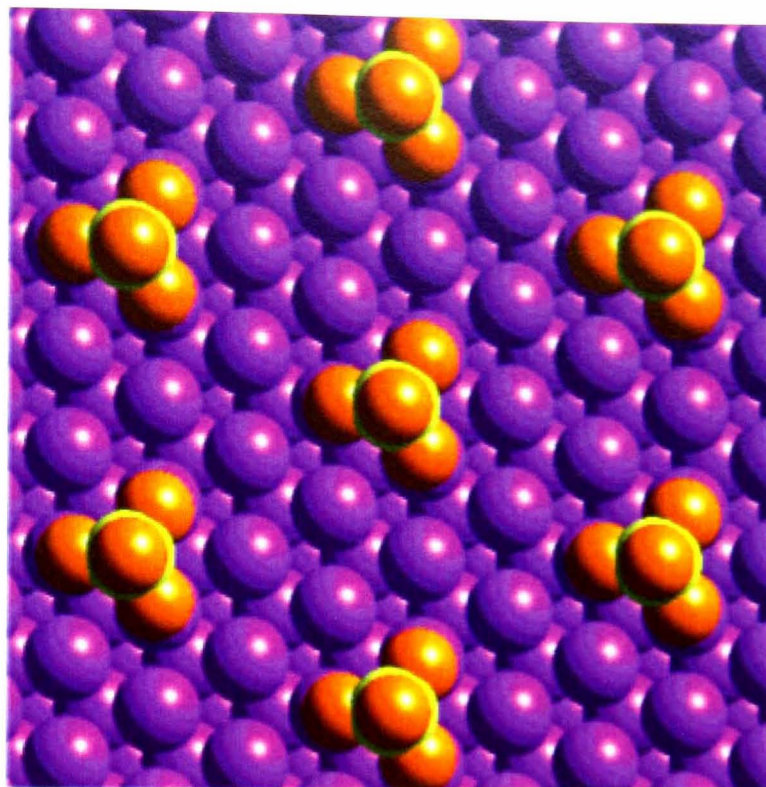


Figure 5.8: SO_4 molecular structure on Pt(111) surface (Lin et al. 2004) - fcc η^3-O_a,O_a,O_a configuration

carrier gas, negligible amounts of SO_2 desorbed from the surface below 1100K. This work indicates the importance of avoiding SO_2 contact with zirconia-based materials at relatively low temperatures.

Many oxygen conducting materials exhibit the perovskite-type crystal structure. Oxide perovskites have a cubic primitive cell with the general formula ABO_3 , where the A cations are at the body centre, B cations are at the face corners and oxide ions are at the edge centres (West 1999). The oxidation states of the A and B cations should sum to six. As with the doped zirconia discussed earlier, substitution of a fraction of the cations with others of lower valency results in the creation of oxide ion vacancies in order to maintain crystal charge neutrality and can allow oxide ion transport through the lattice.

One of the earliest studies into the oxide conductivity of a perovskite structured material was performed on $LaGaO_3$ doped with Sr, Ba or Ca for La and Mg, Al or In for Ga (Ishihara et al. 1994). Strontium and magnesium were found to be the most effective A and B site dopant respectively. A comparison between the oxide conductivities of $La_{0.9}Sr_{0.1}Ga_{0.8}Mg_{0.2}O_3$ and literature data is shown in Figure 5.9. It indicates that $La_{0.9}Sr_{0.1}Ga_{0.8}Mg_{0.2}O_3$ is almost an order of magnitude more conductive than ZrO_2 doped with 9% Y_2O_3 .

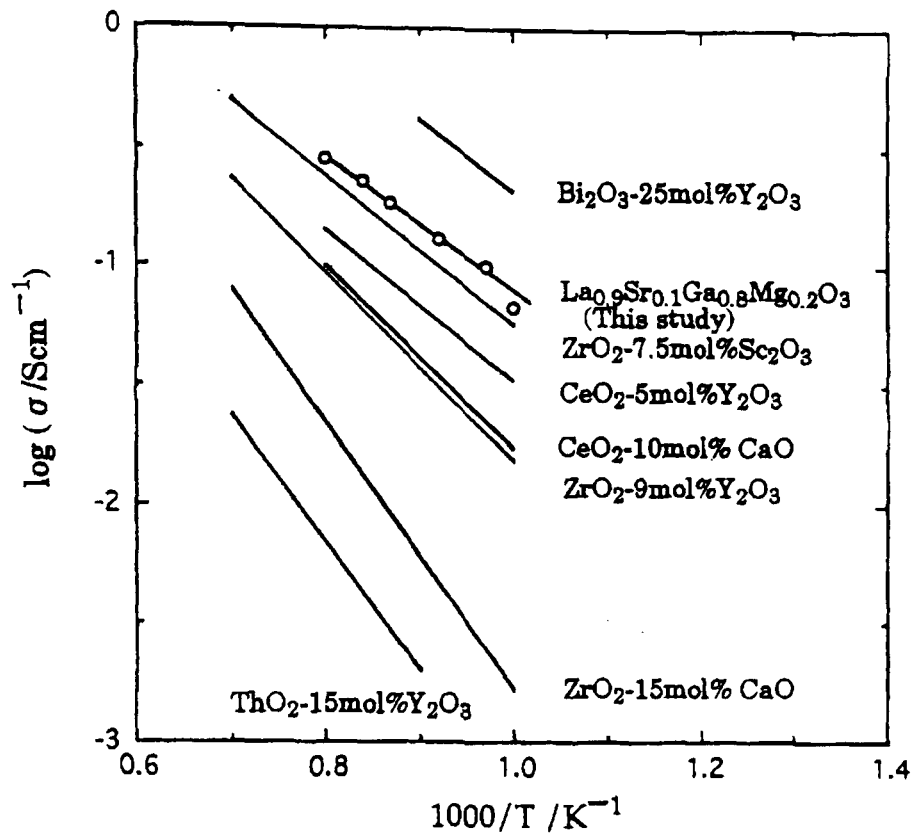


Figure 5.9: Oxide conductivity of $\text{La}_{0.9}\text{Sr}_{0.1}\text{Ga}_{0.8}\text{Mg}_{0.2}\text{O}_3$ compared to other materials (Ishihara et al. 1994)

Yamamura et al. (2003) used molecular dynamics simulations to design a new oxygen ion conductor based on the perovskite structure. Their simulations found LaGaO_3 to be the best base composition for a perovskite oxygen ion conductor. Outside of the La-series, SmAlO_3 was found to give the next highest oxygen conductivity. Ultimately, $\text{Sm}_{0.8}\text{Ca}_{0.2}\text{AlO}_{2.9}$ was found to give the highest experimental total conductivity, which was comparable to that of 8% YSZ (Figure 5.10).

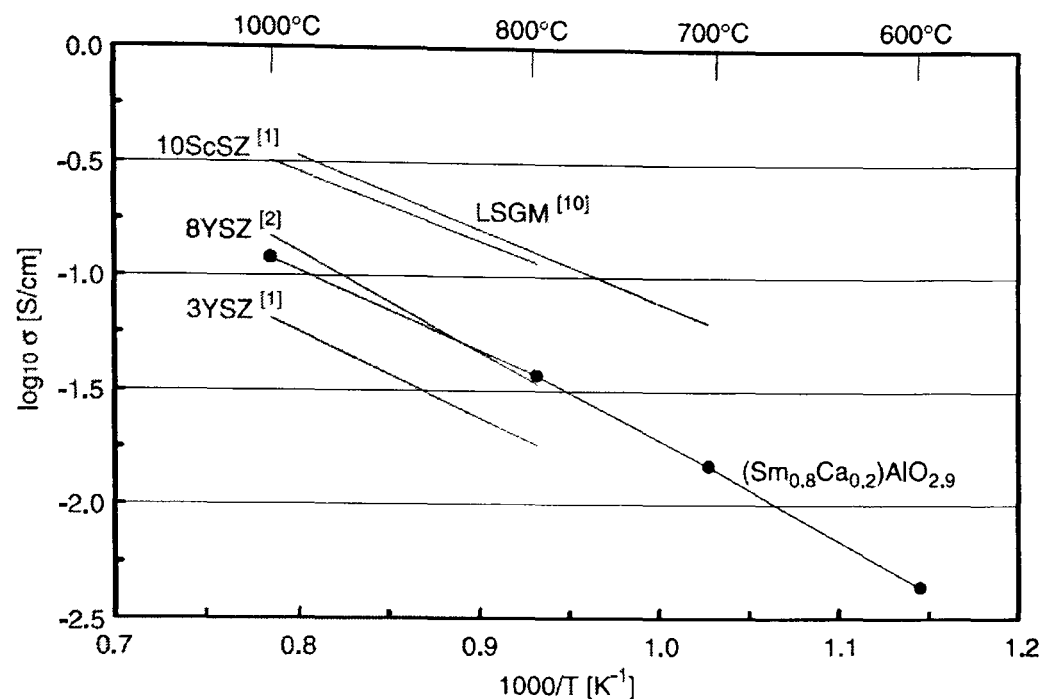


Figure 5.10: Oxide conductivity of $\text{Sm}_{0.8}\text{Ca}_{0.2}\text{AlO}_{2.9}$ compared to other materials (Yamamura et al. 2003)

Shuk et al. (1996) reported that bismuth oxide (BiO_2) exhibited oxygen fluxes an order of magnitude higher than zirconia, at a given temperature. Badwal & Ciacchi (2001) found that doped CeO_2 , BiO_2 , BiMVO_3 and LaGaO_3 can be used for low temperature operation. CeO_2 exhibits the greatest ionic conductivity when doped with SmO_2 and GdO_2 . Doped CeO_2 and LaGaO_3 however have low mechanical strength at room temperature. Doped BiO_2 is also reported by Badwal to have significantly greater ionic conductivity than doped CeO_2 and ZrO_2 . The dopants can be Y_2O_3 , Gd_2O_3 , Er_2O_3 , Dy_2O_3 , Nb_2O_5 , Ta_2O_5 , and others. Materials based on BiMVO_x also exhibit high ionic conductivity. As with CeO_2 and LaGaO_3 , bismuth oxide based materials suffer from low mechanical strength, complicating manufacture.

At 750°C, Badwal & Ciacchi (2001) state that oxygen fluxes of up to $1.5 \text{ cm}^3 / \text{min} \cdot \text{cm}^2$ are achievable with ZrO_2 -based materials. However, no information is given on the process conditions (other than temperature) under which this was achieved.

5.2 Mixed ion/electron conducting dense membranes

Membranes driven by a trans-membrane oxygen partial pressure differential are fabricated from materials which, at high temperatures, conduct both oxygen ions and electrons effectively. These materials are known as mixed ionic and electronic conductors, or MIECs. There is no external electron conduction path and oxygen trans-

port is in the direction of high to low oxygen partial pressure, whilst electrons travel in the opposite direction. A schematic of such a membrane is shown in Figure 5.11.

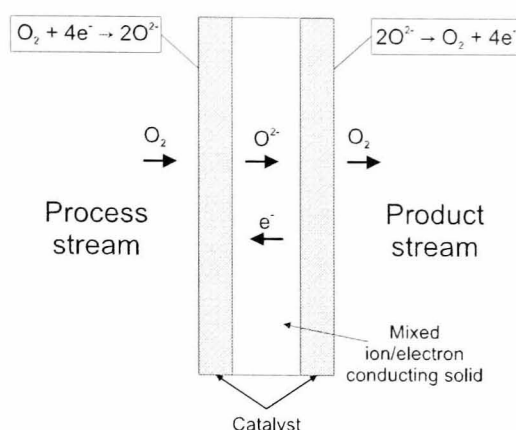


Figure 5.11: Schematic of a dense oxygen separation membrane. This membrane utilises the oxygen partial pressure gradient to provide the driving force for the oxygen ion flux from process side to product side. The membrane operates as an electrochemical device, with oxide ions being transported from cathode to anode and electrons flowing in the opposite direction.

Badwal & Ciacchi (2001) mentions three materials reported in literature to exhibit high oxygen ion conductivity. These are:

- $\text{Sr}_4\text{Fe}_{6-x}\text{Co}_x\text{O}_{13\pm\delta}$
- $\text{La}_{1-x}\text{Sr}_x(\text{Ga}_{1-y}\text{M}_y)\text{O}_{3\pm\delta}$ (LSGM) where M = Fe or Co
- $\text{SrCoO}_{3-\delta}$ doped partially or completely at the “A” lattice site (e.g. with La, Gd, Nd, Sm, Pr, etc.) and at the “B” lattice site (e.g. with Fe, Cr and Ti).

Cutler & Meixner (2003) report on the properties of lanthanum strontium manganite (LSM) materials. LSM materials are perovskite-type materials, often used in solid oxide fuel cells (SOFCs) because of their electronic conductivity and compatibility with ceria and zirconia. As they are poor oxygen ion conductors, they are used as electrically conducting interconnects between layers of the SOFC electrode stack. Cutler studied the addition of gadolinia-doped ceria (CGO) to LSM in order to produce an MIEC material suitable for use as a membrane. It was found however that the oxygen flux would be unacceptably low ($2.0 \text{ sccm}/\text{cm}^2$ at 850°C with an oxygen partial pressure ratio of 7) for LSM-CGO composites used in a pressure driven system. Cutler suggests that pressure driven systems should instead utilise a composite of CGO and a perovskite-type material which exhibits high ionic and electronic conductivity. Such a composite may have good ionic and electronic conductivity and also good mechanical strength.

Marozau et al. (2006) reiterates the point that LSM materials have a relatively low oxygen ionic conductivity and presents $\text{Sr}_{1-x}\text{Ce}_x\text{MnO}_{3-\delta}$ (SCM) materials as an alternative with greater ionic conductivity. SCM materials have a perovskite-type structure down to room temperature and exhibit total conductivity which is two or three orders of magnitude greater than $\text{SrMnO}_{3-\delta}$. Marozau notes that this conductivity is still lower than that of other potential materials, such as $\text{La}_{1-x}\text{Sr}_x\text{Fe}_{1-y}\text{Co}_y\text{O}_{3-\delta}$, but that the ionic conductivity of SCM can be improved by partial substitution of manganese. Doping SCM with Al^{3+} may increase oxygen vacancy concentration (increasing the ionic conductivity) and suppress interactions between this electrode material and stabilised zirconia electrolytes.

Kharton et al. (2003) presents experimental results showing that $\text{Sr}_{0.7}\text{Ce}_{0.3}\text{MnO}_{3-\delta}$ oxygen permeability is higher than $\text{La}_{0.7}\text{Sr}_{0.3}\text{MnO}_{3-\delta}$, but not as high as $\text{La}_{0.8}\text{Sr}_{0.2}\text{Fe}_{0.8}\text{Co}_{0.2}\text{O}_{3-\delta}$. For example, at 950°C , the oxygen permeation flux for 1mm thick membranes with oxygen partial pressures on each side of 2.1kPa and 21kPa was approximately 3.2×10^{-11} , 5.0×10^{-10} , and 2.5×10^{-8} mol/s·cm² for $\text{La}_{0.7}\text{Sr}_{0.3}\text{MnO}_{3-\delta}$, $\text{Sr}_{0.7}\text{Ce}_{0.3}\text{MnO}_{3-\delta}$, and $\text{La}_{0.8}\text{Sr}_{0.2}\text{Fe}_{0.8}\text{Co}_{0.2}\text{O}_{3-\delta}$ respectively.

Kharton notes that the disadvantages of $\text{La}(\text{Sr})\text{Fe}(\text{Co})\text{O}_{3-\delta}$ include high thermal expansion, which would cause sealing difficulties if this material were to be used for a high temperature membrane.

In considering a CMR for a methane partial oxidation process, Zhang et al. (2007) presents literature data for oxygen permeation fluxes of a number of MIEC materials when swept with a reducing gas. Since a reducing gas would be expected to react with the permeating oxygen quickly, the oxygen partial pressure gradient would be higher than if an inert sweep gas were used.

The application of surface catalyst to MIEC materials to aid O_2 dissociation/recombination may or may not be necessary. Kharton et al. (2003) presents data for $\text{Sr}_{0.7}\text{Ce}_{0.3}\text{MnO}_{3-\delta}$ which shows that, for this material:

- The deposition of a platinum catalyst on the membrane surfaces does not increase the oxygen permeation rate;
- The oxygen permeation rate is inversely proportional to the membrane thickness.

The neutral effect of adding platinum to the membrane surface is attributed to “insufficient electrocatalytic activity of platinum and, hence, partial blocking of the surface”. This indicates that if a material is used that exhibits high oxygen permeance (relative

to $\text{Sr}_{0.7}\text{Ce}_{0.3}\text{MnO}_{3-\delta}$) then the addition of platinum catalyst to the membrane surfaces would not be necessary.

Teraoka et al. (2002) investigated the catalytic properties of some perovskites. $\text{SrCo}_{0.8}\text{Fe}_{0.2}\text{O}_{3-\delta}$, $\text{La}_{0.1}\text{Sr}_{0.9}\text{Co}_{0.9}\text{Fe}_{0.1}\text{O}_{3-\delta}$, $\text{La}_{0.2}\text{Sr}_{0.8}\text{Co}_{0.8}\text{Fe}_{0.2}\text{O}_{3-\delta}$ and $\text{La}_{0.6}\text{Sr}_{0.4}\text{Co}_{0.8}\text{Fe}_{0.2}\text{O}_{3-\delta}$ were used as the membrane materials, and LaCoO_3 and $\text{La}_{0.8}\text{Sr}_{0.2}\text{CoO}_{3-\delta}$ were used as catalytic materials. Surface exchange kinetics become more dominant as membrane thickness decreases and therefore bulk diffusion through the lattice becomes less dominant. They found that applying a porous catalyst layer to the anode increased oxygen transport in all cases as a result of the increased surface area available for surface exchange. Only when a catalyst with a high oxygen sorption/desorption capacity was applied to the cathode did it make a positive difference. As an aside, they found that applying platinum to either surface reduced the oxygen permeation flux.

5.3 Dense membrane sulphation calculations

Oxygen ion conducting dense membranes are constructed from mixtures of a number of metal oxides. Porous membranes are also usually fabricated from metal oxides, although they can also be fabricated from silicon carbide. As briefly mentioned in Section 2.3 in relation to catalysts, thermodynamic equilibria dictate that, at lower temperatures, a metal sulphate may be more stable than the metal oxide. Therefore, if a metal oxide is exposed to SO_2 at relatively low temperatures, the metal oxide may convert to the sulphate which would “poison” an oxygen ion-conducting dense membrane, retarding the oxygen flux through that membrane.

5.3.1 Aim

The purpose of this work was to investigate the stability of a variety of metal oxides in the type of conditions to which they would be expected to operate for the sulphuric acid thermal decomposition process. This was accomplished by the use of equilibrium simulations.

5.3.2 Method

The *HSC Chemistry* package was used in order to investigate the equilibrium conditions of the system using Gibbs free energy minimisation.

The package was configured for a two phase gas-solid system. The solid phase initially consisted of 1 kmol of metal oxide. Every other solid species present in the *HSC Chemistry* database consisting of one or more of S, O, H and the metal under investigation was also added with zero initial amount. Similarly, the gaseous phase initially consisted of 100 kmol H_2SO_4 , along with SO_3 , SO_2 , O_2 and H_2O at zero initial amount. This 1:100 molar ratio of solid and gas phases represents the presence of a large excess of gaseous components for the purposes of the solid sulphation reactions.

The package was instructed to calculate the system equilibrium conditions for the temperature range 500-1500°C at 1 and 20 bara.

The oxides of Al, Ba, Ca, Ce, Dy, Eu, Gd, La, Nd, Pr, Rb, Si, Sm, Sr, Y and Zr were investigated. All of these metal oxides are found in ion conducting or MIEC membranes which may be suitable for the proposed process.

5.3.3 Results

A series of graphs was produced from the *HSC Chemistry* simulation data, showing the composition of the solid phase for each of the metal oxides examined. Some of these graphs are presented in this section and the remainder can be found in Appendix B.

Of the 20 metal oxides simulated, only four are calculated to be stable in the temperature range of interest and at both 1 and 20 bara: Si, Sm, Y and Zr. Al, Dy, Eu, Gd and Pt may be stable at part of the temperature range, whilst Ba, Bi, Ca, Ce, Co, Fe, La, Nd, Pr, Rb and Sr are not suitable at any point in the required temperature range.

Silica, in the form of quartz, is the material usually used for lab-scale experimentation involving the high temperature thermal decomposition of sulphuric acid. These equilibrium simulations show that silica is stable at 1 bara (Figure 5.12) and 20 bara (Figure 5.13) over the required temperature range, confirming its suitability for this application. Conversely, alumina, another common engineering ceramic, is less suitable. At 1 bara, the equilibrium composition contains aluminium sulphate, $\text{Al}_2(\text{SO}_4)_3$, below 750°C, with a mixture of oxide polymorphs at higher temperatures (Figure 5.14). Aluminium sulphate is present at up to 900°C at 20 bara (Figure 5.15), hence at this elevated pressure alumina would not be suitable for use with the proposed process.

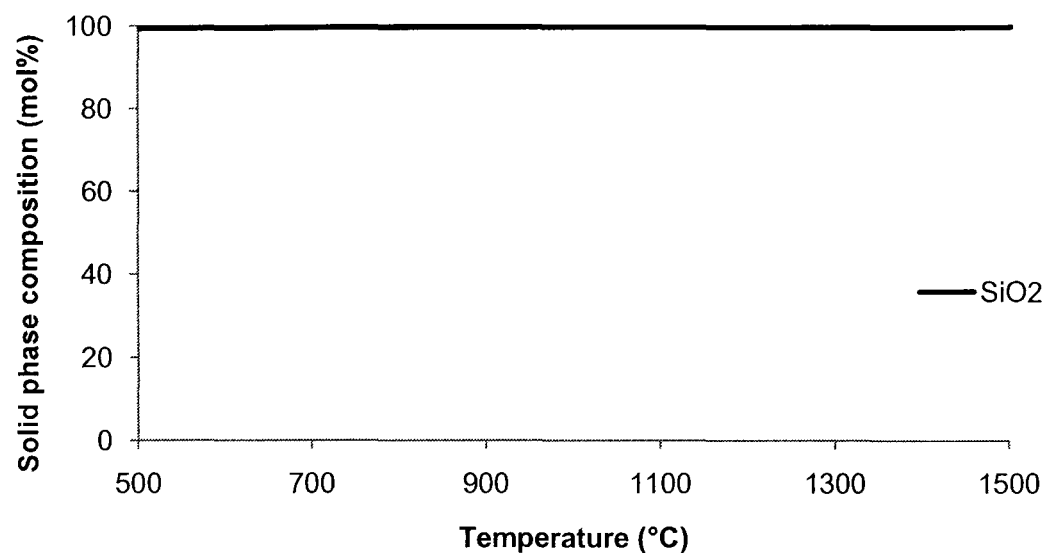


Figure 5.12: Equilibrium calculation of SiO₂ stability at 1 bara, with gaseous phase of H₂SO₄ equilibrium decomposition products in large excess. Calculations carried out by Gibbs minimisation in HSC Chemistry.

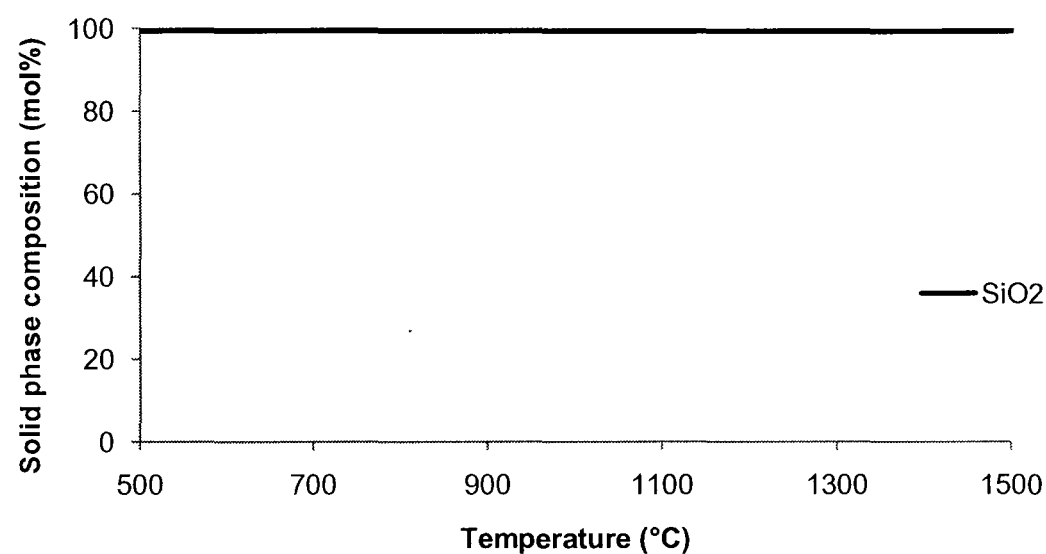


Figure 5.13: Equilibrium calculation of SiO₂ stability at 20 bara, with gaseous phase of H₂SO₄ equilibrium decomposition products in large excess. Calculations carried out by Gibbs minimisation in HSC Chemistry.

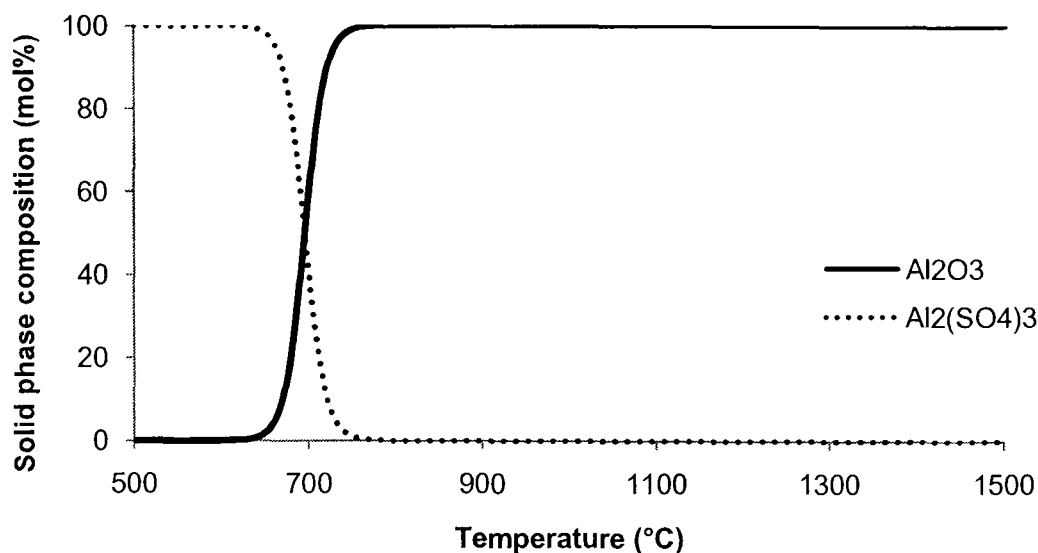


Figure 5.14: Equilibrium calculation of Al_2O_3 stability at 1 bara, with gaseous phase of H_2SO_4 equilibrium decomposition products in large excess. Calculations carried out by Gibbs minimisation in HSC Chemistry.

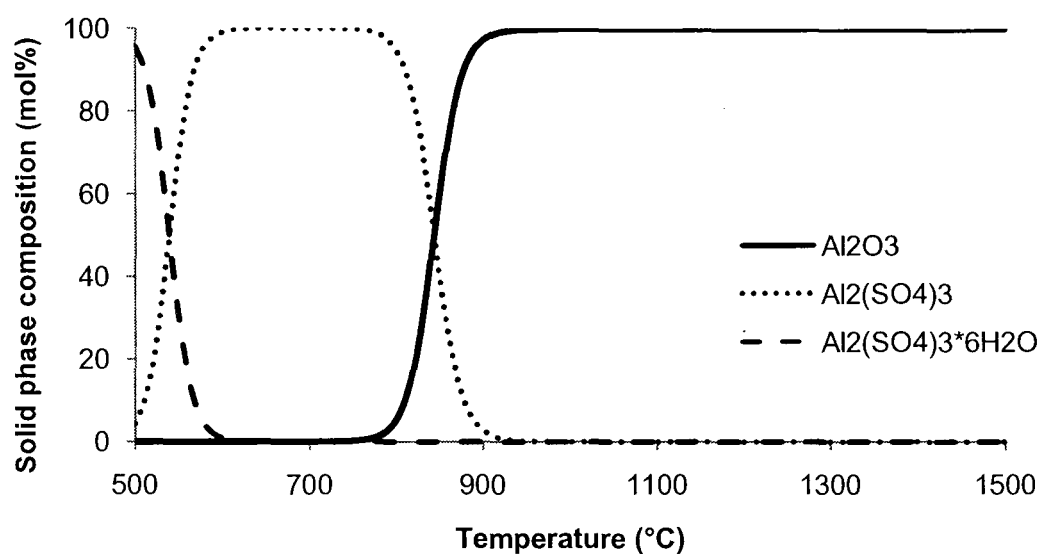


Figure 5.15: Equilibrium calculation of Al_2O_3 stability at 20 bara, with gaseous phase of H_2SO_4 equilibrium decomposition products in large excess. Calculations carried out by Gibbs minimisation in HSC Chemistry.

It is common to use platinum as the electrode material for dense ion conducting membranes. Platinum sulphate is not included in the *HSC Chemistry* database and hence could not be included, however the simulations were performed with those species available, which include platinum metal and platinum oxide. The results showed that at 1 bara, less than 10% of the solid phase was platinum oxide in the temperature range of interest, with the remainder being platinum metal (Figure 5.16). At 20 bara, the percentage of platinum oxide present increased to a maximum of 25% at 700°C (Figure 5.17). The presence of platinum oxide may impair the performance of the elec-

trodes.

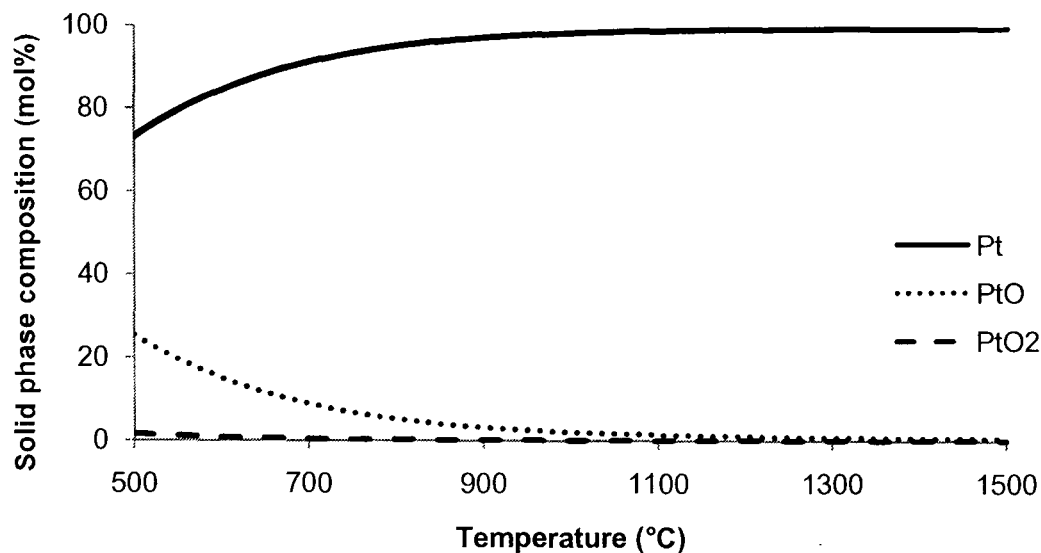


Figure 5.16: Equilibrium calculation of Pt stability at 1 bara, with gaseous phase of H_2SO_4 equilibrium decomposition products in large excess. Calculations carried out by Gibbs minimisation in HSC Chemistry.

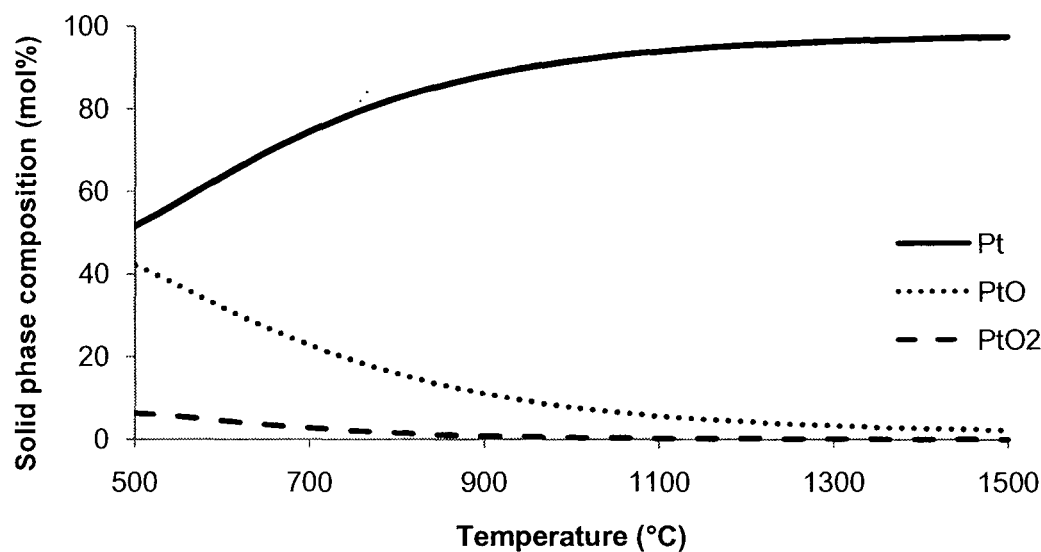


Figure 5.17: Equilibrium calculation of Pt stability at 20 bara, with gaseous phase of H_2SO_4 equilibrium decomposition products in large excess. Calculations carried out by Gibbs minimisation in HSC Chemistry.

Of the three metal oxides other than silica that were calculated to be stable, yttria and zirconia are the most interesting, as yttria stabilised zirconia (YSZ) is a common solid electrolyte used in the manufacture of solid oxide fuel cells. Yttria shows total oxide stability over the temperature range simulated at 1 bara (Figure 5.18), with a hydrated yttrium sulphate being preferred at temperatures below those of interest at 20 bara (Figure 5.19). Although zirconia is preferred over zirconium sulphate above 600°C at 1 bara (Figure 5.20), zirconium sulphate is preferred at up to around 750°C at the elev-

ated pressure of 20 bara (Figure 5.21). This suggests that YSZ may have a limited temperature range at elevated pressures, but otherwise should be stable for use with the sulphuric acid thermal decomposition process. YSZ has the disadvantage that, being a predominantly ionic conductor, it would require the provision of an external electrical circuit, a fact that would ordinarily make MIEC materials such as perovskites more attractive (Julbe et al. 2001). However, since the constituent elements of perovskites appear to be unsuitable from a chemical stability viewpoint, YSZ appears to be the most viable option for applying a separation membrane to this process.

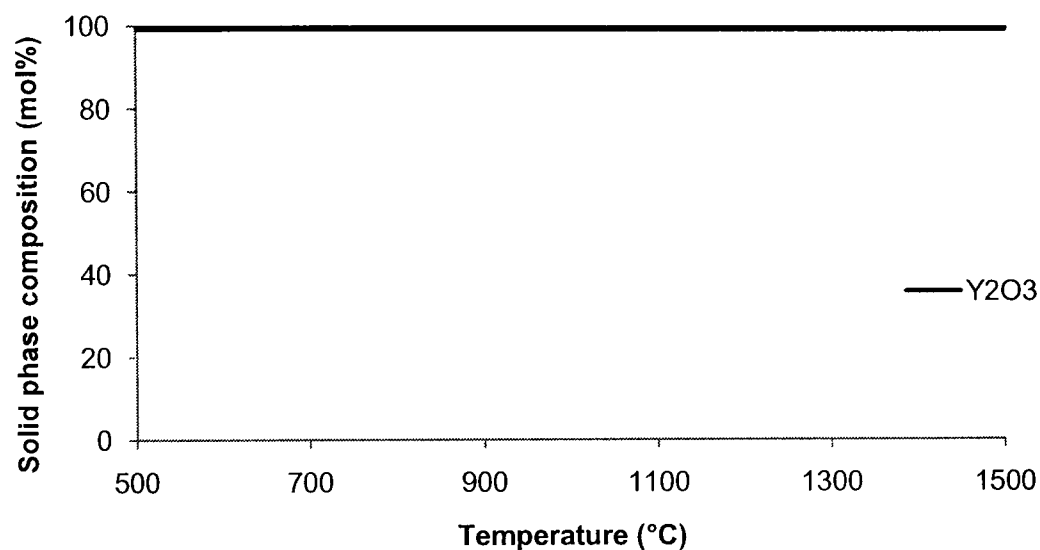


Figure 5.18: Equilibrium calculation of Y_2O_3 stability at 1 bara, with gaseous phase of H_2SO_4 equilibrium decomposition products in large excess. Calculations carried out by Gibbs minimisation in HSC Chemistry.

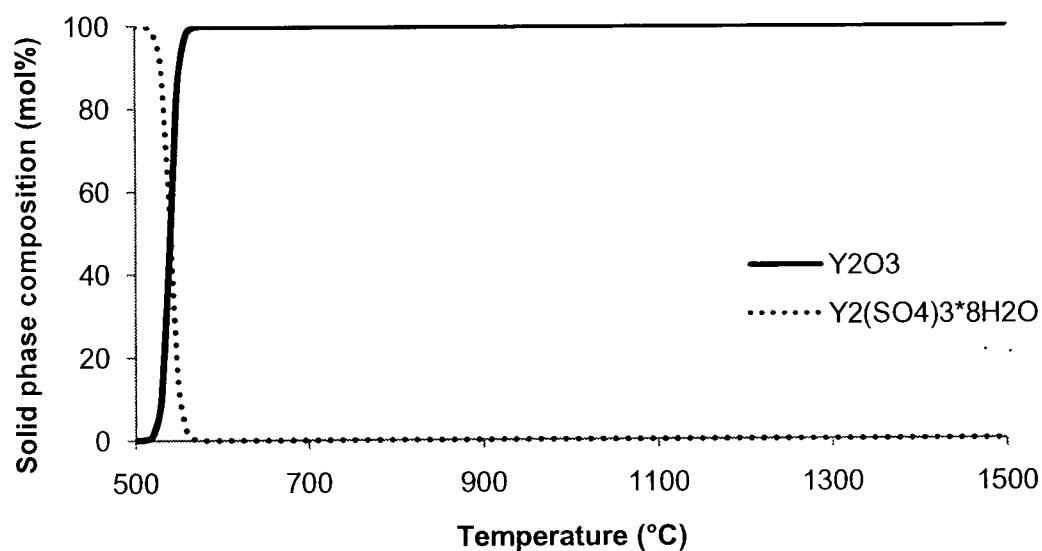


Figure 5.19: Equilibrium calculation of Y_2O_3 stability at 20 bara, with gaseous phase of H_2SO_4 equilibrium decomposition products in large excess. Calculations carried out by Gibbs minimisation in HSC Chemistry.

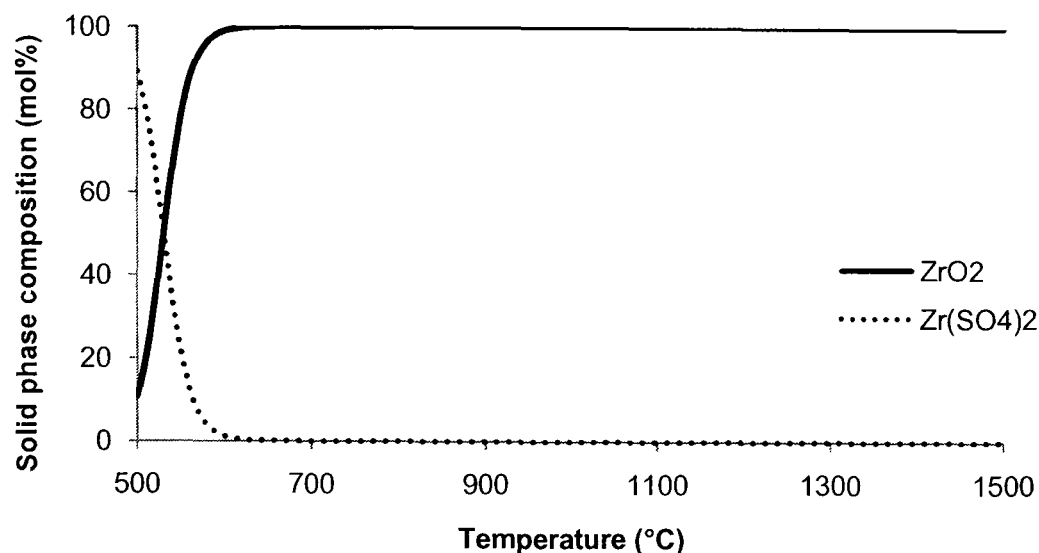


Figure 5.20: Equilibrium calculation of ZrO_2 stability at 1 bara, with gaseous phase of H_2SO_4 equilibrium decomposition products in large excess. Calculations carried out by Gibbs minimisation in HSC Chemistry.

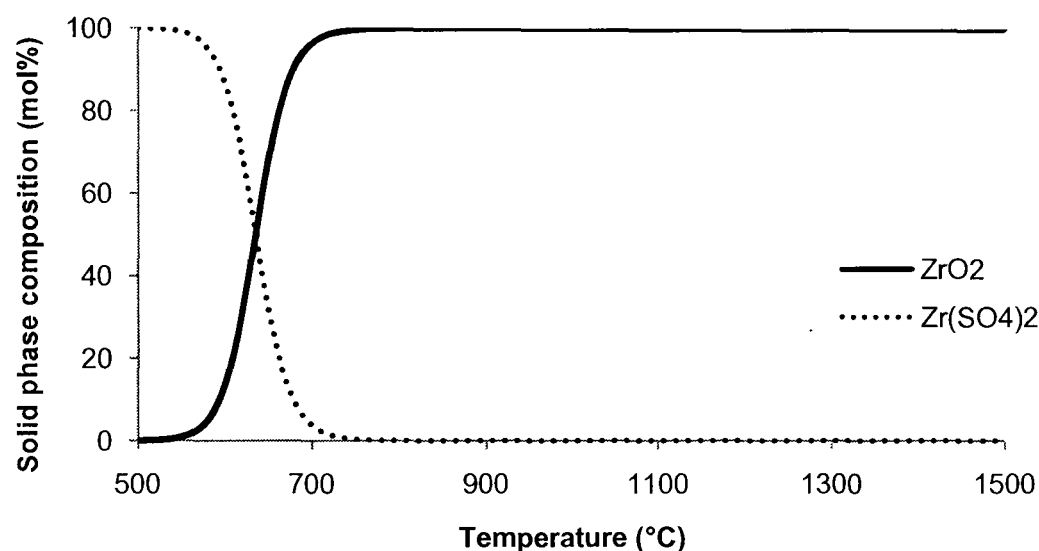


Figure 5.21: Equilibrium calculation of ZrO_2 stability at 20 bara, with gaseous phase of H_2SO_4 equilibrium decomposition products in large excess. Calculations carried out by Gibbs minimisation in HSC Chemistry.

5.3.4 Conclusions of metal oxide equilibrium simulations

The majority of the metal oxides considered here are not suitable for use with the sulphuric acid thermal decomposition process, based on the results of the *HSC Chemistry* equilibrium calculations. The equilibrium data for silica strongly suggests it will be stable in the reaction environment, allowing quartz to be used for high temperature apparatus. Yttria and zirconia were both calculated to be stable in the temperature range of interest, except for zirconia at $<750^\circ\text{C}$ and 20 bara. Because of this, YSZ is a

good candidate material to be used for this process and should be further investigated.

5.4 Conclusions of dense membrane materials investigations

Since it became apparent that porous membranes would almost certainly only be suitable for O₂ separation, the research changed focus to investigation of dense, ion-conducting membranes, as these were likely to give higher separation factors for O₂ separation than porous materials. The materials stability simulations presented in Section 5.3 show that, whilst a number of metal oxides used for MIEC materials are unlikely to be suitable for use in this process, zirconia-based materials may be suitable, as they are not predicted to convert from the metal oxide to the metal sulphate at the required process temperatures, pressures and stream compositions. Since yttria-stabilised zirconia is a commercially used, easily bought solid electrolyte, it was felt that YSZ membranes were the most promising candidate for a first attempt at oxygen separation under these conditions, despite the disadvantage of requiring external electrical circuitry. The application of an external voltage to the membrane will increase the power requirements of the process, but may also enable the use of lower temperature heat sources, negating this disadvantage. It may be that in the future the YSZ layer can be made sufficiently thin to allow operation in a passive mode, with no externally applied electrical potential, yet achieve an acceptable oxygen permeation flux. However, for ease of handling, thick YSZ pellets will be used for these experimental tests and hence the passive mode permeation flux is expected to be very small, requiring the application of an external electrical potential.

No experimental data exists for the exposure of YSZ to H₂SO₄ decomposition process conditions and hence experimental characterisation will be required to confirm suitability. The following chapter describes the experimental apparatus designed and built for this purpose.

Chapter 6

Experimental work: description and design

6.1 Aims

The aims of this experimental programme were:

- to determine the oxygen permeation characteristics of yttria-stabilised zirconia (YSZ) under conditions relevant to its use in the sulphuric acid decomposition process;
- to assess the stability and longevity of YSZ under those same conditions.

6.2 Background

The material stability simulations described in Section 5.3 suggested that YSZ should be stable under sulphuric acid decomposition process conditions. This, along with the fact that YSZ is readily available and already used as an electrolyte in solid oxide fuel cells, is the reason that YSZ was selected for investigation.

No pre-existing equipment for carrying out this type of experimental work was available in the department. Consequently, the experimental apparatus described here was specified, designed, procured and assembled from scratch.

A detailed method for these experiments is given in Section 8.1.2. The general procedure was to:

- characterise each YSZ disk following fabrication;
- record the current and oxygen permeating through the disk with a He–O₂ feed over a period of time;
- record the same with a He–O₂–SO₂ feed;
- characterise the YSZ following exposure.

This procedure was carried out at a constant temperature and pressure. The pressure was limited to atmospheric to simplify the apparatus, but the procedure was repeated at different temperatures within the range used for sulphuric acid decomposition. Recording the oxygen permeation performance with a He–O₂ feed, along with the pre-exposure characterisation, provided a baseline against which the performance in the presence of SO₂ can be compared. Ideally, application of SO₂ should not cause a variation in oxygen permeation performance, assuming that the partial pressure of oxygen in the feed remains constant.

The most authoritative testing programme would involve carrying out the whole sulphuric acid decomposition process at bench scale, along with the membrane separation. However, this would be unnecessarily complex for a feasibility study of this type. Instead, the YSZ membranes were exposed to mixtures of oxygen and sulphur dioxide in a carrier gas, helium, which replaces the water and SO₃ that would be present during 'real' decomposition. If the YSZ does not perform satisfactorily in the presence of oxygen and sulphur dioxide then further experimentation would not be justified. However, if the YSZ can be made to perform satisfactorily, then further experimentation would be warranted.

Only one face of the YSZ membranes was exposed to the test mixture. The 'permeate' face was maintained at zero oxygen partial pressure by sweeping the face with helium.

As discussed previously, YSZ is a poor electronic conductor and requires an external electron conduction path to operate electrochemically. The potential applied across the membrane could therefore be adjusted as required.

6.3 Dense membrane procurement, specification and fabrication

The membranes used were fabricated, with the advice and expertise supplied by the Department of Engineering Materials, in the form of YSZ disks of around 24mm diameter and 2mm thickness.

The disks were produced by compressing 8 mol% yttria YSZ nanopowder (Sigma-Aldrich) in a metal die. The resulting “green” disks were then sintered at 1400°C, producing solid gas-tight ceramic disks of near 100% density.

The disk size was dictated by the size of the dies available. The largest diameter die available was used, in order to maximise the electrode surface area and hence oxygen flux, making permeate oxygen concentrations sufficiently high to facilitate measurements. Similarly, the disks were made sufficiently thick to give them ample mechanical strength for this application. The first disk supplied measured 23.34mm in diameter and 1.84mm in thickness. These measurements were used to fix the size of the membrane holder described later.

Porous platinum electrodes were applied to each face of the YSZ disks. For the first experiments, the electrodes were applied by coating each face with Metalor 6082 platinum ink, supplied by the Department of Engineering Materials. A clean stainless steel spatula was used to paint the ink on to the disk surface in a thin layer. In order to dry the ink sufficiently to allow the opposite face to be painted, the disk was placed in a furnace on a platinum foil-covered alumina boat or block at 200°C for half an hour. Following the ink application, each disk was placed in a furnace at 200°C, heated to 900°C at a rate of 10°C per minute, held at 900°C for two hours, then allowed to cool to 200°C. The heating removed the organic binders from the surface, leaving behind an adhered porous platinum layer.

A different type of platinum ink was used in later experiments and a photographic mosaic showing the stages of the ink application process, taken while applying the second type of ink, is shown in Figure 6.1. The application process was the same for both types of ink, except that a different temperature profile was used.

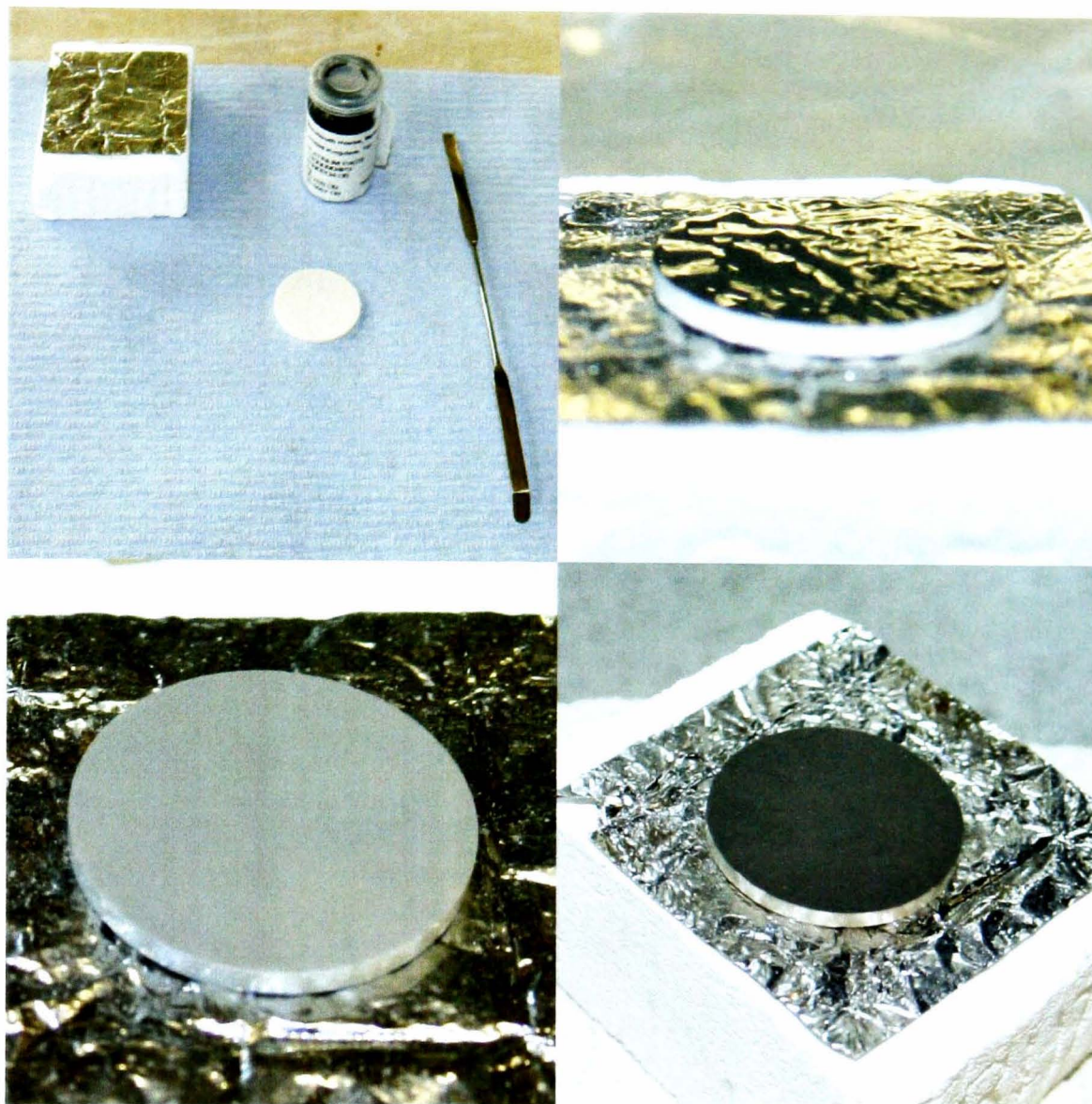


Figure 6.1: Photo mosaic of platinum electrode application process. Platinum ink C2000904P3 from Gwent Electronic Materials being applied. Clockwise from top left: refractory brick, platinum foil, platinum ink, spatula and bare YSZ pellet; pellet after ink application; pellet after drying of ink at 150°C for 15 minutes; pellet after firing of electrode at 1200°C for 12 minutes, with up and down ramp rate of 5°C per minute.

6.4 Membrane exposure/permeance apparatus

6.4.1 Description and schematic

The experimental rig process schematic is presented as Figure 6.3. The rig was designed to allow a measured mix of GC grade helium, high purity oxygen, and/or sulphur dioxide to be fed from high pressure cylinders to the feed side of the membrane. A measured supply of helium was fed to the permeate side to act as the sweep gas, maintaining zero oxygen partial pressure on the permeate side. The gases, supplied

by BOC, were regulated to a pressure slightly above atmospheric. The membrane was held inside a furnace whose temperature could be varied as required. As mentioned previously, an external electrical circuit is required with a YSZ membrane and this was provided by a DC power supply, ammeter and voltmeter all located outside the furnace. A gas analyser in the permeate stream allowed measurement of the oxygen concentration. Figure 6.2 shows the whole experimental apparatus as assembled in the lab.



Figure 6.2: Photograph of experimental apparatus in situ

6.4.2 Tubular furnace

The apparatus described in subsequent sections was inserted into a Carbolite MTF12/38/250 tubular furnace. This furnace has a worktube of 300mm length and 38mm inside diameter and a maximum operating temperature of 1200°C. The furnace was specified with an “L stand” which allows it to be assembled vertically. Figure 6.4 shows the furnace situated in the fume hood.

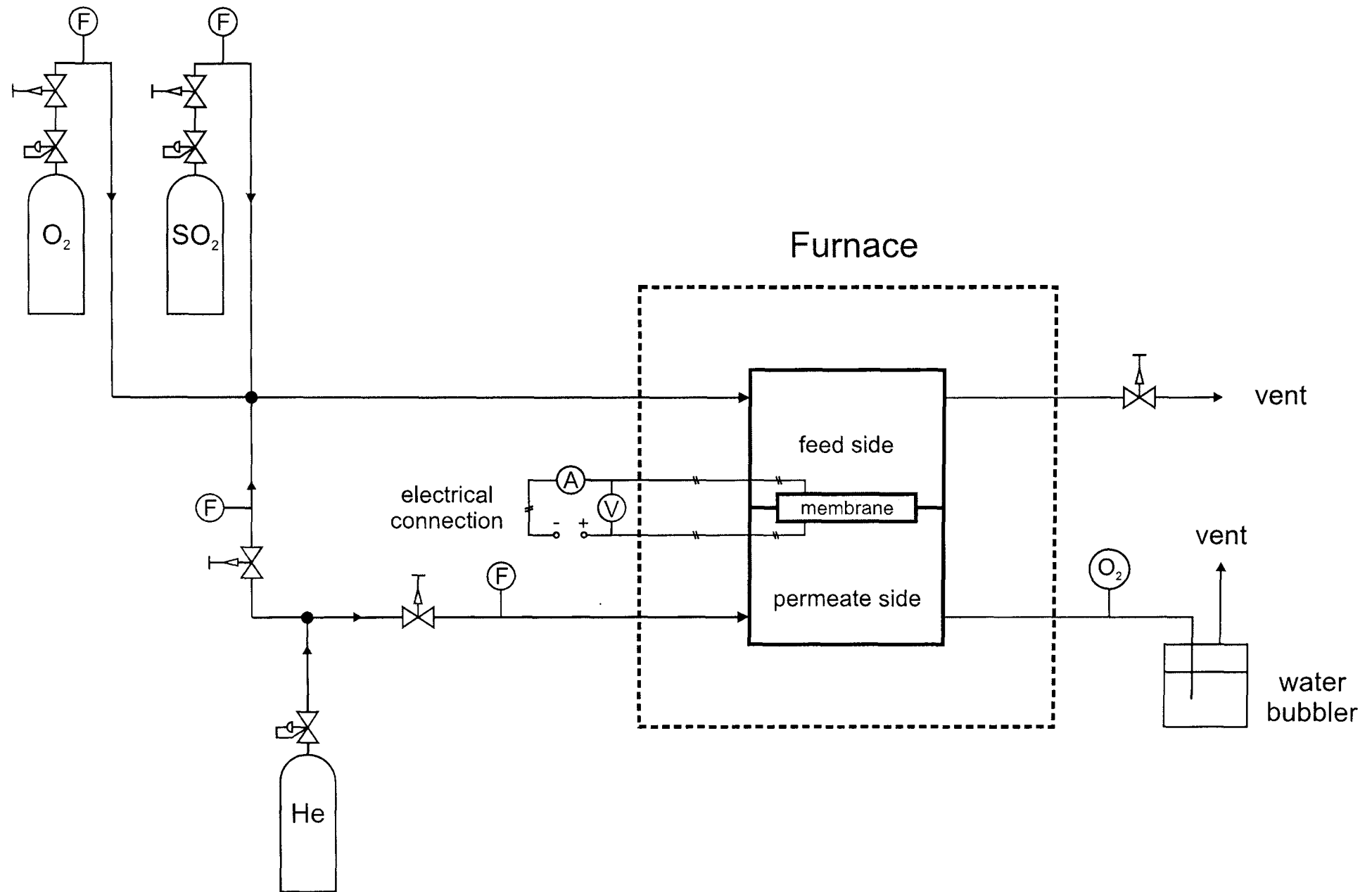


Figure 6.3: Schematic diagram of experimental apparatus. This shows the test gas supplies, membrane (housed in a tubular furnace), membrane power supply and associated instrumentation.

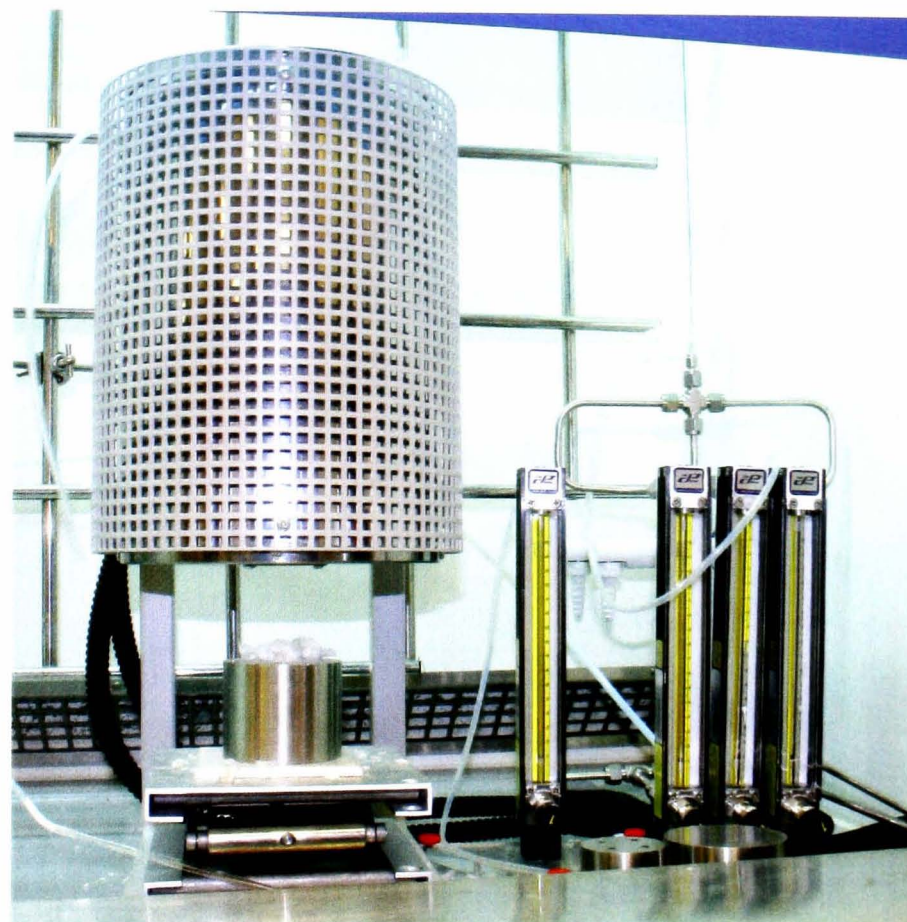


Figure 6.4: Furnace and rotameters assembled in a fume hood

6.4.3 High temperature membrane holder

Design and specification of the membrane holder was the most challenging aspect of the rig design. The membrane holder was required to withstand temperatures of up to 900°C in the presence of high concentrations of oxygen and sulphur dioxide. Standard engineering materials are not capable of withstanding such an environment. Previous work with such conditions reported in the literature used quartz (fused silica) and this material was used here. Use of quartz limited the membrane holder to low pressures.

The designed holder consists of two identical halves and was fabricated by the glass-blowing service of the University of Sheffield Chemistry Department. The membrane holder detailed design is presented as Figure 6.5 and the holder as fabricated is shown in Figure 6.6. The holders were located for each run inside the aforementioned tubular furnace. The disk shaped membrane sat between the two holder halves and was held in place by the weight of the support described in Section 6.4.6. As is good engineering practice, no moving parts, e.g. valves, were placed in the furnace.

CFD simulations of the flow pattern in the membrane holder were carried out during the design process and these are described in Section 6.6.

The holder was designed to ensure it could be passed through the furnace worktube during installation. The inlet tubing accepts a Tygon tube carrying the cold gas feed, whilst the outlet tube terminates in a male ground glass joint to which a straight length of quartz tube can be attached for cooling purposes, as described in Section 6.4.7. The inlet tubing was sized to allow the feed gas to be heated to the furnace temperature within the space available in the furnace, whilst keeping fabrication as simple as possible. Initially a coiled tube arrangement was envisaged, on the understanding that this could be obtained “off the shelf”, but as this was not the case a simple S shape was employed.

Holder heating calculations

The quartz tubing leading to the membrane was sized to allow sufficient time for 50ml/min (STP) of SO₂ to be heated from room temperature to 900°C. SO₂ heating was taken as the basis for the calculation as it has the largest specific heat capacity of the gases to be used.

A flow rate of 50ml/min at STP (273.15K and 101325Pa) equates to a molar flow rate of 3.718×10^{-5} mol/s.

The *Component Plus* utility supplied with *ProSim* gives an ideal gas heat capacity for SO₂ of 38.992 J/mol/K at 273.15K and 55.663 J/mol/K at 1173.15K. These values correlate with those supplied by the *Detherm* thermodynamic property database. The higher value will be used for this calculation.

The required heat duty Q for a 900K temperature rise (more than is required) is:

$$Q = mC_p\Delta T = 3.718 \times 10^{-5} \times 55.663 \times 900 = 1.863 \text{ W}$$

The specified furnace has a thermal power rating of 1000W, therefore it is not envisaged that there should be any difficulty in maintaining the required temperature. If we consider the radiative heat emission from the central 10cm of the 38mm diameter furnace worktube, assuming it is a black body radiator at 900°C, the radiated heat power would be:

$$Q = \sigma T^4 A = 5.67 \times 10^{-8} \times 1173^4 \times (\pi \times 0.038 \times 0.1) = 1281 \text{ W}$$

Since the worktube is not a black body radiator this is an overestimate but still orders of magnitude greater than the required heat duty.

If we were to consider the heat duty to be non-radiative, it can also be expressed as:

$$Q = U_o A_o \Delta T_{LMTD} \therefore A_o = \frac{Q}{U_o \Delta T_{LMTD}}$$

where U_o is the overall heat transfer coefficient, A_o is the area available for heat transfer, both based on the outside of the tubing, and T_{LMTD} is the log mean temperature difference.

The log mean temperature difference is calculated as 231.2K, based on approach temperatures of 900K at the inlet end and 20K at the membrane end of the tubing.

U_o is defined by summing the individual resistances involved in the heat transfer then finding the inverse.

$$\frac{1}{U_o} = \frac{1}{h_o} + \frac{x d_o}{k_{quartz} d_w} + \frac{d_o}{h_i d_i}$$

where h_o and h_i are the outside and inside film coefficients respectively, d_o and d_i are the outside and inside wall diameters, d_w is the average wall diameter and k_{quartz} is the thermal conductivity of quartz (Perry & Green 1998). The film coefficients used are the most resistive approximate values given for heat transfer to/from gases with no phase change by Coulson et al. (1999).

$$\frac{1}{U_o} = \frac{1}{20} + \frac{0.001 \times 0.003}{1.3 \times 0.002} + \frac{0.003}{20 \times 0.001} = 0.2012 \therefore U_o = 4.971 \text{ W/m}^2 \text{ K}$$

The outside tube area required can now be calculated.

$$A_o = \frac{Q}{U_o \Delta T_{LMTD}} = \frac{1.863}{4.981 \times 231.2} = 1.62 \times 10^{-3} \text{ m}^2$$

For tubing of 3mm outside diameter, this equates to 172mm of straight tubing. The design presented in Figure 6.5 provides for over 300mm of tubing. The additional length should ensure the gas is at the correct temperature before contacting the membrane.

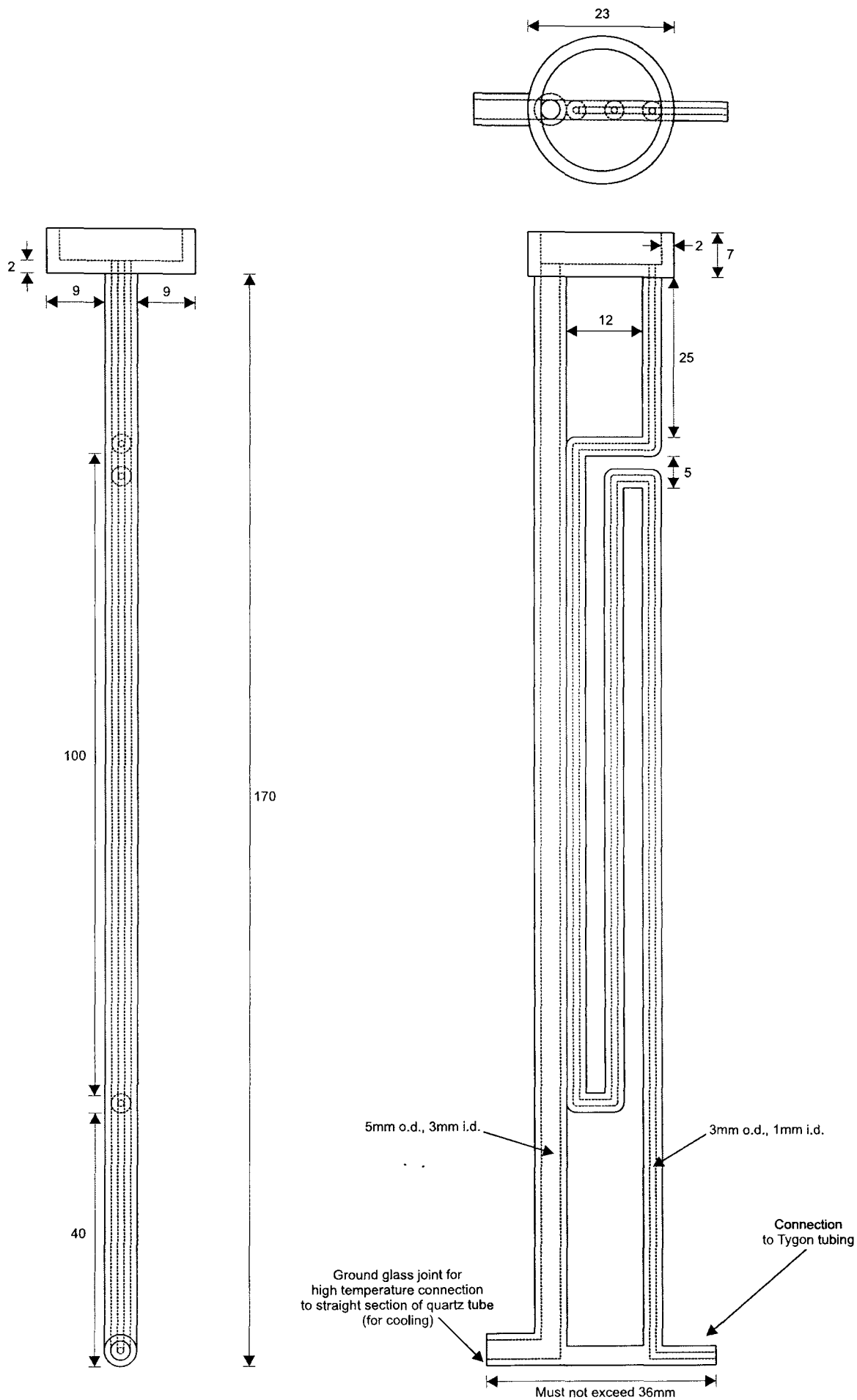


Figure 6.5: Schematic diagram of quartz membrane holder for dense membrane permeance experiments. Two of these halves are used in conjunction with the support and stand presented in subsequent figures. All measurements are in mm.

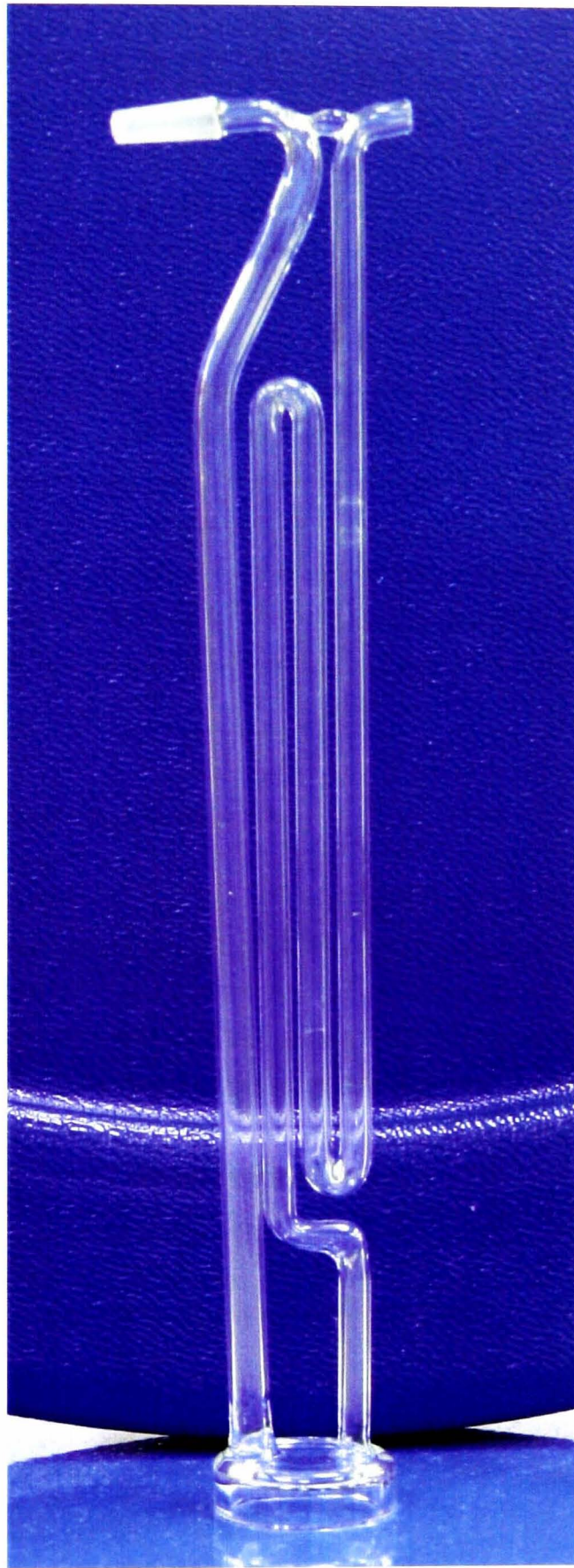


Figure 6.6: Quartz membrane holder for dense membrane permeance experiments. Two of these halves are used in conjunction with the support and stand presented in subsequent figures.

6.4.4 Sealing

The membrane and membrane holder could not be permanently bonded together because of the need to remove the membrane for inspection and because of differential thermal expansion (see Section 7.10). Ring-shaped gaskets were placed between each half of the membrane holder and the membrane itself in order to seal the assembly. The use of quartz meant that only moderate amounts of pressure could be applied for sealing purposes. Graphite was trialled as the gasket material. Graphite seals purchased from Gee Graphite were used to provide the seal between the quartz membrane holder and the membrane disk. The seals were 23mm outside diameter, 19mm inside diameter and 1.5mm thick (before compression). The manufacturers of the seals state that in flange type assemblies, the seals can be used in oxidising conditions at up to 600°C without problems. It was hoped that the graphite seals would be sufficiently durable to survive for the duration of each experimental run, despite the higher temperatures required. This proved not to be the case. Section 7.4 details the testing work carried out on the graphite seals. Gold foil seals were eventually used to provide a durable solution.

6.4.5 Membrane electrical connection

As previously discussed, YSZ requires an electrical connection between the two electroded surfaces. During the graphite trials, the most effective means of providing the connection to each surface was found to be to use the gasket itself, since graphite is electrically conductive. A wire was contacted with the graphite and this wire was then contacted with the adjacent metal support described in the next section. It was important to ensure that these wires were not allowed to come into contact with the furnace wall as this becomes electrically conductive at high temperature and could therefore cause short circuits. When gold foil gaskets were introduced, these could be shaped such that direct contact was made with both the electrode and the metal support, removing the need for a separate wire.

Wires were attached to each half of the stand outside the furnace, with these wires leading to the Kenwood DC power supply, Thorn Avometer multimeter and Maplin multimeter. The digital Maplin unit was employed as the voltmeter and the analogue Avometer was employed as the ammeter.

Given the claim in Badwal & Ciacchi's (2001) review of oxygen fluxes of up to $1.5 \text{ cm}^3 / \text{min.cm}^2$ with YSZ membranes (this is assumed to be at RTP), and the current requirements calculated in Section 5.1, the maximum current possible with a circular

YSZ membrane of 19mm available diameter is 1.14A.

6.4.6 Membrane holder support and stand

Since the membrane was not positively located in the quartz holder, a support was required to hold the assembly together and to reduce leakage of process gases from around the membrane by compressing the gaskets. To achieve this, a stainless steel support and stand was designed. The support was designed such that the quartz membrane holder could be inserted once the membrane itself has been positioned. The support was designed with a number of legs, allowing the membrane to be located in the centre of a vertical tubular furnace with the assembly being supported outside the furnace by a retort stand. A weight was placed on the top of the support, providing sufficient compressive strength to positively seal the membrane to the quartz holder.

The surround was fabricated from grade 310 stainless steel. This grade was selected since it is suitable for intermittent high temperature use at up to 900°C. The stand and weight were fabricated using standard inexpensive carbon steel since they operate at low temperature, being located outside the furnace.

The gold foil or platinum wires contacting the graphite gaskets described in Section 6.4.4 were contacted with the support by placing them between the membrane holder and the support during the assembly process. In order to electrically isolate the support from the furnace walls, insulating wool was wrapped around the stand (i.e. the top part of Figure 6.8) for the first few runs. After these initial runs a continuous insulating oxide layer developed on the surface and the insulating wool was no longer necessary. Because of the oxide buildup, the surfaces that were required to make electrical contact were sanded before each run in order to remove the insulating oxide.

Schematic diagrams of the stand/weight and support are presented as Figures 6.7 and 6.8 respectively.

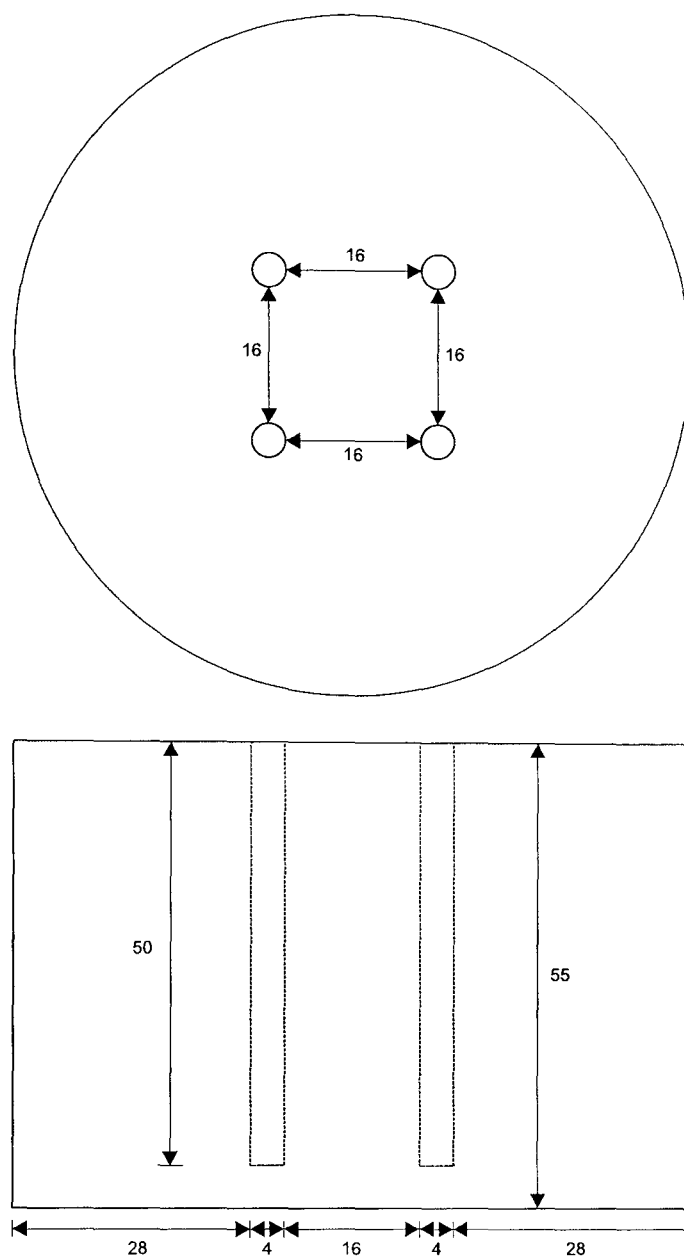


Figure 6.7: Schematic diagram of membrane holder stand for dense membrane permeance experiments. This was constructed from standard steel. All measurements are in mm.

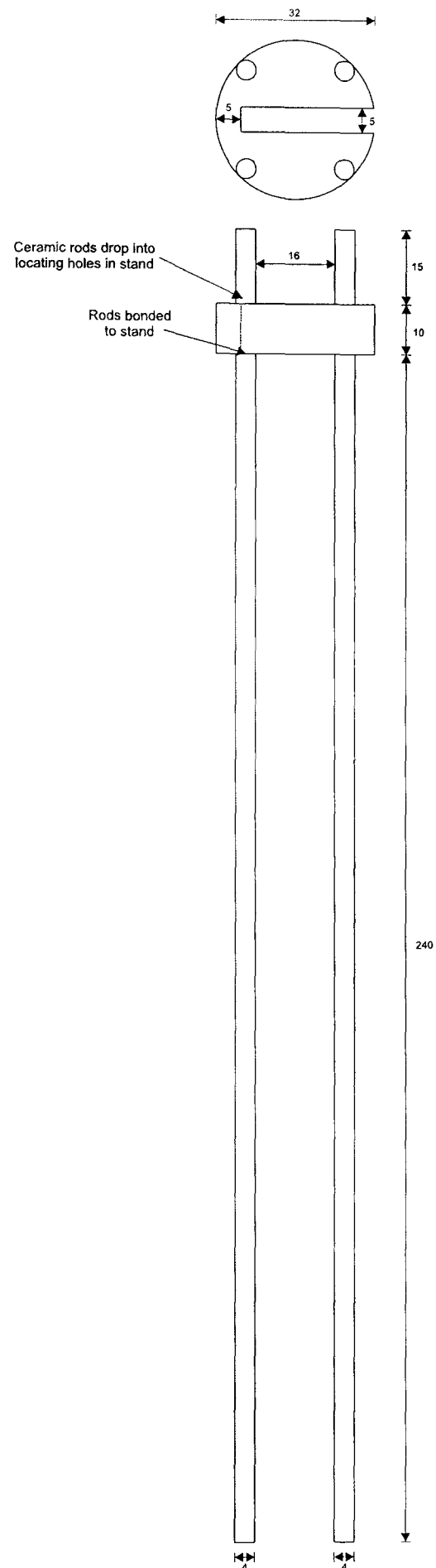


Figure 6.8: Schematic diagram of membrane holder support for dense membrane permeance experiments. This is used around the holder presented in the previous figure and was constructed from grade 310 stainless steel, except for the non-conducting pegs indicated. All measurements are in mm.

6.4.7 Post-furnace cooling

Before feeding into the low temperature downstream tubing, the gases exiting the furnace needed to be cooled to an acceptable temperature.

The cooling was achieved by attaching 30cm long straight sections of quartz tubing to the membrane holder outlets. Tygon tubing was attached to the outlet of the straight quartz tubing to carry the process gases downstream.

6.4.8 Gas analysis

A Servomex 5200 paramagnetic gas analyser was used to measure the permeate O₂ concentration whilst experimental runs were in progress. This analyser requires calibration at the operating flow rate, as flow rate variations cause errors in the indicated values. The oxygen concentration data was logged every two seconds during an experimental run to a PC via an RS232 connection.

6.4.9 Gas venting

It was possible to vent the outlet streams from the rig into the upper section of the fume hood in which the rig was assembled. This negated the need to scrub the vent gases using, for example, iodine solution.

The fume hood in which the rig was built operates with a face velocity of 0.5 m/s. This equates to an air volumetric flow rate of 25500 l/min. The maximum SO₂ flowrate used during this experimental work was 15ml/min. Assuming perfect mixing, this gives an SO₂ concentration of 0.006ppm at the fume hood exhaust exit. The current UK Long Term Exposure Limit (LTEL) is 1ppm, therefore the concentration of SO₂ in the exhaust is acceptable.

6.4.10 Instrumentation

The flow of gases into the rig was controlled and measured by Cole Parmer rotameters with high precision valves, calibrated for the required gas. The rotameters were specified with NIST-traceable calibration certificates. The temperature indicated by the furnace controller was calibrated during commissioning (see Section 7.1.)

6.4.11 Low temperature pipework

The low temperature pipework was constructed from Swagelok 1/4" outside diameter 316 stainless steel tubing, along with compatible 316 stainless steel fittings and valves. Although the long term stability of 316 stainless steel in the presence of SO₂ and SO₃ is questionable, the increase in expense required for exotic alloys was not justifiable. If any section of tubing suffered corrosion during the experimental programme, it could have been replaced as required relatively cheaply. Replacements proved not to be necessary. The thickest walled tubing available was used, in order to minimise the gas inventory in the system as far as possible for safety reasons.

A section of the piping downstream of each gas cylinder regulator was constructed from flexible PTFE tube. This ensured that the gas cylinders could move independently of the rest of the rig, which facilitated cylinder changes and movements.

6.5 Surface analysis

The purpose of analysing the membrane surface was to determine whether the process conditions caused any structural damage to the membrane. Additionally, it must be determined that the membrane has not been chemically altered. Any physical or chemical changes would suggest that the materials used are not suitable for this application.

6.5.1 X-ray diffraction (XRD)

X-ray diffraction, usually shortened to XRD, is a method of identifying phases present at the surface of crystalline solid samples. When a beam of x-rays is directed at the surface of a crystalline lattice, there is assumed to be transmissions to/reflections from parallel planes of the lattice. For a given planar spacing, the reflected radiation will constructively interfere with that reflected from adjacent parallel planes when the incident angle of the x-ray beam is at an angle to the surface known as the Bragg angle, θ .

For a given constructive interference angle, the planar spacing d can be calculated from Bragg's Law:

$$2d\sin\theta = n\lambda$$

where λ is the x-ray wavelength.

A beam of (ideally) monochromatic x-ray radiation is directed at the surface of a powdered sample of the solid. For these purposes, the sintered disks produced for this experimental programme can be considered a randomised powdered sample. A mobile detector records the intensity of the reflected radiation over a range of θ values. The resulting spectrum can be compared to data sets, or “cards”, stored in the International Centre for Diffraction Data (ICDD) database. Each ICDD card contains a set of diffraction peaks for a given crystalline phase. Hence, the phases present on the surface of the sample can be identified.

For this work a Philips diffractometer was used with a copper x-ray source, which produces mostly $K\alpha$ radiation upon being bombarded with a sufficiently energetic electron beam. This is not strictly monochromatic as the relevant electron transition energy can have one of two values depending on the spin state of the $2p$ electron which makes the transition (West 1999). Both $K\alpha_1$ and $K\alpha_2$ radiation is therefore emitted. The different θ values caused by diffraction of $K\alpha_1$ and $K\alpha_2$ radiation are sufficiently small that they are not always resolved into two separate peaks in the XRD spectrum. However, if the two peaks are resolved then the smaller peak caused by the $K\alpha_2$ radiation is disregarded as the ICDD card is based on only $K\alpha_1$ radiation.

6.5.2 X-ray photoelectron spectroscopy (XPS)

XRD, discussed previously, attempts to identify phases present at a surface. In comparison, XPS identifies individual species. The surface is bombarded with monochromatic x-rays, causing the ionisation of electrons from atoms in the sample. The kinetic energy of those electrons that escape the surface can be measured. By calculating the difference between the energy of the bombarding radiation and the energy of the released electrons, the binding energy of the released electrons can be found (West 1999).

The binding energy is specific to the ionisation of an electron from a specific shell and hence the presence of a particular set of binding energies in a spectrum would indicate a particular species. In addition, the binding energy of a particular transition “shifts” depending on the environment in which the atom is located, hence it may be possible to identify, e.g. the oxidation state of the species present or whether it is present as a metal or an oxide. Only electrons ejected within around 5-10nm of the surface have sufficient energy to escape, therefore only those species within 5-10nm of the surface can be identified. The process is carried out under very high vacuum to prevent collisions with the atmosphere scattering the ejected electrons.

6.5.3 Scanning electron microscopy (SEM)

SEM uses a focussed scanning beam of electrons travelling across the surface of a sample to produce a raster image. SEM images are 3D and hence are particularly suitable for examining surfaces. The electron beam interacts with the surface and the resulting secondary electrons, as well as the backscattered electrons are detected and used to form the final image. SEM resolution is around 1-20nm.

6.5.4 Impedance spectroscopy (IS)

Impedance spectroscopy is a technique used to measure the electrical properties of a sample. A constant AC voltage is passed through the sample (in this case across the electrodes on each face) and the resulting current (and phase shift of that current) is monitored as the AC frequency is varied. The capacitance and impedance of the sample at that frequency can then be calculated.

The data can be plotted and interpreted in a number of ways, however a common plot is the Z^* plot, where the real and imaginary components of the impedance are plotted against each other. Each data point refers to the impedance at a particular AC voltage frequency. Depending on the sample and the temperature, the Z^* plot generally consists of one or more arcs (see Figure 8.20 for an example). Each of these arcs relate to an electrical component of the sample, i.e. the grain boundaries, bulk material, electrodes or a surface layer, if present. Components tend to fall into a range of typical capacitances, aiding identification. The width of each arc can be measured and hence the resistance of the component at that temperature deduced. By repeating the measurements at a range of temperatures than the variation of conductivity with temperature can be shown. As shown in the left hand graphs of Figure 8.18, plotting reciprocal temperature against log conductivity enables the calculation of the activation energy for conduction in that component or overall.

6.6 FLUENT simulations of high temperature membrane holder

A series of flow simulations was carried out using the *FLUENT* computational fluid dynamics (CFD) package in order to ascertain the gas flow rate range to use with the high temperature membrane holder described in Section 6.4.3.

It is preferable to minimise the feed flow as much as possible without impairing the ex-

periments. The use of expensive chemicals is reduced, increasing safety and reducing cost, and the emission of those chemicals is also reduced, preventing the additional complication of having to “scrub” the vented gases before allowing them into the atmosphere. However, if the flow rate is so low that there is not good mixing in the membrane holder cavity then a portion of the feed may short-circuit and not interact with the membrane surface.

The flow domain was modelled as a cylinder of height 5mm and diameter 19mm with circular entry and exit holes. The entry and exit holes were 1mm and 3mm in diameter respectively, to imitate the real membrane holder dimensions. The outline of the flow domain, as displayed in FLUENT, is depicted in Figure 6.9.

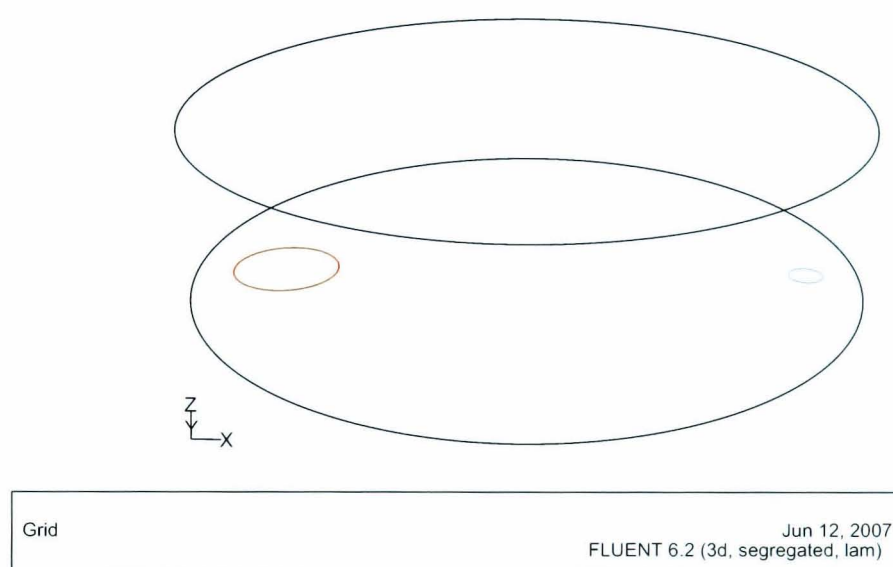


Figure 6.9: Outline of flow domain for FLUENT simulations. The smaller blue hole is the flow inlet and the larger red hole is the flow outlet.

The simulations did not introduce any complexity which is unnecessary at this stage. The flow domain does not account for oxygen permeation through the membrane or any leakage that may be occurring.

Pure helium was used as the flowing gas. The entry velocities were chosen to coincide with those which would be achieved if volumetric flowrates of 25-100ml/min of ideal gas at room temperature and pressure were heated to 900°C and flowed through the 1mm diameter pipe. The calculated entry velocities are shown in Table 6.1.

Volumetric flowrate (ml/min)		Velocity (m/s) (1mm i.d.)
25°C, 1 atm	900°C, 1 atm	
25.00	98.37	2.087
50.00	196.74	4.175
75.00	295.11	6.262
100.00	393.48	8.350

Table 6.1: Gas velocities used in FLUENT simulations, calculated based on room temperature and pressure flowrates of 25-100ml/min, with expansion based on the ideal gas law.

The system was assumed to be isothermal and the laminar flow model was employed. A number of meshes were tested with the 50ml/min RTP flowrate and the largest mesh which did not alter the results was used. This mesh had a nominal cell size of 0.2mm.

6.6.1 Data collection

A range of data was collected for each inlet gas velocity simulation.

The gas velocity magnitude was recorded for a number of lines in the plane between the inlet and outlet holes, perpendicular to the upper face which represents the membrane surface. The same data was recorded for lines perpendicular to those mentioned above. The lines are between 0 and 2mm from the membrane face, in 0.5mm steps. These lines are depicted in Figure 6.10. In addition, graphical output of the path lines emanating from the inlet was recorded. This plane is depicted in Figure 6.11.

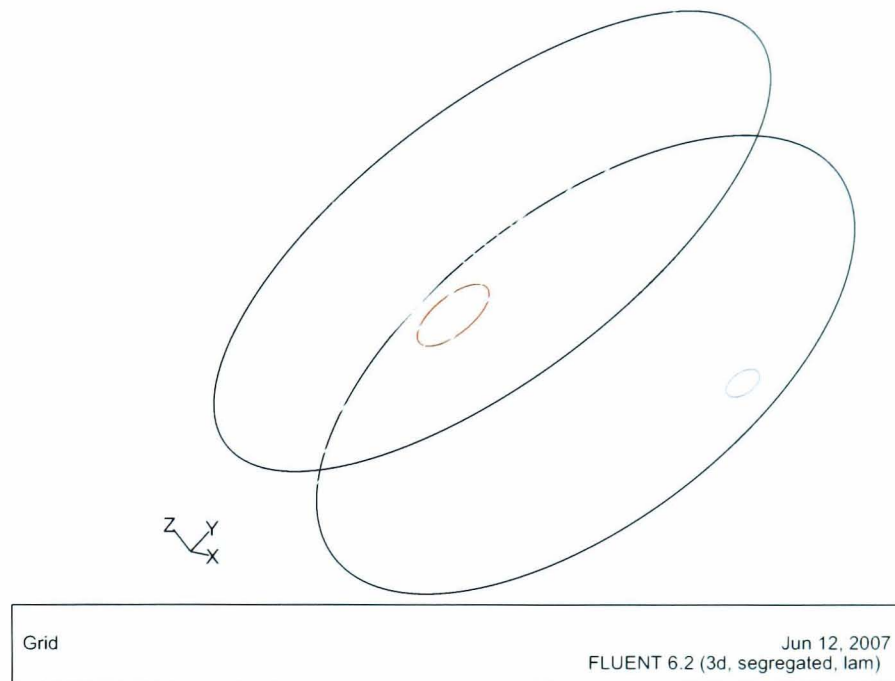


Figure 6.10: Outline of flow domain for FLUENT simulations showing lines along which velocity data is collected. These lines run parallel and perpendicular to an imaginary line joining the entry and exit holes. The lines are 0.0, 0.5, 1.0, 1.5 and 2.0mm from the membrane face.

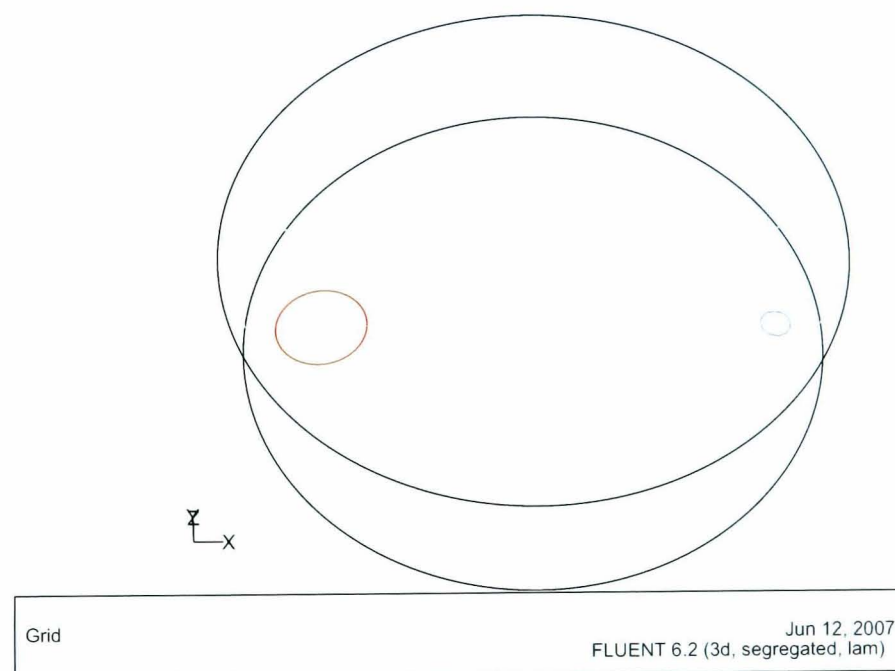


Figure 6.11: Outline of flow domain for FLUENT simulations showing plane in which velocity magnitude is recorded.

6.6.2 Results and discussion

Gas velocities

As mentioned previously, gas velocities in the simulations were measured in several different ways. Firstly, Figures 6.12, 6.13, 6.14 and 6.15 show the velocity contours in the plane indicated in Figure 6.11.

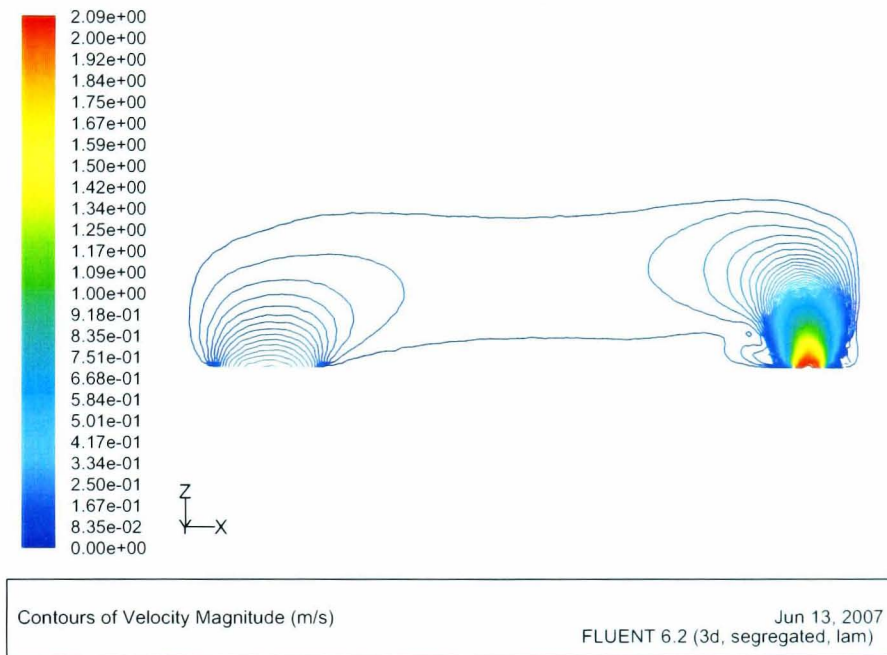


Figure 6.12: FLUENT simulation of membrane holder gas velocity contours in the previously defined plane at 2.087 m/s inlet velocity of helium, equivalent to 25ml/min (RTP)

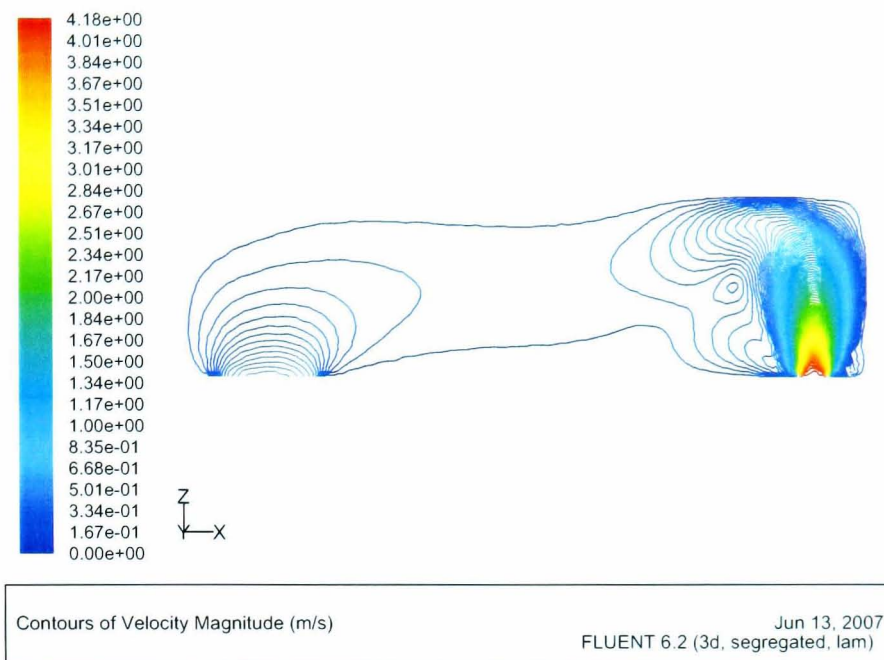


Figure 6.13: FLUENT simulation of membrane holder gas velocity contours in the previously defined plane at 4.175 m/s inlet velocity of helium, equivalent to 50ml/min (RTP)

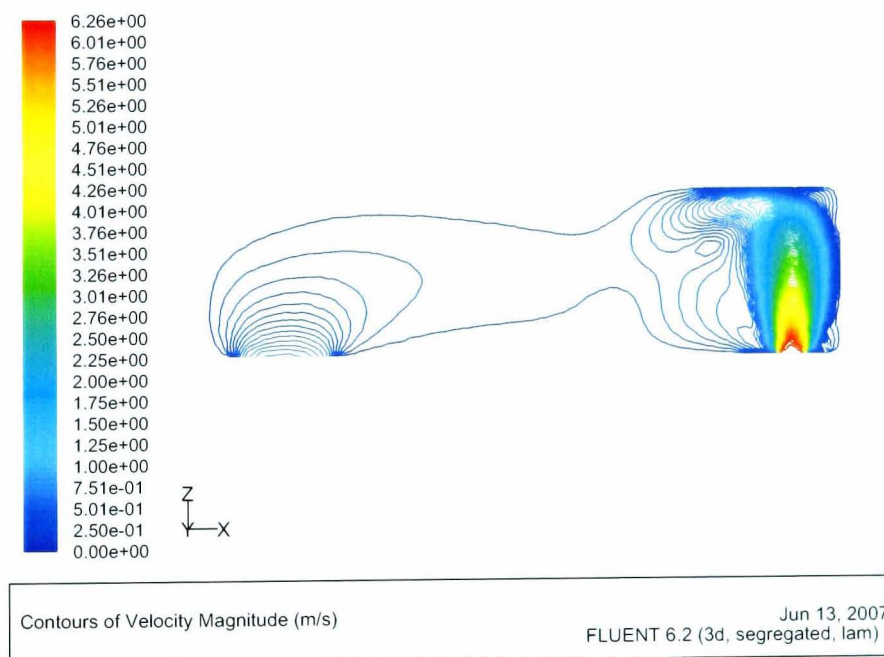


Figure 6.14: FLUENT simulation of membrane holder gas velocity contours in the previously defined plane at 6.262 m/s inlet velocity of helium, equivalent to 75ml/min (RTP)

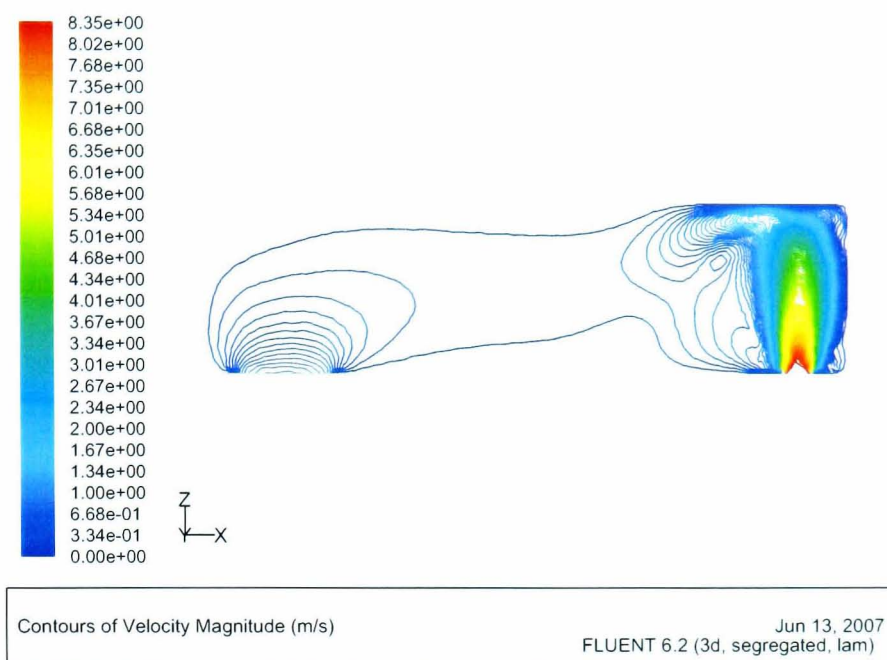


Figure 6.15: FLUENT simulation of membrane holder gas velocity contours in the previously defined plane at 8.350 m/s inlet velocity of helium, equivalent to 100ml/min (RTP)

The above figures show that the flow pattern is significantly different at 25ml/min compared to higher flowrates - the inlet jet does not strongly impinge on the membrane surface. The other three flow patterns appear broadly similar.

Figures 6.16 to 6.21 illustrate the difference in flow velocity between the flowrates simulated along three lines in the flow domain. For 25ml/min feed, the velocity magnitudes at 0.5mm from the surface are very similar across the whole centreline, further showing that the feed jet does not impinge on the surface as it does for higher feed velocities.

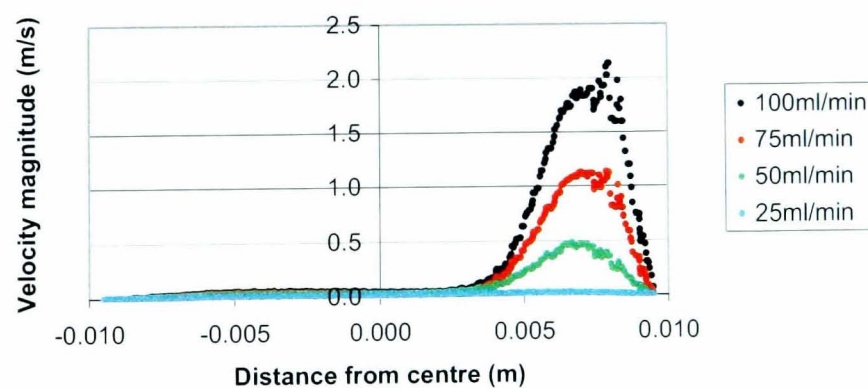


Figure 6.16: Membrane holder full width simulated velocity magnitude profiles from 0.5mm below centreline. Volumetric flowrates are inlet flows at RTP.

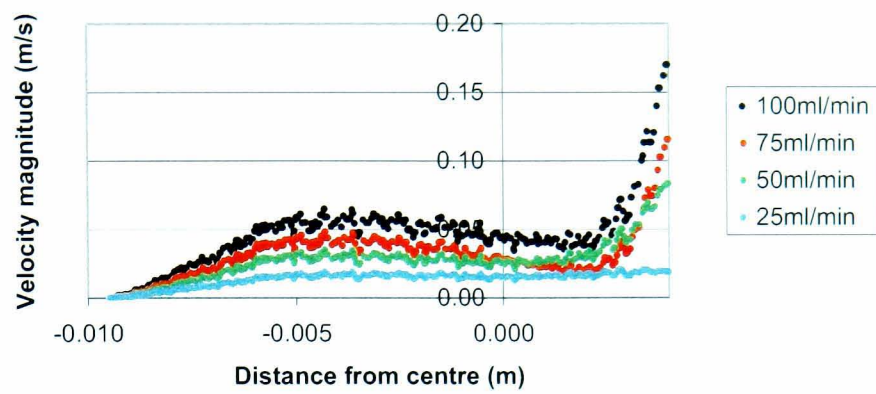


Figure 6.17: Membrane holder partial width simulated velocity magnitude profiles from 0.5mm below centreline. Volumetric flowrates are inlet flows at RTP. This is part of Figure 6.16 rescaled.

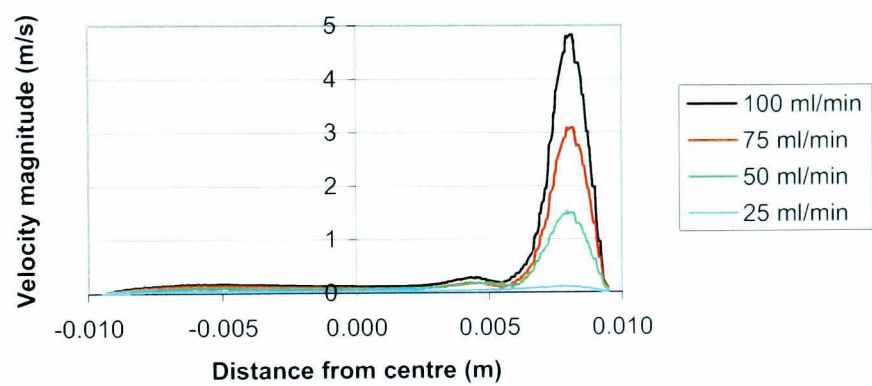


Figure 6.18: Membrane holder full width simulated velocity magnitude profiles from 2.0mm below centreline. Volumetric flowrates are inlet flows at RTP.

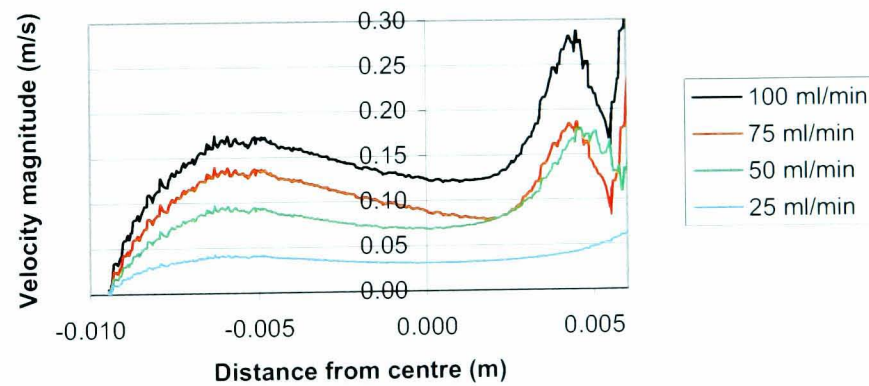


Figure 6.19: Membrane holder partial width simulated velocity magnitude profiles from 2.0mm below centreline. Volumetric flowrates are inlet flows at RTP. This is part of Figure 6.18 rescaled.

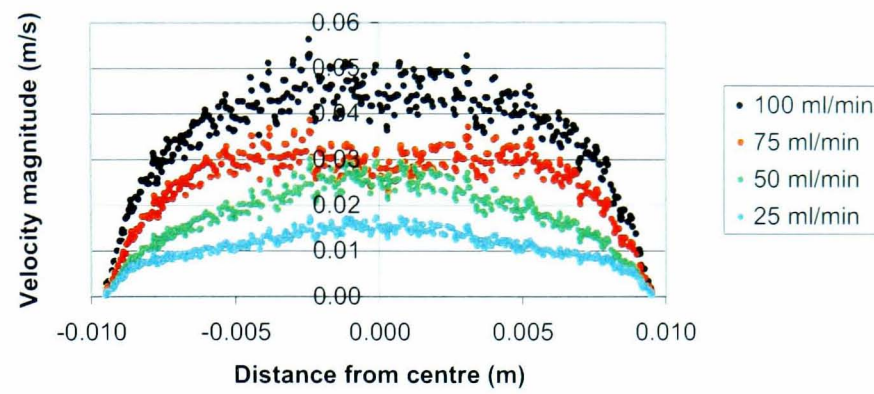


Figure 6.20: Membrane holder full width simulated velocity magnitude profiles from 0.5mm below transverse centreline. Volumetric flowrates are inlet flows at RTP.

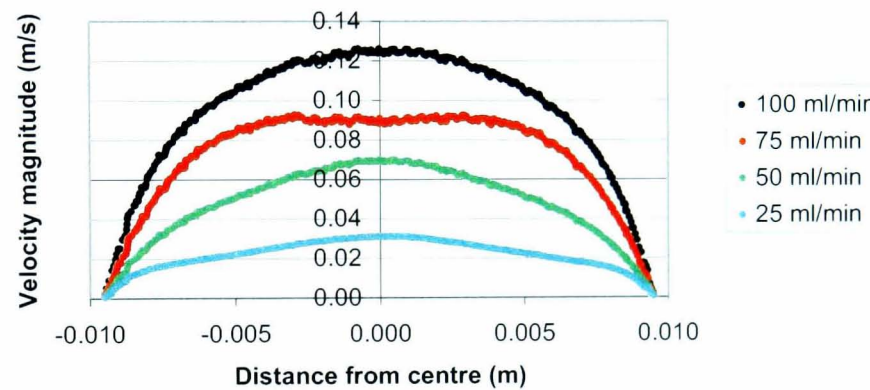


Figure 6.21: Membrane holder full width simulated velocity magnitude profiles from 2.0mm below transverse centreline. Volumetric flowrates are inlet flows at RTP.

Path lines

Figures 6.22 to 6.29 show top and side views of the path lines of theoretical massless particles entrained in the inlet gas flow for all four inlet gas velocities simulated. These path lines give an overall impression of the flow of the gas through the holder.

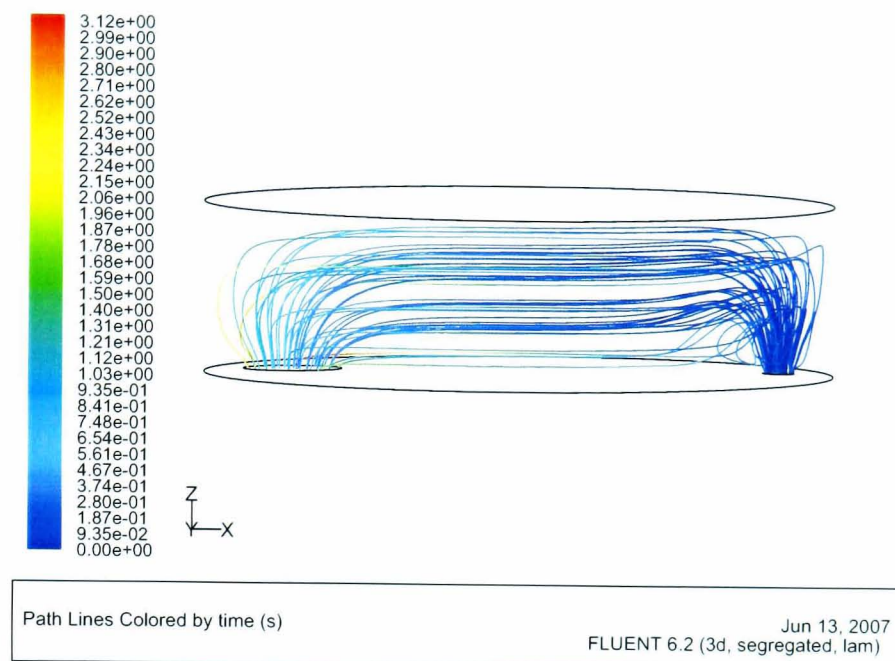


Figure 6.22: FLUENT simulation of membrane holder path lines at 2.087 m/s inlet velocity of helium, equivalent to 25ml/min (RTP) (side view)

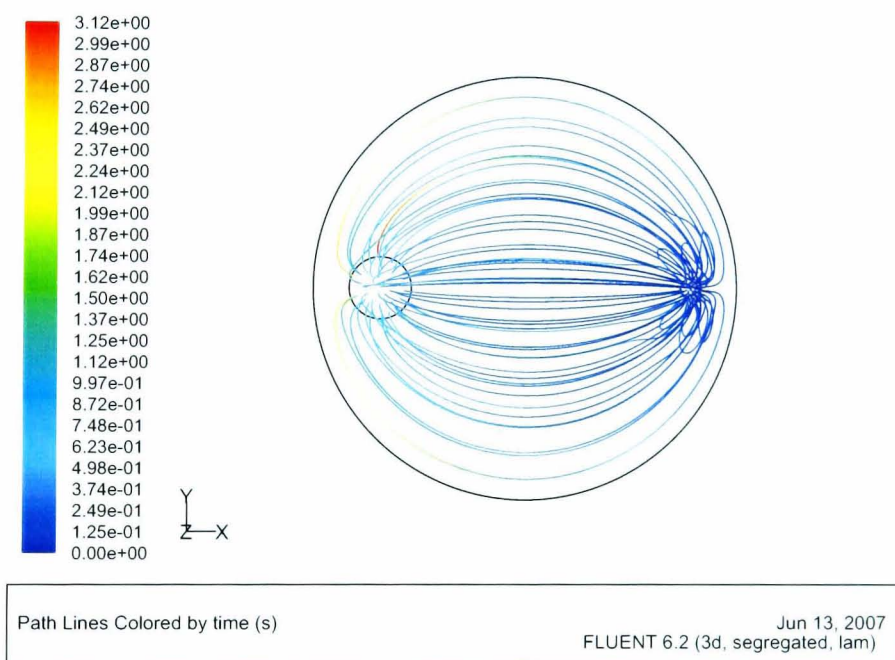


Figure 6.23: FLUENT simulation of membrane holder path lines at 2.087 m/s inlet velocity of helium, equivalent to 25ml/min (RTP) (top view)

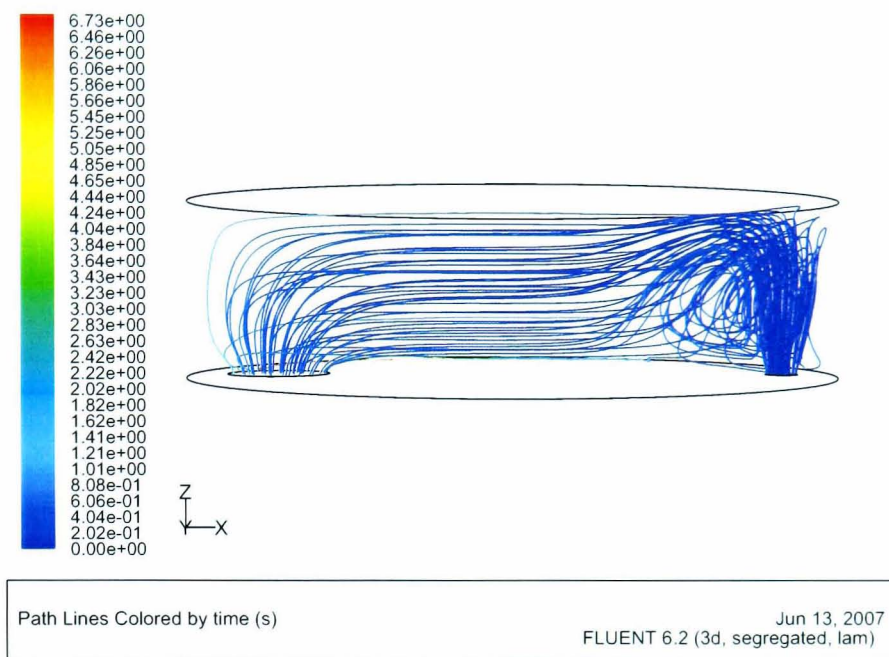


Figure 6.24: FLUENT simulation of membrane holder path lines at 4.175 m/s inlet velocity of helium, equivalent to 50ml/min (RTP) (side view)

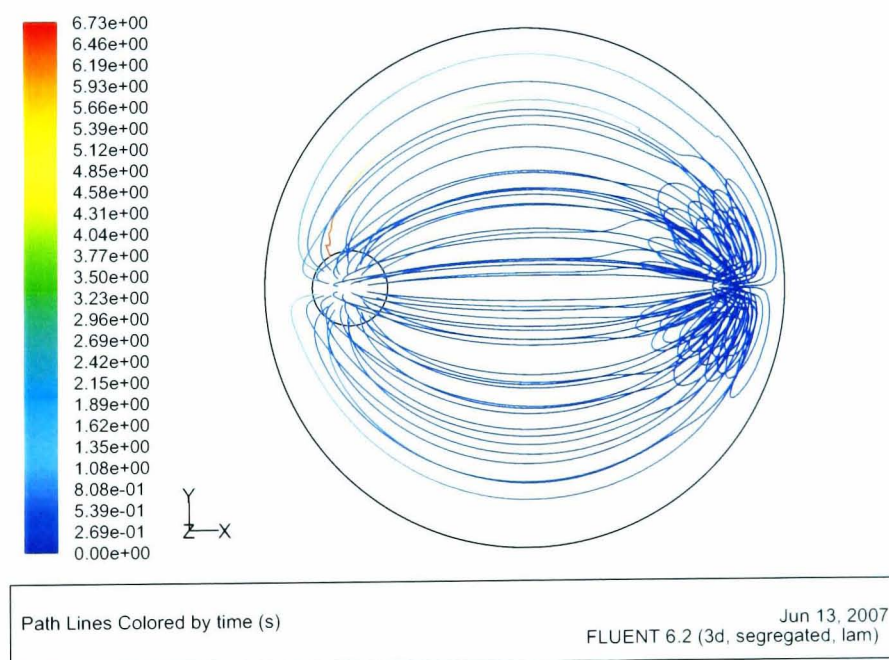


Figure 6.25: FLUENT simulation of membrane holder path lines at 4.175 m/s inlet velocity of helium, equivalent to 50ml/min (RTP) (top view)

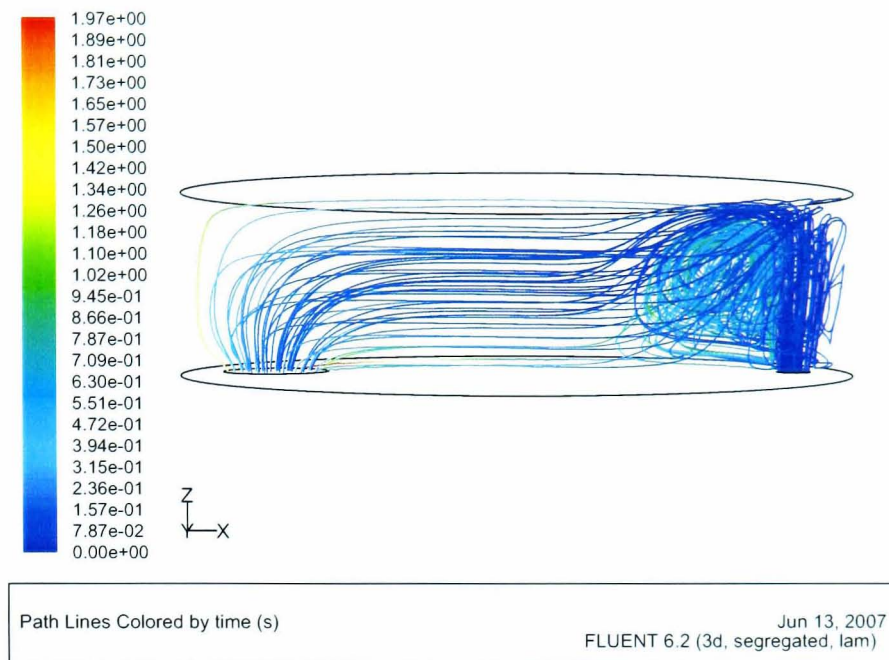


Figure 6.26: FLUENT simulation of membrane holder path lines at 6.262 m/s inlet velocity of helium, equivalent to 75ml/min (RTP) (side view)

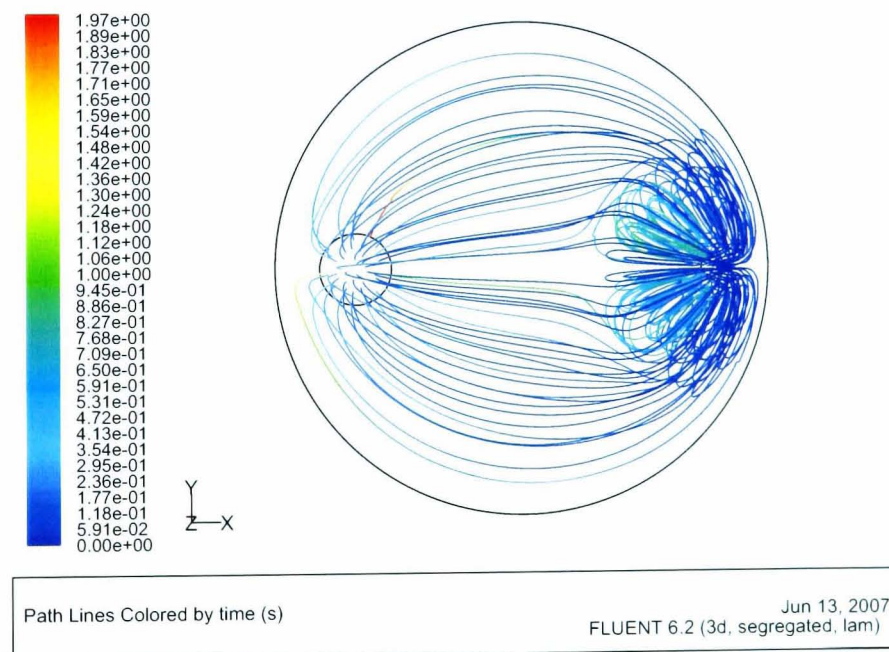


Figure 6.27: FLUENT simulation of membrane holder path lines at 6.262 m/s inlet velocity of helium, equivalent to 75ml/min (RTP) (top view)

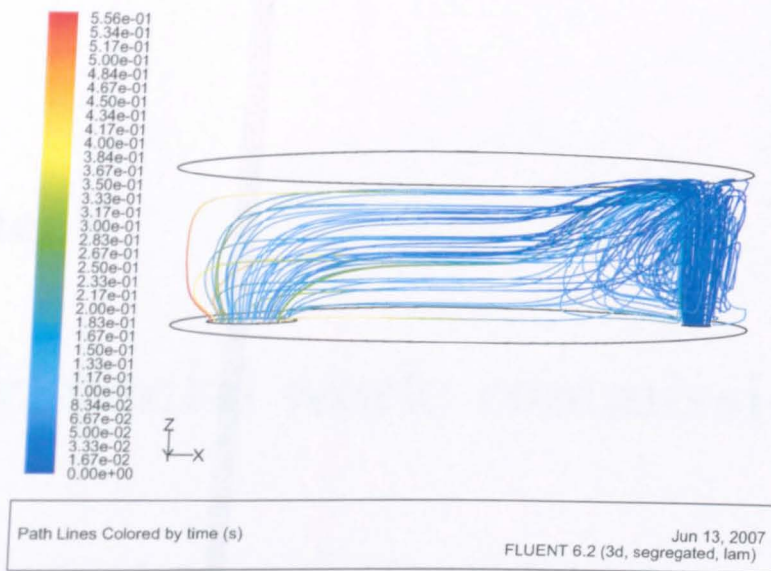


Figure 6.28: FLUENT simulation of membrane holder path lines at 8.350 m/s inlet velocity of helium, equivalent to 100ml/min (RTP) (side view)

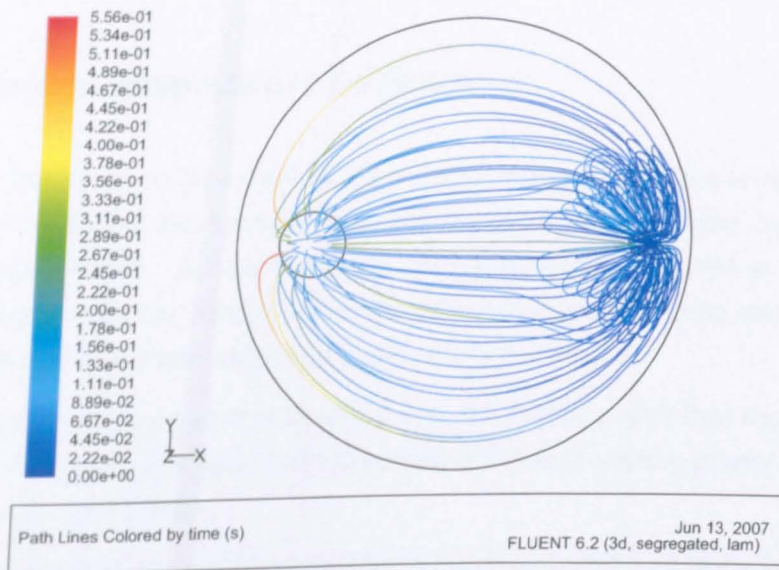


Figure 6.29: FLUENT simulation of membrane holder path lines at 8.350 m/s inlet velocity of helium, equivalent to 100ml/min (RTP) (top view)

These views show that a similar pattern of recirculation around the inlet jet occurs at 50-100 ml/min but not at 25 ml/min. Consequently, a minimum inlet RTP flowrate of 50 ml/min should be used with these membrane holders.

Chapter 7

Experimental work: commissioning

This chapter contains, in chronological order, a number of tests and experiments carried out during and following the assembly of the experimental apparatus. These tests looked at the furnace, metalwork, oxygen gas analyser, membrane gaskets, and a prototype YSZ membrane.

7.1 Furnace temperature calibration

The aim of this test was to establish the relationship between the temperature measured at the centre of the furnace and the temperature indicated by the furnace's built-in thermocouple. As the furnace's thermocouple is embedded in the ceramic worktube along with the heating elements, there is expected to be some discrepancy between that measurement and the furnace temperature.

A thin K type thermocouple was inserted into the furnace such that the tip was at the centre point of the worktube in both the horizontal and vertical planes. Both ends of the furnace were insulated.

With the furnace at room temperature the furnace setpoint was initially set as 700°C and the heating elements activated. The inserted thermocouple's temperature was recorded every minute for 30 minutes, by which point the reading had stabilised. The furnace setpoint was then set to 800°C for 15 minutes followed by 15 minutes at 900°C. The recorded data is presented in Figure 7.1.

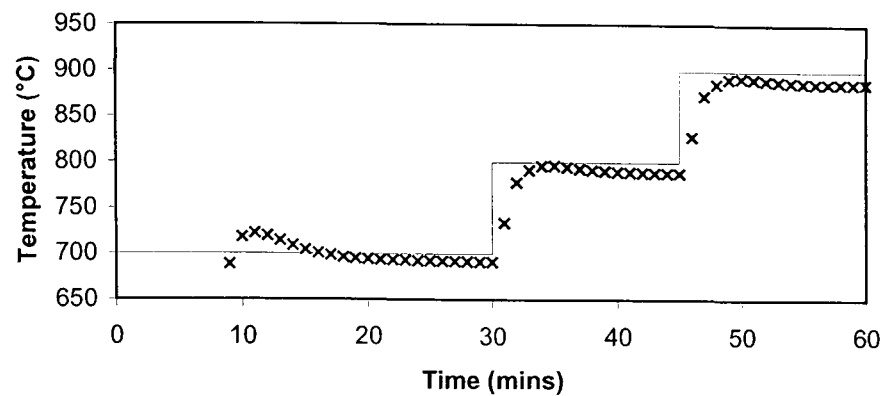


Figure 7.1: Relationship between furnace setpoint and centre temperature during warm-up. Solid line indicates furnace setpoint, crosses indicate measured temperature at centre of furnace using an inserted Type K thermocouple. 0 – 650°C range has been omitted for clarity at the temperature range of interest. Because of this, data points recorded at 0-8 minutes inclusive have also been omitted.

Figure 7.2 shows the variation at steady state between the furnace setpoint (and therefore indicated temperature) and the temperature indicated by the inserted thermocouple. It can be seen that the measured temperature is around 10°C lower than the furnace setpoint and that the variation is linear over the temperature range of interest. This was considered a small deviation considering the potential for convective air flows through the vertical worktube. The furnace setpoint was therefore used as the actual temperature, rather than a corrected value.

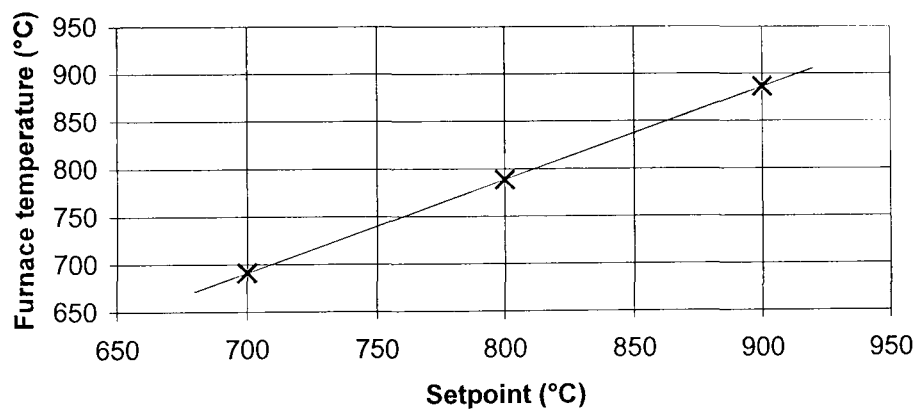


Figure 7.2: Relationship between furnace setpoint and centre temperature at steady state. Crosses indicate measured temperature at the centre of the furnace using an inserted Type K thermocouple.

7.2 Metalwork electrical resistance

In order to determine the electrical resistance of the external circuit, the experimental apparatus was assembled without the membrane in place. A single 4cm length of 0.5mm diameter platinum wire was placed across the membrane holder such that it

contacted both the top and bottom halves of the supporting metalwork. The whole assembly was placed in the furnace and a multimeter attached across the metalwork protruding from the top and bottom of the furnace. The furnace worktube ends were insulated by packing them with insulating wool. The furnace was given a setpoint of 900°C and the heaters activated. Readings were taken every two minutes of the temperature indicated on the furnace controller and the electrical resistance of the circuit until the furnace temperature stabilised at the setpoint of 900°C. The measurements are presented in Figure 7.3.

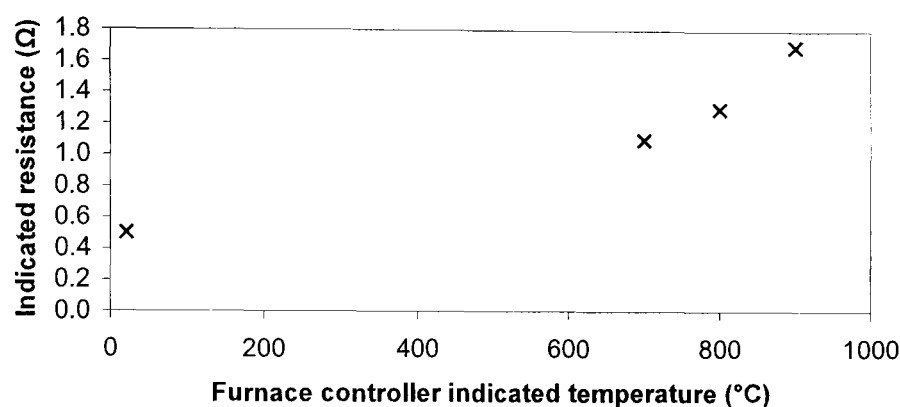


Figure 7.3: Variation of apparatus external circuit resistance with temperature.

As expected, the metalwork resistance increases with temperature. It is noteworthy that at no point was a resistance greater than 2Ω recorded. This is a small resistance that should not impede the use of the apparatus in the passive state, that is, without an external power supply and using the oxygen partial pressure gradient across the membrane as the sole driving force, should this be required.

7.3 Passive oxygen flux prediction

It is possible to estimate the oxygen flux possible under “passive” operation, that is, operation of the apparatus without an external power supply.

The conduction of oxygen ions through the membrane is driven by the potential difference generated across the membrane by the oxygen partial pressure difference. By calculating the resistance of the whole circuit, the current flowing can then be calculated using Ohm’s Law.

Having measured the external circuit resistance in Section 7.2, the YSZ membrane resistance was calculated.

7.3.1 YSZ membrane resistance

West (1999) presents data on the ionic conductivity σ of YSZ at elevated temperatures. This data is replicated below, reformatted, as Figure 7.4.

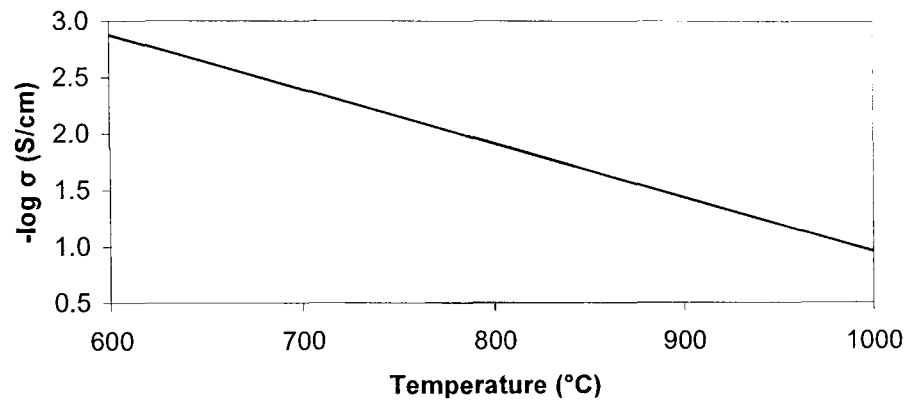


Figure 7.4: Variation of YSZ conductivity with temperature (from West 1999)

Given the membrane face area $A(\text{cm}^2)$ and thickness $L(\text{cm})$, the conductance G of the membrane can be calculated. For example, at 850°C where $\sigma = 0.0211\text{S/cm}$, the conductance is as follows for the membrane of radius 0.9cm and thickness 0.2cm :

$$G = \frac{\sigma A}{L} = \frac{0.0211 \times (\pi \times 0.9^2)}{0.2} = 0.2684\Omega^{-1}$$

The membrane resistance is the inverse of the conductance, that is 3.73Ω .

7.3.2 Current and oxygen flow prediction

The variation of the external circuit resistance with temperature was presented in Section 7.3. Adding this to the membrane resistance calculated above gives the total resistance (see Figure 7.5).

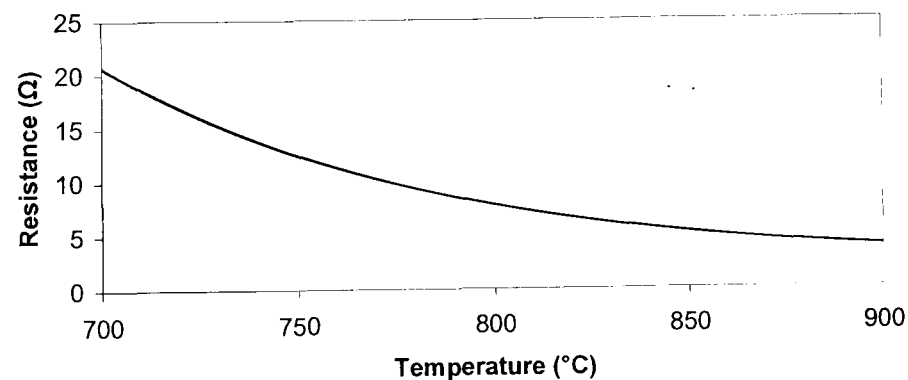


Figure 7.5: Calculated resistance of whole electrical circuit

Figure 5.2 shows the open circuit voltage generated across a membrane by various ratios of oxygen partial pressure. Assuming an oxygen partial pressure ratio across the membrane of 50, the expected whole circuit resistance and generated open circuit voltage are both determined and hence, using Ohm's Law, the current can be estimated (see Figure 7.6). In reality, the voltage across an operational membrane would be less than the open circuit voltage calculated for the conditions, as the resistance of the load across the membranes electrodes is by definition not infinite under closed circuit conditions. Additionally, the resistance used here to calculate the current only accounts for ohmic losses in the membrane and the external circuit. In reality there would be additional polarisation losses associated with the activated dissociation process at the electrode surface and mass transfer limitations. Because of this, the current calculated here is an overestimation.

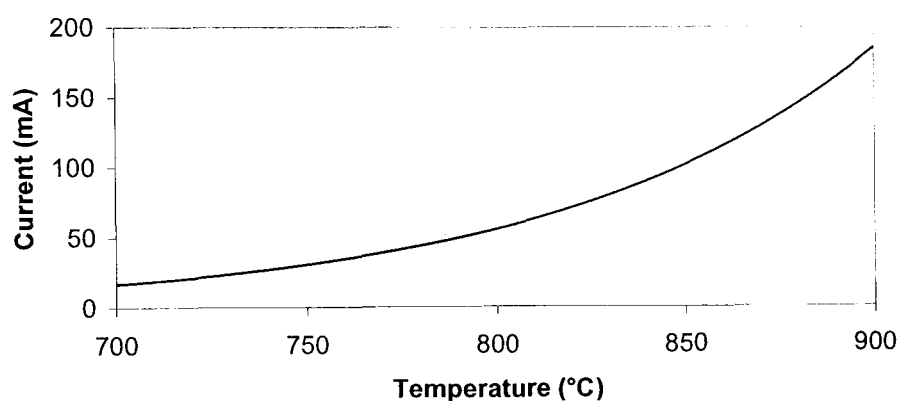


Figure 7.6: Calculated current flow under passive conditions, 50:1 O_2 partial pressure ratio across membrane, assumes that the open circuit voltage for that O_2 partial pressure ratio is present.

Finally, the calculated current can be converted into an amount of charge per minute, then an amount of O^{2-} ions per minute, and finally an O_2 flow rate at RTP. The calculated values are presented in Figure 7.7.

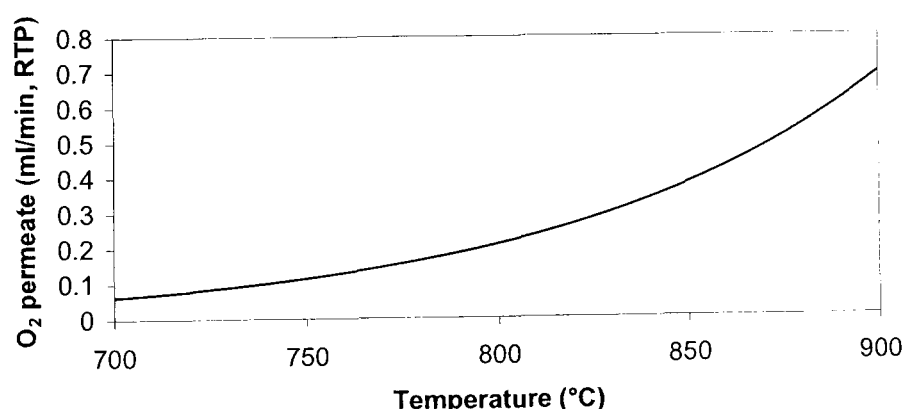


Figure 7.7: Calculated passive O_2 permeate flow rate, assuming 50:1 O_2 partial pressure ratio across membrane and the open circuit voltage is present.

If these values were borne out by experiment, measurable amounts of O₂ permeation would be present in the target temperature range without the use of an external power supply, should this mode of operation be investigated. As previously noted, the voltage during operation would be lower than the open circuit voltage and therefore these values are an overestimate.

7.4 Graphite seal lifespan testing

As a first investigation of a graphite seal's lifespan, the mass loss of the seals in high temperature air was recorded. This gave an indication as to whether the seals would be suitable for use in the rig. The seals need to retain most of their mass for a short number of hours in order to be useful.

When in place in the experimental rig, only part of the seal is exposed to an oxidising environment, i.e. the outward facing edge (into the furnace worktube) and the inward facing edge (into the membrane holder cavity) where a gas stream containing oxygen is being fed to the membrane. Because of this, the results presented here, where all faces of the seal are exposed to air, can be regarded as a pessimistic estimate of the seal's longevity.

7.4.1 Method

These tests set out to quantify the lifespan of the graphite seals in air at high temperature.

A Carbolite oven-type furnace was preheated to the required temperature. The crucible to be used was weighed empty. One graphite membrane of 1g/cm³ density, 23mm outside diameter, 19mm inside diameter and 1.5mm thickness was then weighed in the crucible. It was placed in the furnace and removed at regular intervals to be re-weighed.

The balance used for weighing displays to an accuracy of 0.0001g. Because of air flow in the balance enclosure, the fourth decimal place fluctuated and is not reliable. The most stable value was recorded, with the measurement error taken to be ± 0.001 g.

7.4.2 Results

For the first test, the gasket was heated to 700°C and weighed at 15 minute intervals for four hours. The results are presented graphically in Figure 7.8.

The error because of the fluctuating balance measurements is too small to be shown on the graph. The largest errors are associated with the final data point as a result of the small sample mass. The error is $\pm 7\%$, with the error bars being smaller than the data point itself.

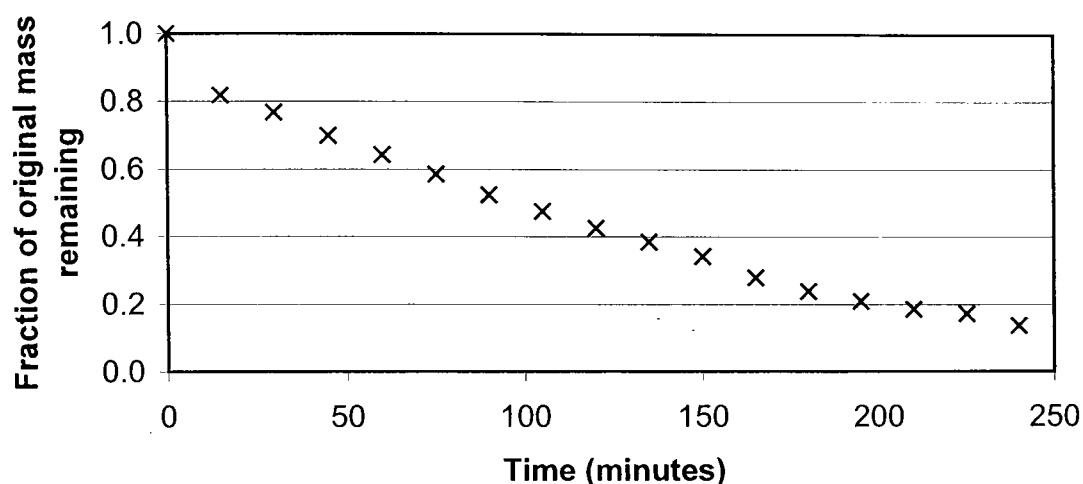


Figure 7.8: Graphite gasket mass loss: 700°C, 15 min recording intervals

There was a concern that the act of removing the crucible from the furnace every 15 minutes for weighing would allow the sample to cool sufficiently to affect the results. For this reason, the preceding test was repeated with 60 minute weighing intervals. The results were found to be similar. Although this data shows an unacceptable mass loss from the gasket, it was known to be pessimistic. The use of graphite gaskets was continued until a more durable solution was found (see Section 7.8).

7.5 O₂ permeation through prototype membrane from He/O₂ mixtures

7.5.1 750°C

This first rigorous test used 100ml/min of pure helium sweep gas on the permeate side, with a feed of 50ml/min of 20% O₂ in He. The furnace was set to 750°C and the voltage adjusted from 1-6V (except 4V) in 1V steps.

Ciacchi et al. (2002) presents results from a similar experiment, where the current required to remove a certain amount of oxygen from a 63ml/min air stream was measured at 750°C. The 3% yttria YSZ tubular membrane used by Ciacchi had approximately ten times the electroded surface of the membrane being used here and was

only a third of the thickness. The larger surface area meant that Ciacchi's membrane operated at much lower current densities and oxygen fluxes than the membrane being used here, but nevertheless the data is included in Figure 7.9 for comparison. Ciacchi's data is broadly comparable to that obtained here. Both sets of data are below the theoretical maximum oxygen concentration possible according to the measured current. This indicates some current leakage, either externally or within the membrane itself. The average calculated total resistance (see Figure 7.10) was 5.33Ω .

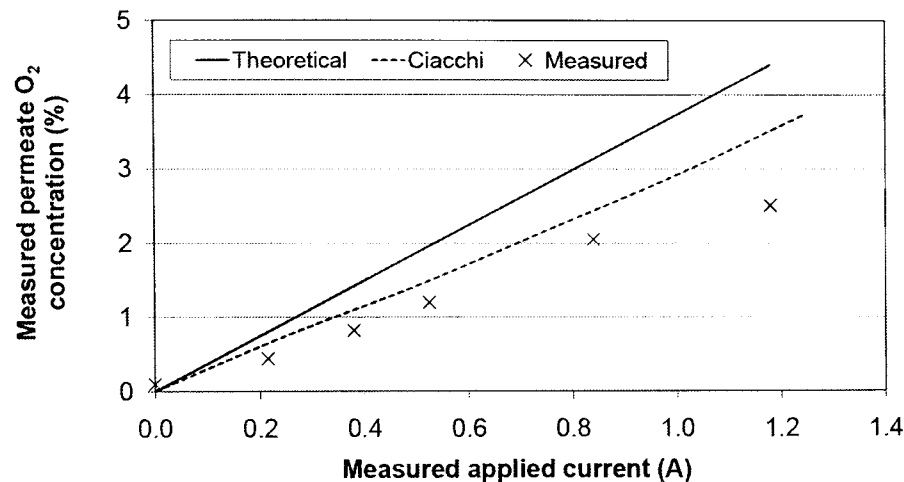


Figure 7.9: O₂ permeation through membrane at 750°C with external voltage application - 100ml/min 100% He sweep gas, 50ml/min 20% O₂ 80% He feed. Dashed line shows values presented by Ciacchi(2002) for O₂ removal from air. Solid line shows oxygen concentration equating to measured current flow. $R^2 = 0.983$

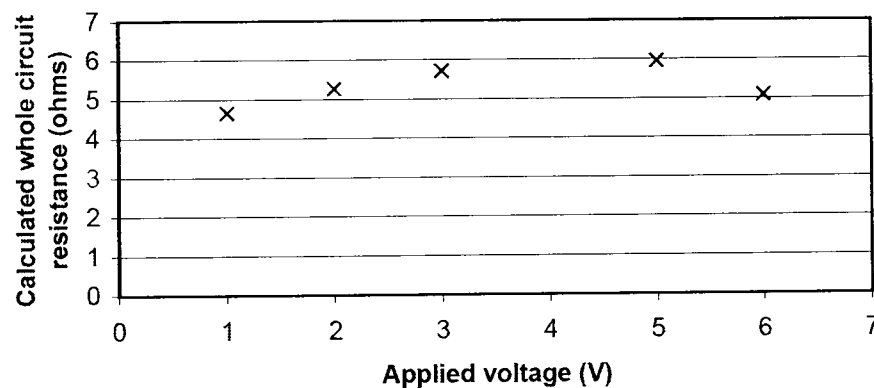


Figure 7.10: Electrical resistance at 750°C - 100ml/min 100% He sweep gas, 50ml/min 20% O₂ 80% He feed.

Figures 7.11 and 7.12 show the graphite gaskets after the run. They were subjected to a 15 minute warmup period to 750°C followed by 45 minutes at operating temperature. At this time, the electrical connection across the membrane failed and hence the furnace heaters were turned off and the apparatus allowed to cool back to room

temperature. Helium was passed through the apparatus once it had reached room temperature and there was still gas flow at the vents. The graphite gaskets had therefore not failed, despite the length of time spent at high temperature.

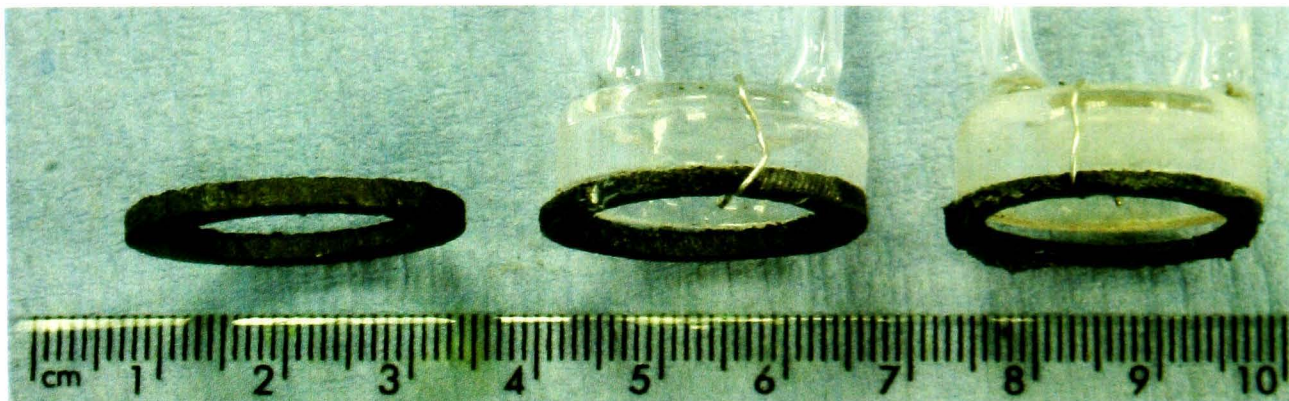


Figure 7.11: Graphite gaskets after run at 750°C, 15 mins warm up, 45 mins operating, natural cool down, 100ml/min pure He sweep/permeate carrier, 50ml/min of 80% He 20% O₂. Left to right are unused gasket, permeate side, feed side.

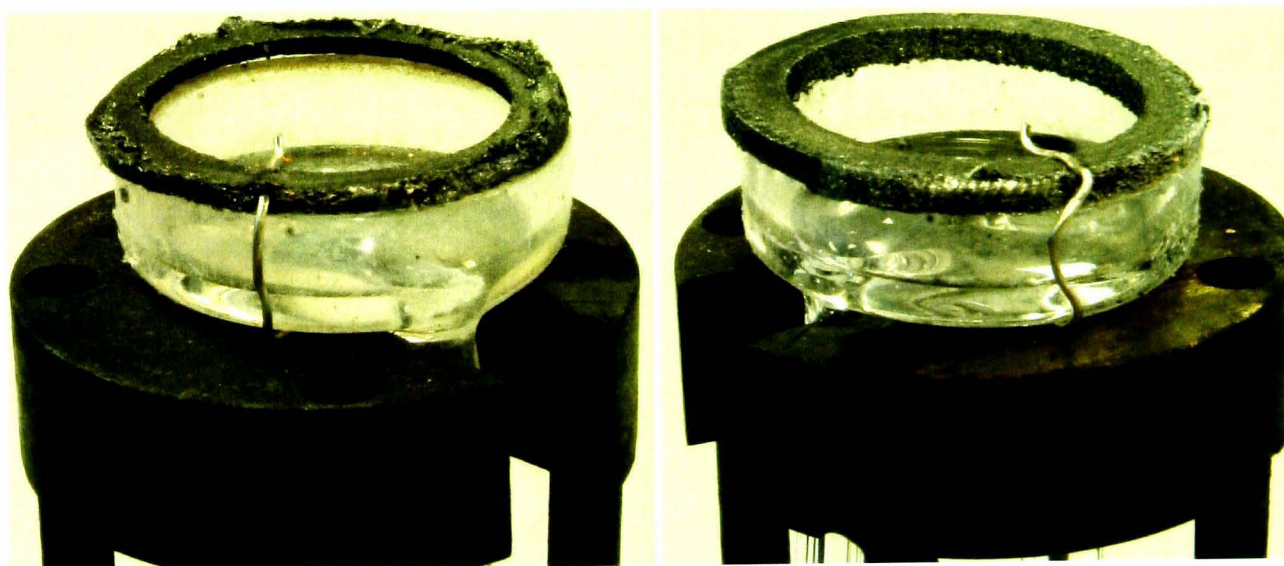


Figure 7.12: Graphite gaskets after same run described for Figure 7.11. Feed side gasket on left, permeate side gasket on right.

It can be seen that the gaskets are largely intact, albeit with some reduction in thickness. The feed side gasket has reduced further in thickness and weight than the permeate side gasket. The weight of each gasket is shown in Table 7.1.

Representative unused gasket	0.3704g
Permeate side gasket	0.1934g
Feed side gasket	0.0949g

Table 7.1: Graphite gasket weights after same run described for Figure 7.11. Weights are accurate $\pm 0.0001\text{g}$.

The permeate side gasket has lost around 50% of its initial mass and the feed side gasket has lost around 75% of its initial mass.

7.5.2 700°C

The next test replicated that performed at 750°C, but with a furnace setpoint of 700°C. Again the flow rates used were 100ml/min of pure helium sweep gas on the permeate side, with a feed of 50ml/min with a composition of 20% O₂ in He. The voltage was varied from 1-6V in 1V steps. Figures 7.13 and 7.14 present the measured O₂ permeation rate and the calculated circuit electrical resistance, which averaged 9.9Ω.

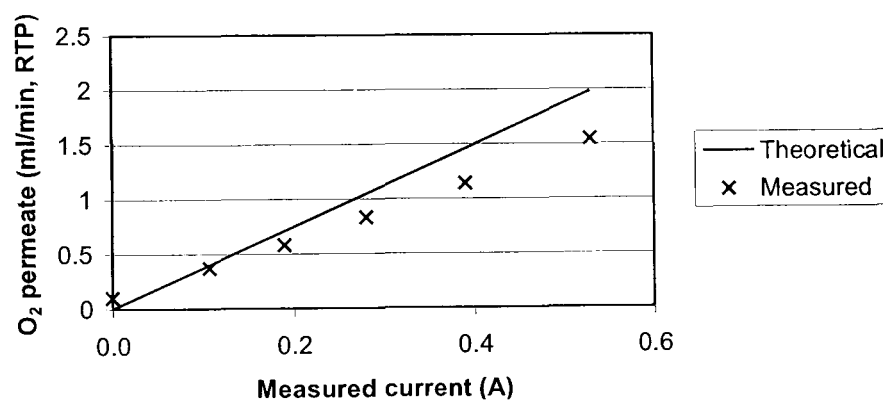


Figure 7.13: O₂ permeation through membrane at 700°C with external voltage application - 100ml/min 100% He sweep gas, 50ml/min 20% O₂ 80% He feed.

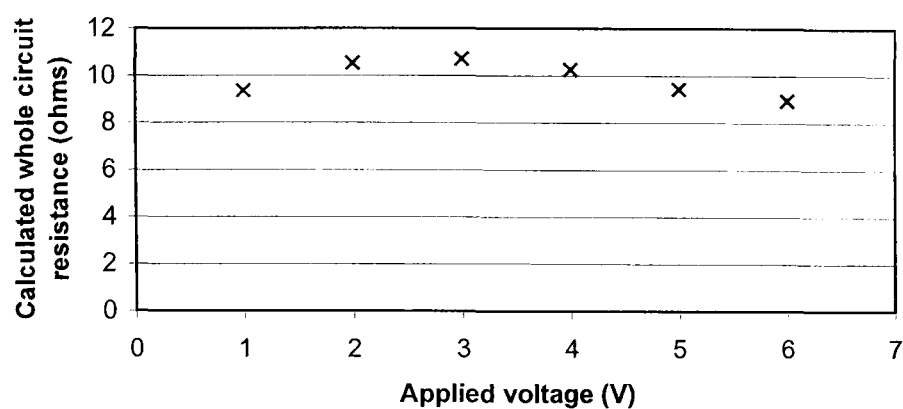


Figure 7.14: Electrical resistance at 700°C - 100ml/min 100% He sweep gas, 50ml/min 20% O₂ 80% He feed.

The graphite gaskets, following post-experiment natural cooling, are pictured in Figure 7.15. It can be seen that the gaskets are visually less damaged than those pictured following the run at 750°C. Indeed, a helium leak test conducted cold after the rig has cooled naturally showed there had been no loss of sealing over the course of the one hour heated period.

Representative unused gasket	0.3634g
Permeate side gasket	0.2477g
Feed side gasket	0.2460g

Table 7.2: Graphite gasket weights after same run described for Figure 7.15. Weights are accurate ± 0.0001 g.

Both the permeate and feed side gaskets lost around 32% mass during the run. This compares favourably with the 50-75% loss seen at 750°C.

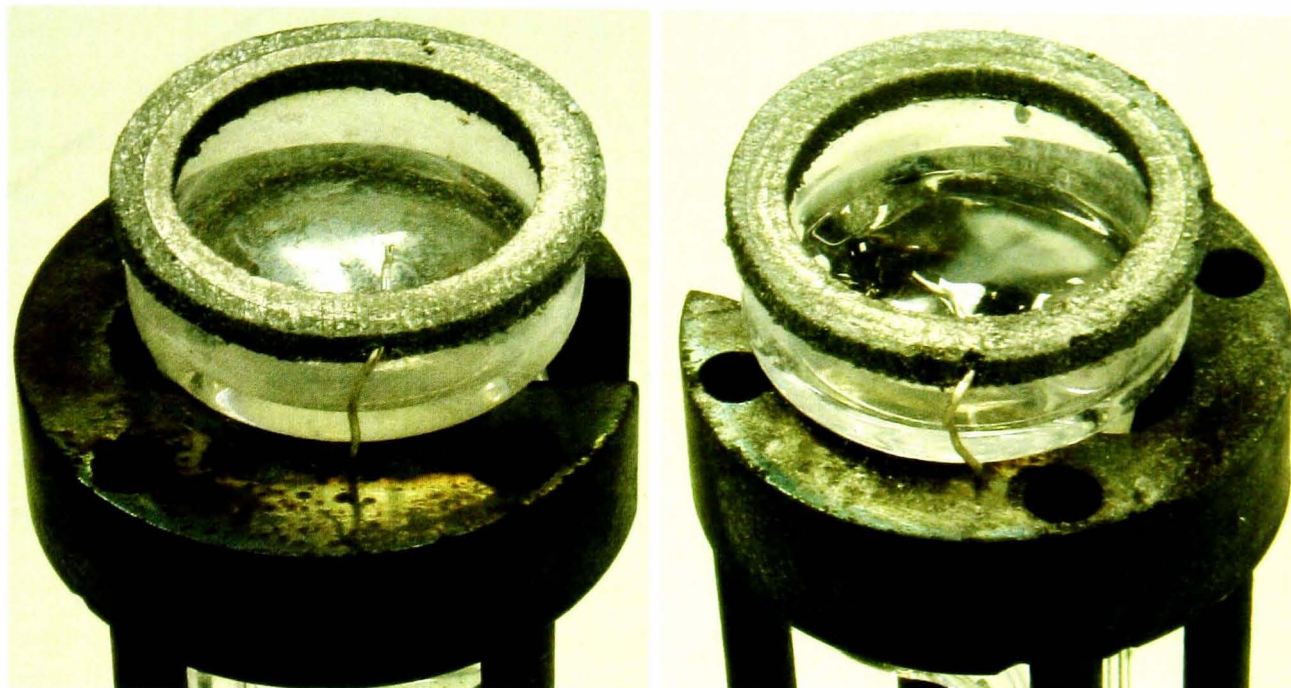


Figure 7.15: Graphite gaskets after run at 700°C, 15 mins warm up, 45 mins operating, natural cool down, 100ml/min pure He sweep/permeate carrier, 50ml/min of mostly 80% He 20% O₂ (composition varied in last few minutes of operation.) Left to right are permeate then feed side gaskets.

The currents used to calculate the circuit resistance were those measured as soon as the voltage was increased. It was observed that at voltages from 4-6V the current increased from that value initially observed to a higher value at equilibrium. When the voltage was reduced back to 3V, the current reading decreased gradually, attaining the originally measured value after a couple of minutes. Figure 7.16 shows the initial and stable currents measured.

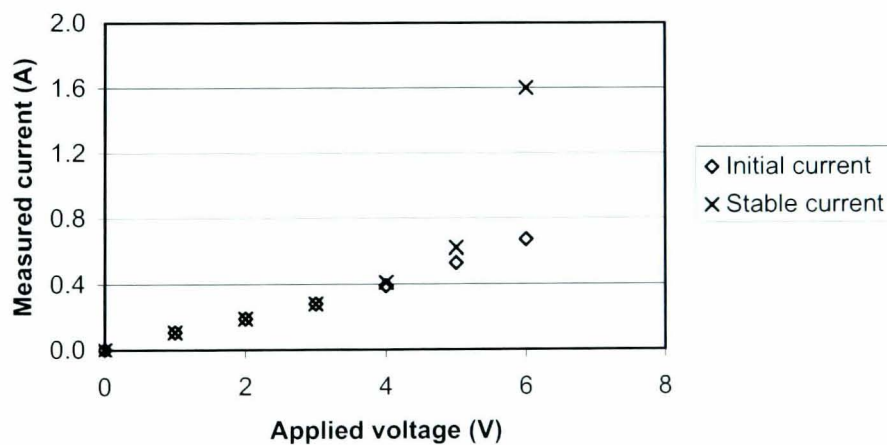


Figure 7.16: Initial and equilibrium current variation with applied voltage at 700°C - 100ml/min 100% He sweep gas, 50ml/min 20% O₂ 80% He feed.

One possibility is that the increase in current was caused by heating of the membrane

as a result of the large potential being applied.

Arima et al. (2004) gives a value for the heat capacity C_p of 8 mol% YSZ of approximately 75 J/mol.K in the temperature range of interest. The membrane being used here weighs 4.55g, or 0.03462mol of 8mol% YSZ. At the initial current reading at 6V, 240J/min passes through the membrane. If all of this energy was used in heating the membrane, it would give a temperature rise rate of 92K/min. At the final current reading at 6V, 576J/min passes through the membrane. If all of this energy was used in heating the membrane, it would give a temperature rise rate of 222K/min. Clearly the power levels at these higher voltages are sufficient to cause significant membrane heating.

Another possible reason for the current anomaly is electrolyte decomposition. The decomposition voltage E of YSZ is variously quoted as 2.5V at 500°C (Pham & Glass 1998), 2.231V at 900°C / 0.21atm O₂ (Weppner 1977) and 2.4V (Mizusaki et al. 1992). It can be calculated from the Gibbs free energy change ΔG , the Faraday constant F and the number of electrons transferred per mole of products, in this case four. Therefore at 700°C, where $\Delta G = 914608$ J/mol according to *HSC Chemistry*, the YSZ decomposition voltage is:

$$E = -\frac{\Delta G}{nF} = -\frac{914608}{4 \times 96485} = -2.37V$$

Decomposition can cause the YSZ to appear blackened. The non-electroded edge of the membrane being used here exhibited this blackening following the tests. Pham & Glass (1998) observed that the blackening of YSZ electrolyte, indicating partial electrolysis of that electrolyte, can increase the oxygen pumping capacity of the system through the introduction of additional electronic conductivity to the surface of the YSZ.

The relevant voltage for assessment of the potential for electrolyte decomposition is that voltage dropped across the electrodes, i.e. the externally applied voltage minus the voltage drops associated with the external circuitry and the ohmic resistance of the electrolyte (Figure 7.17). Figure 7.3 gives the external circuit resistance at 700°C as 1.1Ω, whilst the YSZ ohmic resistance of this membrane can be calculated from Figure 8.18 to be 0.145Ω at 700°C. Since Figure 7.14 shows the total resistance at 3V to be 10.8Ω, the summed electrode resistance is 9.56Ω, or 88% of the total. The fraction of voltage dropped across a load is equal to the fraction of the total resistance imparted by that load (for a series circuit), therefore the voltage dropped across the electrodes is 2.65V. This is slightly above the literature decomposition voltage values quoted above, indicating that electrolyte decomposition probably proceeds at 3V and 700°C, albeit

slowly. Increasing the externally applied voltage and hence the voltage drop across the electrodes would increase the rate of electrolyte decomposition.

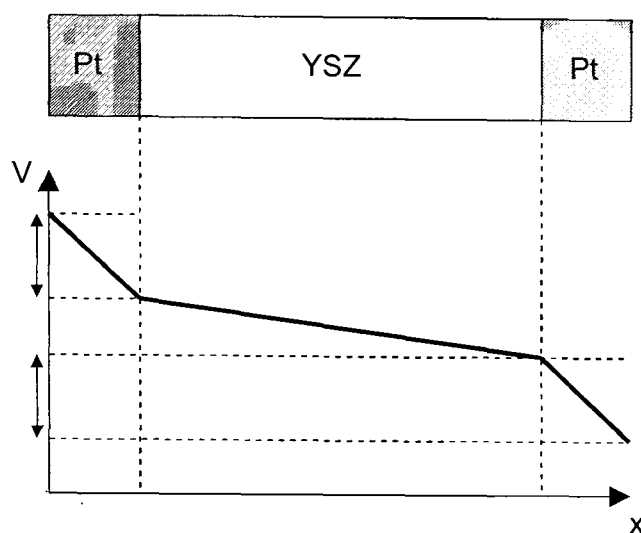


Figure 7.17: Qualitative representation of voltage drop across YSZ/Pt membrane. Voltage relevant to YSZ electrolyte decomposition is the sum of the two arrowed voltages.

Ciacchi et al.'s (2002) work with YSZ tubes of 300-600 μm at 750°C indicated that stable operation could be achieved at current densities of $\leq 300\text{mA}/\text{cm}^2$. This is equivalent to 763mA with the membrane being used here. A voltage of approximately 4V would produce this current at 750°C, based on the experimental data in Figure 7.9.

Ciacchi goes on to say:

on increasing the current density to 450mA/cm², the performance dropped suddenly. Examination of the cell on cooling showed a fracture in the zirconia tube and general weakening of the zirconia matrix. It is well known that if less than the required amount or no oxygen is available to the cathode near the electrode/electrolyte interface and provided the voltage across the cell is sufficiently high, reduction of Zr⁴⁺ to Zr³⁺ or even to Zr metal can occur to sustain the high current densities. This would lead to an expansion of the lattice and then reduction following restoration of the Zr oxidation state on supply of oxygen.

For reference, a current density of 450mA/cm² equates to a current of 1150mA for the membrane being used here. This current was achieved at around 6V.

The only literature found that records the timescale on which YSZ blackening occurs details tests on YSZ samples sealed in glass to prevent oxygen exchange with the atmosphere and subjected to an externally applied voltage at 500°C (Janek & Korte 1999). Under these conditions, with a 20mm long sample, YSZ blackening only extended

1mm in from the cathode after 24 hours at an applied potential of 10V. Application of 100V caused blackening of the whole sample in "several hours".

Given the information from the literature, the most likely explanation of the results observed here is that, at the higher voltages of 3-6V, partial electrolysis of the YSZ was occurring (as evidenced by the blackening of the pellet) and the resulting increase in electronic conductivity reduced the resistance of the YSZ and caused the large increase in current flow.

Consequently, to avoid the possibility of electrolyte decomposition, the applied voltage was kept at $\leq 3V$ for all further tests.

7.5.3 Variation of circuit resistance with temperature

The average circuit resistance at each of the temperatures used so far has been calculated and the results presented in Figure 7.18.

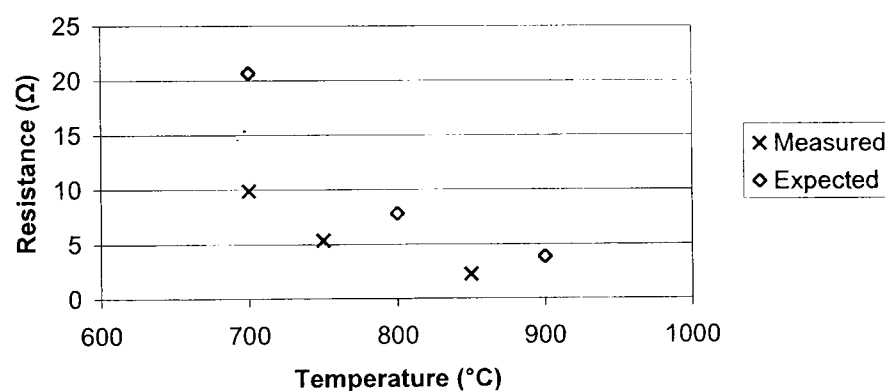


Figure 7.18: Average whole circuit resistance at 700 – 850°C - 100ml/min 100% He sweep gas, 50ml/min 20% O₂ 80% He feed.

Figure 7.3 showed that the metalwork resistance measured during commissioning increases slightly with temperature, from around 1.1Ω at 700°C to around 1.4Ω at 850°C. The decreasing whole circuit resistance exhibited with increasing temperature can therefore be attributed to the increasing YSZ conductivity with increasing temperature.

7.6 O₂ permeation through prototype membrane from He/O₂/SO₂ mixtures

Following the initial tests using helium-oxygen mixtures, the feed mixture was changed to include SO₂.

Runs of a total length of around one hour were carried out whereby the furnace was heated up as before and the O₂ permeation measured at a fixed applied voltage in a similar fashion to that used for the initial tests. Once the O₂ flux stabilised, some of the helium in the feed stream was replaced with SO₂, such that the oxygen feed concentration remained constant. The O₂ flux was then monitored for a period of time, before the SO₂ was removed from the feed.

The results of the first run are shown in Figure 7.19. Data is only plotted from 29 minutes after the furnace was turned on, as it was at this point that the rig was at operating temperature and adequate sealing and electrical connections had been made.

The bottom graph in the set shows the permeate O₂ concentration as read directly from the gas analyser. Comparison with the voltage and current graphs above shows that during those periods when no power is being applied to the rig, the measured permeate O₂ concentration does not return to the same value as that recorded in the early stages of the test. This could be caused by a change in flow rate through the gas analyser or by O₂ permeation not due to the applied voltage. In order to counteract this, the 'raw' O₂ concentration data was corrected to give the O₂ concentration at any given time due to the applied voltage. A curve was produced from those O₂ concentration values that are known to correspond to zero applied potential, i.e. those values where the current flowing through the membrane has been zero for at least one minute. The O₂ value corresponding to zero was then subtracted from the raw data in order to give the corrected values shown in the 4th graph in the set.

The data shows that the current remains steady at around 125mA when the 20% O₂ in He is initially applied. The permeate O₂ concentration at that time, $\approx 0.34\%$, is around 75% of the theoretical maximum possible at that current.

When the feed mixture is changed (after 39 minutes) to 20% SO₂ and 20% O₂ in He, an immediate current decrease was observed. The corrected permeate O₂ concentration also decreased after one minute's lag, but it decreased at a sufficiently slow rate that the values were very close to the theoretical maximum for the current being measured at that time.

The corrected permeate O₂ concentration continued to decrease when the SO₂ feed

was removed, which suggests that the membrane had deteriorated in some way. Temporarily removing the applied voltage from 49-51 minutes showed that the membrane was still functioning, albeit with a significantly decreased flux compared to the start of the run.

This run was repeated using the same conditions and the same membrane. The results are presented, in the same format as the first run, in Figure 7.20.

Upon application of a voltage across the membrane for the first time in the second run, the maximum current achieved was similar to that recorded at the end of the first run. This suggests that persistent damage occurred to the membrane during the first run. If this damage is the type of sulphation discussed in Section 5.3 then it should be possible to reverse the damage by heating the membrane to a higher temperature, causing SO₂ to be released and the membrane to become fully functional once again.

Unlike the first run, application of SO₂ (after 29 minutes) caused an increase in current flowing from around 40mA to around 50mA. This higher value was then maintained until the SO₂ was removed from the feed. The same effect was seen when the SO₂ was applied again.

At the end of this second run the corrected permeate O₂ concentration was 75% of the theoretical maximum, as it was at the start of the first run.

The third run replicated the conditions of the previous runs. A gas analyser was not available for this run. Those results that could be recorded are shown in Figure 7.21.

This run used a slightly different electrical connection to previous runs. In an attempt to reduce leakage through the graphite seals, the wire from the supporting metal-work was only partially pressed into the outer face of the graphite, not punched fully through it (in order to touch the platinum electrodes directly.) It was hoped that the conductivity of the graphite itself would be sufficient to provide an adequate electrical connection to the electrodes.

It can be seen that upon first application of 2000mV to the membrane with 20% O₂ feed, the current achieved was 25mA, exactly the same as was recorded under the same conditions at the end of the second run. This demonstrates that this alternative electrical connection method is just as effective as the old method, whilst vastly improving the sealing of the membrane holder.

As with previous runs, the current could be seen to increase when SO₂ was added to the feed mixture.

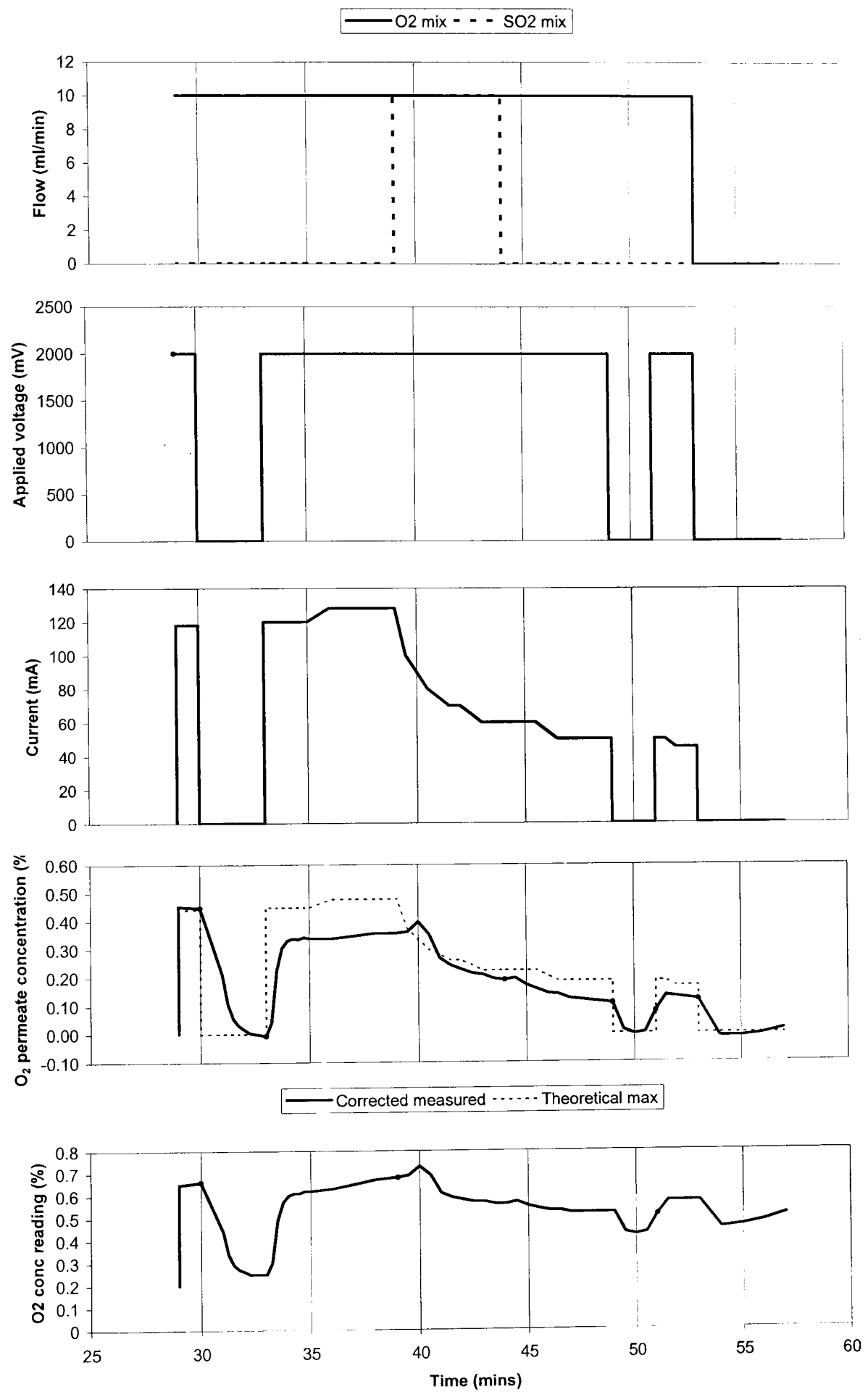


Figure 7.19: Results of first SO₂ run with prototype membrane. Total feed = 50ml/min. Furnace at 700°C.

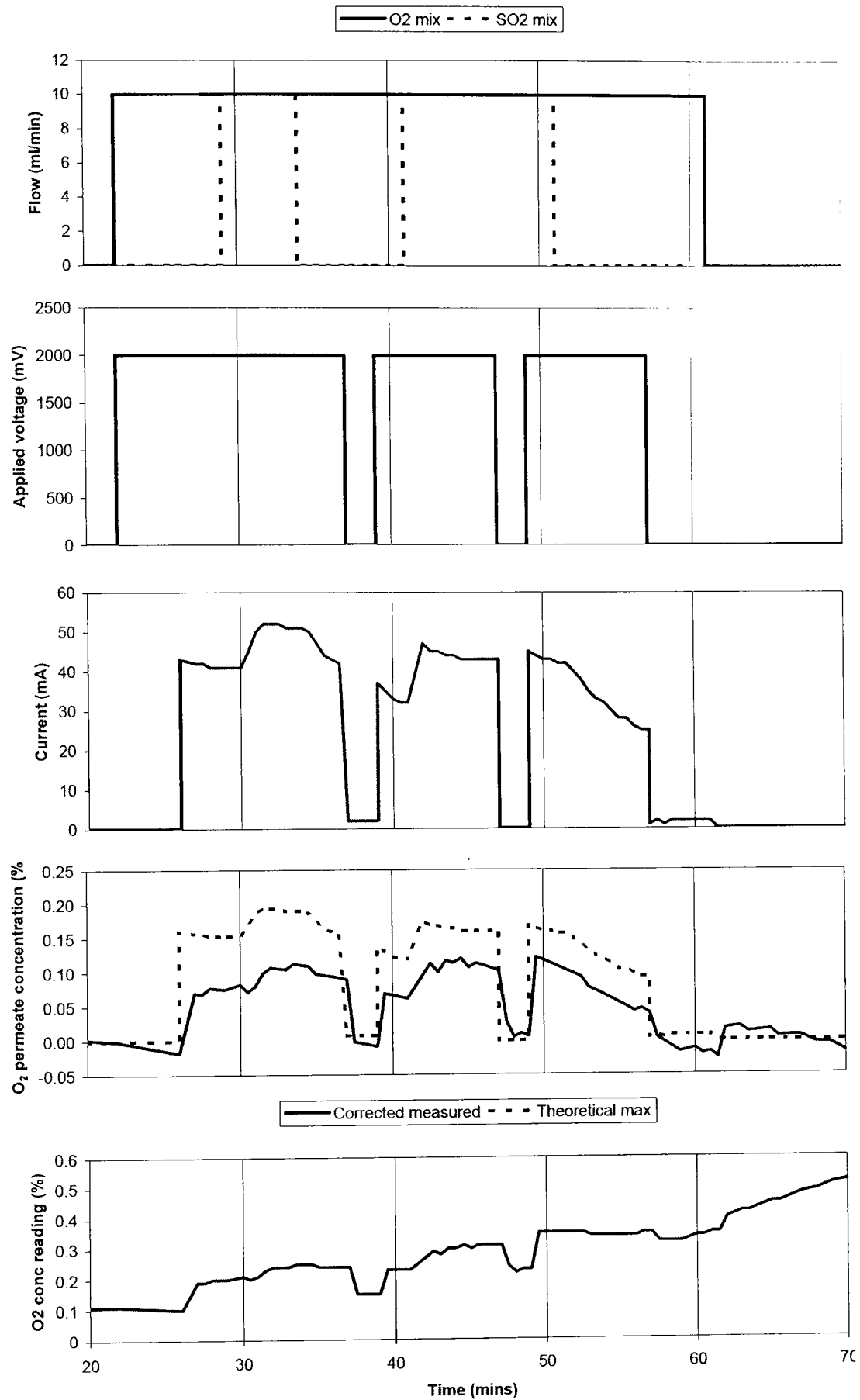


Figure 7.20: Results of second SO₂ run with prototype membrane. Total feed = 50ml/min. Furnace at 700°C.

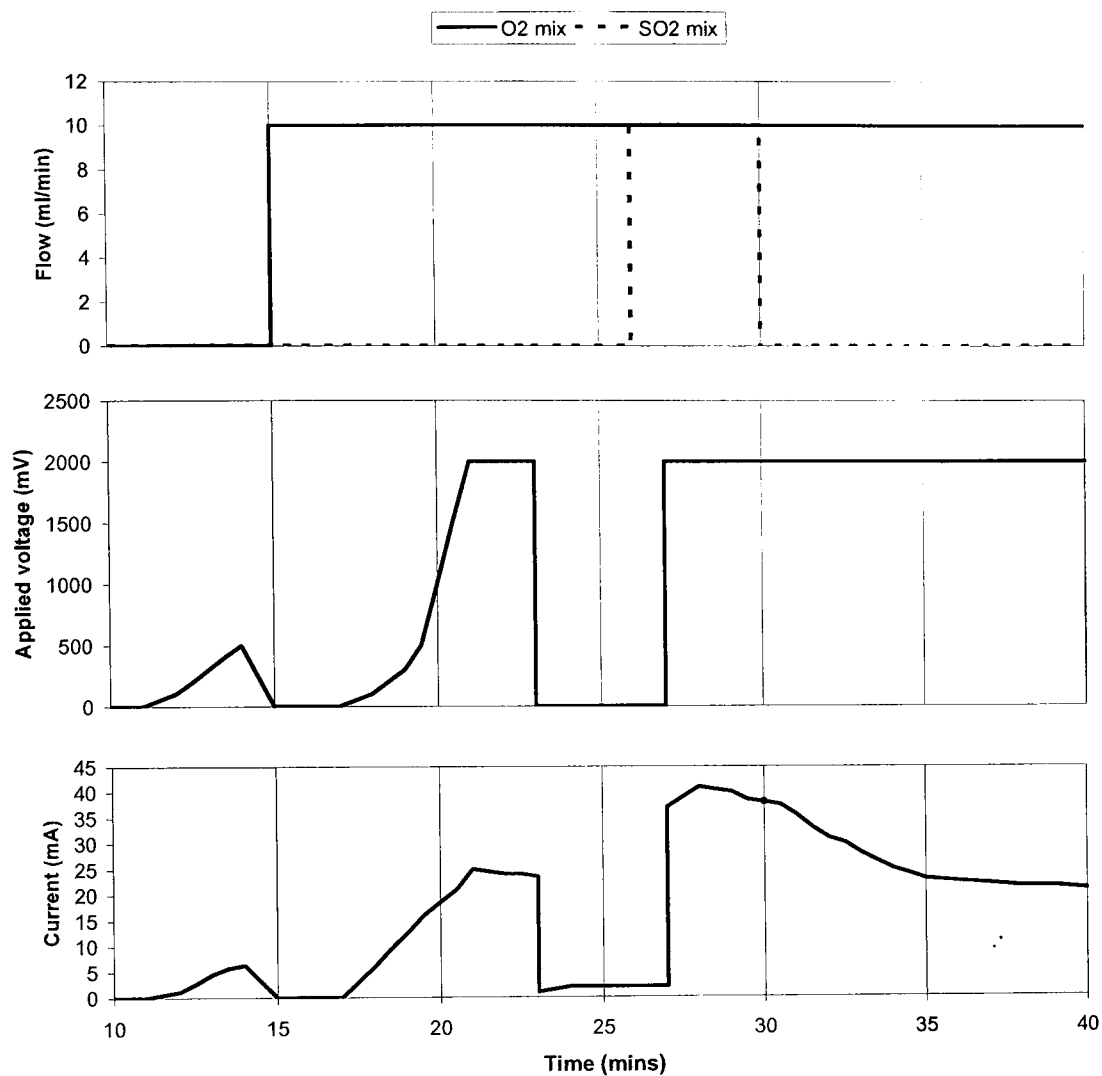


Figure 7.21: Results of third SO_2 run with prototype membrane. Total feed = 50ml/min. Furnace at 700°C .

7.7 XRD analysis of prototype membrane

At this point, after three experimental runs, the membrane was sent for XRD analysis by the Engineering Materials department. The resulting chart is presented as Figure 7.22.

The expected peaks for the platinum and YSZ phases present have been superimposed on to the data and it can be seen that they are a good match. It can also be seen that there are additional peaks at approximately $2\theta = 10-11^\circ$ and $2\theta = 31-32^\circ$. At this stage, the additional peaks were not identified.

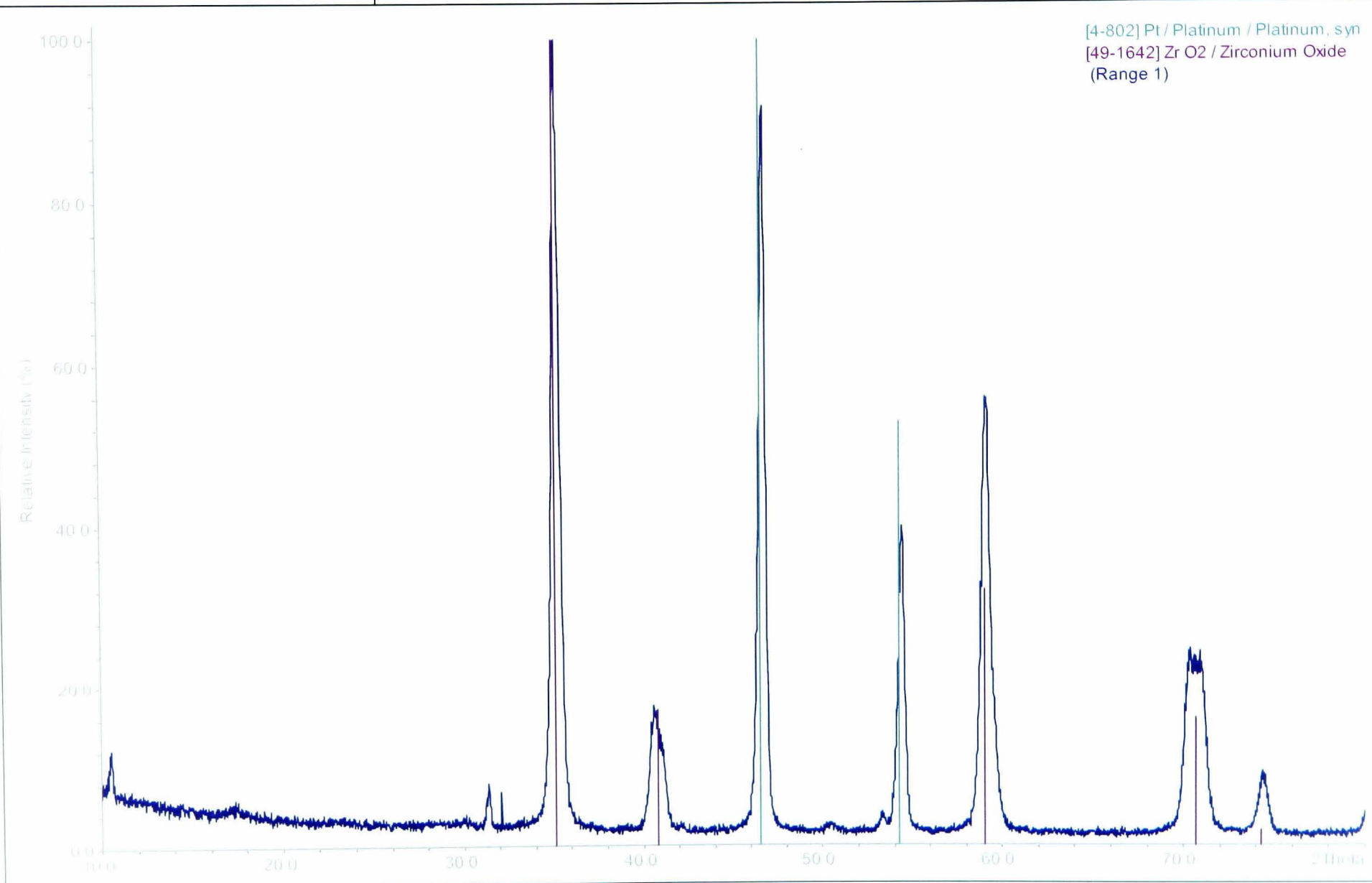


Figure 7.22: XRD data for prototype membrane, post-exposure

7.8 Graphite seal coating testing

There was some concern about the limited longevity of the graphite seals at higher temperatures. Gold is known to be compatible with the high temperatures required, but it is expensive and more difficult to compress. It was hoped that combining gold and graphite in some way could produce resilient, compressible and relatively inexpensive seals.

7.8.1 Aim

The aim of these experiments was to determine if graphite gaskets could be combined with gold in some way as to increase their longevity at high temperatures.

7.8.2 Gasket types

Standard uncoated graphite gaskets were tested as a control case. Gold was then applied to the gaskets in the form of sputtering or foil. A gold sputtered gasket is shown in Figure 7.23.

Initially it was planned to apply gold foil to the gaskets by wrapping thin gold foil strips around the gasket. Two strips of approximately 75x4mm were initially acquired from the Department of Engineering Materials. These strips were wrapped around a gold sputtered gasket as shown in Figure 7.24. It was decided that an excessive amount of gold would be required to wrap each gasket and that it would be very difficult to seal the edges sufficiently to achieve the desired effect. This method was therefore abandoned.

It was also suggested that gold foil rings could be applied to each side of the gasket. Foil rings, shown in Figure 7.25, were cut from squares of gold foil to be large enough to prevent the sandwiched graphite making contact with the quartz or, if it had been used, the membrane.

As a final test, a single gold foil ring was used without any graphite in order to assess the sealing capability of the gold on its own.



Figure 7.23: Gold sputtered graphite gasket, with uncoated gasket for comparison. Scale in cm.



Figure 7.24: Gold sputtered graphite gasket with some foil wrapping

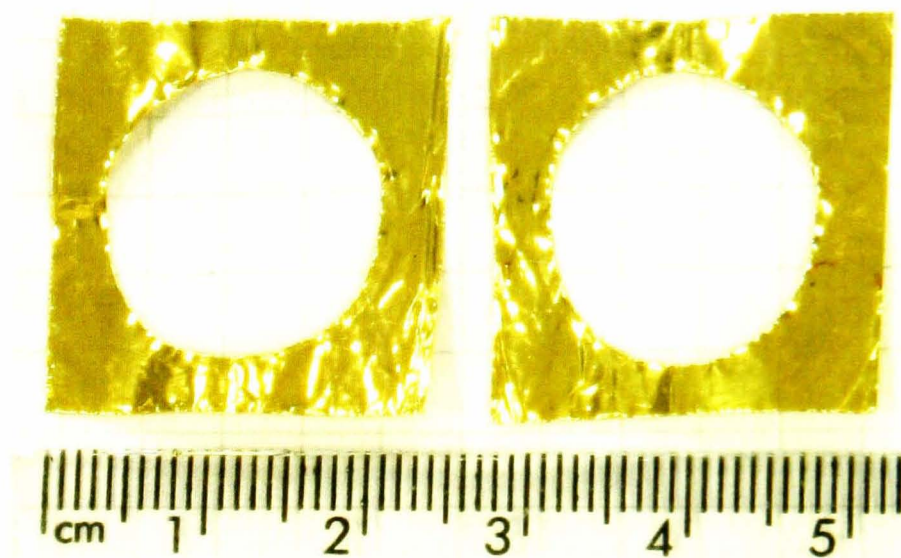


Figure 7.25: Gold foil rings, to be placed either side of a standard uncoated graphite gasket

7.8.3 Method

For each case, the test gasket and/or gold foil was sandwiched between the two quartz membrane holder halves and inserted into the furnace, supported by the metal stand. The upper holder half was connected to the rotameter bank on the inlet side and a gas flow meter on the outlet side, via a straight length of quartz tube for cooling purposes. The inlet and outlet connections of the lower holder half were attached together by a single short piece of Tygon tubing to prevent leakage from the system.

With the system at room temperature, 20% O₂ in He was supplied to the holder. The outlet flow rate was periodically recorded until either the gasket/foil leaked catastrophically or a set period of time elapsed, whichever occurred first.

The first batch of tests used a rotary gas flow meter. As this meter performed one rotation every 1000ml, readings were taken at room temperature for the first 1000ml after the stopwatch was started and the furnace heaters were then switched on, with a set-point of 900°C. Every 100ml the time elapsed and furnace temperature was recorded.

As the results show, this rotary gas flow meter produced very noisy results. Subsequent tests therefore used a “bubble” flow meter. When this meter was being used, the time elapsed for a given volumetric flow was recorded. Where possible, this flow was 50ml, the maximum recordable by the bubble flow meter. However, the bubble sometimes burst before reaching the top of the scale and hence the largest intermediate value was recorded instead. Four readings were taken with the furnace heaters off, then the heaters were switched on, with a set point of 900°C.

7.8.4 Results

Figure 7.26 summarises the results of the first batch of tests which used the rotary flow meter. The data points are an average of the 500ml leading to that point in time. The averaging was necessary to smooth out the very noisy data. However it can still be seen that the data is very variable. General trends can be obtained from the data. All of the seal types involving graphite seal well at room temperature, with the flow rates oscillating around the input flow rate of 80ml/min. Sealing at this point in the experiment may be aided by the Parafilm used to hold the membrane holder halves together during the assembly process and which burns off during the furnace heating phase.

It can be seen that, long term, the highest output flow rate is achieved by the use of a single gold foil ring, with the output flow rate oscillating around 70ml/min.

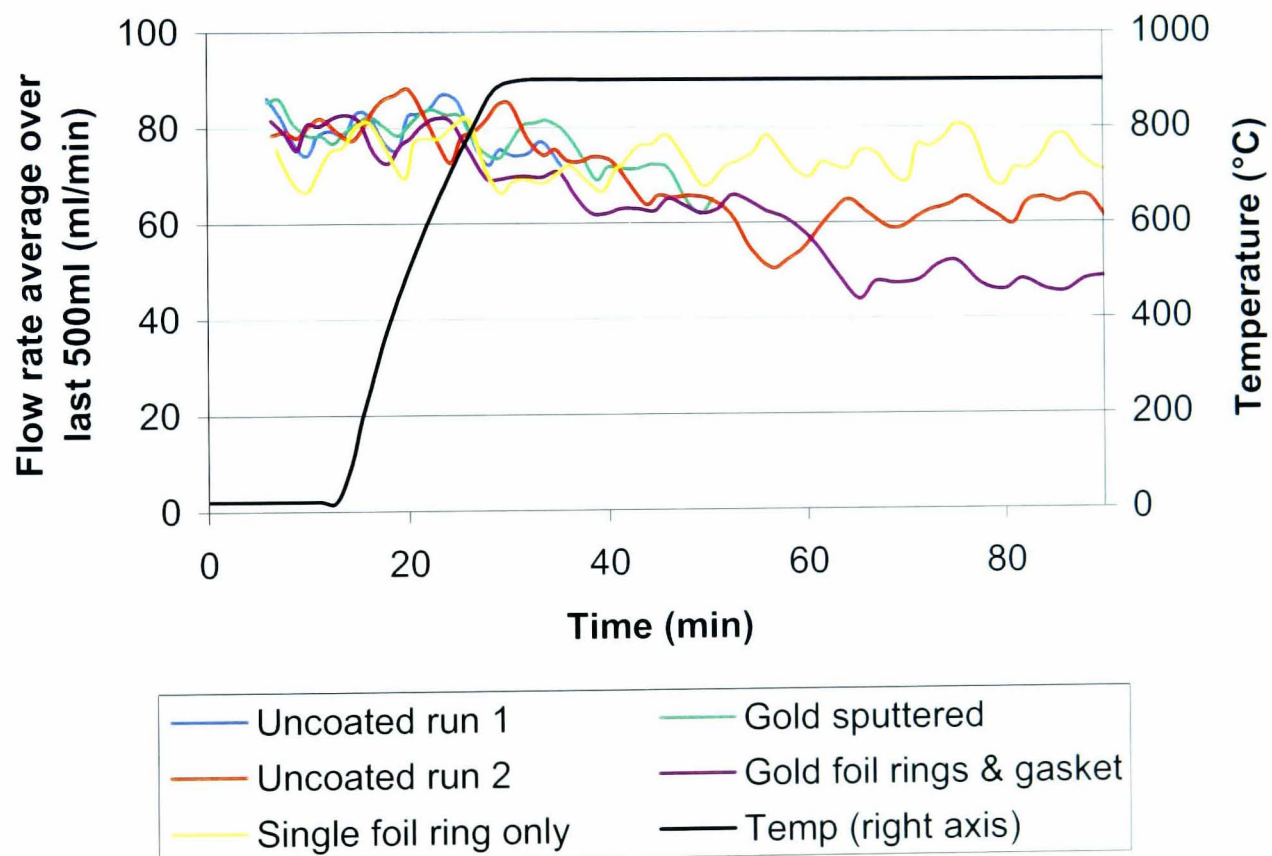


Figure 7.26: Timed flow results for graphite/gold gasket tests. Values are averaged over the previous 500ml. Input flow is 80ml/min of 20% oxygen in helium at room temperature and pressure.

A further test was carried out on a single gold foil ring, using the bubble flow meter. The input flow rate was reduced from the 80ml/min used previously to 50ml/min. Since full scale on the bubble flow meter was 50ml, this gave an expected bubble transit time of one minute. The results, presented in Figure 7.27, show that perfect seal-

ing was achieved whilst the apparatus was still at room temperature. As before, this could be attributed to the sacrificial Parafilm applied during assembly. Once the apparatus reached a sufficient temperature to burn off the Parafilm, the flow rate reached a steady 40ml/min. When the experimental run was finished, the apparatus was allowed to cool overnight.

Applying the same flow again to the cold rig the next day produced a flow rate of 41.7ml/min, demonstrating that the seal had not been lost during the cooling process. The previous day's run was then repeated. The results, presented in Figure 7.28, show that a constant level of sealing was maintained throughout the cold, heat-up and hot phases of the run. As the outlet flow rate was so constant, it was decided to increase the inlet flow rate to 80ml/min in order to draw comparisons with the initial run using the rotary gas flow meter (see Figure 7.26). A constant outlet flow rate of 73.2ml/min was measured at 80ml/min inlet flow. The initial run showed a flow rate oscillating in the range 70-80ml/min, therefore the results are comparable.

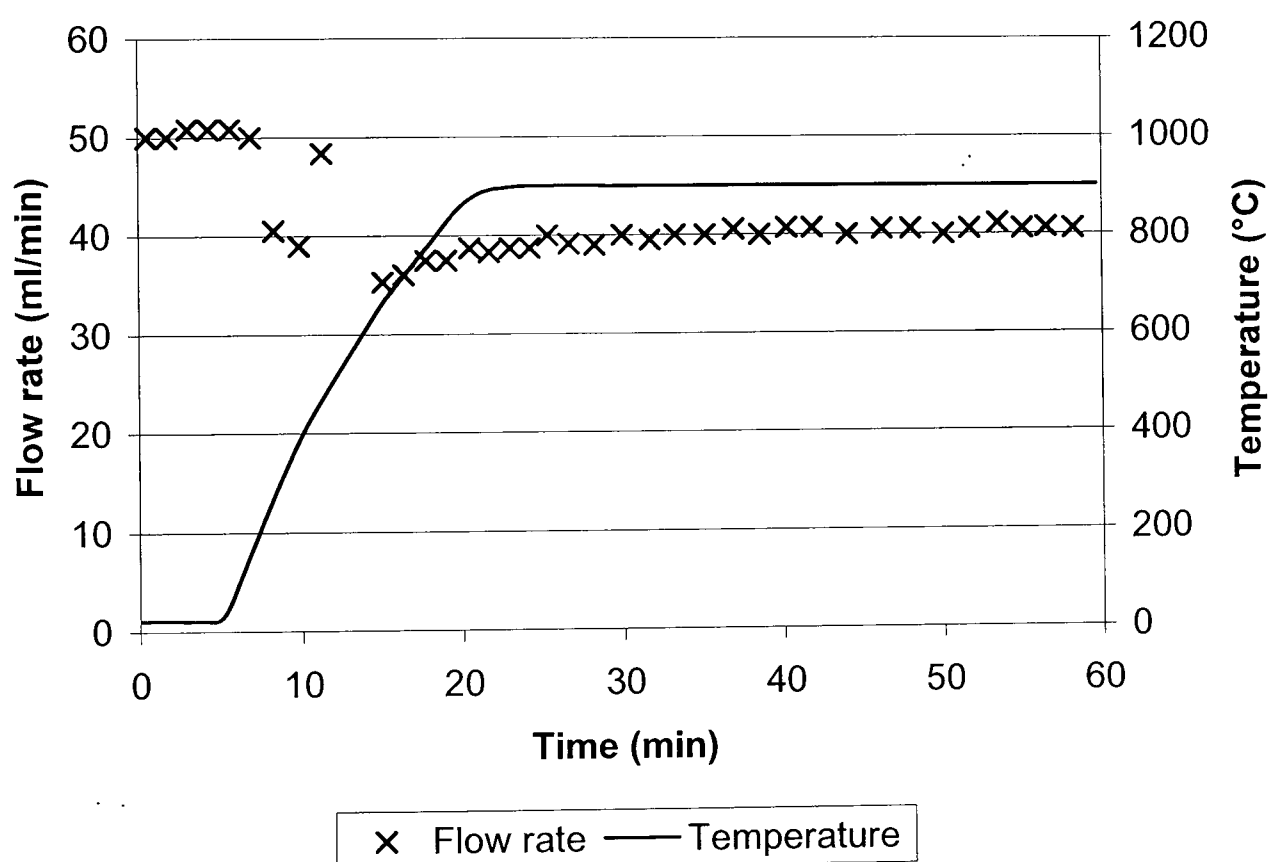


Figure 7.27: Timed flow results for gold foil gasket test. Values use bubble flow meter and are not averaged. Input flow is 50ml/min of 20% oxygen in helium at room temperature and pressure.

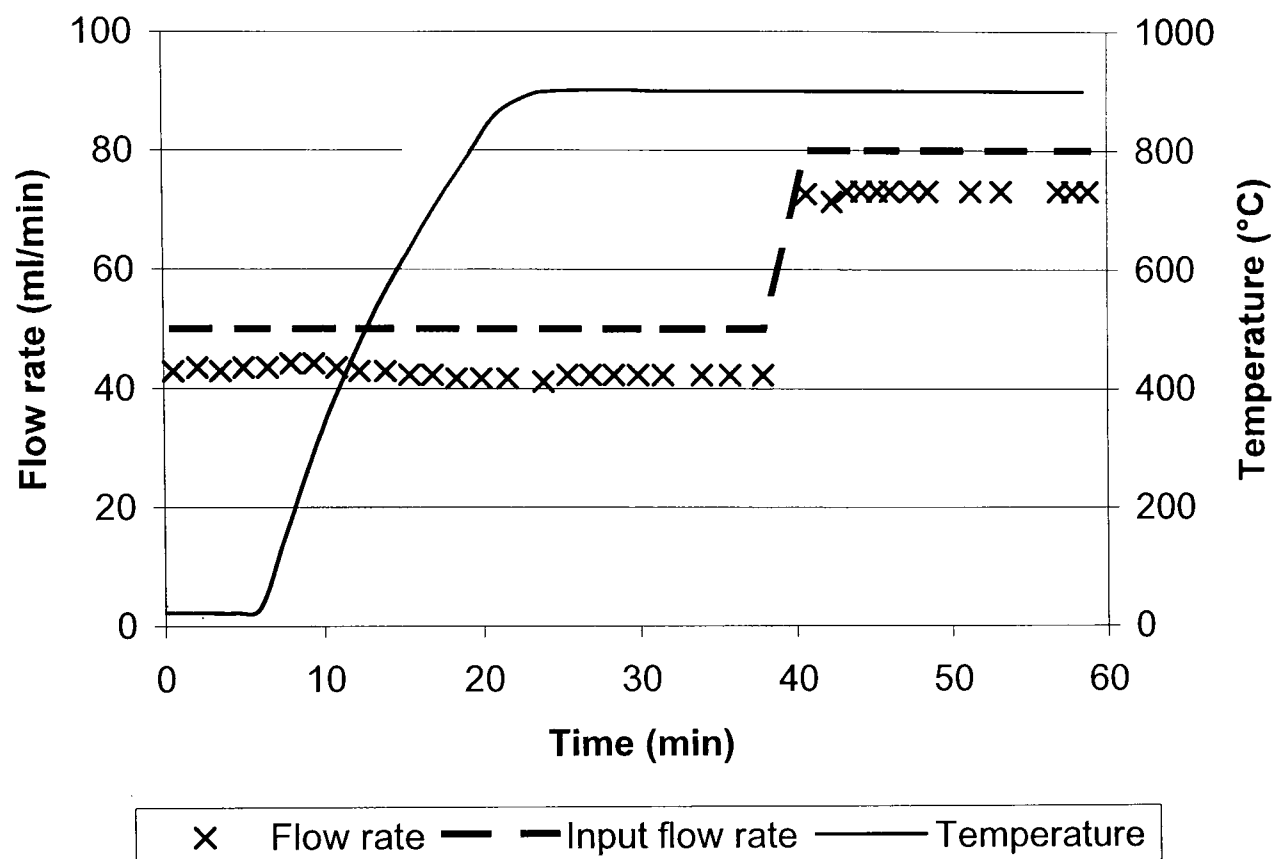


Figure 7.28: Timed flow results for gold foil gasket test 2. Values use bubble flow meter and are not averaged. Input flow is 20% oxygen in helium at room temperature and pressure. This test was carried out the day after that reported in Figure 7.27 with disassembly/reassembly of the equipment. Sacrificial Parafilm was therefore not present during the cold and heating phases.

The sealing solutions used here are not ideal, as the graphs show. The amount of leakage being seen is however considered acceptable. It is considered that, on the membrane permeate side, the pure helium inlet will be well mixed with the oxygen desorbing from the platinum surface. Therefore, the gas leaking will be of the same composition as that retained and passed to the oxygen analyser. Provided the analyser is calibrated according to the actual flow reaching it, the results obtained are still accurate.

7.8.5 Conclusions

The immediate conclusion of this work is that any of the seal types which combine graphite and gold are inferior in longevity to gold foil seals. Gold foil seals were shown to exhibit no decrease in sealing capability over two one hour experimental runs at 900°C. The next stage of testing was to test the use of gold foil seals with a YSZ disk to ensure that adequate sealing occurred when the full apparatus was used.

7.9 Gold foil/membrane sealing

7.9.1 Aim

The aim of this test was to show that gold foil gaskets would seal the YSZ/platinum membrane to the quartz membrane holder effectively.

7.9.2 Method

The membrane and holder halves were assembled together, with gold foil rings acting as gaskets and thin gold foil strips running between each gasket and the holder metal-work. The gold strips acted as the electrical connection between the external circuitry and each face of the membrane, via the gold gaskets. The membrane holder halves, gaskets and the membrane itself were held together by Parafilm during insertion into the furnace.

Once the rig was fully assembled, 80ml/min of 20% O₂ in He was passed through each side of the membrane holder and a "bubble" flow meter used to record the outlet flow rate. The rig was then heated to 900°C and the flow rate measurements repeated.

Finally, some short oxygen permeation tests involving various applied voltages and feed compositions were carried out to confirm that the rig was operating correctly, in terms of electrical connectivity and sealing. These were successful.

7.9.3 Results

The upper and lower membrane holder halves were each tested three times when cold and three times when at 900°C. A standard stopwatch was used to time the flow through the bubble flow meter. Since this stopwatch only increments in whole seconds, the midpoint of the possible value is quoted.

	Cold (Parafilmed)			900°C				
	Time for 50ml flow ($\pm 0.5s$)			Flow rate (ml/min)	Time for 50ml flow ($\pm 0.5s$)			Flow rate (ml/min)
Top half	38.5	38.5	37.5	78.6	39.5	39.5	39.5	75.9
Bottom half	37.5	37.5	37.5	80.0	38.5	38.5	39.5	77.3

Table 7.3: Gold foil/YSZ membrane sealing test results

The results in Table 7.3 show that the flow rate is only reduced by 2.7ml/min once

the Parafilm has burned off and the furnace has reached operating temperature. This small amount of leakage is acceptable.

7.10 Alumina adhesive testing

7.10.1 Aim

As an alternative to using expensive gold foil seals it was proposed that a high temperature adhesive could be used to bond together the YSZ pellet and the quartz membrane holder halves. The aim of this test was to determine if a leak-tight seal could be achieved with an adhesive and if the pellet could be separated cleanly from the membrane holders following an experimental run.

7.10.2 Method

A bead of high alumina adhesive was applied to the pellet mating surface of one quartz membrane holder and a YSZ pellet was applied to the holder. The assembly was placed on one half of the metal support and inserted into the furnace. The assembly was put through an adhesive baking cycle of 2 hours at 950°C, with a 5°C/min ramp up rate and natural cool down.

7.10.3 Results

Upon removal of the assembly from the furnace it was immediately clear that the quartz had failed during the baking process. Figures 7.29, 7.30 and 7.31 show the fractures. It would appear that differential thermal expansion of the alumina adhesive that had set inside the holder cavity caused the quartz to fracture multiple times.



Figure 7.29: Broken quartz following baking with alumina adhesive



Figure 7.30: Broken quartz following baking with alumina adhesive

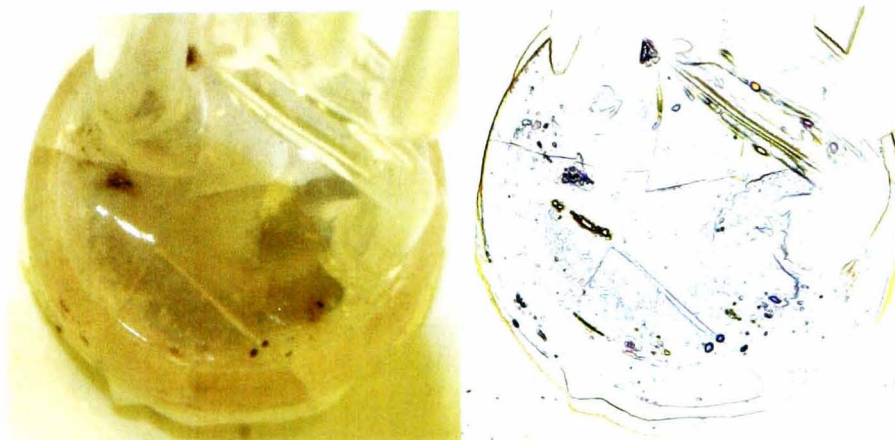


Figure 7.31: Underside of broken quartz membrane holder following baking with alumina adhesive. Left image shows photograph, right image is the result of edge detection of the same photograph using Corel PHOTO-PAINT, enhancing the detail of the cracks.

7.10.4 Conclusions

Because of differential thermal expansion of the alumina, quartz and YSZ, alumina adhesive is not suitable for bonding together this experimental apparatus. Gold foil seals still appear to be the best sealing solution for this apparatus.

7.11 Conclusions of commissioning work

This commissioning work verified the satisfactory operation of the experimental rig in advance of the main experimental programme. Gold foil was found to provide the best sealing of the YSZ pellet to the quartz membrane holder over an extended period of time. Graphite rings had an unacceptably short lifespan, including when sputter coated with gold, whilst differential thermal expansion caused alumina adhesive to fracture the quartzware.

The oxygen permeation flux at 750°C using a prototype membrane with a He–O₂ feed was found to be comparable to literature data. The total electrical resistance of the system with a He–O₂ feed was found to average 5.3Ω at 750°C and 9.9Ω at 700°C, which is within the expected range.

Stable currents could only be achieved at applied potentials of 3V and lower, therefore future tests should only be conducted in the 0-3V range. Electrolyte decomposition is indicated at potentials of 3V and above.

The first tests using He–O₂–SO₂ feeds, using the same prototype membrane as before at 700°C, showed a rapid decrease in oxygen permeation upon addition of SO₂ to the feed. A second run under the same conditions showed that the membrane had not recovered in the interim period.

It is clearly necessary to repeat these tests under more controlled conditions, using membranes with a documented history and under a wider range of temperatures. Chapter 8 presents this work.

The additional tests are carried out in the temperature range 700 – 900°C, and the apparatus assembly instruction can be found in Section 8.1.2. For all of these tests the membrane was brought up to the required temperature whilst synthetic air (20% O₂ in He) was flowed over both sides. Once at the required temperature, the gas flowed over each side of the membrane was changed and 1V was applied across the membrane. The permeate side received pure helium (100ml/min) while the feed side received 10% O₂ in helium for one hour, followed by 30% SO₂ and 10% O₂ in helium.

Chapter 8

Experimental work: results

Having gained operational experience with the prototype membrane and chosen gold foil as the best sealing material (Chapter 7), a more rigorous experimental programme was initiated to assess the performance of YSZ as an oxygen separation material for the sulphuric acid decomposition process. YSZ pellets with platinum electrodes were exposed to $\text{SO}_2\text{-O}_2\text{-He}$ mixtures at 800°C , 850°C and 900°C . Gold electrodes were also tested at 800°C . Two types of platinum ink were tested at 850°C in order to determine the effect of additives to the ink on performance. Finally, the effect of applied potential variation on membrane performance when exposed to SO_2 was investigated.

The membranes were analysed by XPS, XRD and IS and imaged using SEM.

8.1 SO_2 exposure at 900°C

This experiment took a fresh, unused YSZ pellet of the same specification as the prototype previously discussed and exposed it to an $\text{SO}_2\text{-O}_2\text{-He}$ feed for several hours whilst applying an external voltage. The oxygen permeating into the He permeate stream was measured, as was the current flowing. The membrane was analysed before and after SO_2 exposure to determine what changes had taken place, physically and electrically. This experiment provided more information on the effects of SO_2 exposure than the previous tests on the prototype, as the exact conditions to which the membrane was exposed were recorded.

8.1.1 Aims

The aim of this experiment was to document the gradual decrease in oxygen permeation through the pellet at a given applied voltage and to carry out analyses to show whether the changes causing the performance decrease were chemical, physical, electrical, or a combination of the three.

8.1.2 Method

The apparatus was assembled in the same fashion as for the prototype membrane tests.

Gold foil gaskets were cut from a foil sheet of thickness 0.025mm. Each gasket consists of a 25mm square of foil, with a circle of diameter 19mm cut out of the centre with a scalpel (Figure 7.25 shows examples). Two of these gaskets were used to seal the YSZ membrane to the two quartz holders (Figure 6.6), one either side. The end of a gold foil strip of approximately 3mm width and 20mm length was compressed between the gold gasket and the quartz holder such that the strip passed around the outside of the holder and could contact with the metal support, analogous to the position of the platinum wire in Figures 7.11 and 7.12. In order to assemble the quartz, gold gaskets and strips and the membrane into a single unit, the gold was first attached to the quartz using sticky tape. The membrane was sandwiched between the two quartz/gold assemblies and held together between the fingers. Parafilm was wrapped around the whole unit by a colleague such that the quartz, gold and membrane would remain aligned until assembly into the furnace. The sticky tape and Parafilm burns off during the furnace heating process.

Before insertion into the furnace, the electrical connection face of the metal support was sanded to remove the oxide layer laid down by previous tests and to ensure that a good electrical connection was made. The lower half of the metal support, along with the quartz/gold/membrane assembly, were carefully lowered into the vertical Carbolite tubular furnace. The legs of the support were inserted into a stand (Figure 6.7) placed below the furnace tube. The stand sat on a heatproof tile, which itself was placed on a height-adjustable stand, such that when everything was assembled the membrane was at the centre of the furnace. The top metal support was then lowered down into the furnace tube so that it sat on top of the quartz assembly. A second metal support "stand" was inserted into the legs of the upper half to provide compression of the assembly. Insulating wool was inserted into both ends of the furnace tube to reduce heat loss.

At this stage, crocodile clips were used to connect one leg of each metal support to the external electrical circuitry, which was wired as per Figure 6.3. The outlet of the quartzware was connected on the permeate side to a Servomex gas analyser via a straight 30cm section of quartz tube followed by Tygon tubing, whilst the feed side vented into the continuously operating fume hood. The feed to each side of the membrane was supplied by Tygon tubing linking the quartzware to the barbs on the rotameter outlets.

The test began by heating the furnace and apparatus to 700 °C, with a single feed of 20% O₂ and 80% He (total 75ml/min) from the feed rotameter bank split, by way of a T-piece in the Tygon tubing, to enter both inlets. There was therefore no oxygen partial pressure gradient across the membrane at this stage. Small voltages were applied to the membrane, with the resulting current measured and recorded. A similar pre-test was carried out on membranes used for the other tests described in this chapter to ensure that they offer broadly similar performance when new.

Following the pre-test, the furnace and apparatus was then heated to 900 °C. The T-piece in the Tygon tubing was removed and the tubing to the permeate side entry connected directly to the dedicated sweep gas helium rotameter. The tubing to the feed side entry was connected directly to the outlet barb of the SO₂-O₂-He rotameter bank. The permeate side was fed with 100ml/min of pure helium, whilst the feed side was fed with 50ml/min of 20% O₂ and 80% He. The external electrical circuit, which was previously open, was closed at this time and the power supply turned on. The applied voltage was maintained at 1.00V for one hour and the current flowing and permeate oxygen concentration was recorded regularly.

At this point the feed was changed to 50ml/min of 30% SO₂, 10% O₂ and 60% He. The voltage was maintained at 1.00V and the current flowing and permeate oxygen concentration continued to be recorded. At the end of the work day the feed side was flushed with pure helium under no applied voltage for 10 minutes before the gas flows were stopped and the furnace was switched off. At the start of the work day the apparatus was heated to 900 °C whilst pure helium was fed to both sides of the membrane. Once the temperature had stabilised the experiment carried on with the same feed composition and applied voltage as the previous day.

The feed side of the membrane was exposed to 50ml/min of 30% SO₂ and 10% O₂ in He for a total of 870 minutes over a three day period. The experiment was ended after 870 minutes as the recorded values were approaching steady state and it was considered that further exposure time would be of little interest.

8.1.3 Results

Experimental data

As described in the method section, the current flowing and permeate oxygen concentration achieved when an applied voltage of 1.00V was maintained was recorded throughout the experiment.

At the end of each day's SO₂ exposure period, the permeate oxygen concentration for zero applied voltage was recorded and this value was subtracted from the values recorded that day in order to produce a 'corrected' permeate oxygen concentration representing that oxygen which was transported through the membrane as a result of the applied voltage and not because of internal electronic transport. This, and the current recorded throughout the test, is shown in Figure 8.1.

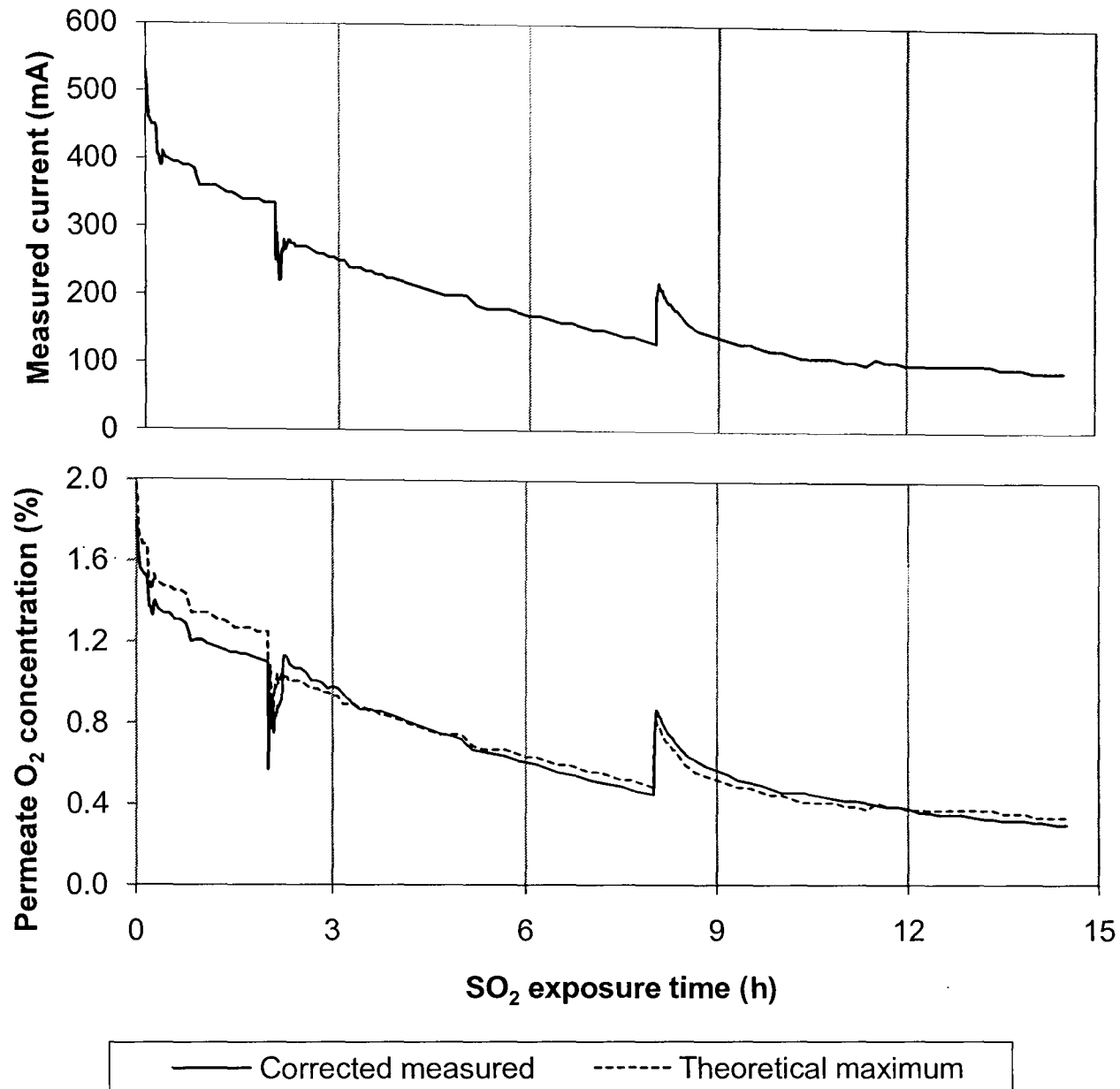


Figure 8.1: Current and permeate oxygen concentration vs. SO₂ exposure time during 900°C test

The abrupt changes at 2 and 8 hours signify the start and end points of each day's run. There were some electrical connection problems at the start of the second day, which manifest themselves as the low current values for 10 minutes starting at 2 hours. The theoretical and measured permeate O₂ concentrations are very similar during the second and third days. The expected O₂ concentration on the first day is however higher than the measured values by up to 0.2%. Since the second and third day values show no current leakage, the variation seen on the first day may have been caused by a temporary short circuit of some description, causing some current leakage.

The membrane electrodes were photographed when the rig was disassembled following the test. Figures 8.2 and 8.3 show the feed and permeate sides respectively. The

feed side of the membrane does not appear to have suffered any significant discoloration during the test. The permeate side by comparison was noticeably darker in appearance.

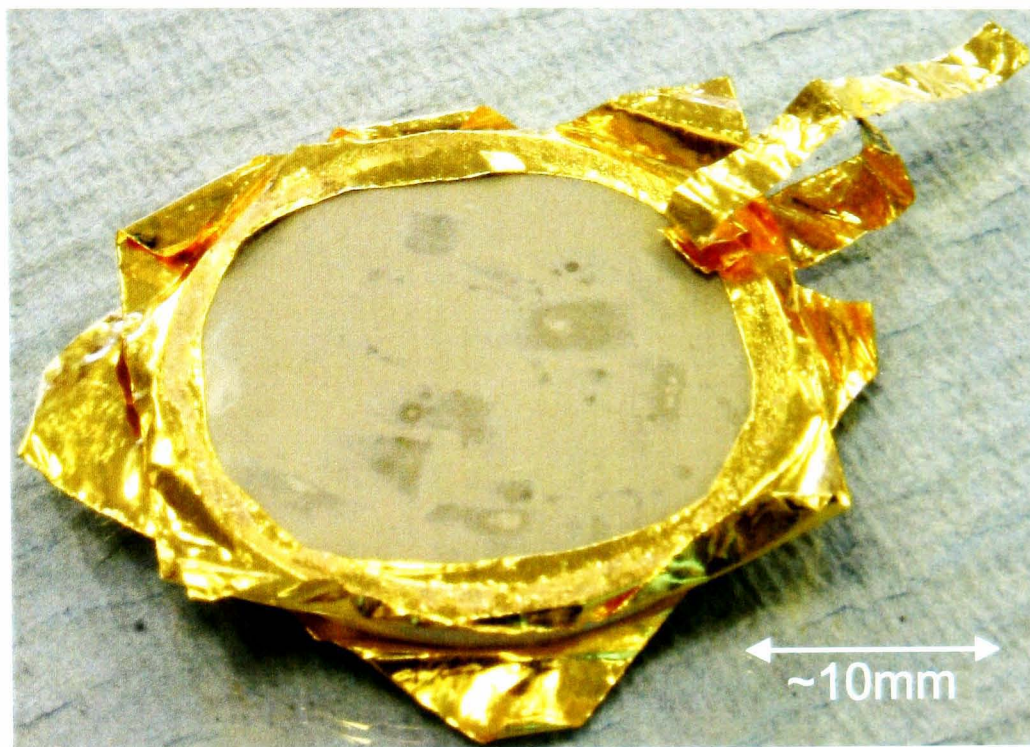


Figure 8.2: YSZ membrane feed side after exposure to SO₂ for 870 minutes at 900 °C

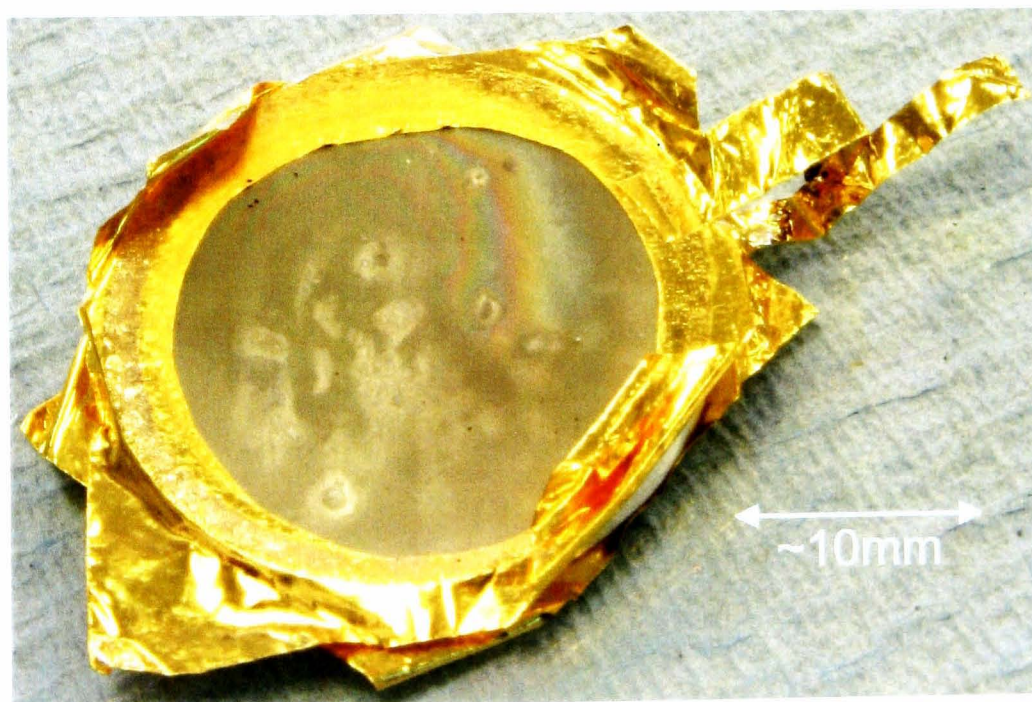


Figure 8.3: YSZ membrane feed side after membrane feed side exposure to SO₂ for 870 minutes at 900 °C

An interesting observation during the experimental run was fuming from the feed side

outlet. Allowing dampened universal indicator paper to contact the fumes produced a strongly acidic response. Furthermore, a brown liquid collected at the lowest point in the straight quartz cooling tube downstream of the feed side of the membrane. When exposed to air during disassembly, this liquid fumed strongly. These two observations suggest that SO₃ was produced in the feed side of the experimental apparatus. Upon contact with moist air, SO₃ reacts with H₂O to produce H₂SO₄ fumes. The platinum electrode may have catalysed the oxidation of SO₂ to SO₃. This would reduce the concentration of oxygen available at the feed side electrode surface for dissociation and transport through the membrane. However, as the current and oxygen flux are in agreement for most of the experiment, any reduction in the amount of O₂ available for transport has not affected the results.

XRD analysis

X-ray diffraction spectra were obtained for both sides of the pellet after exposure. The spectra were compared to those recorded for an unused pellet. Figure 8.5 shows the data for the permeate side of the membrane. Despite the discolouration of the electrode, it can be seen that there is no discernible change in the XRD spectrum following SO₂ exposure. In contrast, the feed side data shown in Figure 8.6 shows the presence of an additional peak at $2\theta \approx 28^\circ$. Searches for suitable ICDD cards found that this additional peak is most likely caused by the presence of a monoclinic zirconia phase. Figure 8.7 shows a section of the exposed feed side spectrum with ICDD card peaks superimposed for platinum, tetragonal zirconia and monoclinic zirconia.

By referring to the ZrO₂-Y₂O₃ phase diagram (Figure 8.4), it can be seen that the presence of a monoclinic zirconia phase in the sample at room temperature suggests that the cubic phase is no longer stabilised down to room temperature and in fact the yttria concentration has decreased sufficiently to allow a monoclinic/cubic solid solution to be formed as the pellet cooled to room temperature. The monoclinic/cubic solid solution is only favourable at room temperature at Y₂O₃ concentrations of approximately 1.5-6.5%. A reduction in the yttria concentration at the pellet surface would result in a reduction in lattice oxygen vacancies and hence reduce the oxygen transmission capacity of the pellet, should this layer become the rate limiting step. This could contribute to the performance decrease during SO₂ exposure.

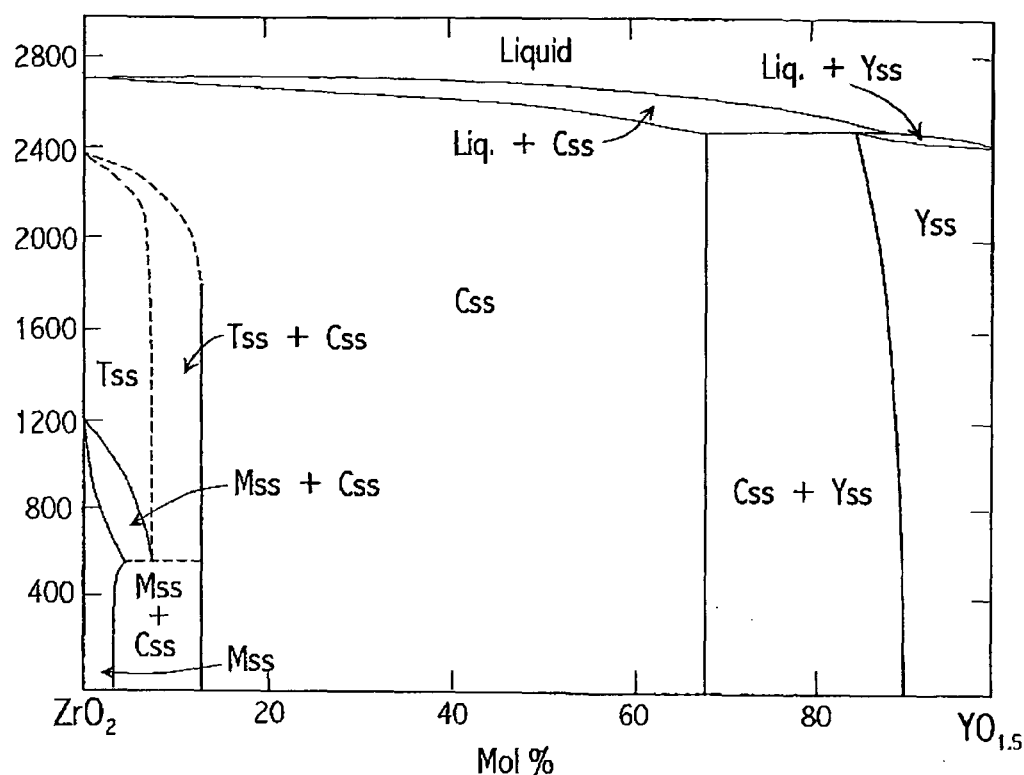


Figure 8.4: YSZ phase diagram (West 1999)

Impedance spectroscopy (IS) analysis

After the XRD analysis, the membrane was analysed using impedance spectroscopy. An AC voltage of 100mV was applied over a frequency range of 40Hz to 1MHz.

At room temperature and slightly elevated temperatures the membrane was too resistive to give accurate data. Instead, the membrane was heated directly to the highest temperature at which an impedance spectrum was recorded before the membrane was used, i.e. $\approx 369^\circ\text{C}$. After 75 minutes of heating the thermocouple stabilised at 371°C . Spectra taken every 10 minutes for 50 minutes showed no change, confirming the stabilisation.

Figure 8.8 summarises the data collected before and after the SO₂ exposure, using both Agilent and Solartron analysers. The Solartron analyser allowed data collection over a wider range and was used for further analyses. The before and after data from the Agilent, although at a limited number of temperatures, shows no significant change in bulk or grain boundary conductivity following SO₂ exposure. The values calculated by the Solartron spectrometer following the SO₂ exposure were at least an order of magnitude higher than those from the Agilent. The reason for this was unclear, but comparing before and after results from a single analyser showed little change following exposure.

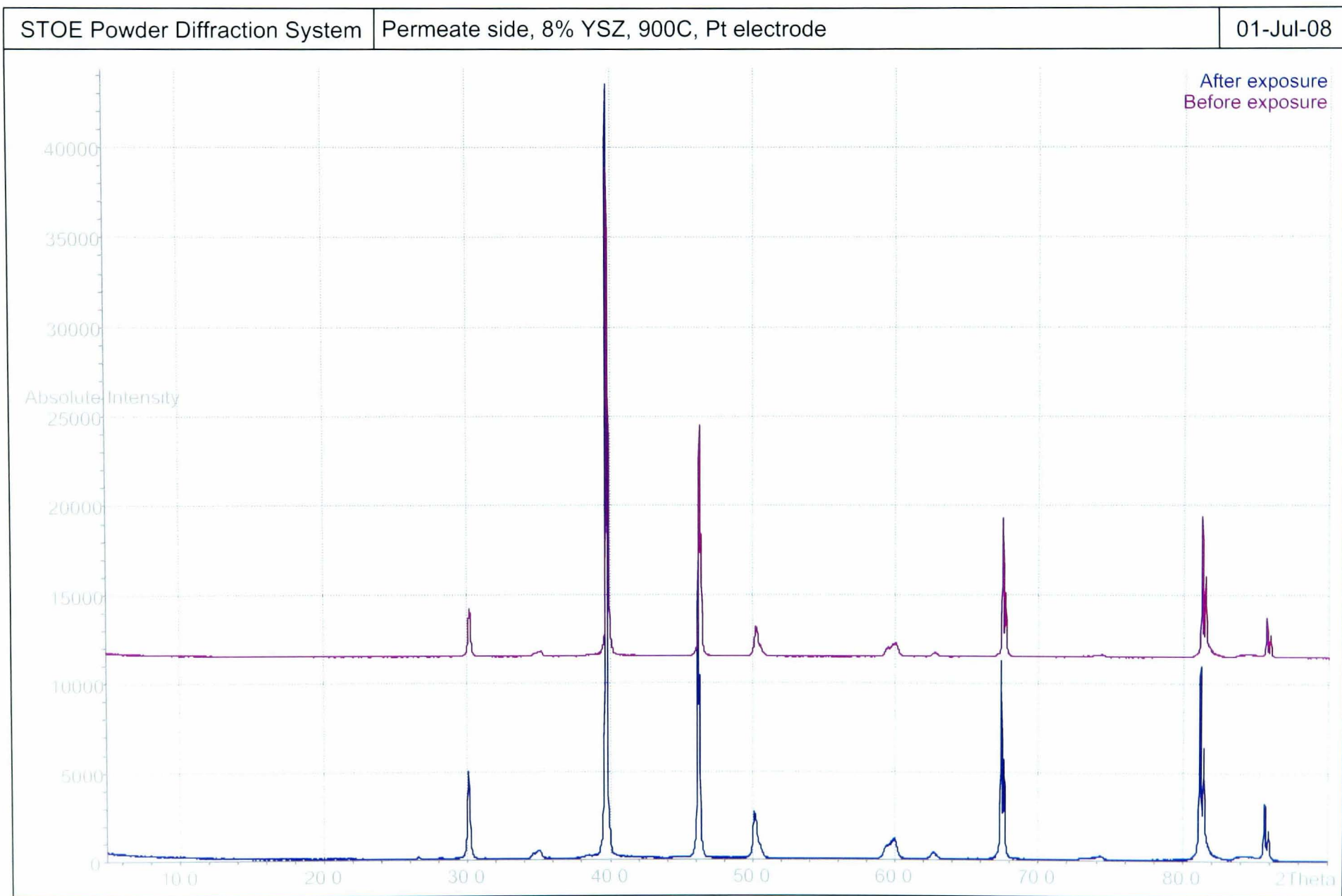


Figure 8.5: Pre- and post-SO₂ exposure XRD data for YSZ/Pt pellet, 900°C permeate side

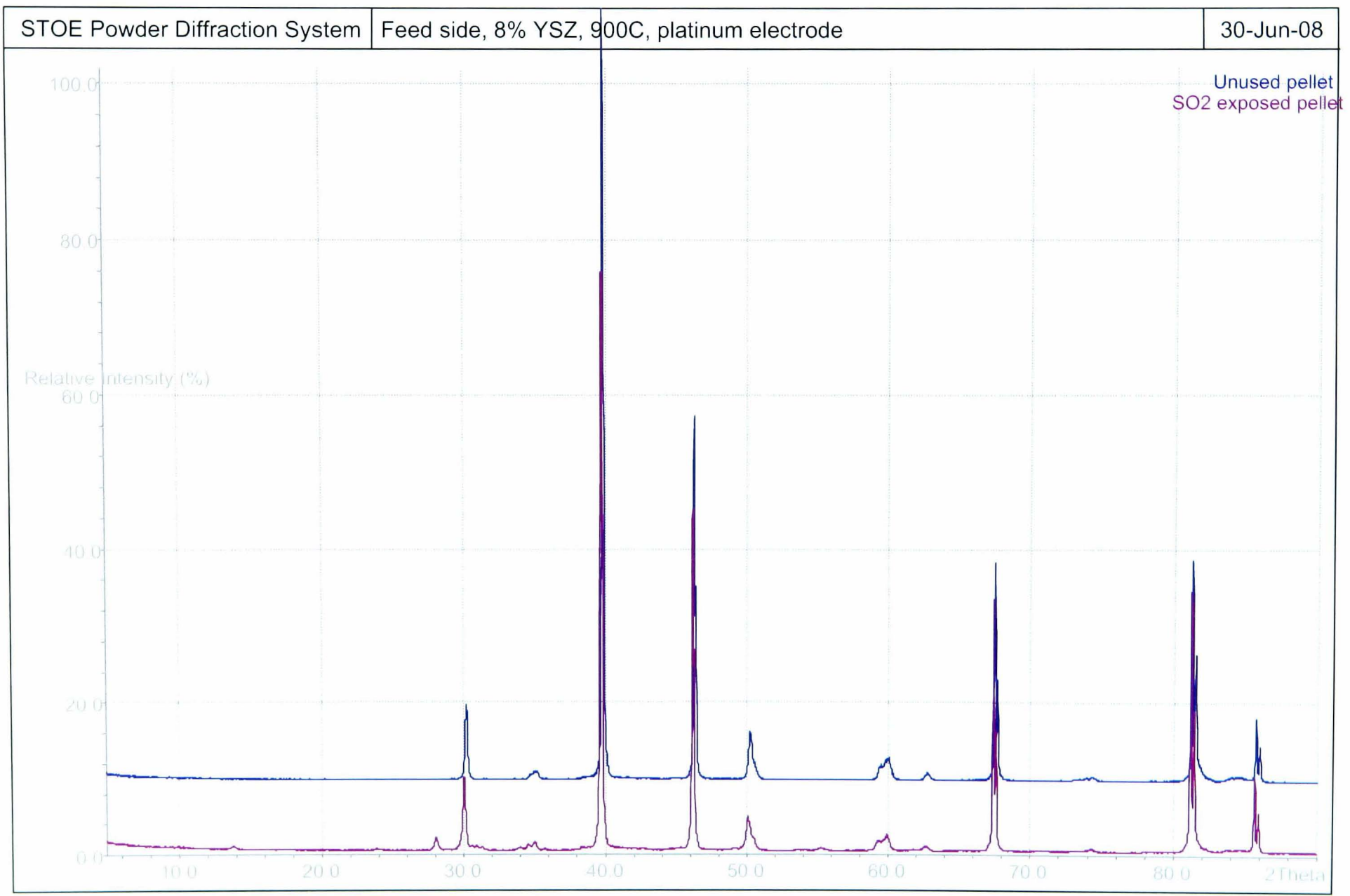


Figure 8.6: Pre- and post-SO₂ exposure XRD data for YSZ/Pt pellet, 900°C feed side

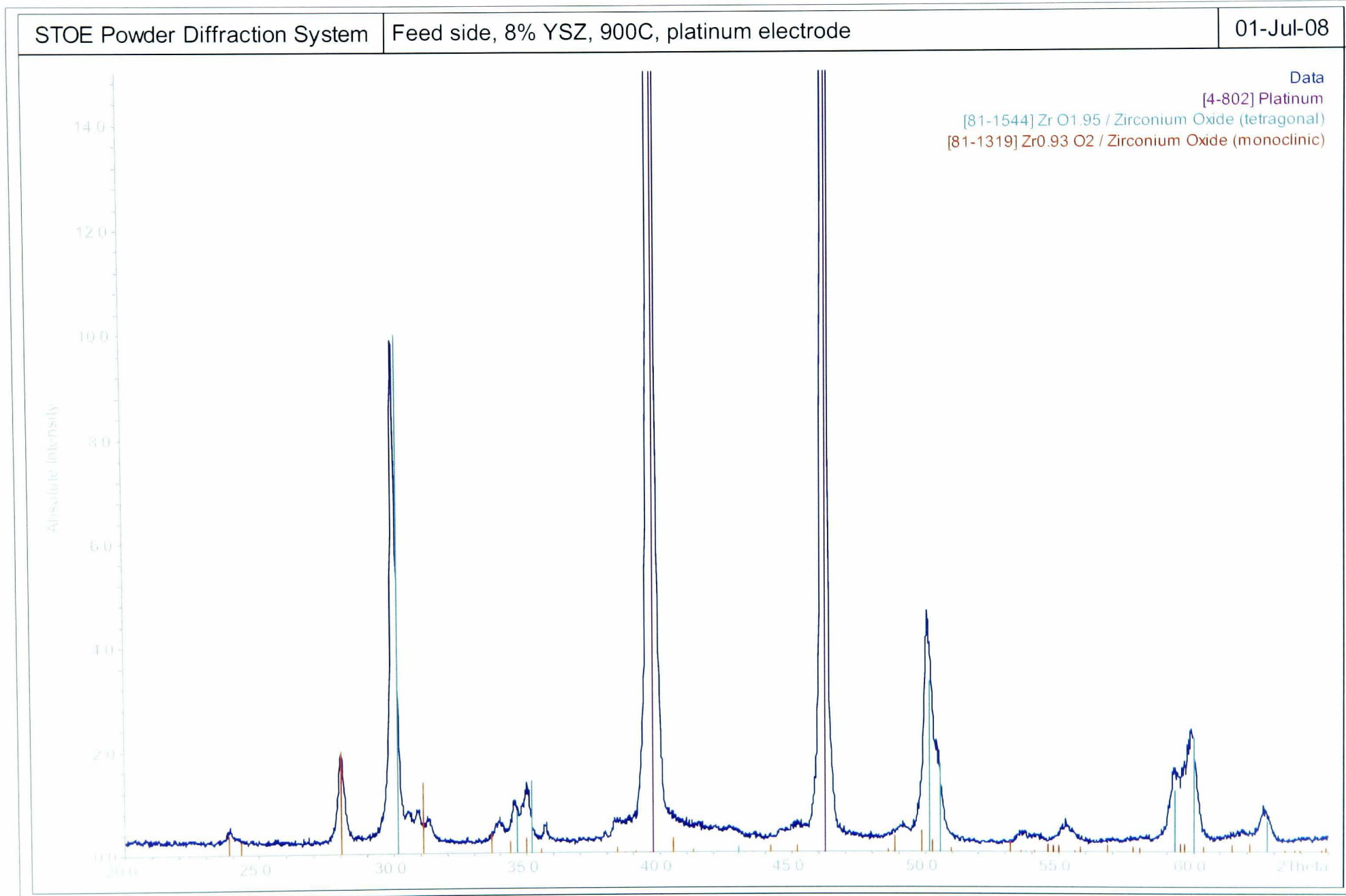


Figure 8.7: Partial post-SO₂ exposure XRD data for YSZ/Pt pellet, 900°C feed side

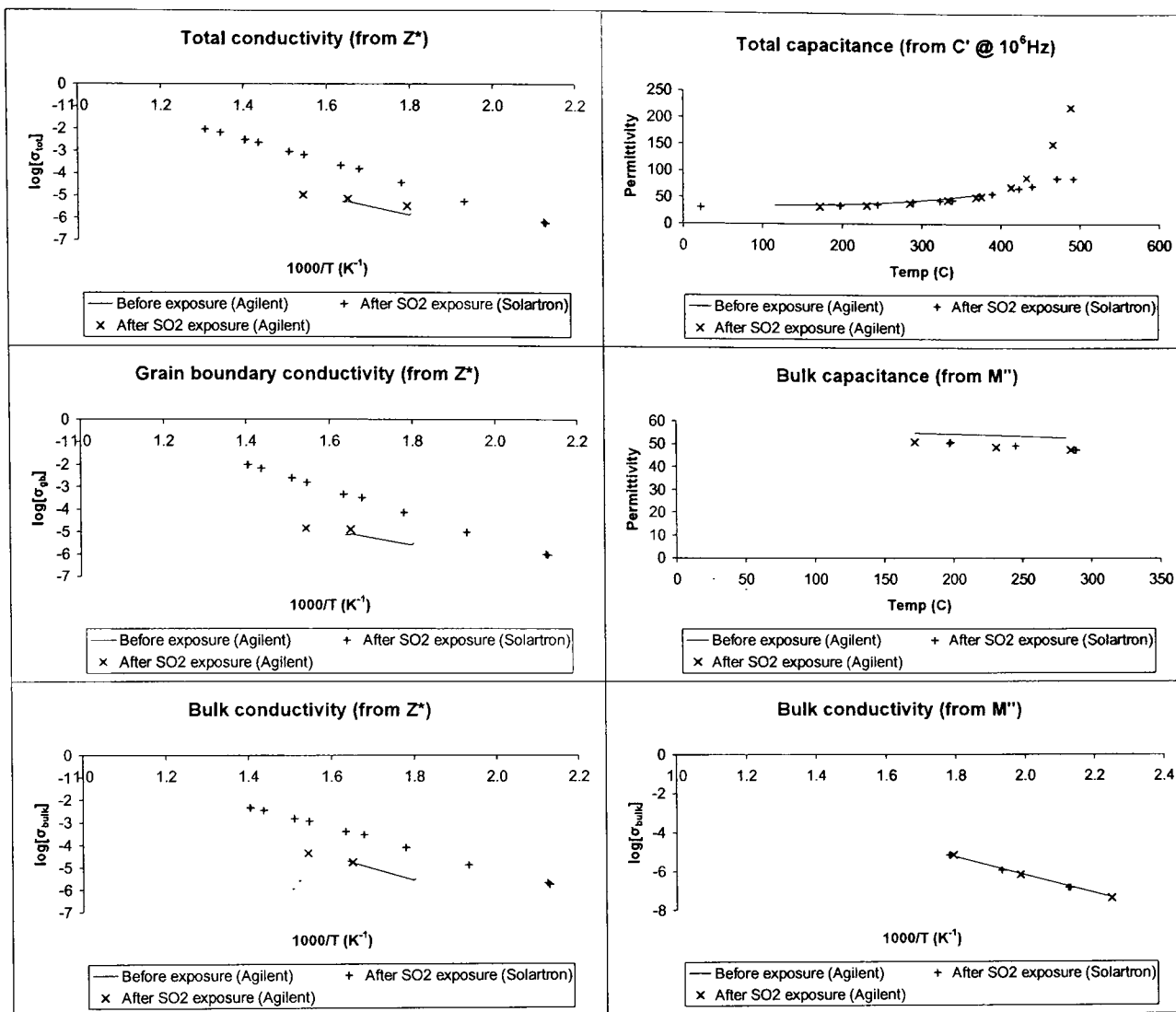


Figure 8.8: Summarised impedance spectroscopy for YSZ/Pt before/after 900 °C SO₂ exposure. Unused pellet was analysed using Agilent analyser over the frequency range 40Hz - 1MHz, whilst SO₂ exposed pellet was analysed using both the Agilent analyser (over the same frequency range) and the Solartron analyser over the range 0.1Hz - 1MHz.

Figure 8.9 shows a Z^* plot of the SO₂ exposed pellet at 245 °C. The bulk crystal response is the arc furthest to the left, with the response from the grain boundaries immediately to the right. The smooth transition from the grain boundary arc into the straight line of the electrode may hide an additional small response from, e.g. a surface layer. This would tie in with the appearance of an extra XRD peak. Higher temperature impedance spectroscopy would be more conclusive about the presence of a surface layer, since the bulk and grain boundary responses would be very small, because of their decreased resistance at higher temperatures.

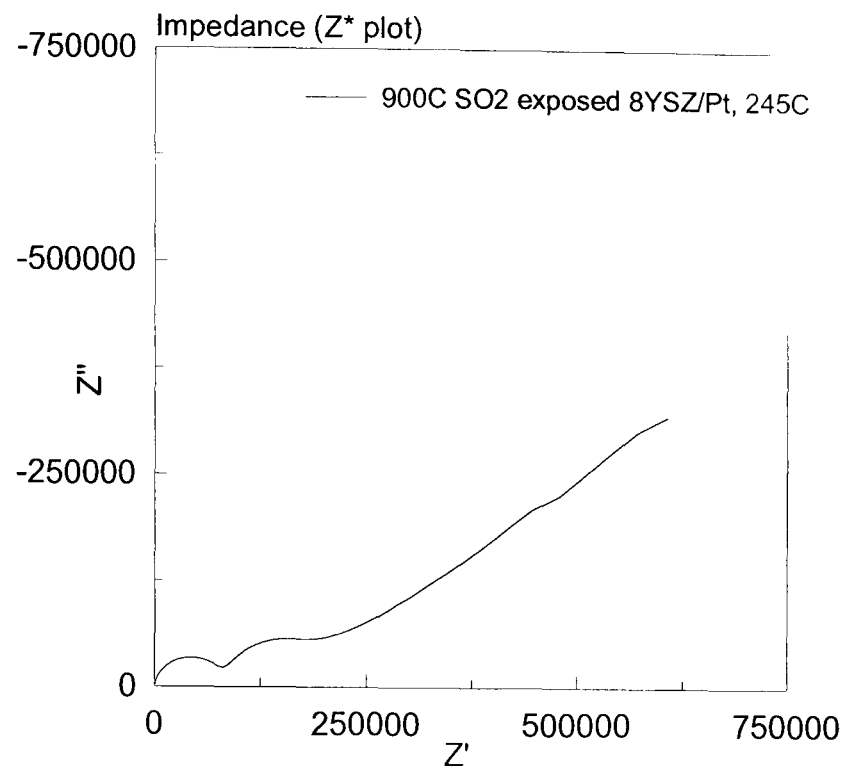


Figure 8.9: Z^* plot for YSZ/Pt at 245°C after SO₂ exposure at 900°C

8.1.4 Implications for experimental programme

The outcome of this experimental run raised a number of important points:

- Carrying out a run over a number of days introduced uncertainty into the results;
- Better recording of O₂ permeate concentration values at no applied voltage was required, in order to make accurate adjustments to the results;
- The platinum electrodes appeared to catalyse the SO₂ oxidation reaction, which is undesirable;
- The ceramic/electrode combination tested here suffered strongly decreased oxygen permeation performance such that after 14 hours under these conditions the oxygen flux was one sixth of the initial value.

In order to address these issues, the following action was taken for further experiments:

- Each run was carried out in one day - the furnace temperature was reduced to 800°C as this enabled the current and permeate oxygen concentrations to approach steady state in the time available;

- The external electrical circuit was opened periodically during each test - this allowed more accurate data analysis through the calculation of a permeate O₂ concentration under open circuit conditions;
- Gold electrodes were tested, to determine if they exhibit the same catalytic activity as platinum.

8.1.5 Conclusions

When exposed to 30% SO₂ and 10% O₂ at 900°C, a rapid decrease in permeate O₂ concentration was observed, with an accompanying decrease in current for a constant applied voltage of 1.00V. Current leakage (i.e. the deviation between the measured O₂ concentration and that expected for the measured current) was very low. Uncertainty was introduced into the test by having to conduct it over a number of days, hence the test was repeated at a lower temperature of 800°C (Section 8.3) where the current and permeate O₂ concentration reached steady state sufficiently quickly that the whole experiment could be conducted in one working day. Comparing the XRD and impedance spectroscopy carried out pre- and post-SO₂ exposure suggested that a surface layer may have been formed on the feed side membrane surface. The impedance spectroscopy also showed that there had not been a significant change in the bulk or grain boundary electrical conductivity of the membrane as a result of SO₂ exposure. In order to ascertain if this unchanged electrical conductivity meant that the membrane had “recovered” in the interim period, the membrane was tested a second time with an O₂–He feed to examine its performance.

8.2 Recovery test at 900°C

The impedance spectroscopy carried out post-SO₂ exposure at 900°C suggested that there had not been a significant change in the electrical properties of the membrane as a result of the SO₂ exposure. It was decided to measure the oxygen permeation and current flow through the same membrane at 900°C with a He-O₂ feed to determine if the pellet had in some way recovered, giving rise to the IS spectra similar to an unused pellet.

8.2.1 Aim

The aim of this test was to compare the oxygen permeation and current flow values recorded at the end of the SO₂ exposure test with those recorded subsequently with a He-O₂ feed, in order to determine if membrane performance recovery had occurred.

8.2.2 Method

The apparatus was assembled in the same manner as described previously. New gold seals were used and the pellet was inserted in the same orientation as that used for the previous SO₂ exposure tests.

Following the same procedure as the SO₂ exposure test, the apparatus was first heated to 700°C and allowed to stabilise at that temperature. With 20% O₂ in He being applied to both sides of the membrane, current measurements were then taken at applied voltages in the range 0-500mV, in order that these results could be compared to previous runs. The results were found to be similar.

The permeate side was then supplied with 100ml/min He and the feed side with 50ml/min of 10% O₂ in He and the furnace heated to 900°C. Once the apparatus stabilised at 900°C, the circuit was closed and 1V applied. The resulting permeate O₂ concentration and current flow was then recorded. The gas analyser automatically logged the O₂ concentration while the currents were recorded manually.

The circuit was periodically opened for two minutes in order to record the gas analyser O₂ concentration reading for no applied voltage. These values enabled the calculation of the corrected permeate O₂ concentration. The experiment was run for four hours then shut down. It was then run for a further three hours the following day.

8.2.3 Results

Experimental data

The measured and calculated permeate O₂ concentrations and the corresponding current values are presented in Figures 8.10 and 8.11 and for the first and second day of the run respectively.

The raw permeate oxygen concentration data shows that during the open circuit periods an O₂ concentration of approximately 0.8% was detected. This may be caused by some ionic conduction through the YSZ, effectively short-circuiting the process and

allowing some oxygen conduction despite the external electrical circuit being open. Additionally, there may be a small ingress of atmospheric oxygen through the gold seals. Having subtracted this open circuit reading from the closed circuit readings, the corrected O₂ concentrations are very close to that calculated from the measured currents. This indicates that electronic flow through the membrane is sufficiently low as to be neglected and hence leakage is the most likely cause of the "background" O₂ readings under open circuit conditions.

It can immediately be seen that there has been significant recovery in the performance of the membrane over the course of this run. The O₂ concentration increases from 0.29% to 1.10% over the four hours of the first day. The O₂ concentration at the start of the second day has decreased back to 1.00% and after three hours it has only increased to the same value seen at the end of the first day. Before the pellet was exposed to SO₂, the permeate O₂ concentration was 1.79%. There has therefore only been a partial recovery in performance.

The measured permeate O₂ concentration and that expected based on the measured current are very similar throughout this test. After approximately 25 minutes of the first day, there is a step change in the current flowing and an equivalent change in the permeate O₂ concentration. Both before and after this step change the permeate O₂ concentration is very close to the theoretical maximum achievable given the measured current flow. This indicates that the initial lower O₂ concentration was not caused by an electrical short circuit which rectified itself, as occurred during the first day of SO₂ exposure. It is more likely that the resistance of the external electrical circuit decreased suddenly. This may have been caused by an initial poor connection between the gold foil and the membrane holder metalwork.

Given that some recovery in the performance of the pellet was observed after this exposure to O₂-He mixtures, the XRD and IS analyses were repeated in order to identify any changes that may have occurred.

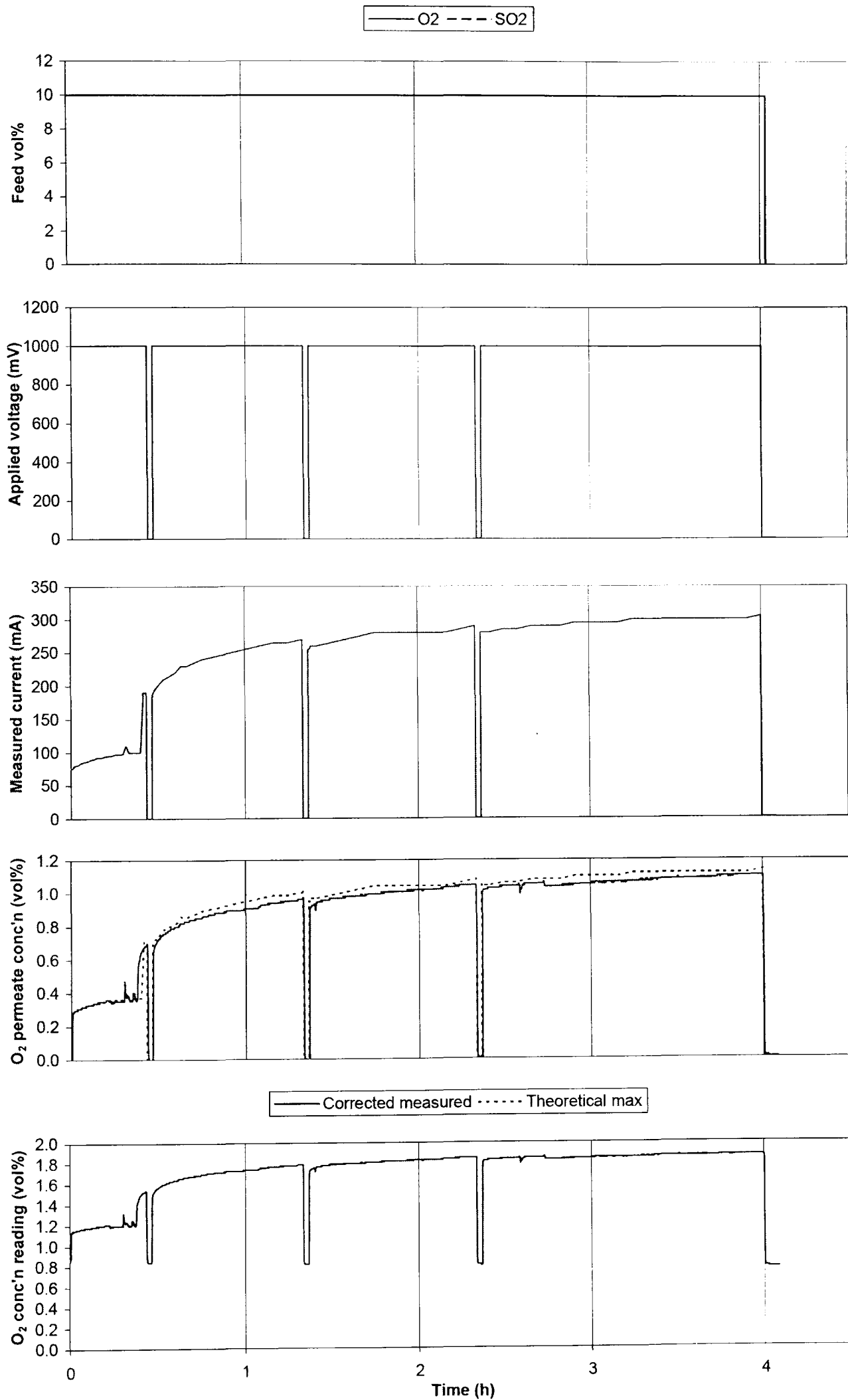


Figure 8.10: Retest of YSZ/Pt pellet previously exposed to SO₂ at 900°C with O₂ - day 1 results

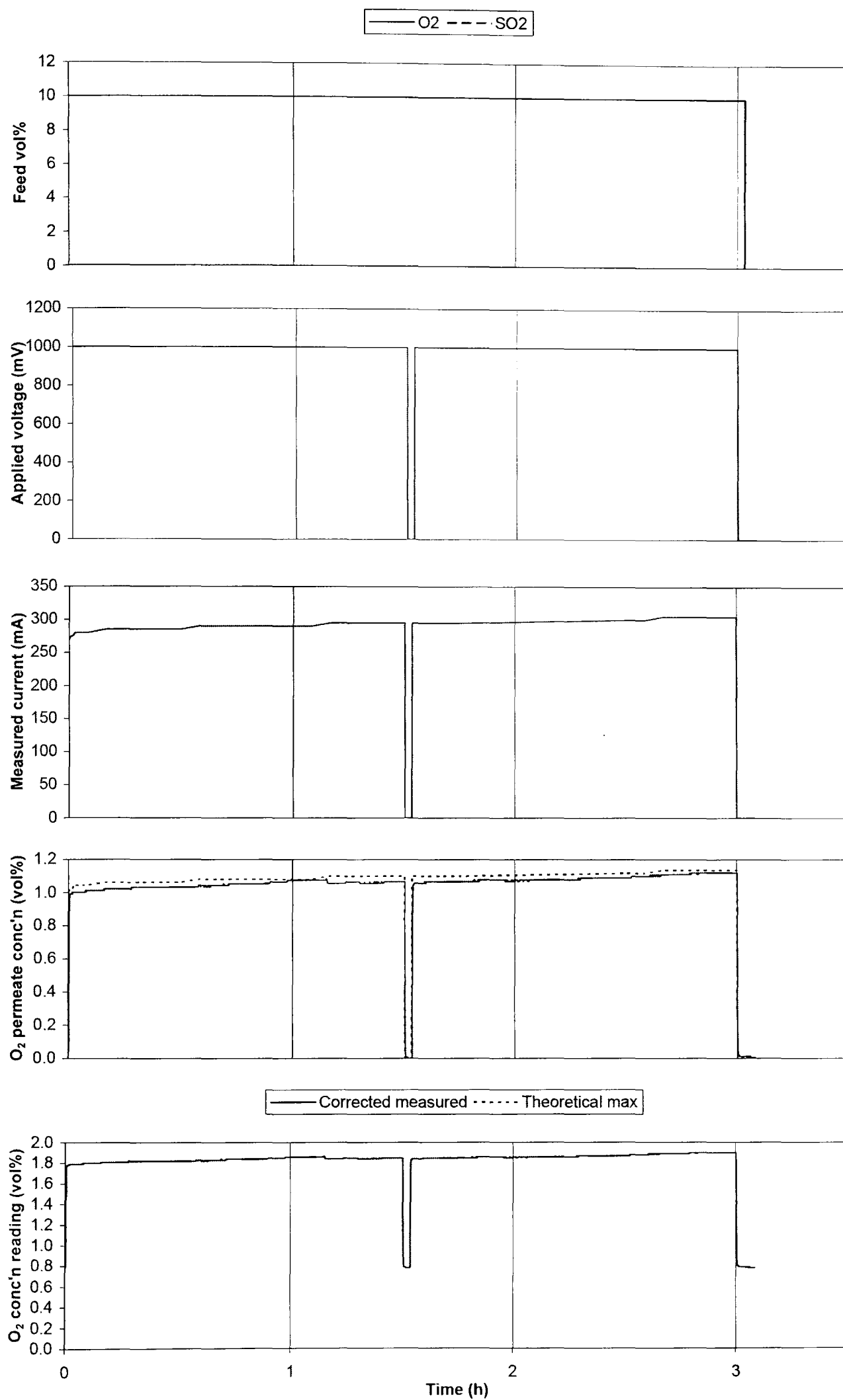


Figure 8.11: Retest of YSZ/Pt pellet previously exposed to SO₂ at 900°C with O₂ - day 2 results

XRD analysis

Figure 8.13 shows the XRD pattern before and after the recovery test. In fact, it can be seen that there have been no fundamental changes in the XRD pattern. The additional peak at $2\theta = 28^\circ$ has decreased in magnitude but is still present. The peaks associated with the YSZ have also decreased in magnitude, so this may present an analytical variation, perhaps caused by placing the pellet in the XRD chamber in such a way that a thicker section of platinum electrode was presented to the x-ray detector.

IS analysis

Using the Solartron analyser, with an AC voltage of 100mV and a frequency range of 0.1Hz to 1MHz, the pellet was tested before and after the recovery run at a range of temperatures. Figure 8.12 summarises these results.

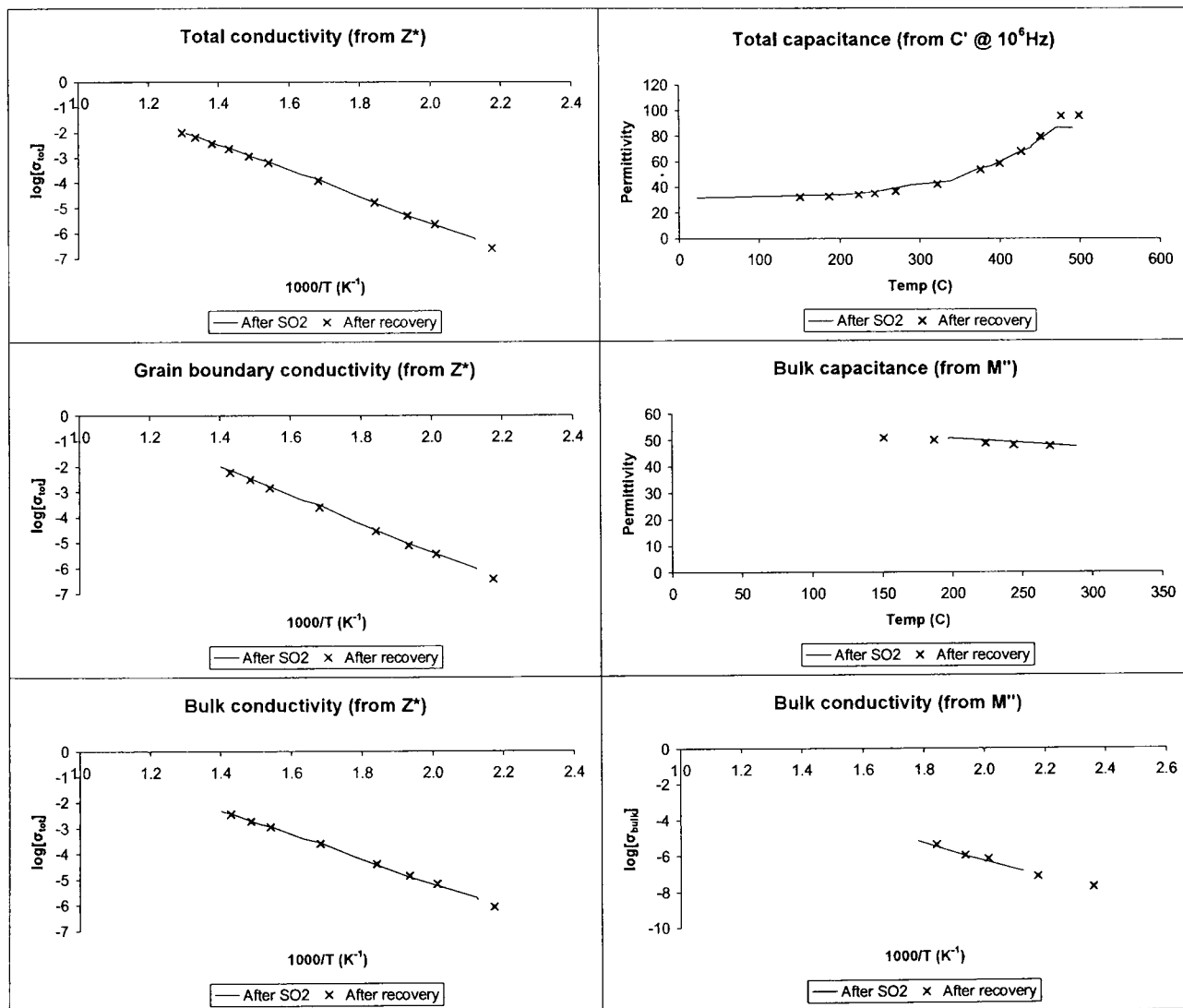


Figure 8.12: Summarised impedance spectroscopy for YSZ/Pt before/after 900°C O_2 "recovery" exposure

It can again be seen that there has been no significant change in bulk conductivity, grain boundary conductivity or total capacitance. Bulk capacitance appears to have slightly decreased. The bulk and grain boundary conductivities appear to be unrelated to the performance variations observed at 900°C.

8.2.4 Conclusions

Since the permeate O₂ concentration at the start of this test was equal to that recorded at the end of the previous SO₂ exposure test, it can be stated that whatever causes the increase in electrical resistance is a permanent effect. The effect can be reduced through exposure to a 10% O₂ in He atmosphere at 900°C, but the exposure produces little change in the bulk and grain boundary conductivity of the pellet or the XRD spectrum.

8.3 SO₂ exposure at 800°C (Pt and Au electrodes)

Having investigated the use of a YSZ pellet with Pt electrodes at 900°C in Sections 8.1 and 8.2, a similar membrane was then tested at 800°C in order that the relative longevity and ability to recover could be measured. The equilibrium studies in Chapter 2 indicated that zirconia would be more likely to suffer sulphation at lower temperatures. Because of this, it is expected that membranes exposed to SO₂ at 800°C will suffer a greater percentage decrease in O₂ permeation performance, provided the reaction rates are sufficiently fast to be neglected.

In addition, an identical YSZ pellet (pressed and sintered at the same time as the YSZ/Pt pellet) but with gold electrodes instead of platinum was tested to compare the O₂ permeation performance and to determine if gold electrodes promoted the same catalytic activity seen with platinum electrodes which caused SO₃ to be produced from the SO₂-O₂ feed.

8.3.1 Aim

The first aim of this test was to measure the change in performance with time of an YSZ/Pt membrane when exposed to SO₂-O₂-He and O₂-He mixtures at 800°C. This could then be compared to the data recorded at 900°C.

The second aim of this test was to determine if gold electrodes have the same performance as platinum electrodes in terms of initial permeate O₂ concentration and

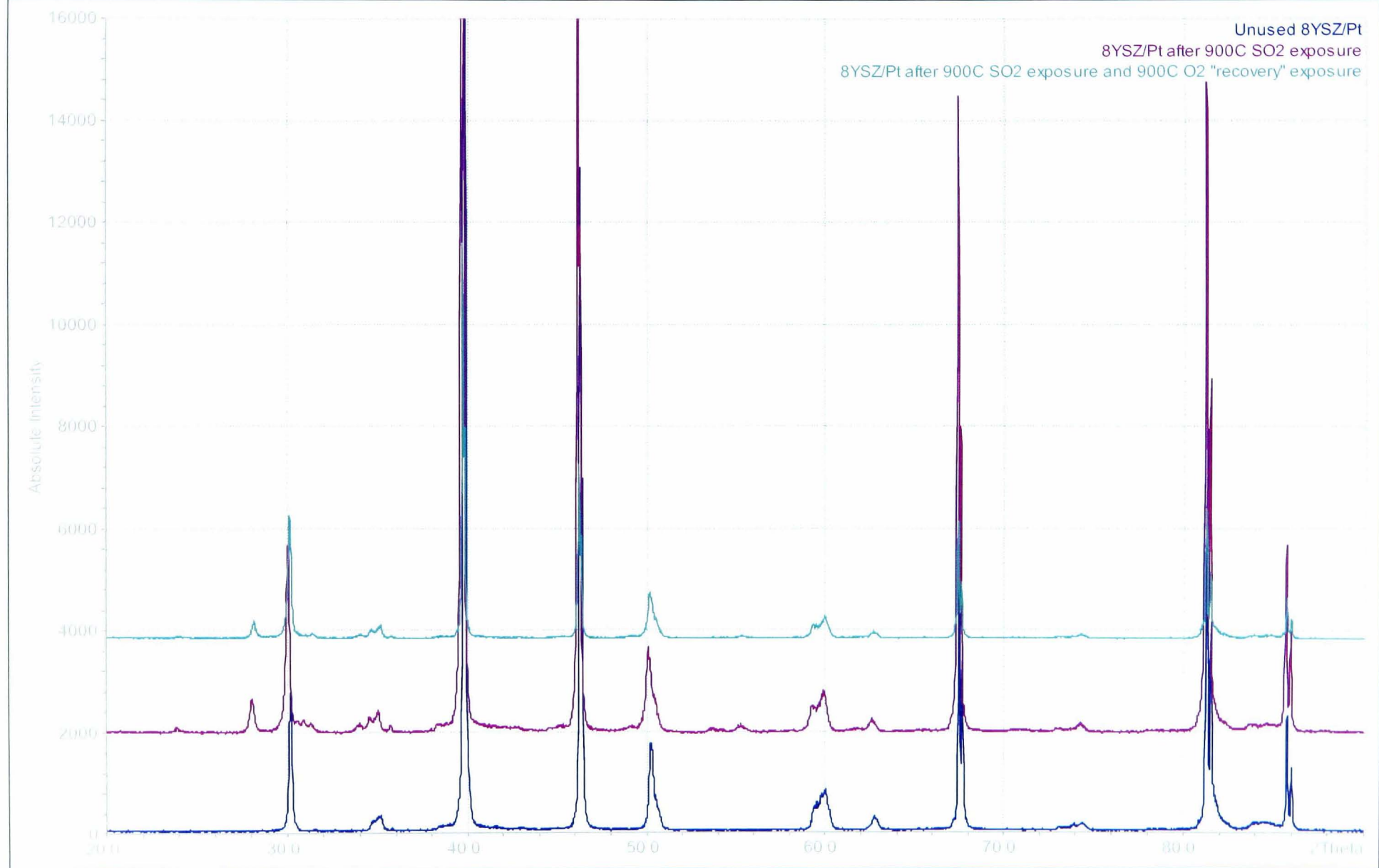


Figure 8.13: XRD data for unused YSZ/Pt membrane, after 900°C SO₂ exposure and after 900°C O₂ exposure

reduction in O₂ transport with time and SO₂ exposure.

8.3.2 Method

The method employed was identical to that used for the 900°C run, as described in Section 8.1.2, except that the furnace operating temperature was 800°C not 900°C.

Once at 800°C, with 1V being applied across the electroded faces, the feed side was supplied with 10% O₂ in He (total 50ml/min) for one hour. The feed was then changed to 30% SO₂ and 10% O₂ in He (total 50ml/min) for two hours. Between 60 and 90 minutes into this two hour SO₂ exposure period the electrical circuit was opened. This was carried out in order to determine if any increase in the O₂ permeate concentration occurred after a "rest" period of no externally applied voltage. Following the two hour SO₂ exposure period, the feed changed to 10% O₂ in He (total 50ml/min) for one hour, in order to replicate the O₂-He recovery test carried out on the 900°C membrane. Finally, the feed reverted to 30% SO₂ and 10% O₂ in He (total 50ml/min) for one additional hour, before the experiment was ended.

8.3.3 Results

Experimental data

The operating parameters during the run and the resulting measurements are all presented in Figure 8.14 for the YSZ/Pt membrane and Figure 8.15 for the YSZ/Au. Additionally, Table 8.1 shows some of the key comparison data between the platinum and gold electroded membranes.

Between 2.0 and 2.5 hours into the run, SO₂ and O₂ were being supplied to the membrane feed side whilst the electrical circuit was open. No recovery in membrane O₂ permeation performance was observed as a result of this open circuit period for either membrane. That the O₂ concentrations before and after the open circuit period describe a similar path suggests that the degradation in performance is independent of external voltage application or amount of O₂ permeating. A similar result can be seen for the one hour "recovery" period where an O₂-He feed was supplied. Within five minutes of reapplying the SO₂-O₂-He feed, the permeate O₂ concentration decreases to that which, extrapolating the pre-recovery values, would be expected at that time. This suggests that replacing the SO₂-O₂-He feed with an O₂-He feed does not extend the membrane life but may merely mask a continuing decrease in performance.

It can be seen from the ratios at the bottom of Table 8.1 that the gold electroded YSZ has a greater decrease in O₂ permeation over the course of the run compared to the platinum electroded membrane. Interestingly, the ratio of initial to final permeate O₂ concentrations for the 900°C YSZ/Pt SO₂ exposure test was measured as 5.97 (after 14.5 hours of SO₂ exposure), almost the same as that seen with a similar membrane after three hours of SO₂ exposure at 800°C.

Additionally, the YSZ/Au only “recovers” by 18% during the one hour O₂–He feed period, compared to the 88% O₂ permeation increase in the YSZ/Pt membrane. By way of comparison, the O₂ permeation of the YSZ/Pt membrane exposed to SO₂ at 900°C increased by 316% over the first hour of the recovery test described in Section 8.2.

A qualitative observation was the continued emission of fumes from the feed side vent when the YSZ/Au membrane was being tested. A similar quantity of brown liquid collected in the quartz cooling tube during the YSZ/Au run as during the YSZ/Pt run. This suggests that gold catalyses the SO₂ oxidation reaction in the same way as platinum and hence gold electrodes cannot be used as a means of mitigating this effect.

Permeate O ₂ concentration (%) Measurement point	Electrode	
	Pt	Au
Initial	1.25	1.13
After 1h O ₂ –He feed	1.14	1.07
After 10m SO ₂ –O ₂ –He feed	0.49	0.54
After 2h SO ₂ –O ₂ –He feed	0.26	0.17
After further 1h O ₂ –He feed	0.49	0.20
After final 1h SO ₂ –O ₂ –He feed	0.21	0.12
Ratio after:before further 1h O ₂ –He	1.88	1.18
Ratio initial:final	5.95	9.42

Table 8.1: Comparison of key results at 800°C for YSZ membranes with platinum or gold electrodes

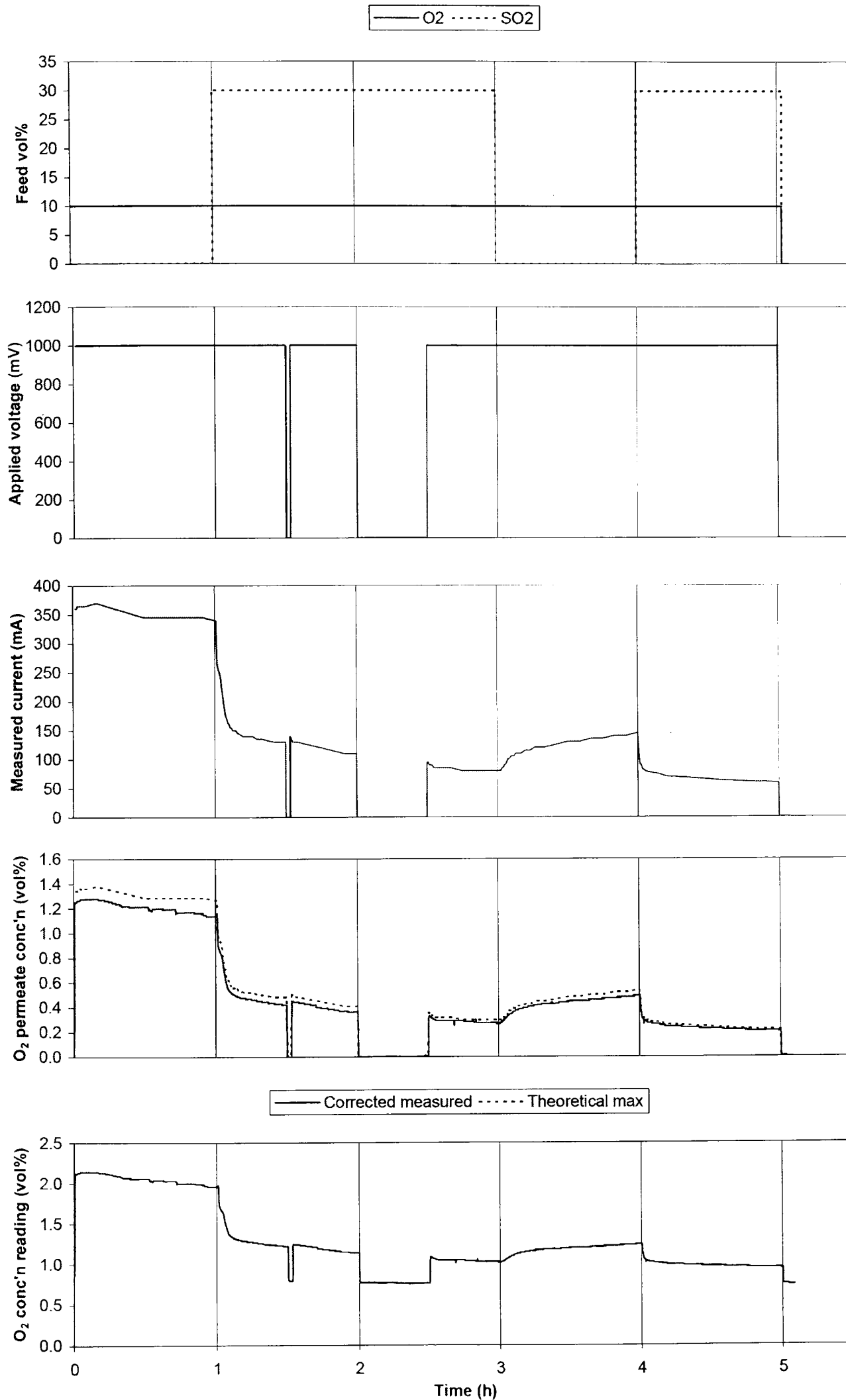


Figure 8.14: Experimental data for exposure of YSZ/Pt pellet to SO₂ and O₂ at 800°C

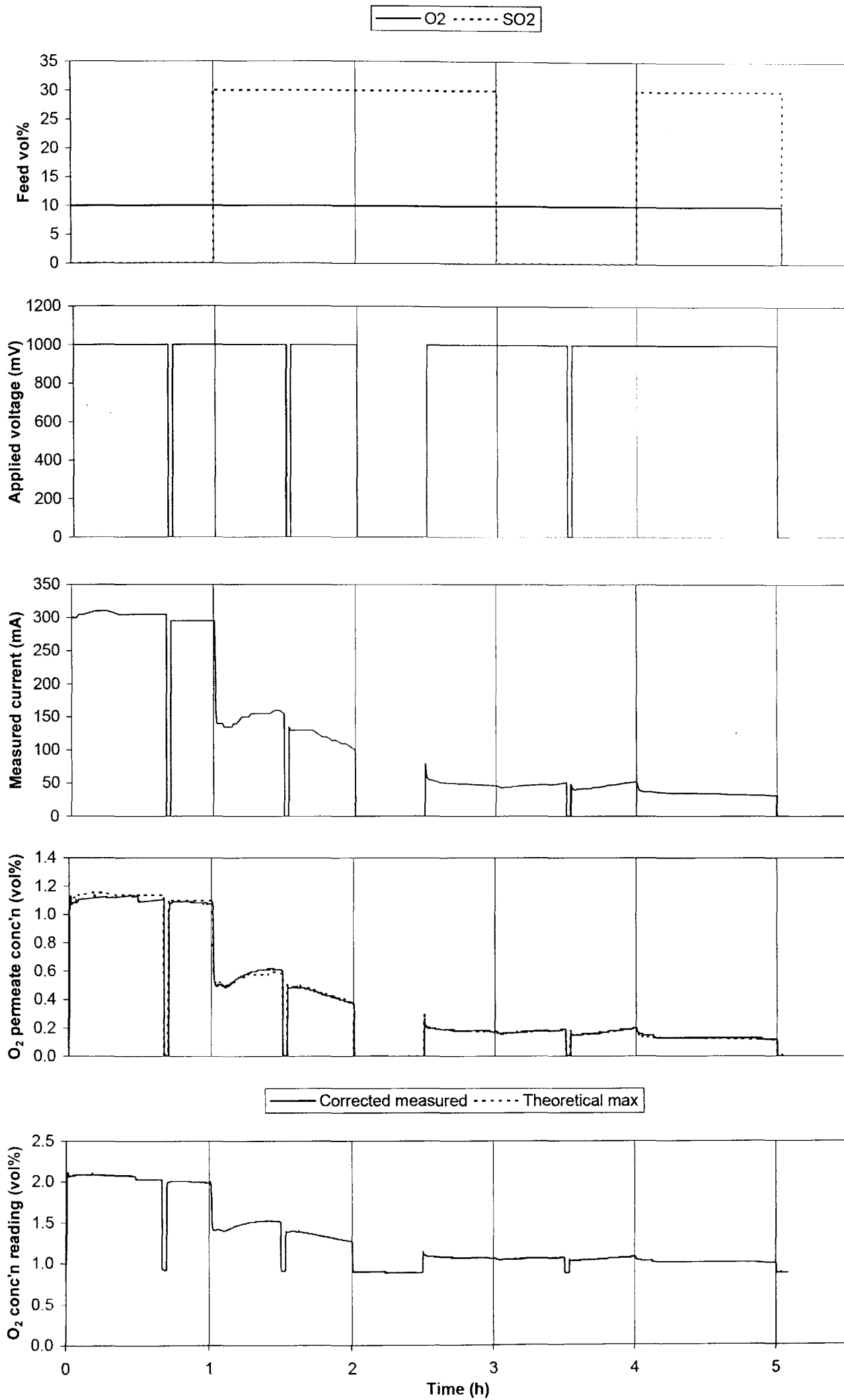


Figure 8.15: Experimental data for exposure of YSZ/Au pellet to SO₂ and O₂ at 800°C

XRD analysis

Figures 8.16 and 8.17 show XRD data for the YSZ/Pt and YSZ/Au experiments at 800 °C respectively. These XRD results are interesting in the way that they vary from those recorded following the SO₂ exposure of a YSZ/Pt pellet at 900 °C (see Section 8.1.3). In that test, the appearance of an extra peak on the SO₂ exposed side of the pellet suggested that a layer of monoclinic YSZ may have developed, reducing the O₂ flux and increasing electrical resistance. Although the same resistance increase and O₂ flux decrease was observed in these 800 °C tests, that extra peak at around $2\theta = 28^\circ$ did not appear on the feed side. Instead, the $2\theta = 28^\circ$ peak appeared on the *permeate* side of the gold electroded pellet and did not appear at all on the platinum pellet, with a peak appearing instead at around $2\theta = 45^\circ$ on *both* sides of the pellet. The peak at $2\theta = 45^\circ$ could not be matched to an ICDD data card for any substance containing solely one or more of Pt, Y, Zr, O and/or S and hence remains unidentified. That a peak at $2\theta = 28^\circ$ did not appear on the SO₂ exposed face of these pellets suggests that this may not be indicative of the cause of the reduction in O₂ transport across the pellet and related increase in electrical resistance. Alternatively, the peak may have been present but masked by the presentation of a thicker area of platinum to the x-ray detector.

IS analysis

Impedance spectroscopy was carried out on the pellets before and after exposure, using a Solartron analyser set to 100mV AC voltage and frequencies between 0.1Hz and 1MHz. At lower temperatures some of the lower frequency data was invalid or noisy and was removed from the data file.

Figure 8.18 summarises the before and after results for the YSZ/Pt. The bulk capacitance increased after SO₂ exposure, although the increase is not a significant amount. The bulk conductivity, as measured on the Z^* plots at each temperature, changes gradient such that the conductivity is lower at low temperatures and higher at high temperatures. This change is not however replicated in the bulk conductivity values calculated from the peak values of the Debye peaks in the M'' spectroscopic plots. The latter set of calculations show no change in bulk conductivity after SO₂ exposure of the pellet. It is therefore considered that the SO₂ exposure has not affected the bulk or grain boundary conductivity of this pellet.

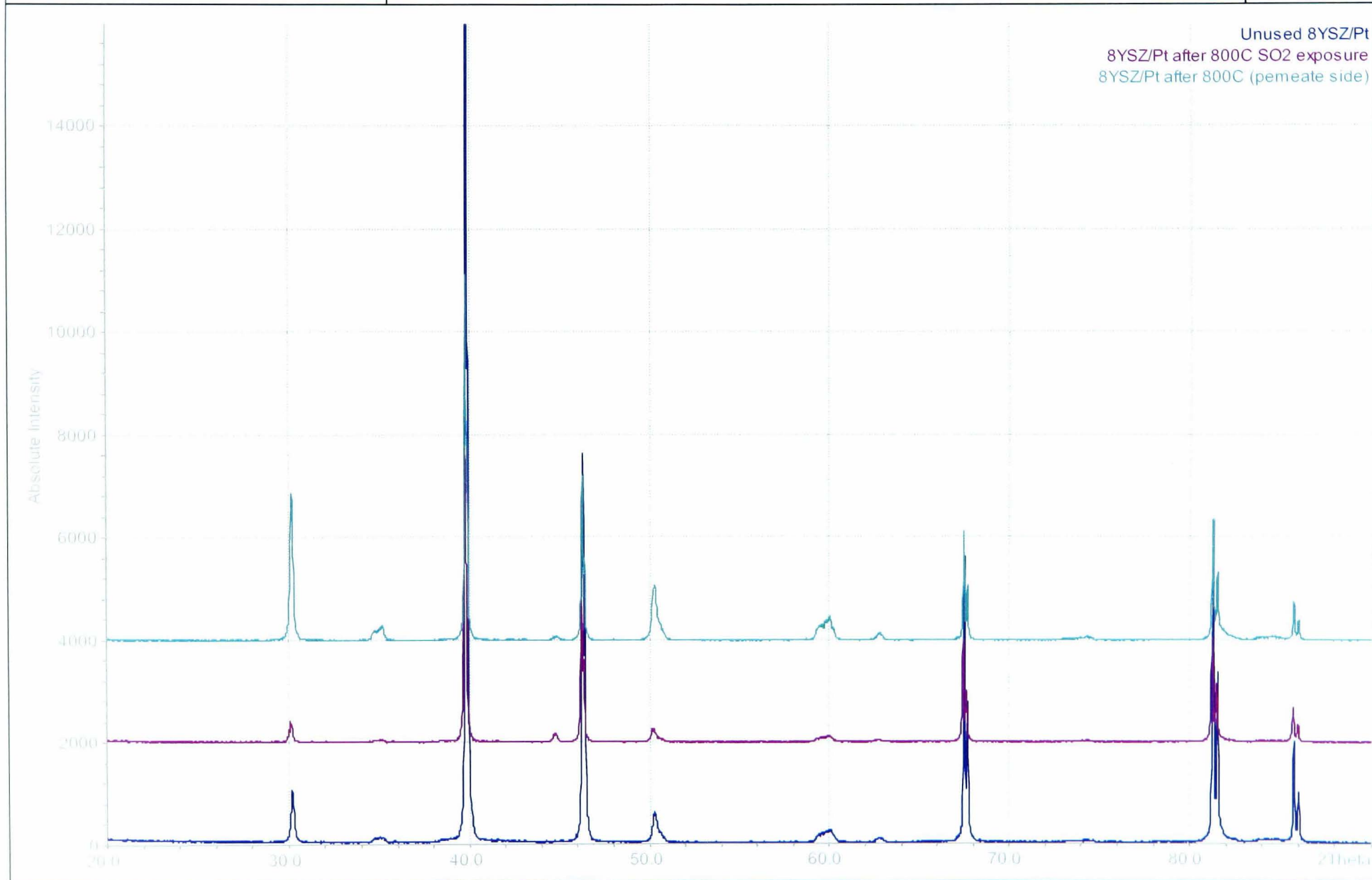


Figure 8.16: Before and after XRD data for YSZ/Pt membrane, 800°C SO₂ exposure

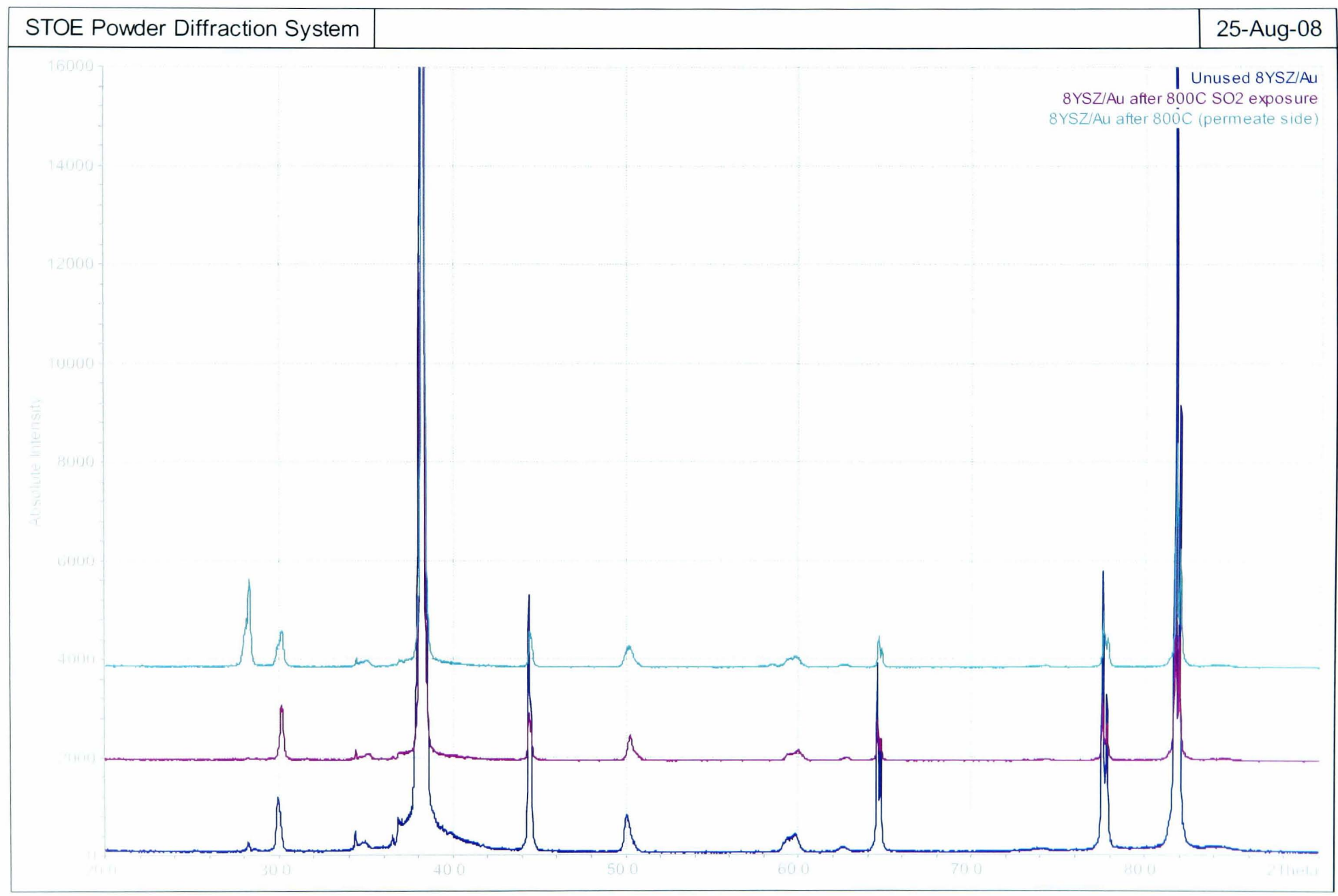


Figure 8.17: Before and after XRD data for YSZ/Au membrane, 800°C SO₂ exposure

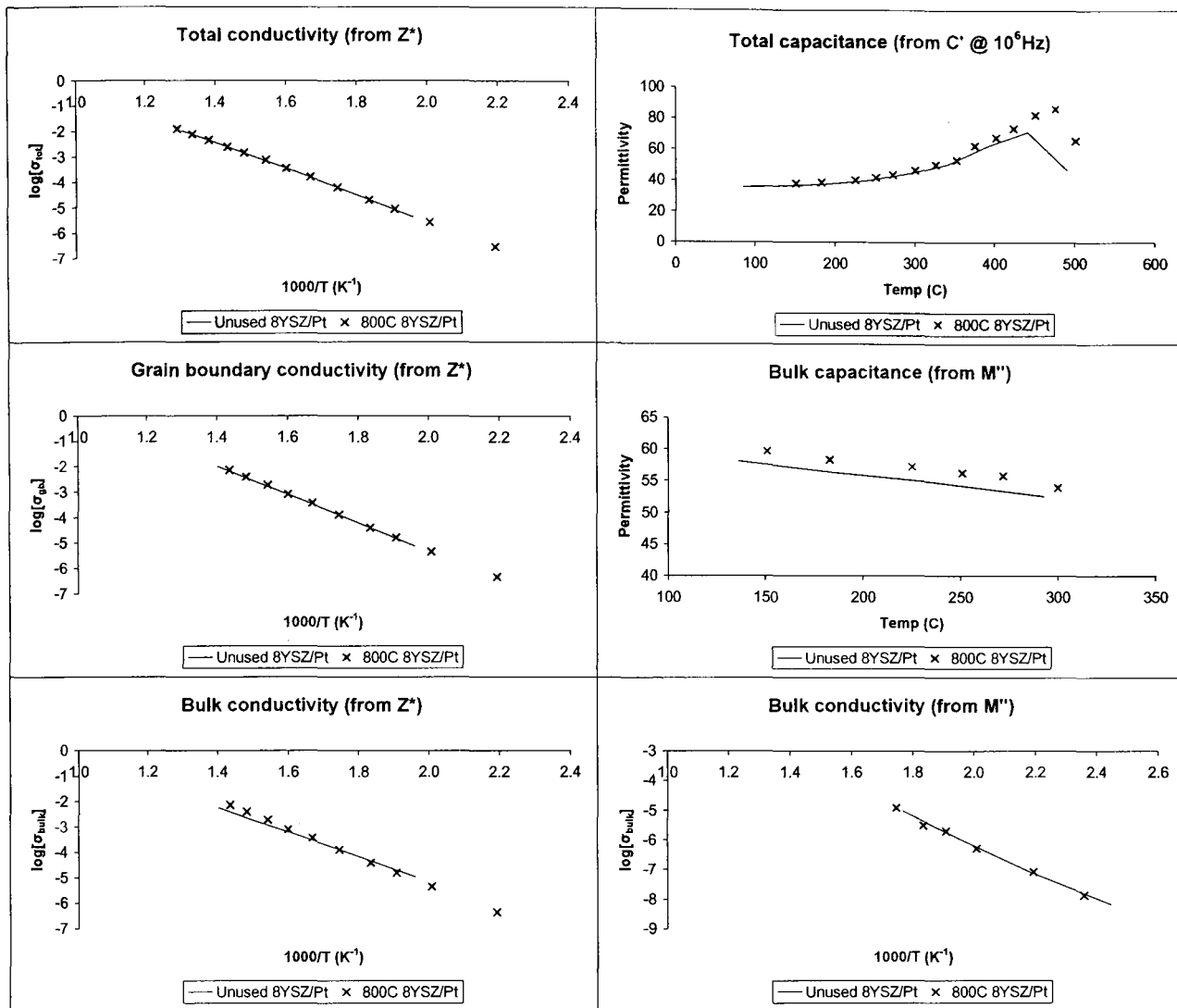


Figure 8.18: Summarised impedance spectroscopy for YSZ/Pt before/after 800 °C SO₂ exposure

The total YSZ conductivity measured experimentally and presented in Figure 8.18 can be seen compared to various literature values in Figure 8.19. West (1999), Komine & Munakata (2005), Herle et al. (1994) and Takebe et al. (2002) give data for 10, 8, 6 and 4 mol% Y₂O₃ respectively. It can be seen that there is a significant spread in the literature data, with measured conductivities two orders of magnitude apart at some temperatures. The conductivity values measured in this work are in the expected range for YSZ both before and after SO₂ exposure.

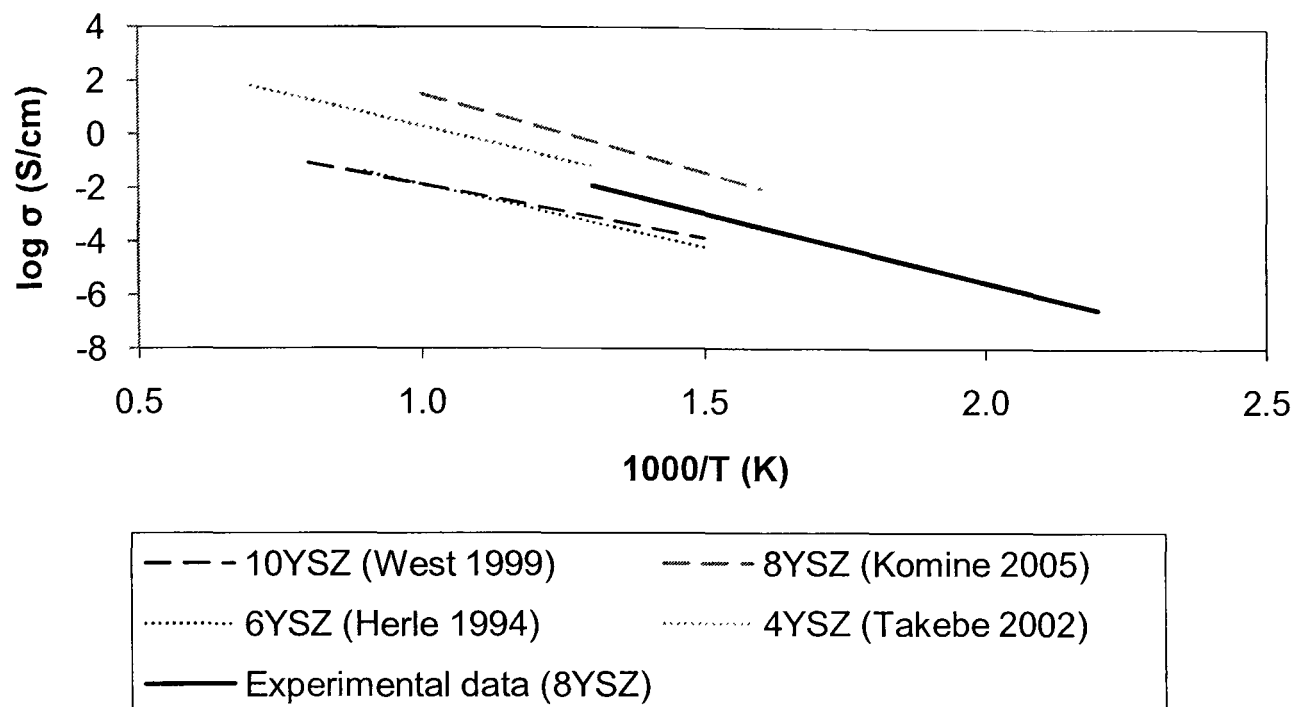


Figure 8.19: Comparison of experimental YSZ conductivity with literature values. Experimental data is bulk and grain boundary conductivity data from Z^* plots.

There was evidence in the Z^* plots of a surface layer being present on the SO₂ exposed pellet. This could be deduced from the presence of a point of inflexion in the data at immediately lower frequencies than the grain boundary response. Figure 8.20 shows a Z^* plot (at 293°C) before SO₂ exposure, with Figure 8.21 showing the changes (at 300°C) after the SO₂ exposure. The inflexion can be seen at approximately $Z' = 24000\Omega$. The arc immediately to the left of the inflexion relates to the grain boundaries of the pellet, with the leftmost arc relating to the bulk YSZ.

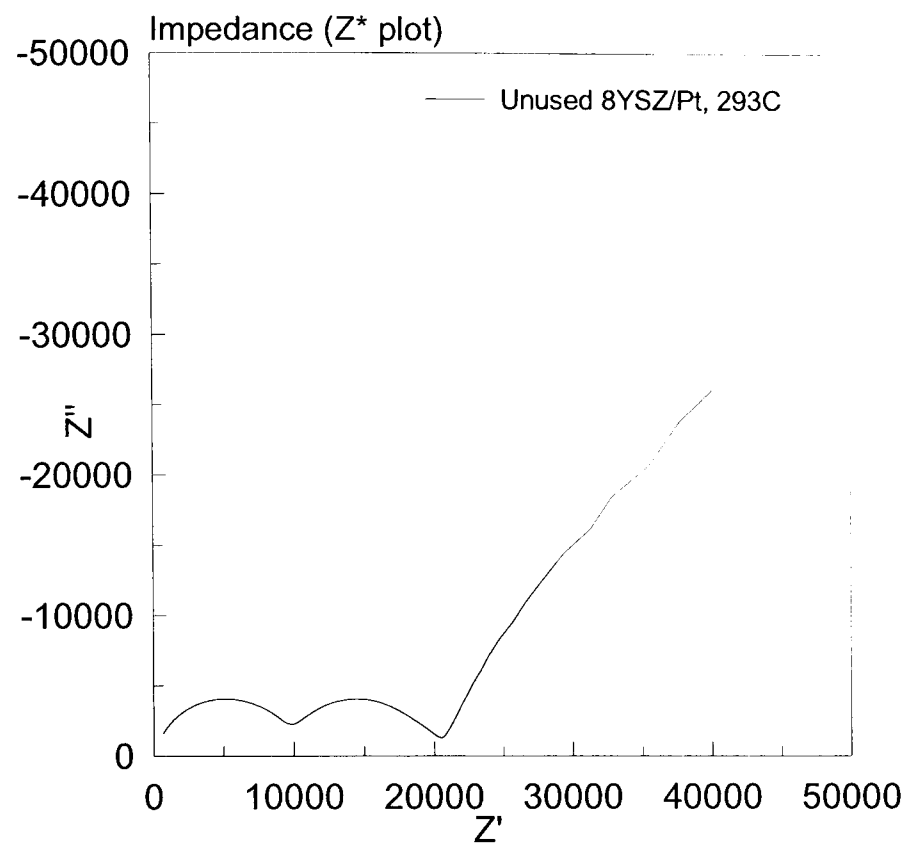


Figure 8.20: Z^* plot for unused YSZ/Pt at 293°C

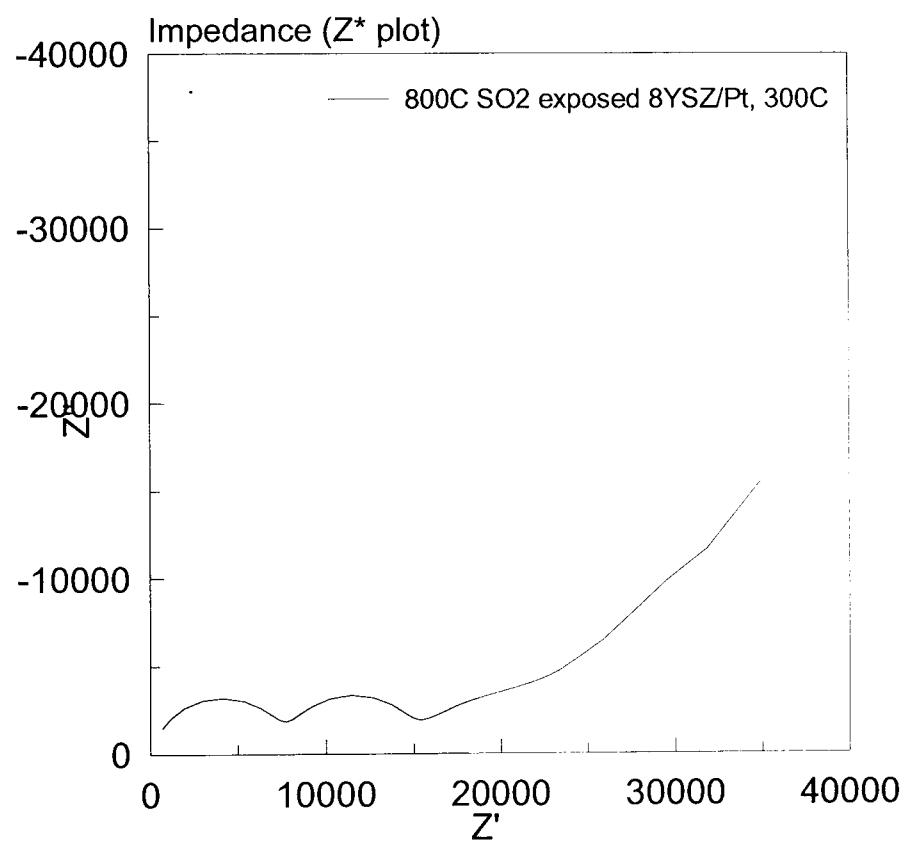


Figure 8.21: Z^* plot for YSZ/Pt at 300°C after SO₂ exposure at 800°C

The effect can still be seen at higher temperatures. Figure 8.22 shows a Z^* plot (at 441°C) before SO₂ exposure, with Figure 8.23 showing the changes after the SO₂ exposure. Because the region of interest is very small on a Z^* plot of the whole frequency range at this temperature, a magnified view is also shown. The inflexion can be seen at this temperature at approximately $Z' = 325\Omega$. The Z' value range at this temperature approximately doubles after SO₂ exposure, from 1359 Ω to 2585 Ω . The previous figures showed a small decrease in maximum Z' value in the 293 – 300°C measurement temperature range.

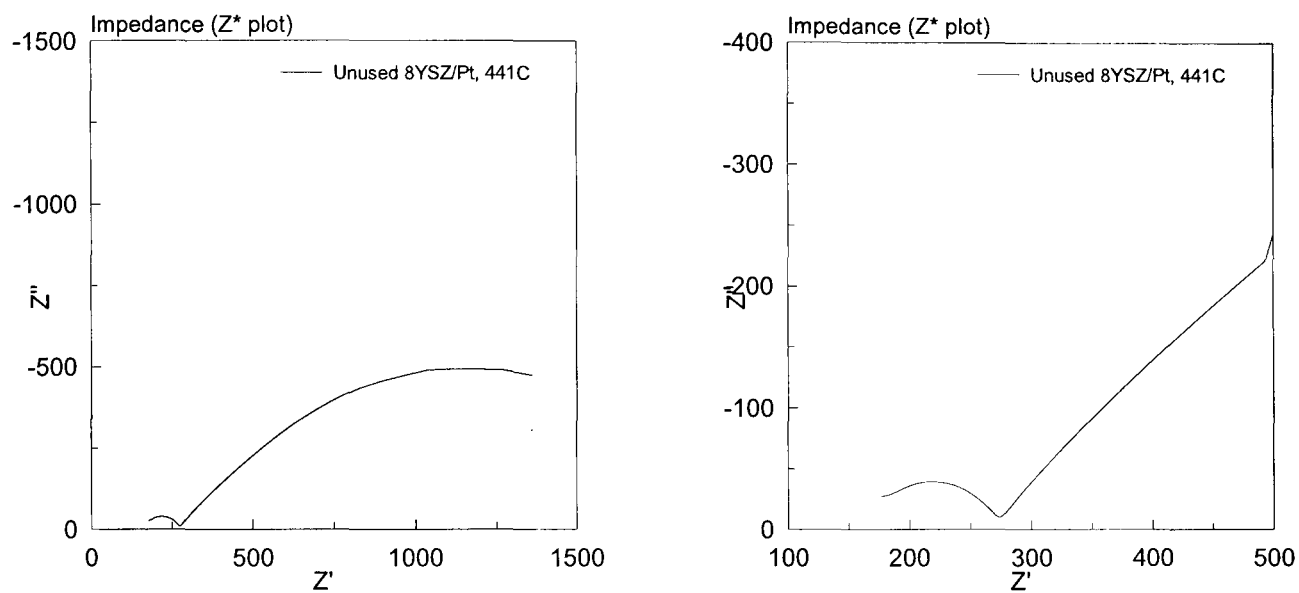


Figure 8.22: Z^* plots for unused YSZ/Pt at 441°C. Full range on left, higher frequencies only on the right.

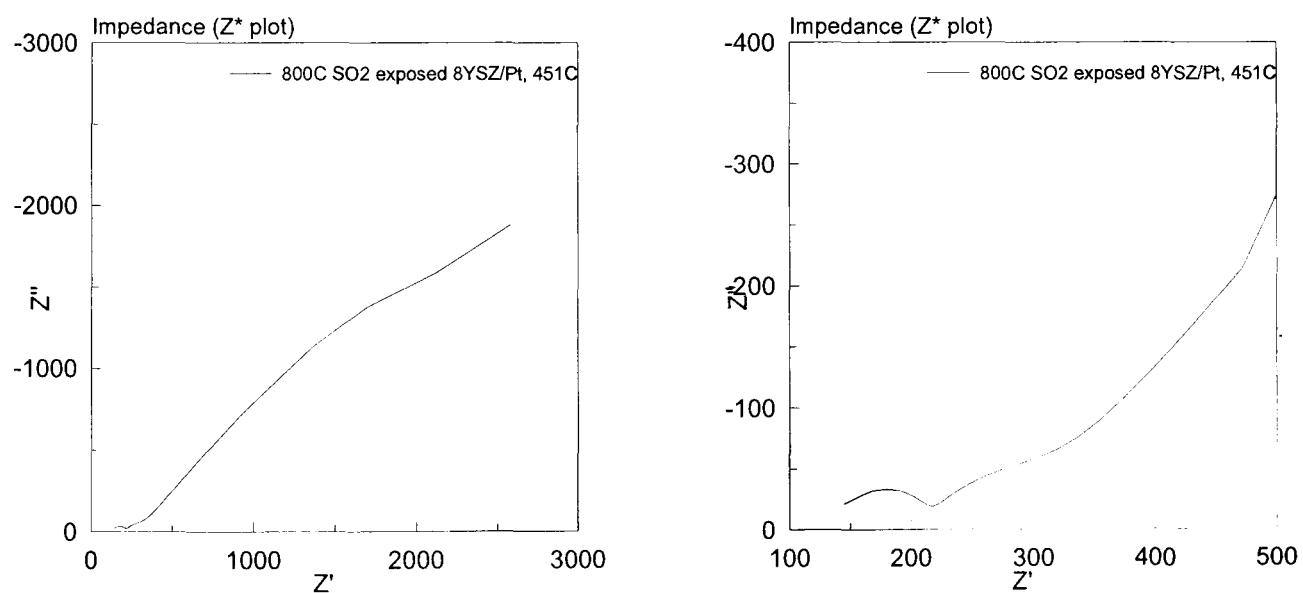


Figure 8.23: Z^* plots for YSZ/Pt at 451°C after SO₂ exposure at 800°C. Full range on left, higher frequencies only on the right.

Figure 8.24 summarises the before and after results for the YSZ/Au. Bulk conductivity in the YSZ/Au appears unchanged after exposure, whilst the total and grain boundary conductivities decreased slightly. The YSZ/Pt impedance spectra showed an increase in bulk capacitance after exposure, but the opposite was true for the YSZ/Au. The decrease in capacitance is small however and is within the bounds of experimental error.

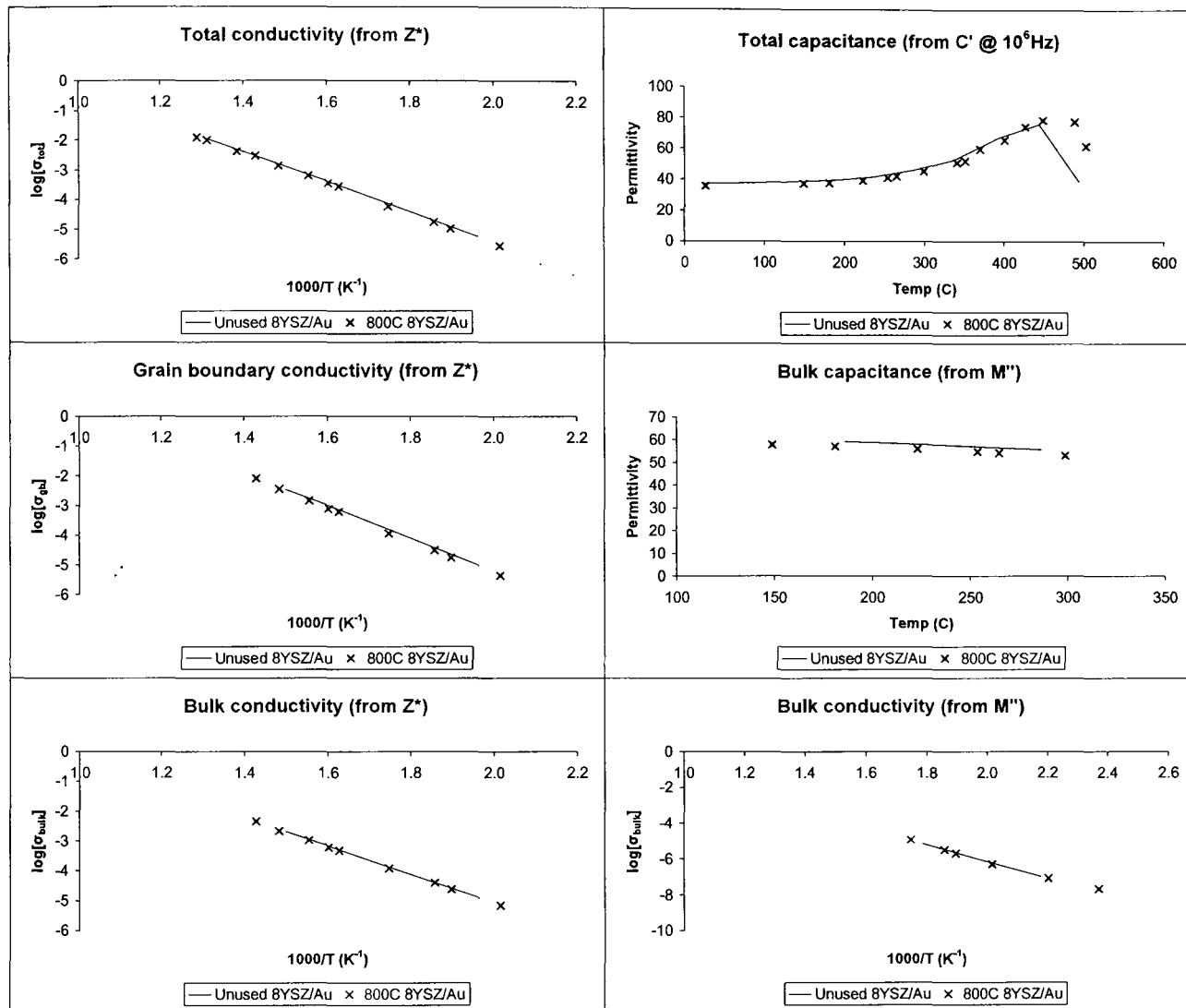


Figure 8.24: Summarised impedance spectroscopy for YSZ/Au before/after 800 °C SO₂ exposure

Unlike the YSZ/Pt, individual Z^* plots did not appear to indicate the presence of a surface layer being formed on the pellet during SO₂ exposure. Figure 8.25 shows a Z^* plot (at 337 °C) before SO₂ exposure, with Figure 8.26 showing the changes (at 341 °C) after the SO₂ exposure.

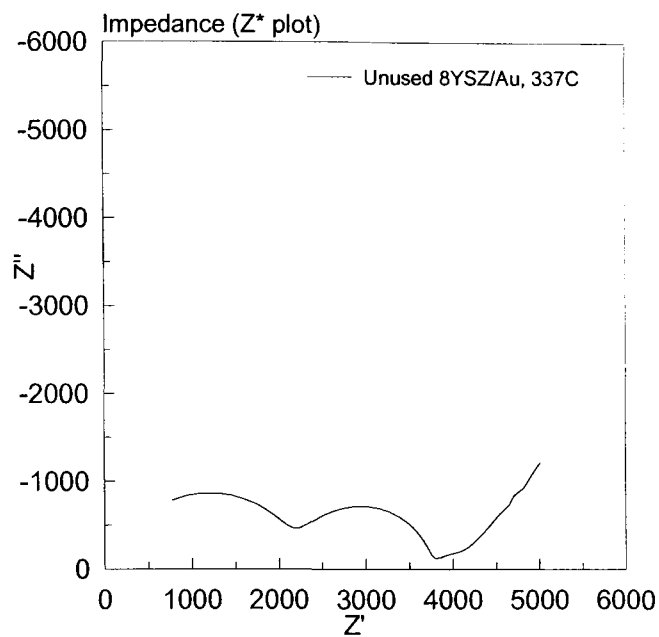


Figure 8.25: Z^* plot for unused YSZ/Au at 337°C. Full frequency range of 0.1Hz - 1MHz is shown.

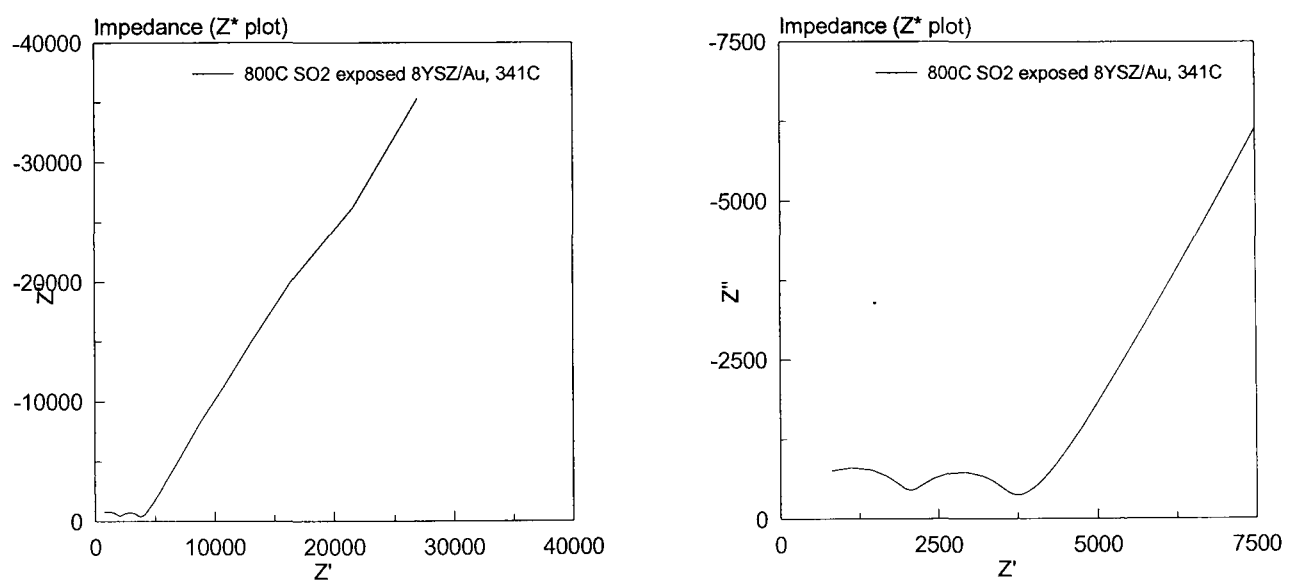


Figure 8.26: Z^* plots for YSZ/Au at 341°C after SO₂ exposure at 800°C. Full range on left, higher frequencies only on the right.

Higher temperature spectra also show no indications of a surface layer. Figure 8.27 shows a Z^* plot (at 444°C) before SO₂ exposure, with Figure 8.28 showing the changes after the SO₂ exposure.

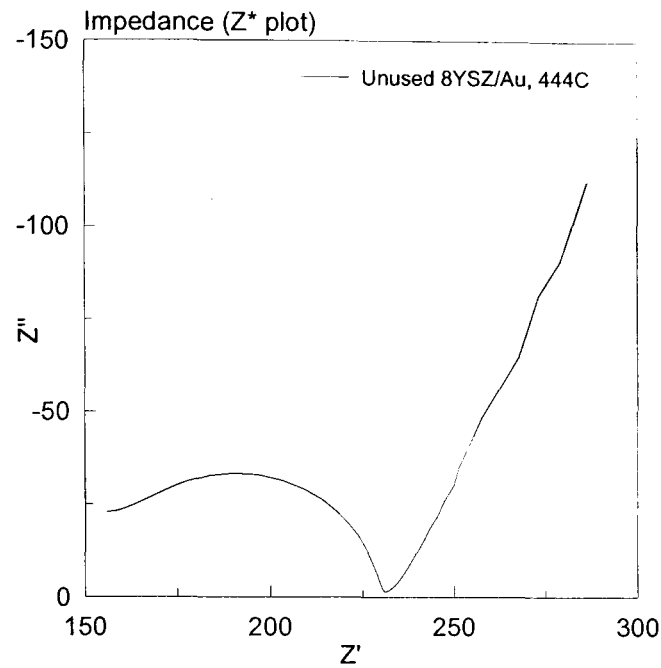


Figure 8.27: Z^* plot for unused YSZ/Au at 444°C. Full frequency range of 0.1Hz - 1MHz is shown.

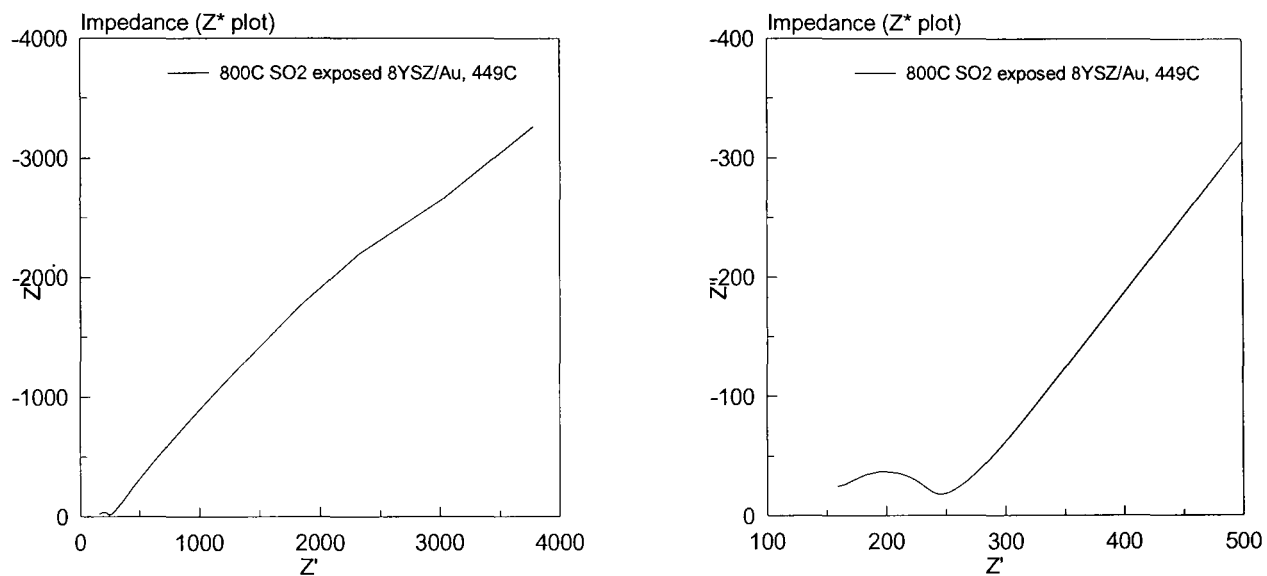


Figure 8.28: Z^* plots for YSZ/Au at 449°C after SO₂ exposure at 800°C. Full range on left, higher frequencies only on the right.

What is noticeable for each of the two sets of figures here is the increase in maximum Z' value after SO₂ exposure. For the YSZ/Pt the maximum Z' value decreased slightly at the lower measurement temperature presented and approximately doubled at the higher measure temperature presented. For the YSZ/Au figures here, the maximum Z' value increases from 5014Ω to 27013Ω for the lower measurement temperature and from 286Ω to 3777Ω at the higher temperature. These Z' increases are of the same order as the resistance increases observed during the experimental run (Fig-

ure 8.15), yet the bulk and grain boundary conductivity values do not change significantly with SO₂ exposure. Since the Z^* plots do not indicate the presence of a surface layer on the SO₂ exposed YSZ/Au pellet, the resistance increase may be caused by changes to the electrode itself.

Since analysis of the IS data shows for both pellets that the bulk and grain boundary conductivities are essentially unchanged, the decrease in O₂ permeation and conductivity must be caused by a surface effect of some description. Therefore, surface analysis must be undertaken to ascertain the precise chemistry of the pellet surface both before and after SO₂ exposure. This is best achieved by the use of x-ray photoelectron spectroscopy, or XPS.

Firstly, the feed side electrode was sanded off the YSZ/Pt pellet, a new platinum paste electrode applied and the test repeated. If the O₂ flux returns to the values seen at the start of the first test using that pellet, it would confirm that it is a change to the feed side surface that causes the loss of performance.

Secondly, the test for the YSZ/Pt pellet was repeated with new YSZ/Pt pellets. The pellets were analysed by XPS to determine the surface composition before and after exposure. XPS requires very clean samples that have not e.g. been stored in plastic sample bags, as pellets were up to this point. The new pellets were handled more carefully and stored in Petri dishes to reduce contamination.

8.3.4 Conclusions

The IS data indicates the presence of a surface layer on the YSZ/Pt pellet following SO₂ exposure. The XRD data shows an extra, as yet unidentified peak that may be related to the surface layer, although the extra peak was not in the same position as that observed with a YSZ/Pt pellet after SO₂ exposure at 900°C - that peak indicated the possible presence of a monoclinic zirconia phase.

The YSZ/Au pellet had a significantly lower final permeate O₂ concentration than the YSZ/Pt pellet. Since the experimental run and the pellet itself were identical, this suggests that the electrode may be involved in the process that reduces the O₂ transport capability of the pellet. The IS data did not indicate the presence of a surface layer after SO₂ exposure of the YSZ/Au, but did show an impedance increase as the frequency tended to zero of the same order as that observed in the experimental current data. This may also suggest that the electrode itself is responsible for the resistance increases.

The YSZ/Pt pellet had the feed side electrode removed and reapplied before being re-

tested. This aimed to confirm that the reduction in permeation performance is caused by the pellet feed side surface.

Because the IS data rules out changes to the bulk electrolyte as the cause of the O₂ permeation, attention must turn to characterisation of the pellet surface. New pellets were prepared such that XRD and XPS could be carried out before and after SO₂ exposure.

8.4 SO₂ exposure at 800°C (replacement of Pt electrode)

The SO₂ exposure experiment carried out at 800°C indicated that the reduction in oxygen permeation and increased electrical resistance of the membrane was caused by a surface change. In order to confirm this, the platinum-electroded pellet from that run had the feed side electrode sanded off and a new electrode applied. This was to show that the original performance of the pellet could be restored by removing the feed side surface.

8.4.1 Aim

The aim of this experiment was to show that the pellet's performance could be restored by removing and replacing the feed side electrode.

8.4.2 Method

The feed side electrode was removed from the previously SO₂ exposed pellet using fine sandpaper. Upon removing the metal electrode an XRD spectrum was taken. Since this did not match pure YSZ, further sanding took place until an additional XRD spectrum showed that only YSZ was present.

The electrode was then re-applied, using the same Metalor ink as was used for all previous tests. The rig was reassembled and an identical run performed to that performed initially on this pellet (Section 8.3).

8.4.3 Results

XRD analysis

XRD spectra were taken during the sanding process (Figure 8.29) and compared to those recorded previously. It was noted during the post-exposure XRD analysis in the previous section that the feed side of this pellet did not give rise to the extra XRD peak at $2\theta \approx 28^\circ$ seen after the 900°C test. It can be seen here however that following removal of the metallic electrode this peak is clearly visible and disappears upon further sanding. This indicates that the extra peak is associated with the surface of the YSZ itself.

Experimental data

Following reapplication of the electrode, the SO₂ exposure experiment previously performed was repeated and the results recorded in the usual way (Figure 8.30). The results follow a very similar pattern to that seen previously.

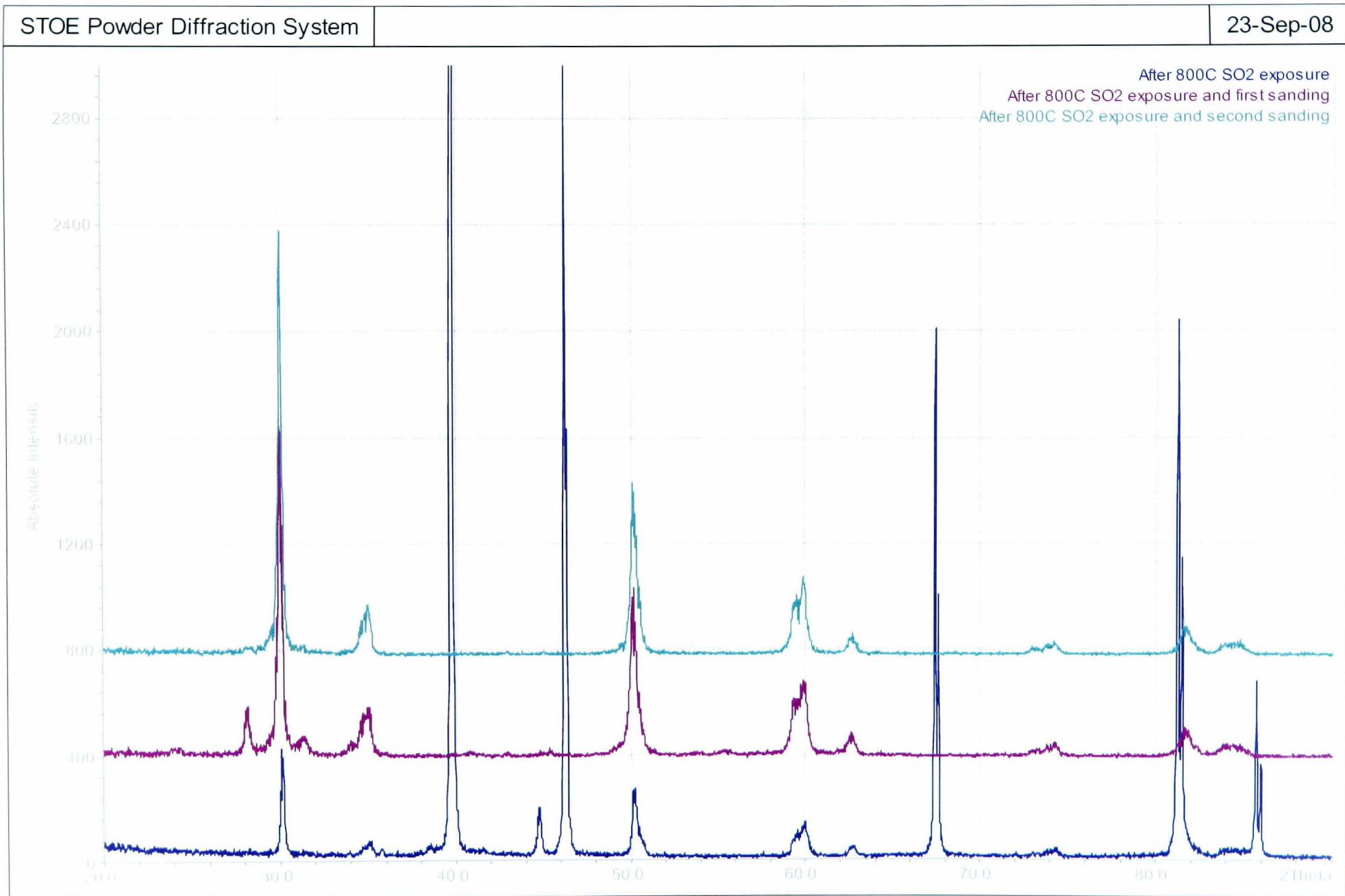


Figure 8.29: XRD data for YSZ/Pt membrane after initial 800°C SO₂ exposure and during post-exposure sanding

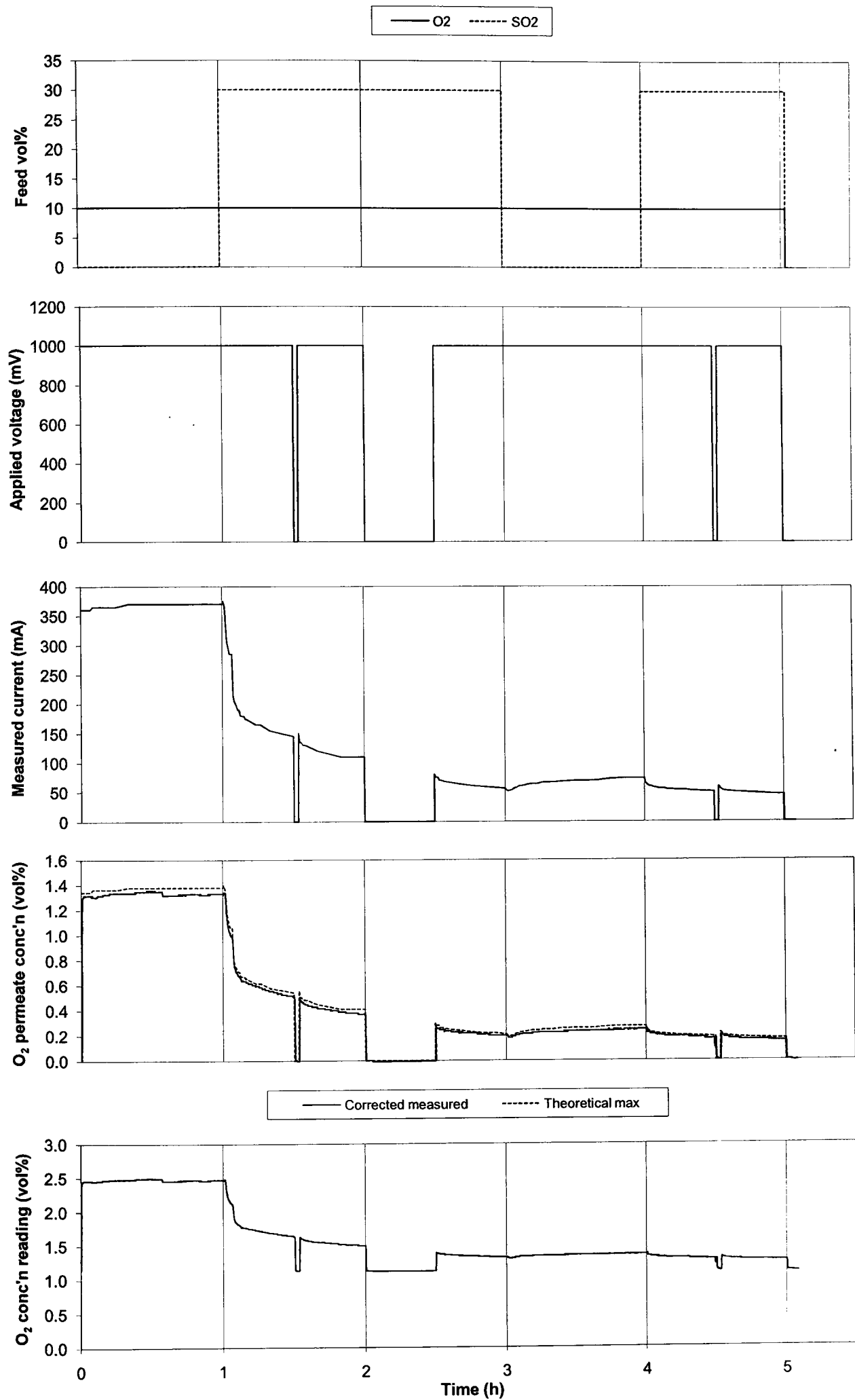


Figure 8.30: Experimental data for re-exposure of YSZ/Pt pellet to SO₂ and O₂ at 800°C following removal and re-application of the feed side electrode

The recorded oxygen permeate concentrations for both the initial and repeat runs are compared in Figure 8.31. It can be seen that the initial O₂ concentration, during the O₂-He feed hour, has returned to the values seen in the first run. Additionally, the final permeate O₂ concentration, after four hours of SO₂ exposure, was very similar to that recorded on the first run.

This data indicates that the performance of the pellet can be restored by removing and re-applying the feed side electrode, and hence the cause of the performance reduction is electrode or triple phase boundary-related.

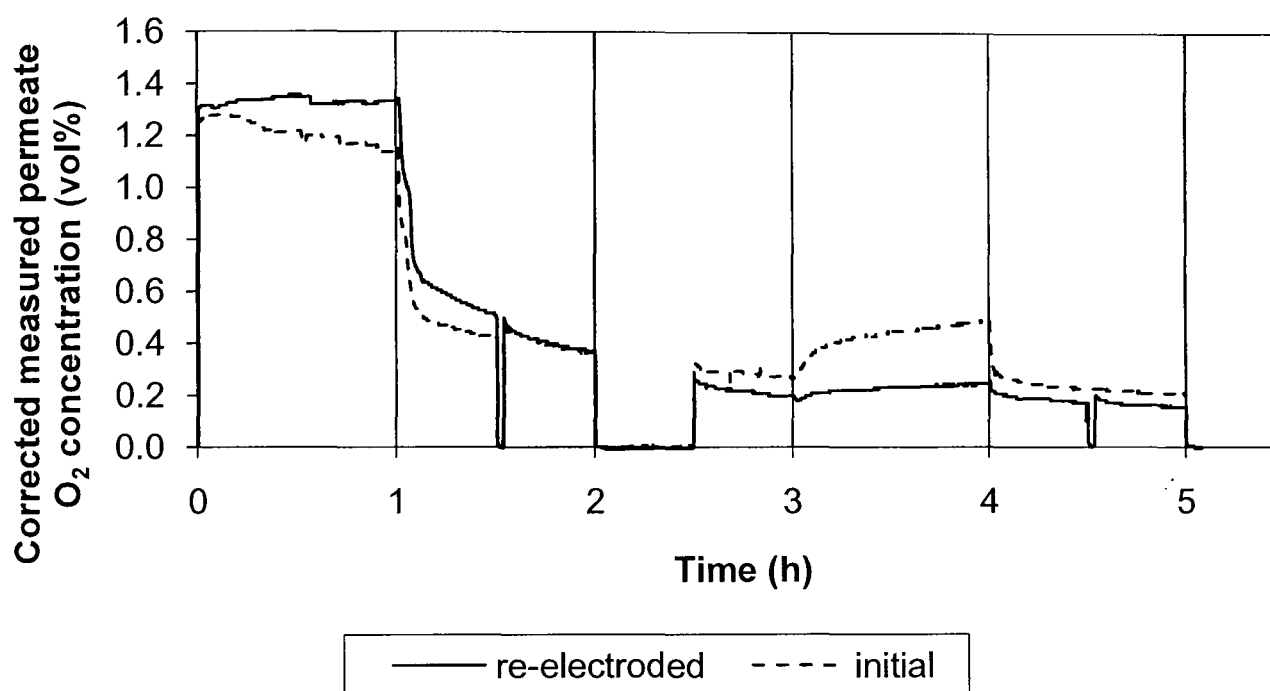


Figure 8.31: Comparison of O₂ permeation during first and repeat exposure of YSZ/Pt pellet to SO₂ and O₂ at 800°C (repeat exposure follows removal and re-application of feed side electrode)

8.4.4 Conclusions

By removing and replacing the feed side electrode it was possible to restore the performance of the YSZ/Pt to the levels recorded prior to SO₂ exposure. This confirmed that the cause of the performance reduction is surface-related, and further work was then performed to identify the nature of the surface change.

8.5 SO₂ exposure at 850°C (Metalor Pt ink)

The experiments described previously indicated that a surface effect of some description was the primary cause of the reduction in oxygen permeation performance of the

YSZ/Pt pellets. It was therefore decided that those previous runs should be repeated, with greater emphasis on surface analysis. In order to comply with the specifications of the EU HycycleS consortium, with which this work was now associated, this run was carried out at 850°C.

By carrying out XPS, SEM, and XRD both before and after SO₂ exposure, the pellet surface was comprehensively characterised.

The time taken for the oxygen permeation rate to reach pseudo-steady state was expected to be between those values observed at 800°C (\approx 14 hours) and 900°C (\approx 5 hours). During the 800°C and 900°C runs, periods were inserted where the external circuit was opened and where no SO₂ was supplied in the feed gas mixture. The results showed that these periods did not affect the rate of decrease of oxygen permeation rate or current flowing. Because of this, no such periods were inserted into this experimental run - the same SO₂-O₂-He mixture was used for the whole exposure time.

8.5.1 Aim

The aims of this experiment were to determine the time taken for pseudo-steady state to be reached in terms of oxygen permeation rate and current flow at 850°C, and to determine any changes in the surface chemistry and topology of the membrane through the use of XPS, XRD and SEM.

8.5.2 Method

As with the previous experiments, 8 mol% yttria YSZ pellets were produced by compression of Sigma-Aldrich YSZ nanopowder, followed by sintering at 1400°C. Platinum electrodes were applied by painting Metalor 6082 platinum paste on to each surface. The wet pellets were placed in a furnace at 200°C. The furnace temperature was increased to 900°C at 10°C per minute, held at 900°C for two hours, then allowed to cool back to 200°C. The pellets underwent XRD, XPS and SEM analysis before and after electrode application.

The apparatus was assembled in the same manner as that used for the runs at 800°C and 900°C.

With the apparatus assembled inside the furnace, the furnace was heated to 850°C, with a single feed of 100ml/min 20% O₂ in He being split and supplied to both sides of the pellet. Once at the setpoint temperature, the feed side was supplied with 10% O₂ in He (total 50ml/min) for one hour and a potential of 1V applied across the

membrane. The permeate side was fed with 100ml/min of pure He. Once the first hour had elapsed, the feed was then changed to 30% SO₂ and 10% O₂ in He (total 50ml/min). The resulting oxygen concentration in the permeate gas was recorded by a Servomex paramagnetic oxygen analyser linked to a computer for data logging purposes. The current flowing across the membrane (and hence around the external electrical circuitry) was measured by an Avometer multimeter. The feed mixture and applied potential were maintained until the permeate oxygen concentration and current measurements reached pseudo-steady state.

Following the exposure, the pellet was analysed by XPS, SEM, and XRD. The analyses were carried out in that order as the techniques are ordered in terms of sensitivity to contamination. Because plastic bags can contaminate a pellet to the extent that a useful XPS analysis would not be possible, the pellet was kept in a Petri dish from manufacture throughout the experimental process, with the feed side facing up to prevent contact with the plastic container. The pellet was only handled by the edges.

8.5.3 Results

Experimental data

The data resulting from this run is presented in Figure 8.32. As with previous runs, there was a rapid drop in oxygen permeation immediately following the application of SO₂ to the membrane feed side. The period of time over which the rapid drop occurs is around ten minutes, a similar period to that observed at 800°C with platinum electrodes. The final corrected permeate oxygen concentration measured in this run was around one quarter of the initial value, compared to the runs at 800°C and 900°C where the final concentration was around one sixth of the initial value.

The bottom graph, showing the raw permeate oxygen concentration data from the gas analyser, shows that the open circuit oxygen concentration, expected to be zero, is higher than that in previous tests. This indicates that the sealing of the membrane holder to the membrane by the gold seal was not as complete as that in previous tests. Although the increased open circuit oxygen concentration has been allowed for, as in previous runs, it introduces a level of uncertainty into the oxygen concentration data. The corrected oxygen concentration data, shown in the second to bottom graph, does however correlate well with the oxygen concentration expected given the measured current flow (indicated by the dashed line.) In addition, the open circuit oxygen concentration does not vary significantly over the course of the experiment, therefore any leakage that is occurring is in a stable predictable fashion.

The corrected permeate oxygen concentration data shows a concentration in the range 0.95-1.06% during the first hour of the run, where the feed consists of 10% O₂ in He. It would be expected that this concentration would increase with operating temperature, as the ionic conductivity of the YSZ increases with temperature. However, this figure is lower than that at 800°C ($\approx 1.2\%$) and 900°C ($\approx 1.6\%$). As previously mentioned, the permeate oxygen concentration measured here at 850°C correlates with the measured current flow and hence this experimental run exhibited a higher electrical resistance than expected. It could be seen visually before the experimental run that the platinum electrode layers were thinner than those applied to previous pellets. This is the most likely reason for the increased circuit resistance, but a poor electrical contact elsewhere in the circuit could also have occurred.

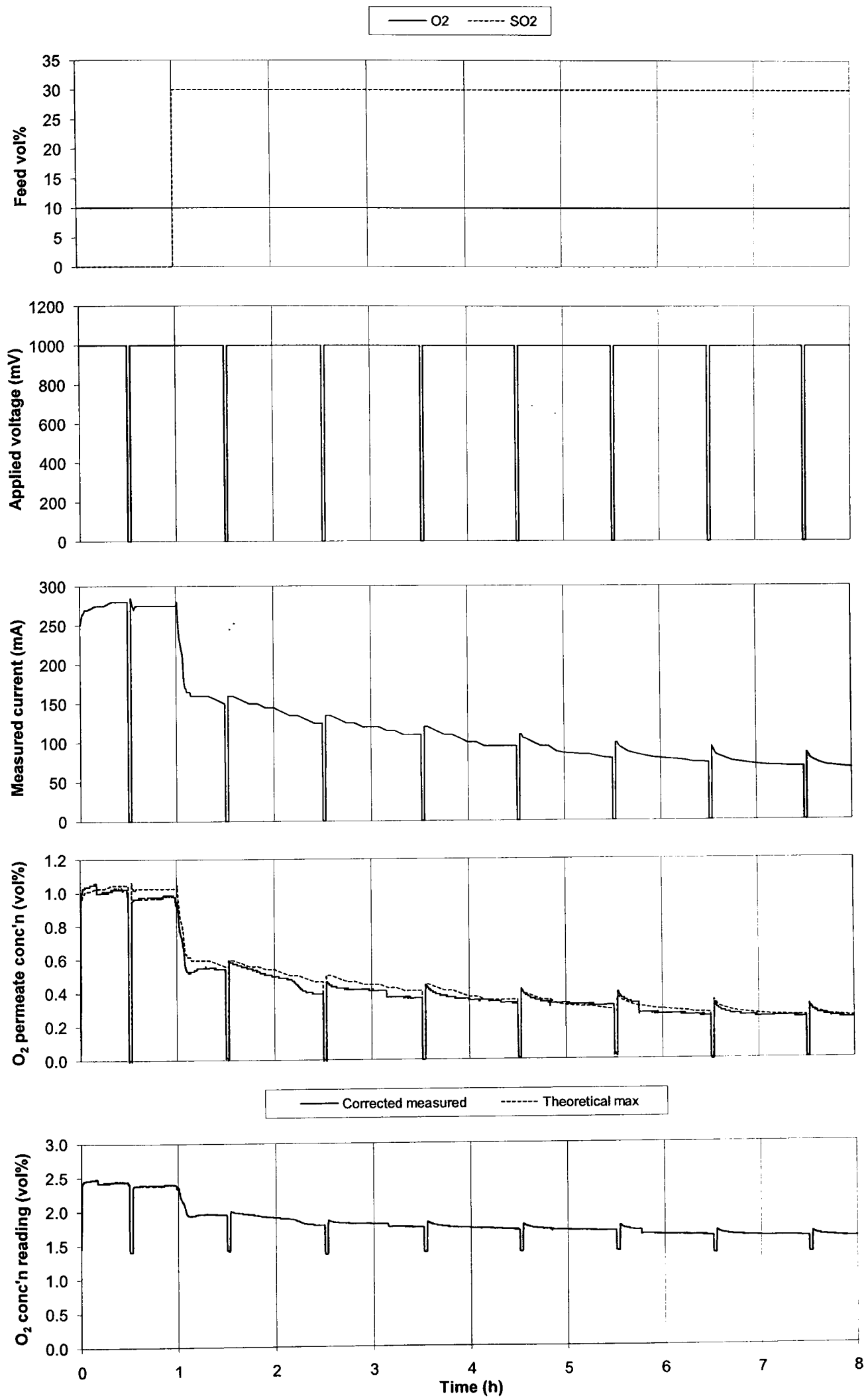


Figure 8.32: YSZ/Pt pellet exposed to SO₂ and O₂ at 850°C

XPS data

Figure 8.33 shows a wide range XPS spectrum for the YSZ pellet prior to being coated with platinum electrodes. XPS spectra were recorded at a number of points on the pellet surface and were very similar. As would be expected for a bare YSZ pellet, peaks are present for zirconium, yttrium and oxygen. A peak for the carbon 1s transition is also present and can be attributed to surface contamination.

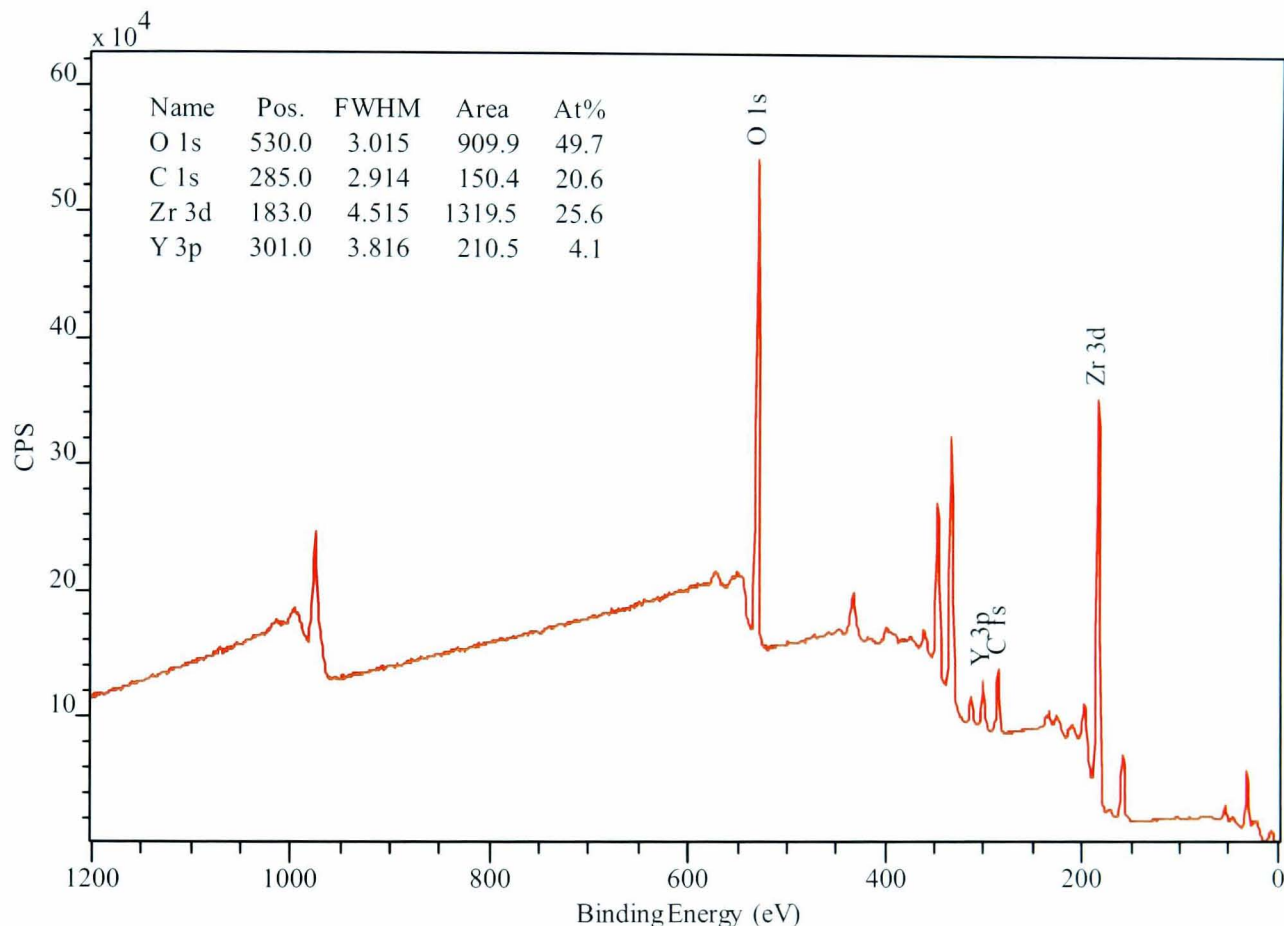


Figure 8.33: XPS wide scan of unelectroded YSZ pellet

Once the platinum electrodes had been applied, XPS spectra were recorded at four points on one of the pellet surfaces. As would be expected, an additional peak is present for platinum metal. However, the binding energy at which this 4f peak appears (75.0eV) is higher than that that would be expected for platinum metal (around 70eV). The actual peak position is more indicative of platinum present as part of platinum oxide or platinum dioxide. However, this may indicate the bonding of the platinum to the metal oxide surface of the ceramic pellet itself, rather than the presence of bulk platinum oxide.

Because of the varying thickness of the electrode, there was more variation in the individual spectra than was apparent with the unelectroded sample. In particular, the

area of the platinum peak varied considerably. Figures 8.34 and 8.35 show the two spectra with the smallest and largest platinum peaks respectively.

It can be seen that there are also peaks that have been matched to bismuth. Upon making enquiries, the manufacturer of the platinum paste used, Metalor, indicated that a small amount of “bismuth-based flux” is present in the paste to facilitate bonding to the surface. This was not included on the material safety data sheet (MSDS). These XPS spectra show that there is in fact a significant amount of bismuth on the surface of the electroded pellets. The ratio of platinum to bismuth detected is not constant across the spectra recorded here. Where the platinum peak is smallest, the ratio of platinum to bismuth is around 2, whereas for the spectrum with the largest platinum peak the ratio is around 4. This may point to variation in the concentration of platinum in the paste when applied.

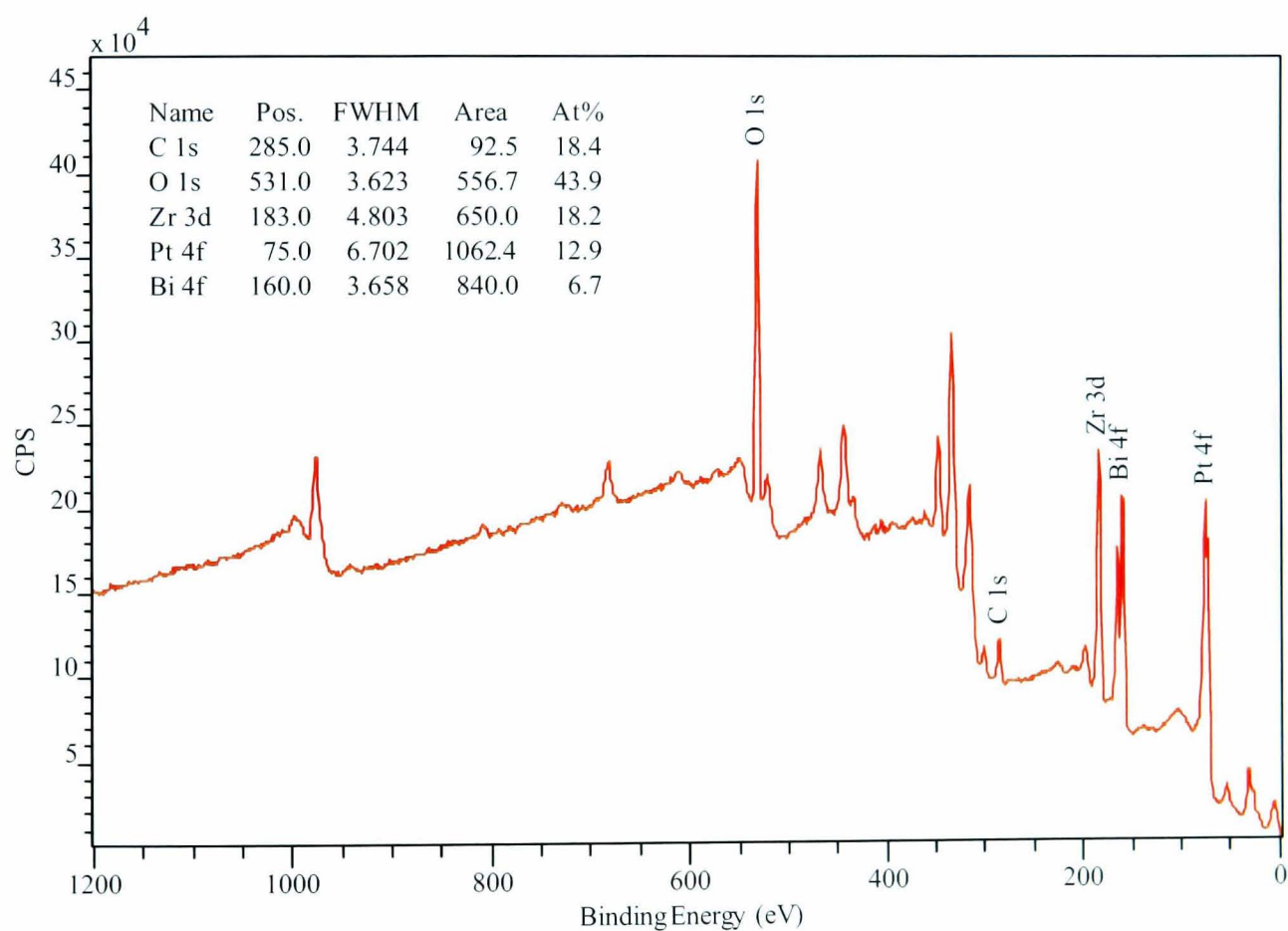


Figure 8.34: XPS wide scan of unused YSZ/Pt pellet - thin electrode point

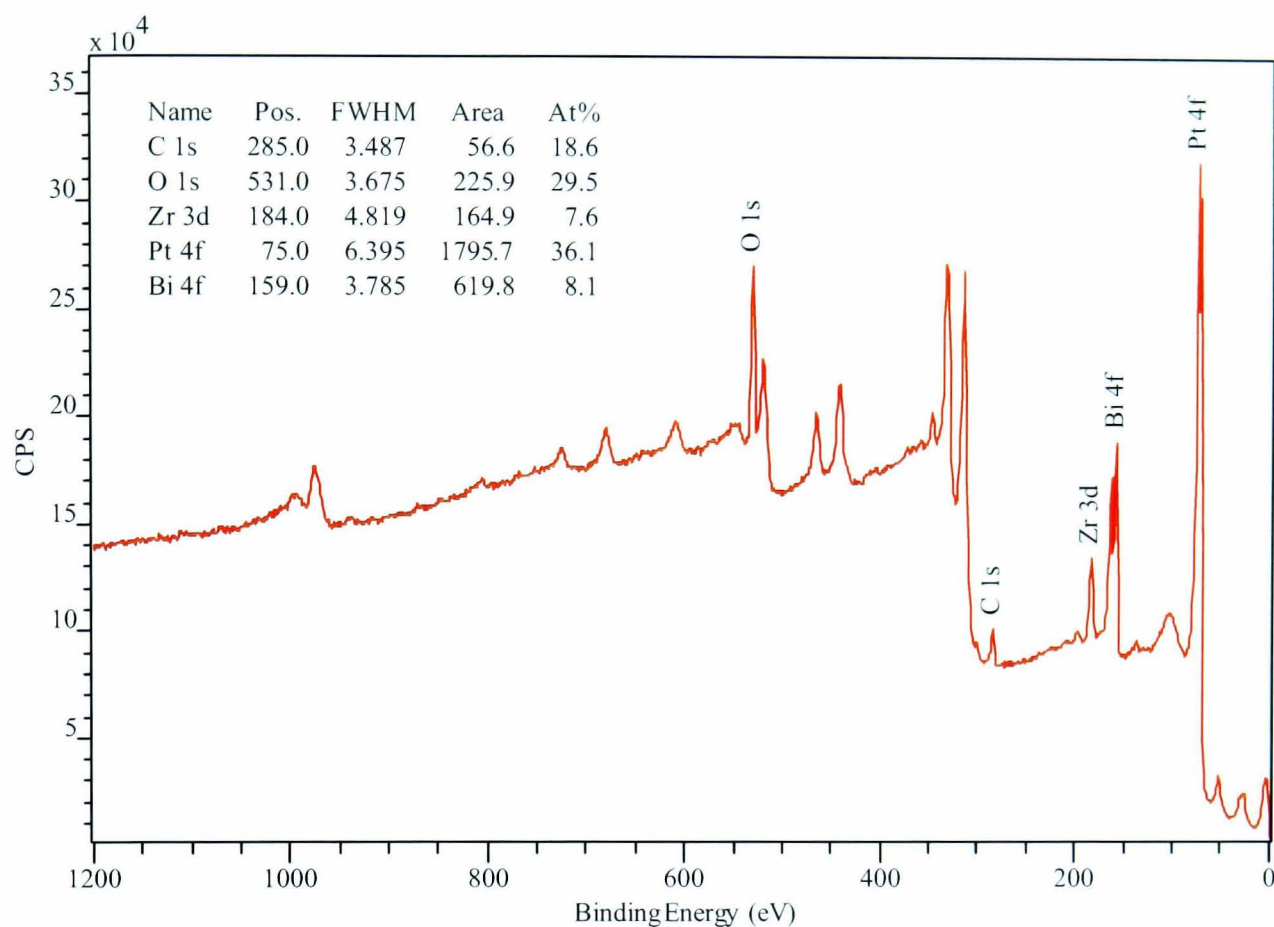


Figure 8.35: XPS wide scan of unused YSZ/Pt pellet - thick electrode point

XPS spectra were also taken following the SO₂ exposure. As before, spectra were taken at four points on the pellet feed side surface and these points showed a variation in the amount of platinum present. Figures 8.36 and 8.37 show the spectra with the least and most platinum present respectively. The following observations were made from these spectra:

- There was sulphur present on the pellet surface following exposure;
- The proportion of oxygen on the surface increased significantly;
- The ratio of yttria to zirconia detected increased following the SO₂ exposure;
- None of the metal peaks shifted significantly following exposure.

There has been significant yttria migration towards the surface. As a proportion of total yttria and zirconia present, there was an average of 5.7% yttria on the pellet surface before exposure and an average of 42.4% following exposure. Looking at the absolute values, the amount of yttria on the surface has increased and the amount of zirconia has decreased. Given the *HSC Chemistry* equilibrium simulations described

in Section 5.3, it would be expected that of the metals present, bismuth is most likely to be present as a sulphate following SO₂ exposure of the pellet. No literature XPS data has been found relating directly to bismuth sulphate. The sulphur 2s peak is present at 233eV. For bismuth sulphite (Bi₂S₃), this peak would be present at ≈225.8eV (Liufu et al. 2006), therefore the sulphur observed here is not related to bismuth sulphite. However, since bismuth is the metal most likely to form a sulphate (according to the equilibrium calculations) it will be necessary to repeat these tests with an ink that does not contain bismuth in order to either confirm this or to rule it out. Ruling out the presence of bismuth sulphate would leave adsorbed sulphur oxide species as the most likely source of the sulphur peaks observed here.

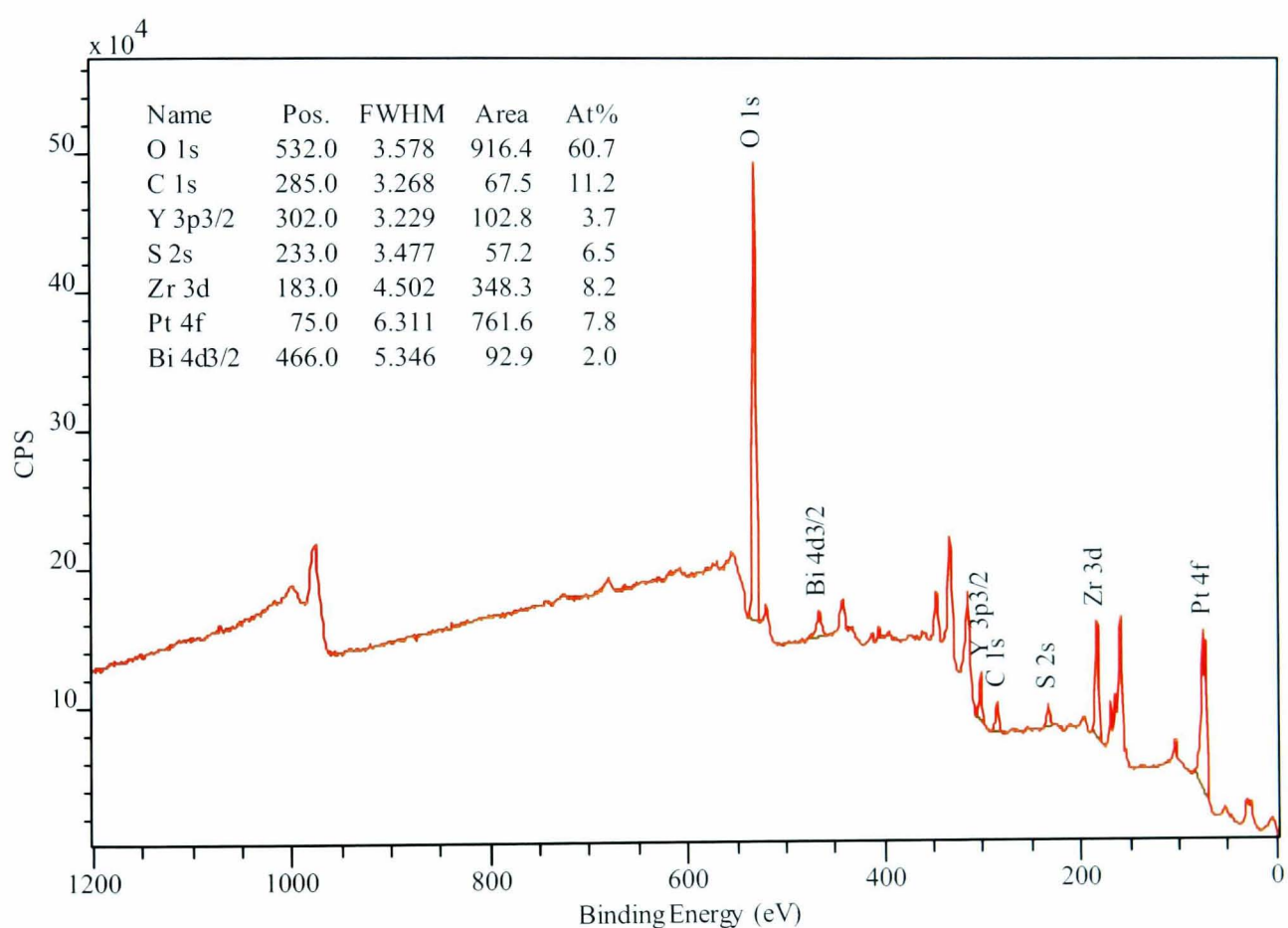


Figure 8.36: XPS wide scan of used YSZ/Pt pellet - thin electrode point

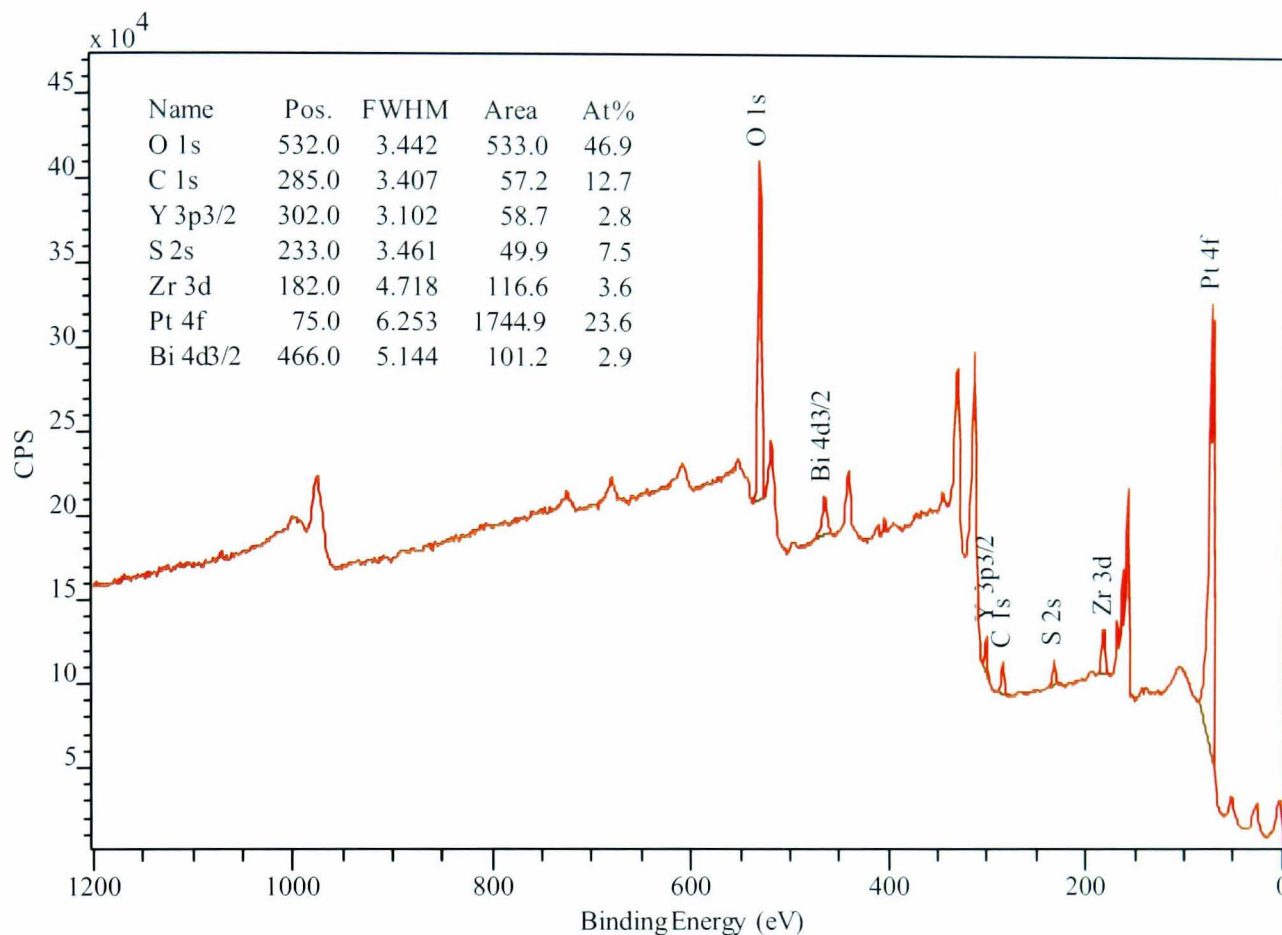


Figure 8.37: XPS wide scan of used YSZ/Pt pellet - thick electrode point

SEM images

SEM images were taken of the pellet before the platinum electrode was applied, after electroding and after SO₂ exposure. In order to preserve the pellets for further experimentation, no metal coating (e.g. sputtered gold) was applied as would usually take place in order to increase the surface conductivity and hence increase the image contrast. Because of this, some of the images are quite low contrast but still offer useful information.

Figure 8.38 shows the unelectroded YSZ pellet at 3000x magnification using the Cam-scan SEM. The sub-micron powder particles are visible, indicating the grain size prior to sintering. The contrast is quite low and the features can be identified more easily in Figure 8.39, which was taken on the same SEM at the same resolution but after application of the platinum electrode, and Figure 8.40, taken on the electroded pellet at 10000x magnification with a JEOL6400 SEM. The larger features on the surface of the pellet are areas of platinum coverage. That the images contain such a small amount of platinum in the field of view is indicative of the poor surface coverage achieved by applying the electrode with this platinum ink. Viewing the same area at 1500x magni-

fication (Figure 8.41) demonstrates that platinum coverage across the pellet surface is not consistent, an observation confirmed by the variability seen in the XPS platinum signal discussed previously. If the oxygen permeation of the pellet is surface area limited, improving the surface coverage of platinum would increase the oxygen flux per unit surface area at a given temperature, and there is clearly scope for improving the platinum deposition. Screen printing, as used by Rotureau et al. (2005), may give more predictable results.

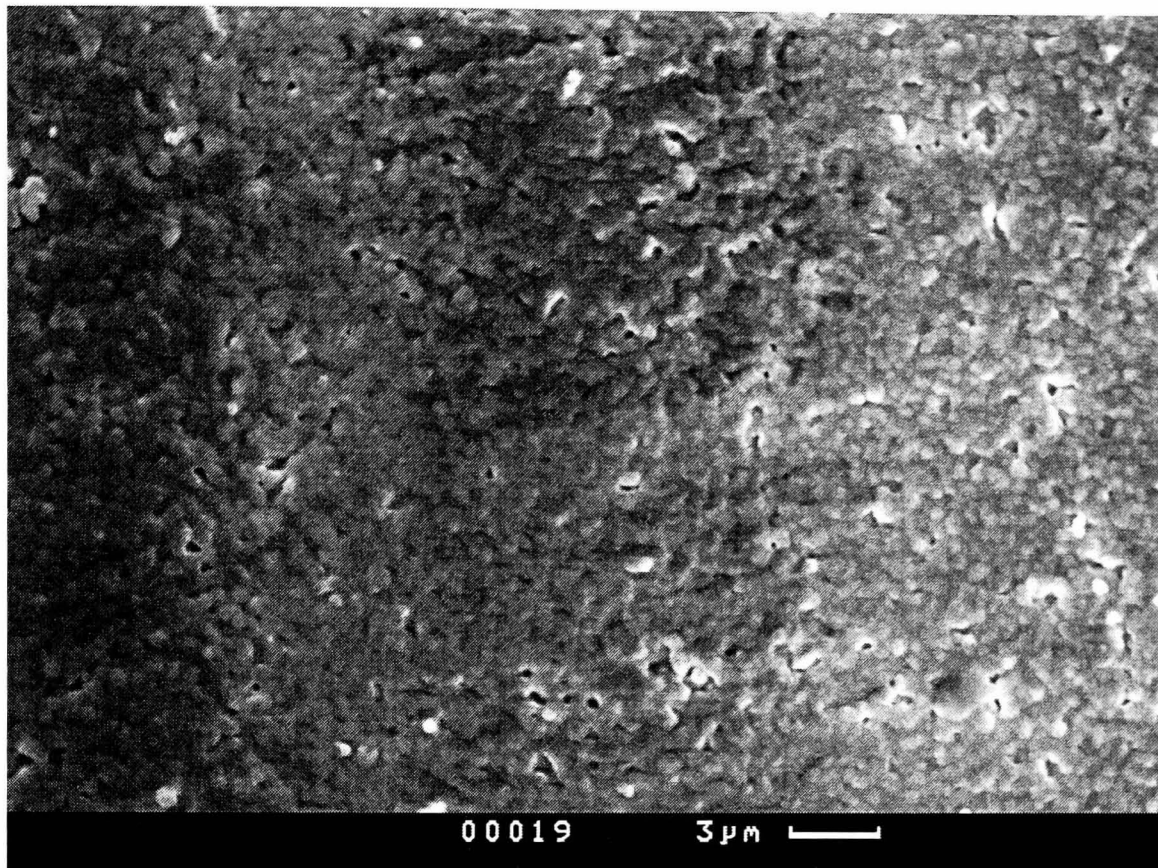


Figure 8.38: SEM image of unelectroded YSZ pellet, 3000x magnification, Camscan SEM

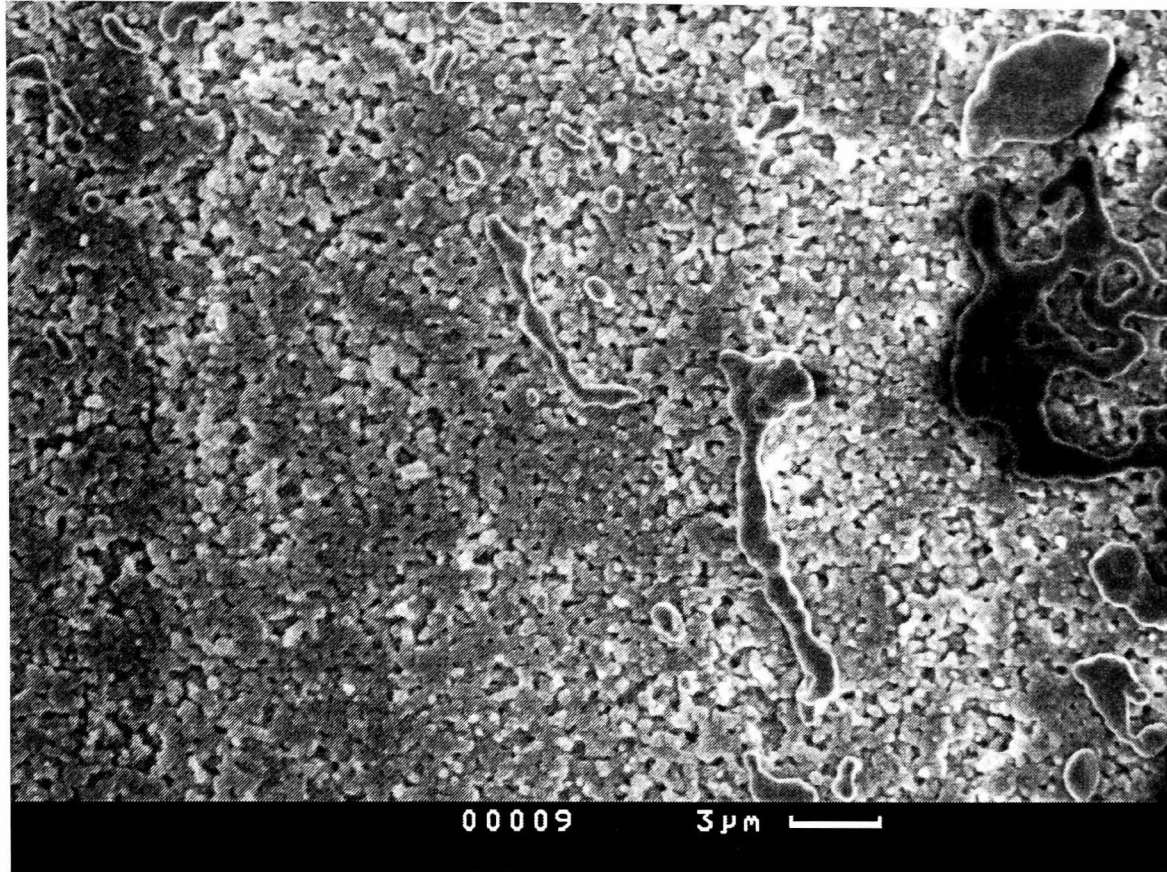


Figure 8.39: SEM image of electroded YSZ pellet, 3000x magnification, Camscan SEM

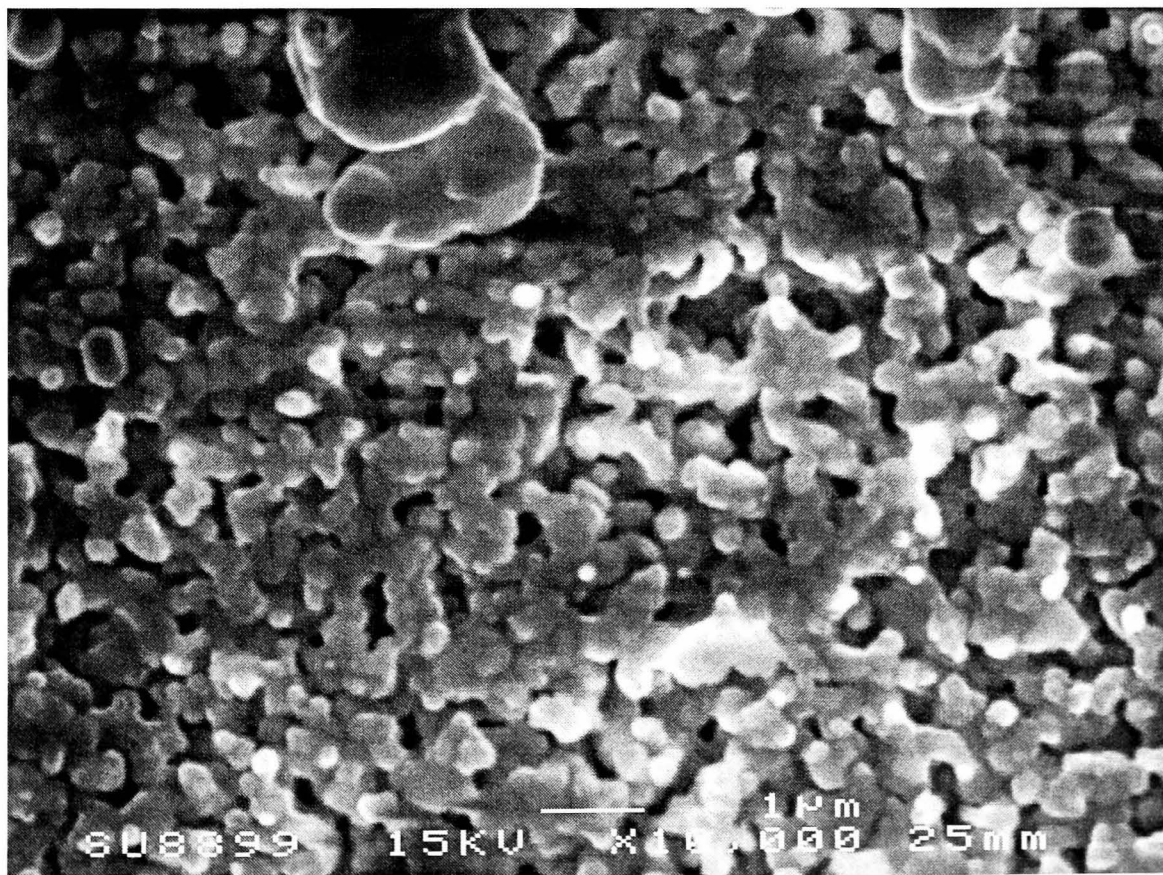


Figure 8.40: SEM image of electroded YSZ pellet, 10000x magnification, JEOL6400 SEM

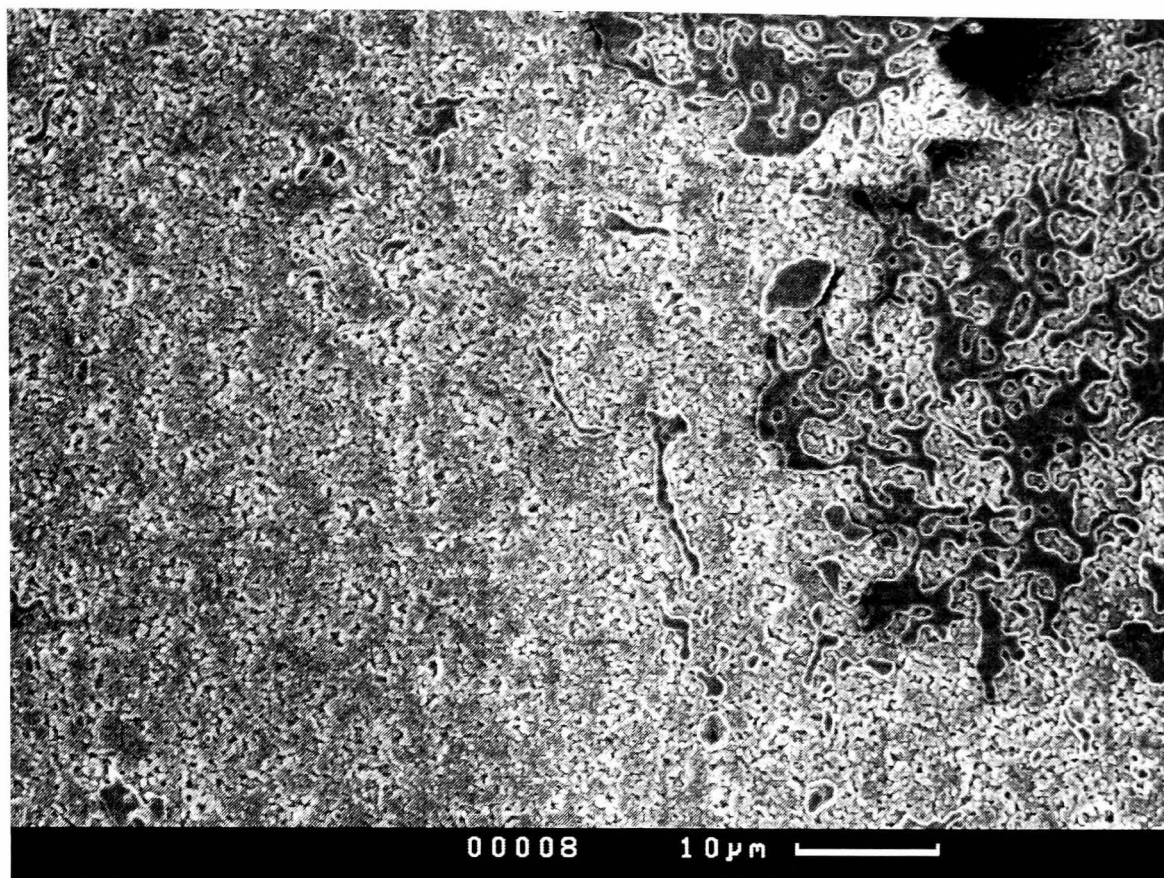


Figure 8.41: SEM image of electroded YSZ pellet, 1500x magnification, Camscan SEM

Further SEM images were taken following the experimental run. Two of these are shown as Figure 8.42 (2000x magnification) and Figure 8.43 (10000x magnification). Because of the poor platinum electrode coverage on this pellet, it is difficult to make quantitative judgements regarding any changes to the pellet surface following SO₂ exposure. However, it can be qualitatively stated that there has not been significant coarsening of either the YSZ powder or the electrode coating. It is certainly true that the large reduction in pellet oxygen flux cannot be attributed to a large change in available electrode-YSZ-gas triple phase boundary length on the pellet surface.

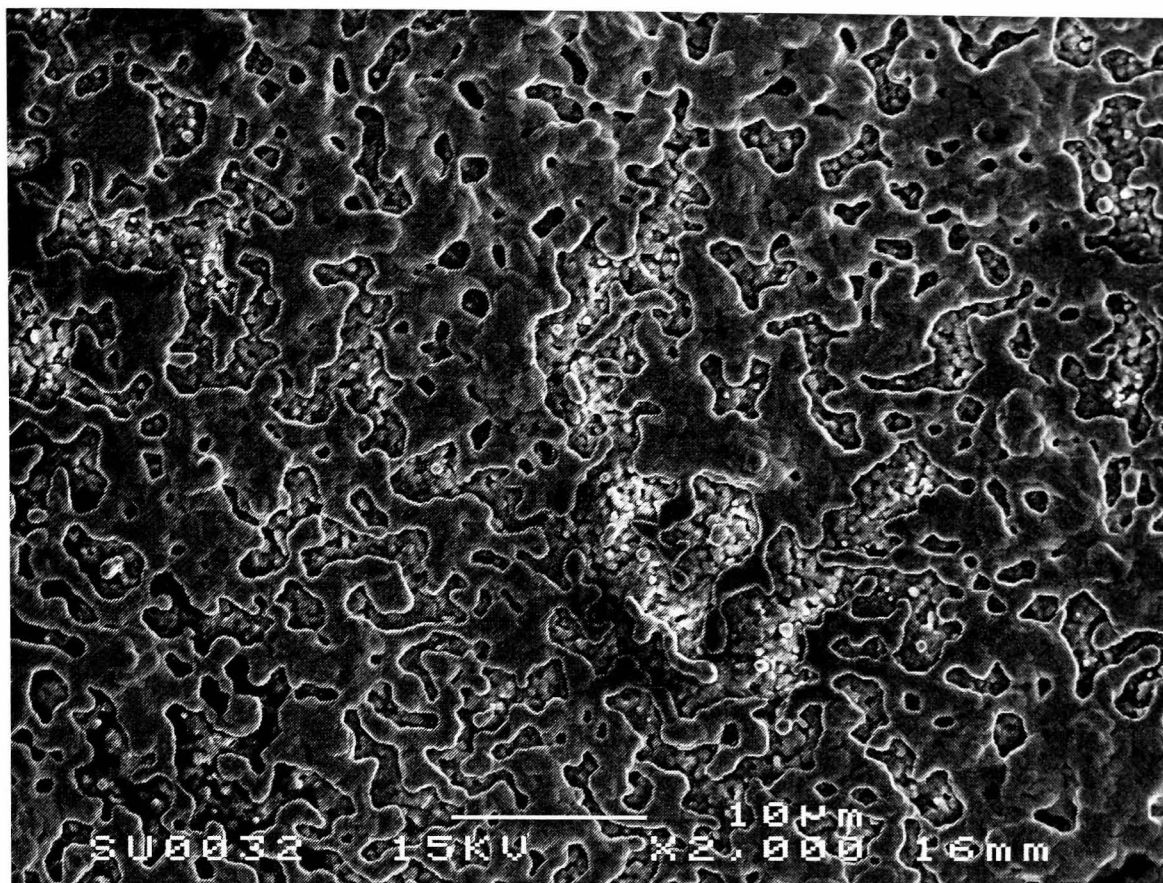


Figure 8.42: SEM image of SO₂ exposed YSZ pellet, 2000x magnification

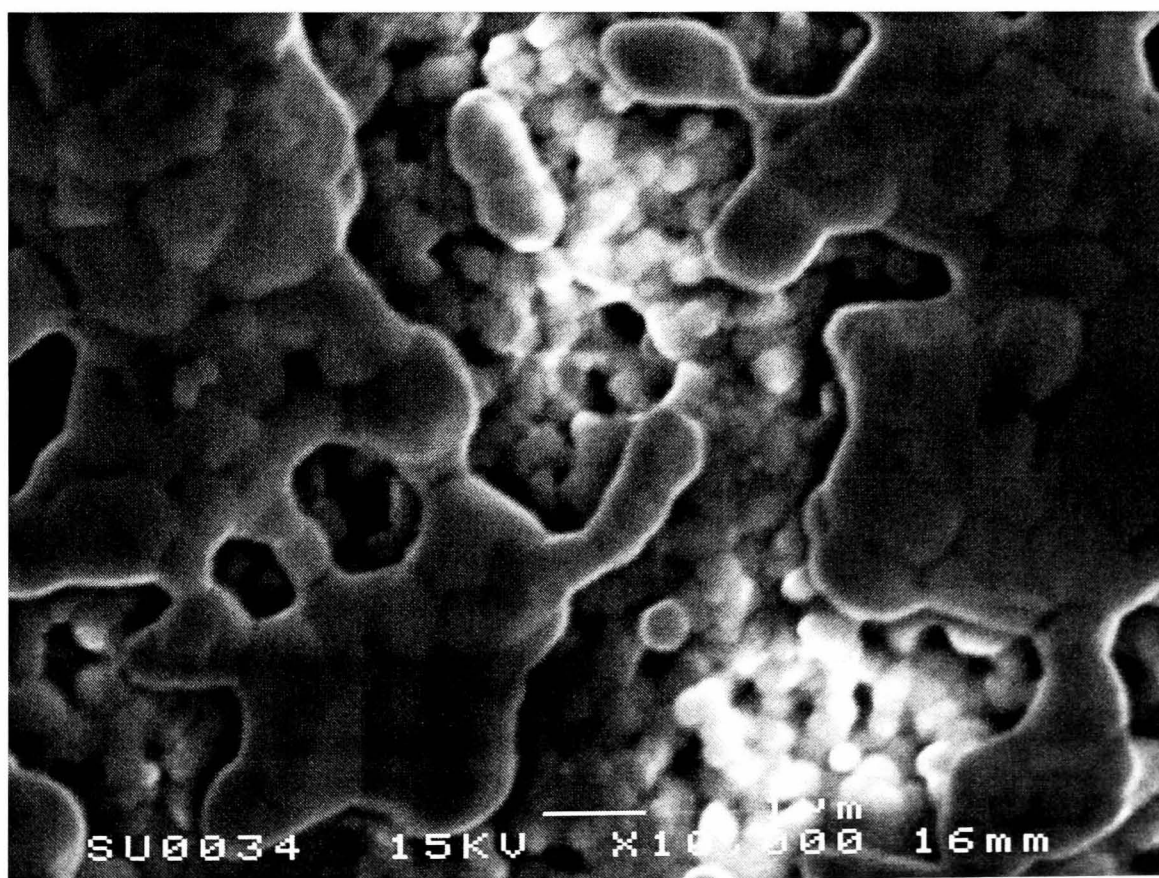


Figure 8.43: SEM image of SO₂ exposed YSZ pellet, 10000x magnification

XRD data

As with previous runs, XRD data was recorded for both sides of the exposed pellet with the intention of comparing it to data for a freshly electroded YSZ pellet. The data is presented in Figure 8.44. Unfortunately, the permeate side pellet surface was contaminated with adhesive from the SEM imaging carried out previously. The contamination has caused the permeate data to be very noisy, but the major peaks can still be identified. Comparison with data collected at 800 and 900 °C shows that the post-exposure peaks are in the same positions.

8.5.4 Conclusions

The results obtained here are similar in nature to those recorded at 800 and 900 °C, except that the current and O₂ permeation were lower than expected. This was attributed to poor platinum electrode coverage. XPS revealed the presence of bismuth on the pellet surface and the platinum ink supplier confirmed that the ink contained bismuth-based frit, despite not being listed on the Material Safety Data Sheet. Since bismuth oxide was calculated to be unstable under the conditions used here, it was necessary to repeat this 850 °C test using a platinum ink that did not contain bismuth. Ruling out the presence of bismuth sulphate leaves adsorbed sulphur oxides as the most likely cause of the performance decrease.

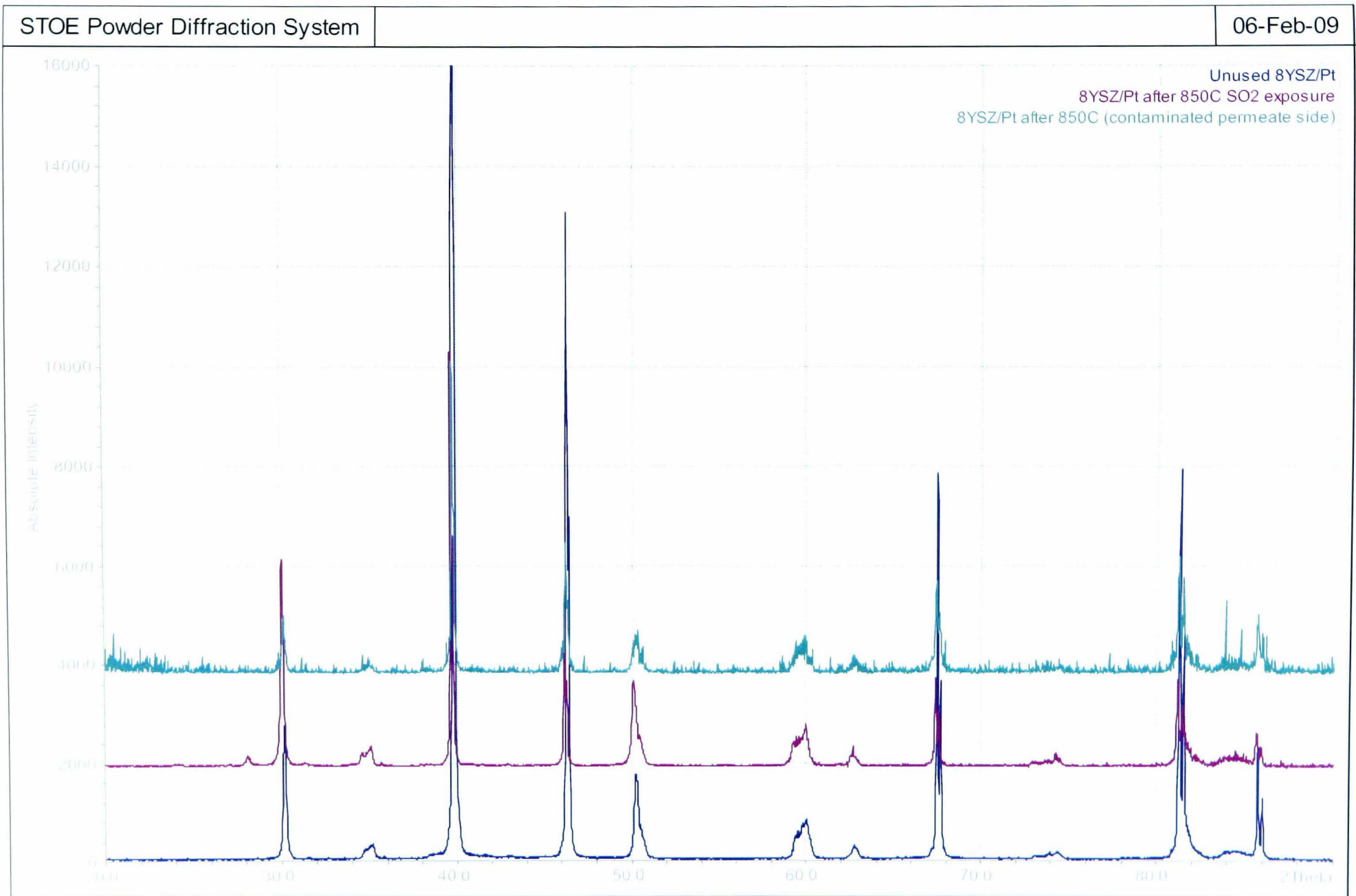


Figure 8.44: Before and after XRD data for YSZ/Pt membrane, 850°C SO₂ exposure

8.6 SO₂ exposure at 850°C (GEM Pt ink)

The previous experiment, carried out at 850°C, was the first to use XPS to gain a greater understanding of the pellet surface composition before and after SO₂ exposure. The XPS data showed that bismuth was present on the surface before and after exposure and that sulphur was present on the surface following exposure. It was determined that the platinum ink used to date, supplied by Metalor, contained a bismuth-based frit to aid surface adhesion. Equilibrium calculations described previously indicated that bismuth oxide is unstable under the process conditions being used here and that bismuth sulphate would be stable. The XPS data could not be used to prove conclusively that the sulphur detected on the pellet surface was associated with bismuth sulphate, although it was suggested. In order to determine if this was the case, the 850°C test was repeated, using identical conditions and method, except that a bismuth-free platinum ink was used to create the platinum electrodes.

8.6.1 Aim

The aim of this experiment was to determine if the decrease in oxygen permeation previously demonstrated, and the presence of sulphur on the pellet surface following SO₂ exposure, can be attributed to the bismuth present in the platinum ink previously employed. This was shown by repeating the experiment with a bismuth-free ink.

8.6.2 Method

A fuel cell grade platinum ink, product code C2000904P3, was procured from Gwent Electronic Materials. The ink was applied to YSZ pellets fabricated in the same way as described previously. Photographs showing the application process can be found in Figure 6.1. This ink required a different temperature profile during the process of “firing” the electrode, that is, removing the organic binders from the ink to leave behind a porous platinum layer. The ink was dried at 150°C for 15 minutes, allowing the other side of the pellet to be coated. The required temperature for firing of the electrode was 1200°C for 12 minutes, with an up and down ramp rate of 5°C per minute.

The experimental method was identical to that for the previous run at 850°C except for the post-run shutdown procedure. In previous runs, the furnace and gas feeds were turned off 2 minutes after disconnecting the electrical circuit. However there was a possibility that the sulphur detected on the feed side surface following the

previous run could have been the result of residual SO₂ or SO₃ left in the piping during the rig cool-down period. In order to remove this possibility, a small helium flow of 10ml/min was left running through the feed and permeate membrane holders overnight during the rig cool-down period.

8.6.3 Results

Experimental data

The current flow and permeate oxygen concentration were recorded in the same way as for previous runs (Figure 8.47). It can be quickly seen that the outcome of this run is very similar to that carried out using Metalor ink under the same process conditions (Figure 8.45). There is still a rapid decrease in current and permeate oxygen concentration following the addition of SO₂ to the feed gas after one hour. Following the initial rapid decrease, the current and permeate oxygen concentration decrease slowly for the remainder of the experiment.

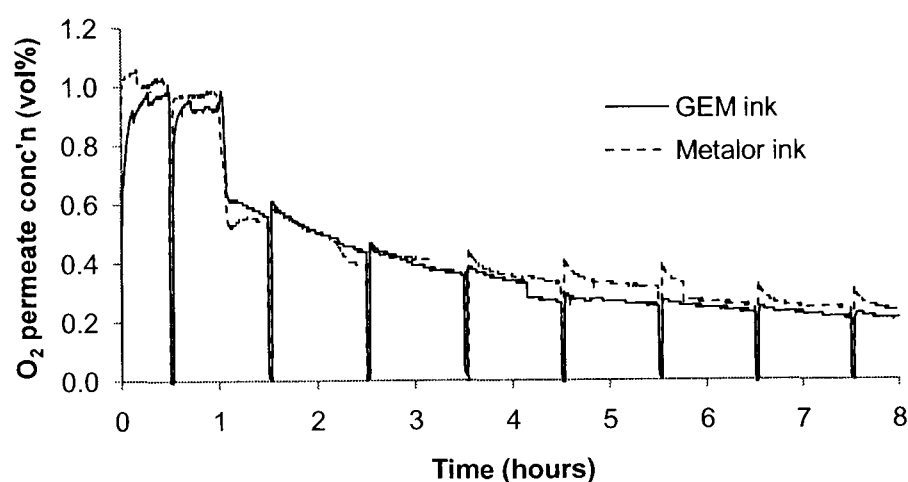


Figure 8.45: YSZ/Pt pellet exposed to SO₂ and O₂ at 850°C - comparison of permeate oxygen concentration with GEM and Metalor inks

There is a step change in the raw permeate oxygen concentration value at around 4.2 hours of experiment time. This is not accompanied by a corresponding reduction in current flowing. This indicates that the permeation drop is not caused by a drop in current and that the step change is probably as a result of a change in the sealing of the membrane or by an increase in the sweep gas flow rate.

A further literature search at this point uncovered work by Fu et al. (2009) on a PEM fuel cell (Nafion 212 membrane, platinum electrodes supported on carbon paper) using an air feed containing 25ppm of SO₂ (Figure 8.46). Whilst operating the fuel cell

at a constant voltage of 0.7V, the resulting current follows a similar profile to that seen in the experimental runs carried out in this work. Fu found that the performance decrease could be “ascribed to the increasing of the charge transfer resistance caused by the loss of the electrochemical surface area” due to SO₂ adsorption on to the platinum active sites. They also found that the oxidation and adsorption behaviour of the SO₂ depended on the potential across the fuel cell. It appears that Fu suggests that a sulphur-poisoned platinum electrode can be recovered through application of a potential of >1.2V. In their case, this was applied by cyclic voltametry. The electrode was recovered because the absorbed SO₂ was oxidised. Additionally, reducing the voltage to 0.05V allowed oxidised platinum to be reduced, increasing the number of active sites available for oxygen adsorption.

Given these findings, it was necessary to repeat this run, again using the GEM ink, in order that different applied potentials could be used and the results compared. For example, the work by Fu et al. (2009) suggests that using a potential of 1.5V should cause O₂ adsorption to become the dominant process and hence reduce or prevent SO₂ adsorption on to the surface of the platinum. Briefly reversing the polarity was also tested to determine if this aids SO₂ desorption and/or platinum oxide reduction.

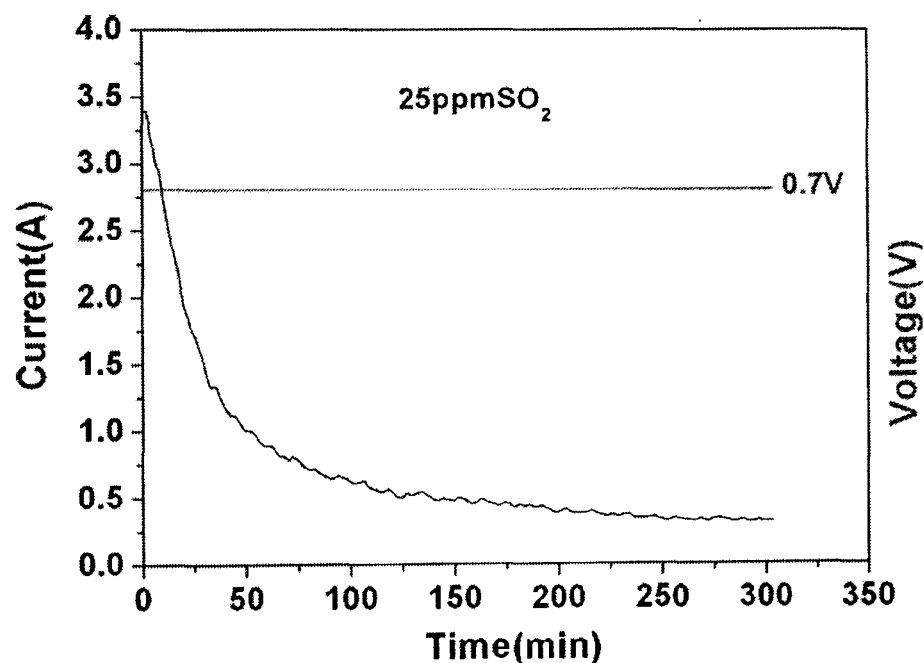


Figure 8.46: SO₂ poisoning of PEM fuel cell cathode (Fu 2009) - 25ppm SO₂, operating at 70°C

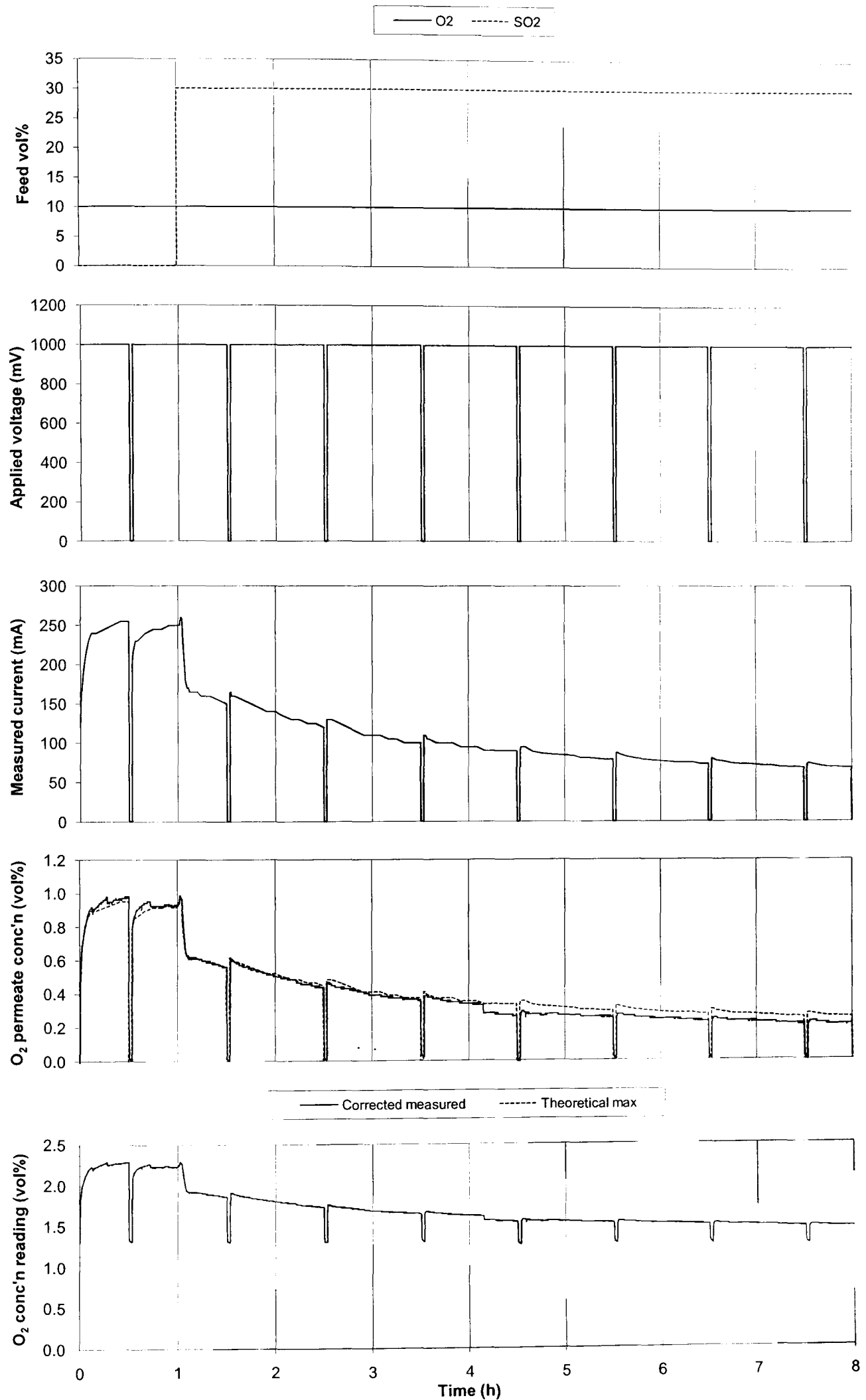


Figure 8.47: YSZ/Pt pellet exposed to SO₂ and O₂ at 850°C - GEM ink

XPS data

Figure 8.48 shows the XPS wide scan taken after application of the platinum electrodes. In comparison to previous scans where the Metalor ink was used (Figures 8.34 and 8.35) it can be seen that yttrium and zirconium have not been detected here. Importantly, bismuth was also not detected, confirming that it is not present in this new ink. Because the YSZ was not detected, there was initially a concern that the electrode firing procedure had inadvertently produced a dense platinum layer. However, as the following section shows, it was found through SEM imaging that this was not the case and in fact a much more prominent platinum layer had been deposited, shielding the YSZ surface from analysis using XPS. Four points were analysed using XPS with no significant difference in the spectra obtained at each point, indicating that the electrode coverage is much more complete with the GEM ink than the Metalor ink.

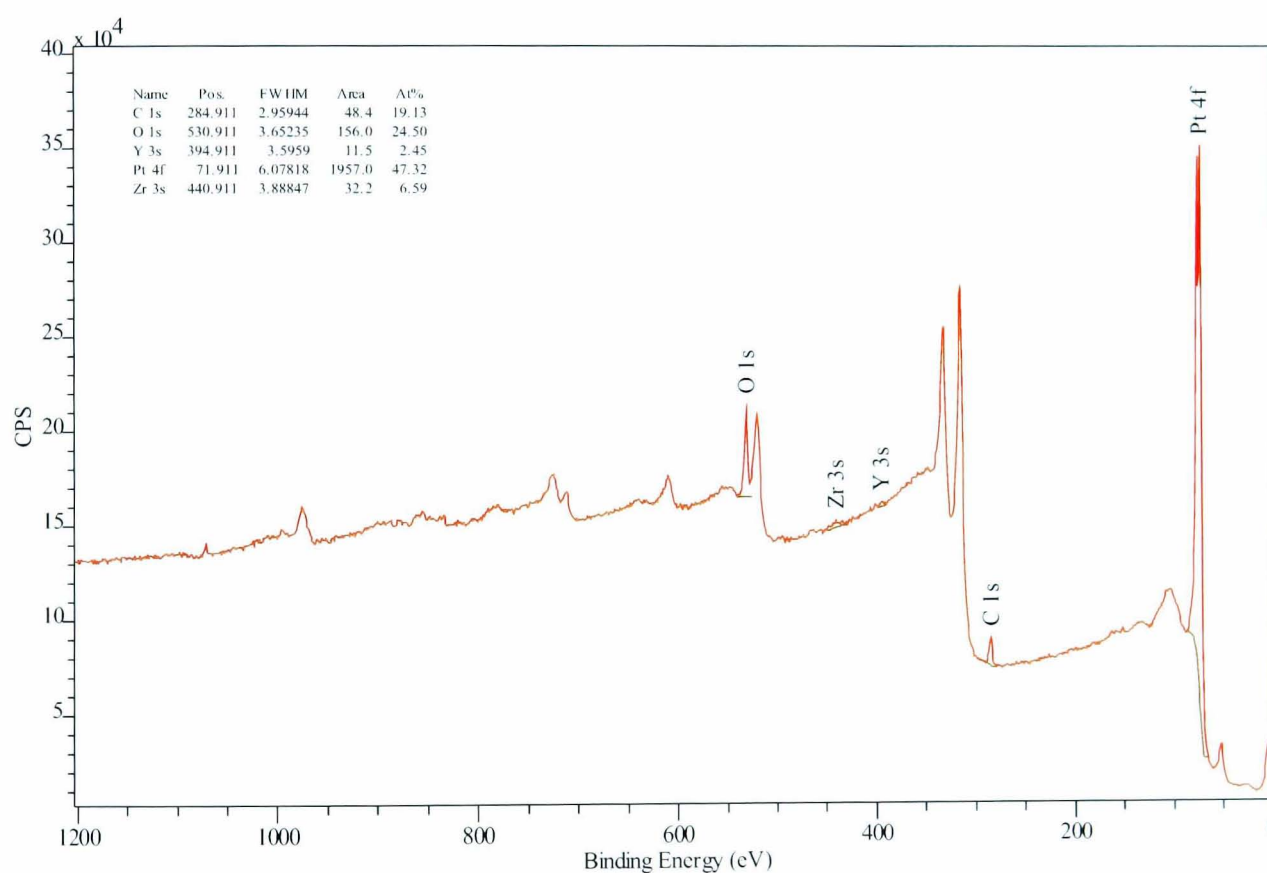


Figure 8.48: XPS wide scan of unused YSZ/Pt pellet (GEM ink)

Following exposure of the pellet to SO₂, further XPS spectra were taken. It was possible to remove the platinum electrode from part of the feed side surface by peeling it away. Hence, spectra are presented from both the electroded (Figure 8.50) and non-electroded (Figure 8.49) feed side surface. Both spectra indicate the presence of sulphur on both the platinum and YSZ surface. It seems most likely, now that bismuth

is no longer present in the platinum ink, that the sulphur seen in the XPS spectra can be attributed to sulphurous species adsorbed on to the pellet surfaces. Additionally, because helium was flowed across the feed side surface post-experiment until the rig was disassembled, the possibility that the sulphur seen on the surface was as a result of post-experimental inadvertent exposure has been discounted.

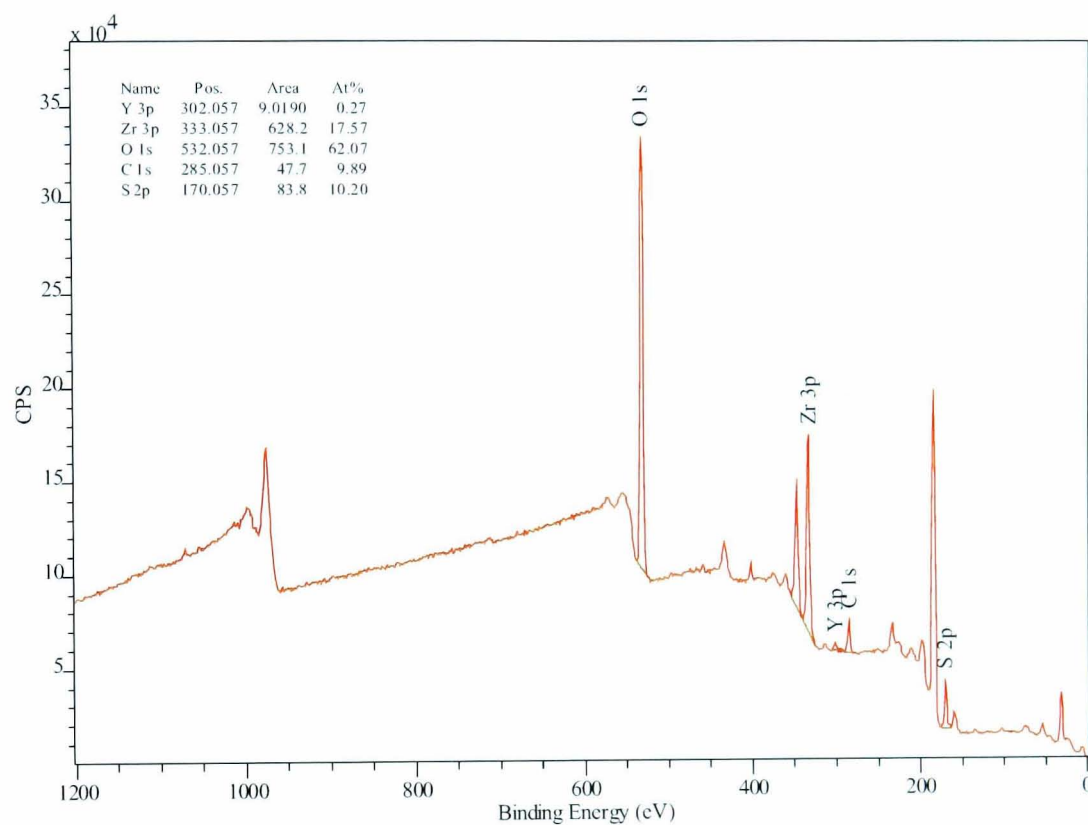


Figure 8.49: XPS wide scan of 850°C SO₂ exposed YSZPt pellet (GEM ink, platinum removed)

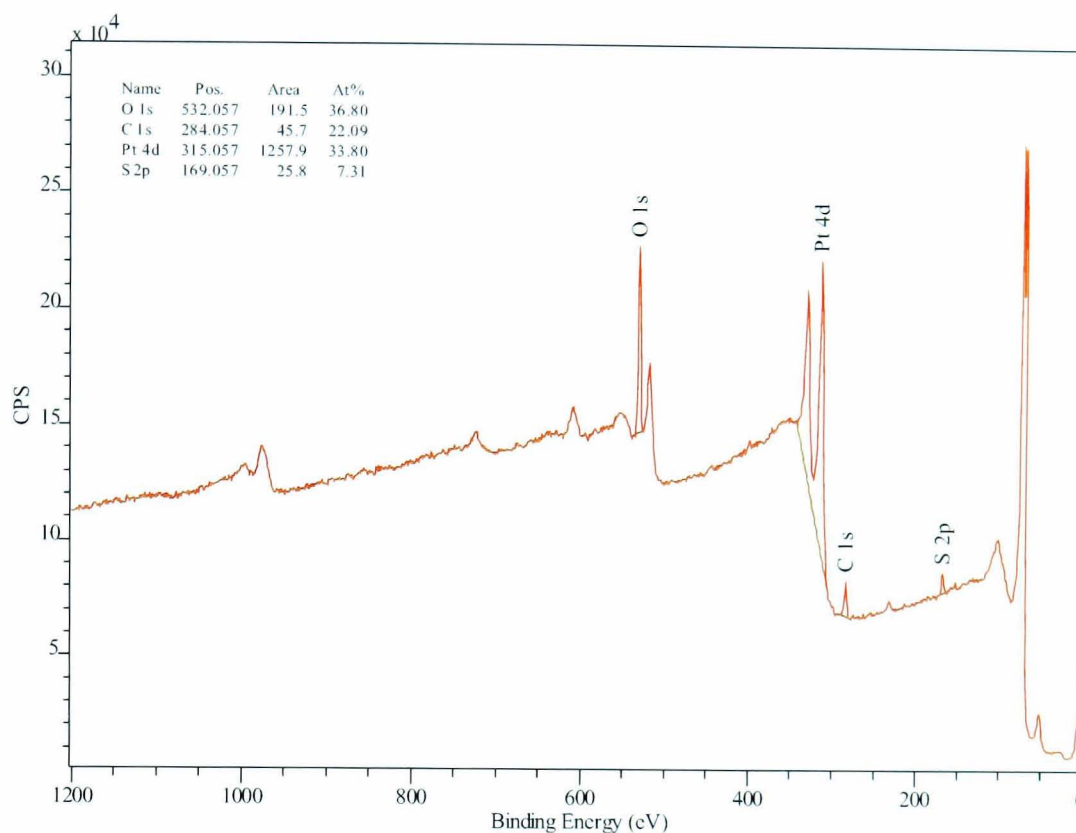


Figure 8.50: XPS wide scan of 850 °C SO₂ exposed YSZ/Pt pellet (GEM ink, platinum in place)

SEM images

As with the previous run using Metalor ink, SEM images were taken before and after SO₂ exposure of the pellet. There is a marked difference in the coverage and porosity of the platinum electrode between the two inks. Comparing Figure 8.51 with 8.41 and Figure 8.52 with 8.39, taken at 1500x and 3000x magnification respectively, shows the vastly improved platinum coverage achieved with the GEM ink. In addition, these images explain why yttria and zirconia were not detected in the pre-exposure XPS analysis. The increased electrode thickness and tortuosity make the likelihood of obtaining YSZ characteristics by XPS analysis much less likely than with the previous ink. The operator of the SEM indicated that the surface coverage appeared to be similar across the pellet surface, unlike the variations in electrode coverage that were achieved with the Metalor ink.

When the feed side of the pellet was imaged following the SO₂ exposure (Figures 8.53 and 8.54) there were no significant changes in the appearance of the surface. The focussing of the images taken after SO₂ exposure is slightly worse than that of the pre-exposure images, making identification of individual features more difficult.

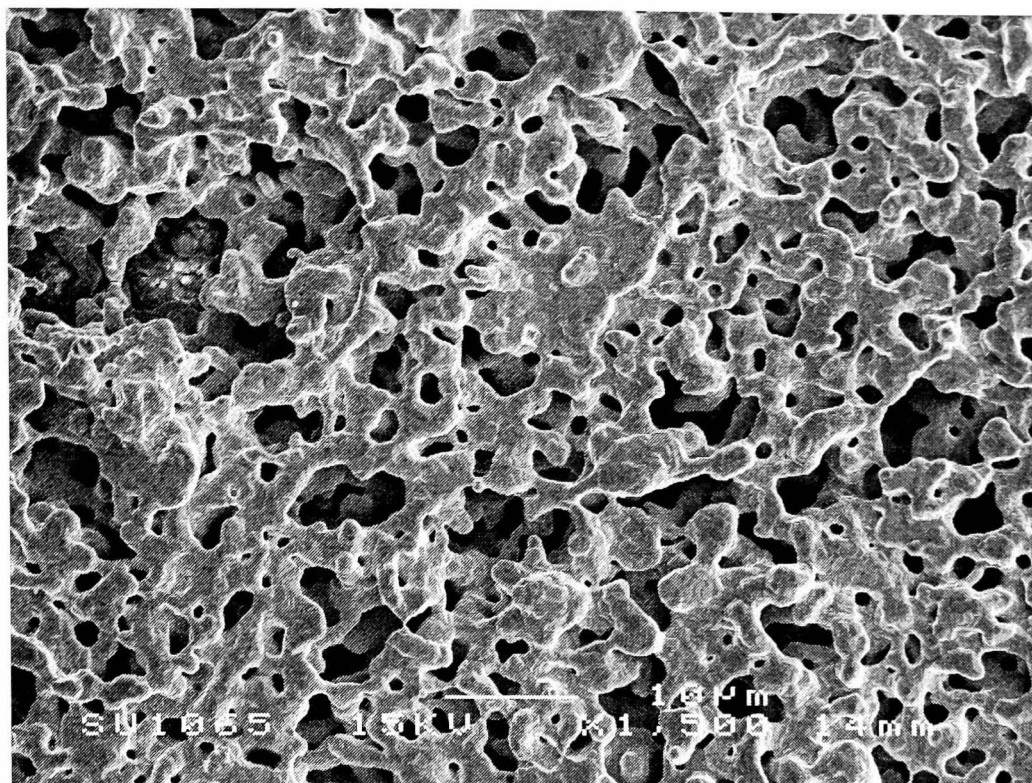


Figure 8.51: SEM image of electroded YSZ pellet (GEM ink), 1500x magnification, JEOL6400 SEM

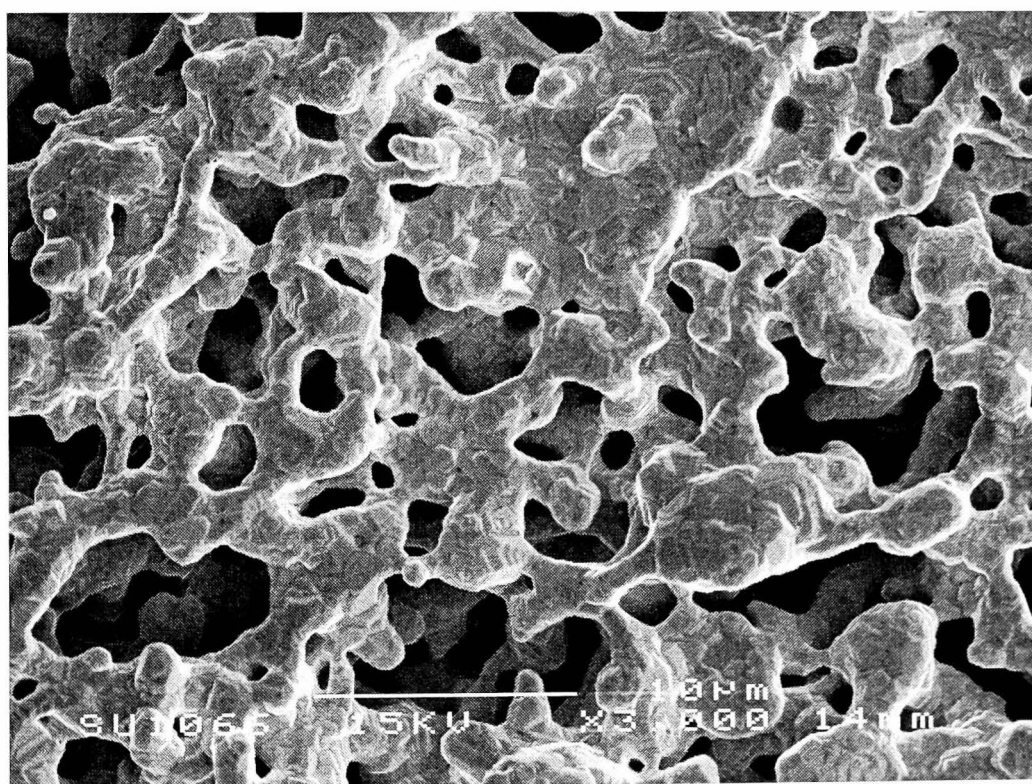


Figure 8.52: SEM image of electroded YSZ pellet (GEM ink), 3000x magnification, JEOL6400 SEM

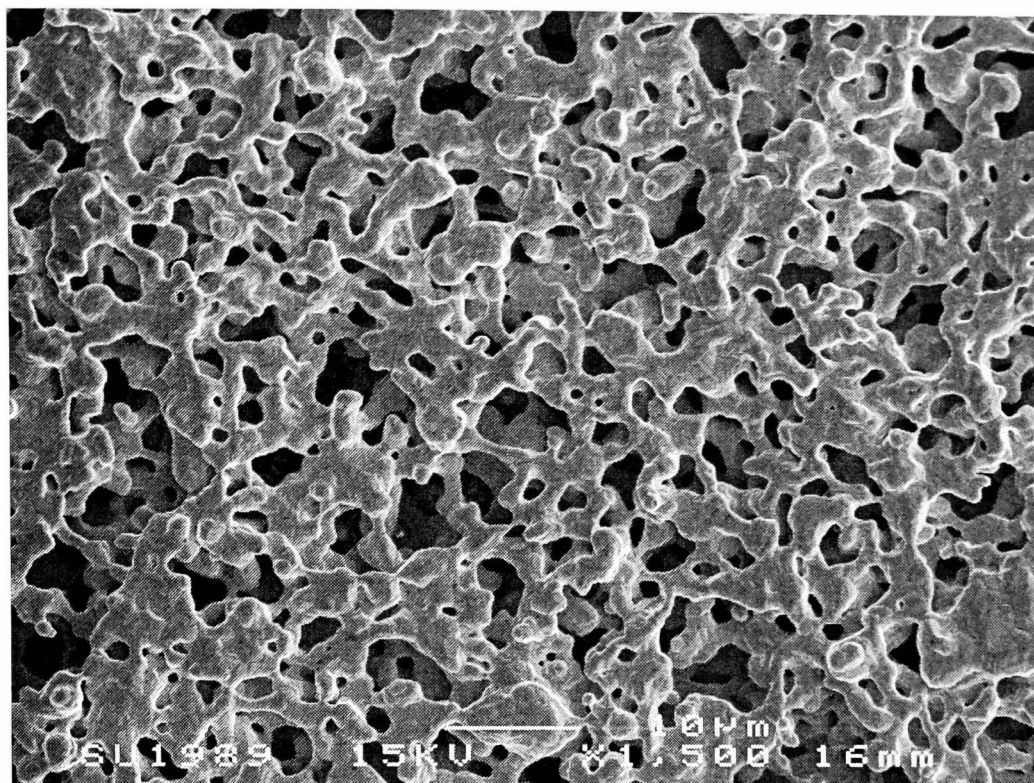


Figure 8.53: SEM image of SO₂ exposed YSZ pellet (GEM ink), 1500x magnification, JEOL6400 SEM

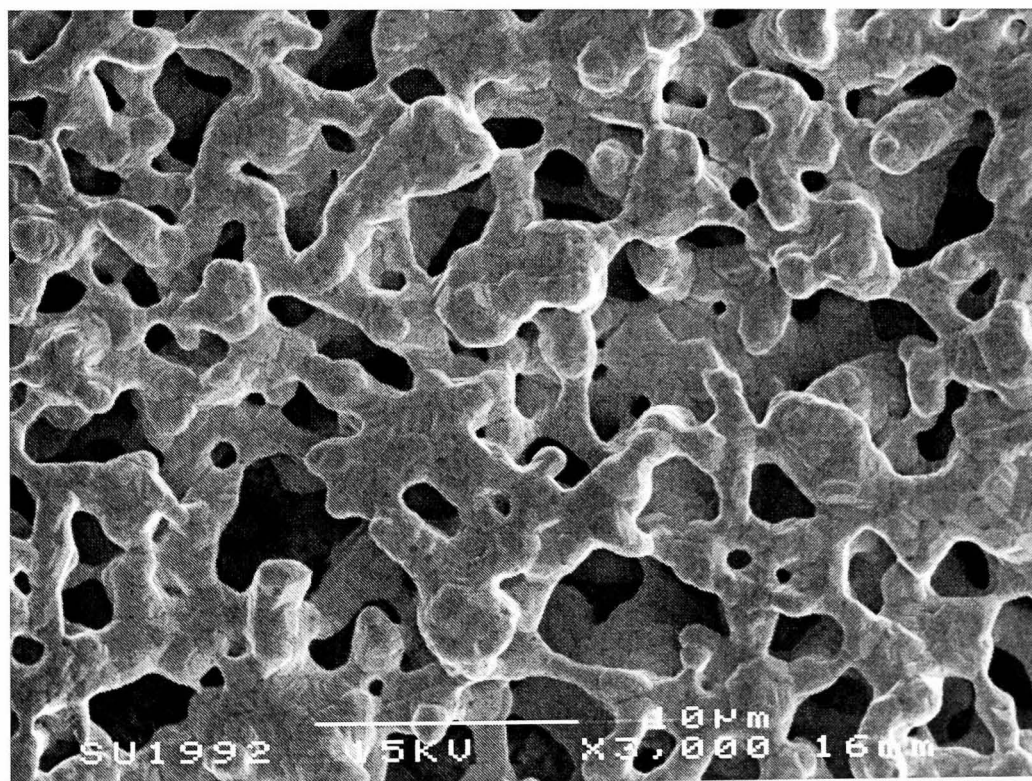


Figure 8.54: SEM image of SO₂ exposed YSZ pellet (GEM ink), 3000x magnification, JEOL6400 SEM

XRD data

Because of limited equipment availability, a cobalt radiation source was used to acquire an XRD spectrum for the feed side following SO₂ exposure. Figure 8.55 compares the post-exposure spectra for the GEM and Metalor inked pellets. The comparison is made of $1/D$ values (where D = interplanar spacing), since this is independent of the radiation wavelength employed. There are two features to be noted. Firstly, the platinum peaks are relatively stronger than the zirconia peaks with the GEM ink. As with the XPS spectrum, this can be attributed to the increased thickness and tortuosity of the deposited platinum electrodes with the GEM ink, decreasing the response from the underlying YSZ. Secondly, it can be seen that there is a shift in the position of the peaks between the Metalor and GEM pellets. The most likely cause for this shift is a difference in the sample height in the diffractometer. Small differences in sample height can cause significant peak shifts and it is possible that the sample was slightly misaligned in the diffractometer.

8.6.4 Conclusions

The primary outcome from this run, borne out by the oxygen permeation/current data, is that the fuel cell grade platinum ink used here exhibits similar performance to the bismuth fritted ink used previously, under these conditions. According to the new literature, the performance and longevity of the membrane in the presence of SO₂ may be increased through the use of different applied potentials to that used here. Hence, the final experimental run repeats this run using the same conditions, except that the applied potential was increased to 2.00V in an effort to promote oxygen adsorption on the platinum surface in preference to SO₂ adsorption.

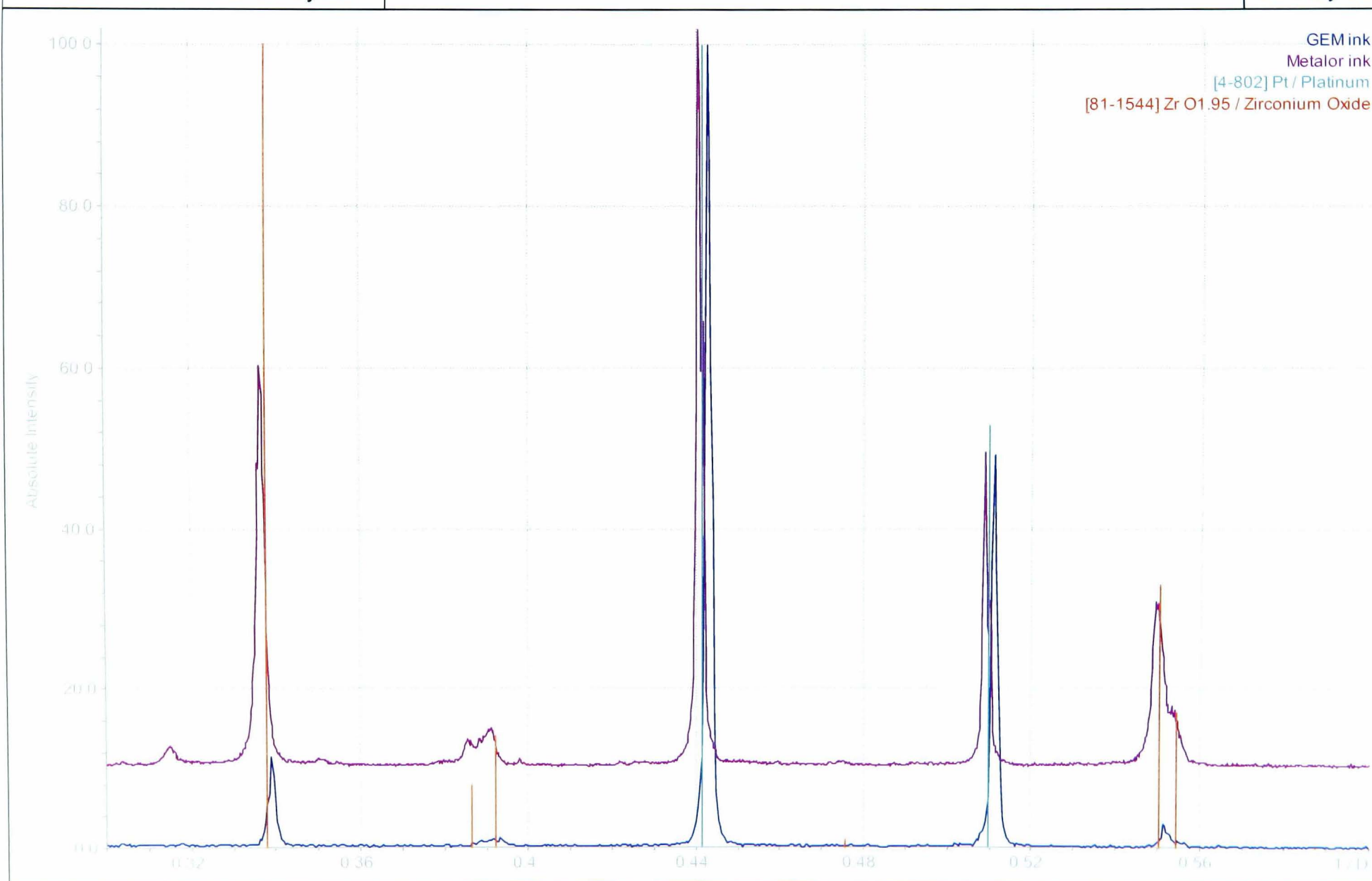


Figure 8.55: Feed side XRD data for YSZ/Pt membranes with Metalor and GEM inks, 850°C SO₂ exposure. Note the use of 1/D for the abscissa, because of the use of Co radiation for the GEM ink spectrum (as opposed to Cu radiation for all other XRD spectra presented). 1/D is radiation wavelength independent.

8.7 SO₂ exposure at 850°C (varying applied potential)

The similar results produced by the membranes electroded with the Metalor and GEM inks (Sections 8.5 and 8.6 respectively) ruled out the presence of bismuth frit as a cause of the oxygen permeation decrease upon exposure to SO₂. A paper by Fu et al. (2009) suggested that the applied potential may have an effect on the amount of SO₂ adsorbed on to the platinum surface. Although time constraints prevented pre and post-analysis of the pellet, it was decided to carry out a further test to identify the change in performance, if any, with varied applied potentials.

8.7.1 Aim

The aim of this experiment was to determine if the decrease in oxygen permeation performance previously observed was related to the applied potential across the membrane. This was achieved by repeating the previous experiment but with a higher applied voltage.

8.7.2 Method

The rig was set up as for all previous experiments. The furnace was heated to 850°C and the feed set to 10% O₂ in He (50ml/min total) and the permeate side fed with 100ml/min of pure He. 2V was applied for one hour, after which the feed composition was changed to 10% O₂ and 30% SO₂ in He (50ml/min total).

In the later stages of the experiment, once the response of the membrane at 2.00V had been adequately recorded, the applied voltage was reduced to 1.50V. Additionally, brief periods of reversed polarity (one of 30 seconds and one of 2 minutes) at 1.50V were applied. A forward voltage of 3.00V was also applied for 2 minutes.

As with previous experiments, the external electrical circuit was opened for 2 minutes per hour in order to establish the oxygen analyser reading corresponding to zero induced flow. This enabled the calculation of the "corrected" permeate oxygen concentration to which the current flowing is compared.

8.7.3 Results

The experimental data is presented in the familiar format in Figure 8.57. The current flowing equalised at the end of the one hour He–O₂ feed period. The current recorded at the end of the one hour He–O₂ period at 2V (640mA) is over 2.5 times that recorded

under otherwise identical conditions at 1V (250mA). This indicates that the resistance of the system is not constant under varying voltages.

The change in current and permeate oxygen concentration upon addition of SO₂ to the feed (after 1 hour of the experiment) follows a different profile to that observed previously with 1V (Figure 8.56). After an initial drop from 640mA to 500mA, the current (and permeate oxygen concentration) began to climb again, stabilising at 560mA. 30 minutes after adding the SO₂, the current had declined slightly to 550mA. However, the effect of the 2 minute open circuit period was the opposite to that previously observed at 1V operation. With 1V operation, the current immediately following the closing of the circuit again was higher than immediately before the circuit was opened. At 2V the opposite was true. It can be hypothesised that by opening the circuit, the SO₂ adsorption retarding effect caused by the high applied voltage is lost and hence there is a significant drop in performance that is not recovered upon reapplication of the voltage. The same effect is seen later in the test when 1.5V is being applied, albeit to a lesser extent.

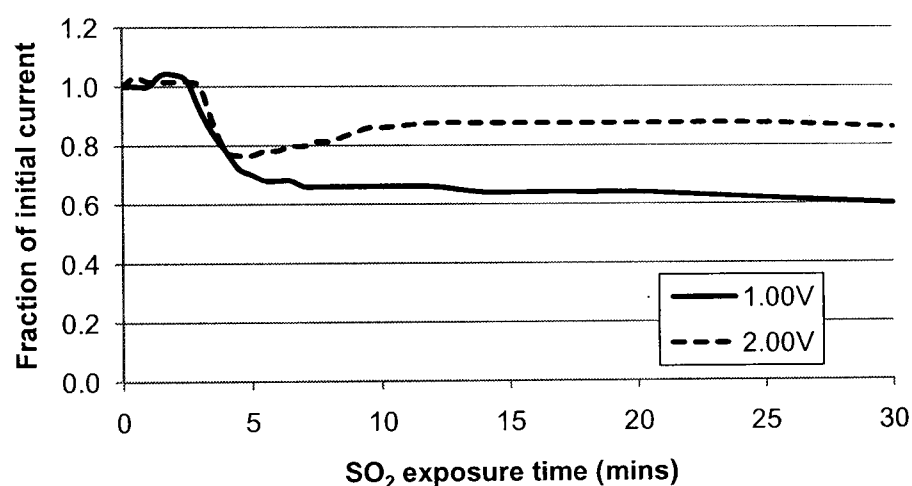


Figure 8.56: YSZ/Pt pellet (GEM ink) exposed to SO₂ and O₂ at 850°C - comparison of current upon SO₂ application at 1V and 2V applied potential. Current at point of SO₂ addition to feed taken as baseline.

The variable resistance of the system was demonstrated once again during the brief period of 3V applied voltage, when the recorded current (630mA) is 4.2 times that recorded at 1.5V immediately before the voltage increase (150mA). Examining the graphs it can be seen that the rate of decrease in measured current (and permeate oxygen concentration) is similar before and after the 3V period, but there was a performance increase following the 3V period. This raises the possibility of operating at a relatively low voltage but with short periods of high voltage in order to maintain the membrane performance at a high level.

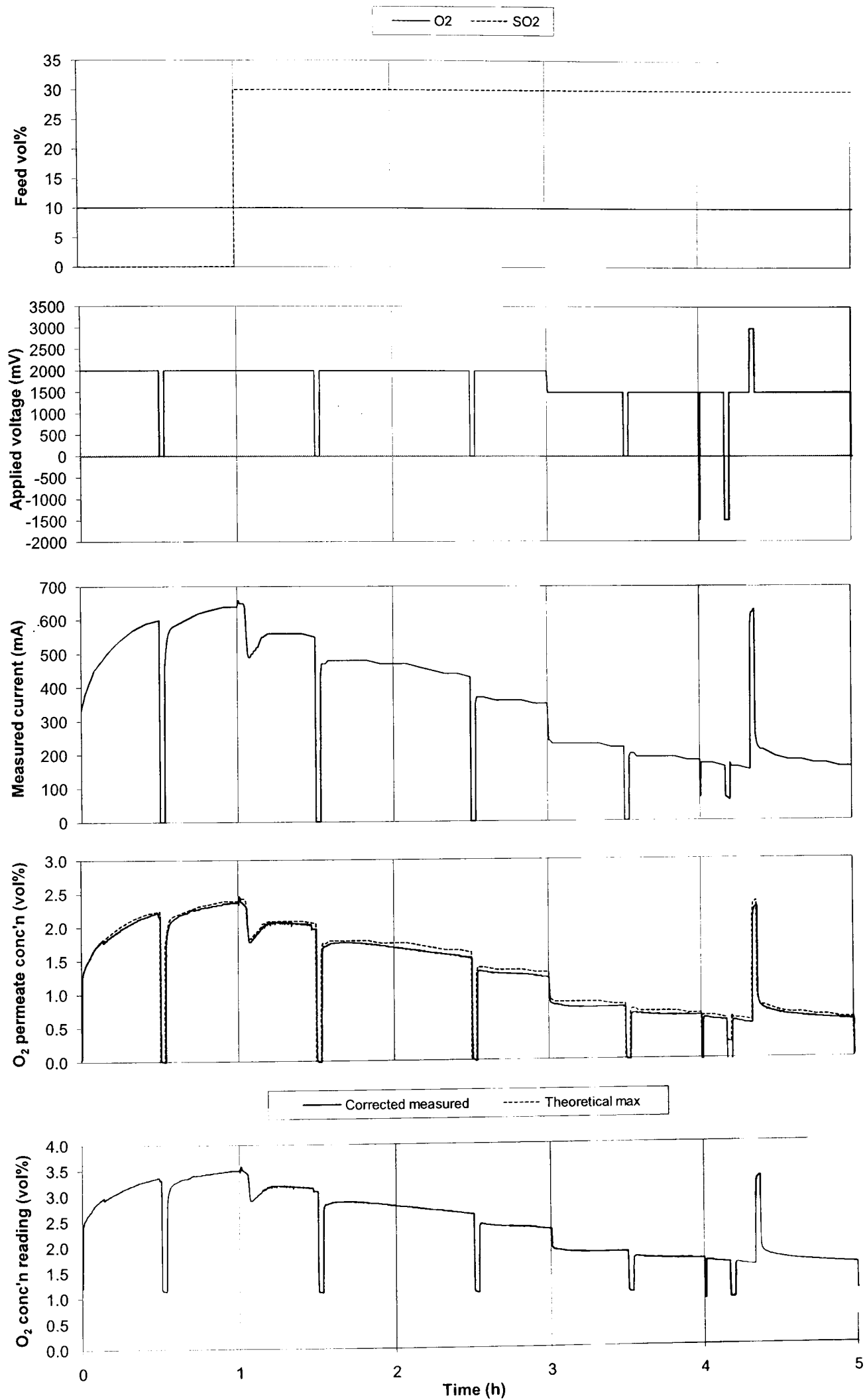


Figure 8.57: YSZ/Pt pellet exposed to SO₂ and O₂ at 850°C - GEM ink, variable voltage

As was discussed in Section 7.5.2, the decomposition potential of YSZ is in the region 2.0-2.5V, however there is little literature regarding the kinetics of the decomposition. During the commissioning tests with He–O₂ mixtures at 700°C, rapid increases in the current flow (on the order of seconds) was observed at 6V, with slower current increases at 4-5V (Figure 7.16). This led to blackening of the YSZ electrolyte, indicating that YSZ reduction had taken place. The literature indicates that a small amount of YSZ reduction may be beneficial, as it increases electronic conductivity at the YSZ-Pt interface. In the commissioning test, 5V appears to be the optimum voltage for a small amount of electrolyte decomposition. That voltage corresponded to a nominal current of 600mA. That test was however conducted at 700°C. Applying 5V to a similar membrane at 850°C would produce a much higher current, because of the increased ionic conductivity of the electrolyte. In this test, 600mA current was recorded during the first hour, when the He–O₂ mixture and 2V was used. Also, 600mA was achieved during the brief period of 3V application later during the SO₂ exposure period. Literature suggests that stable operation is possible at a current density of 300mA/cm² (equivalent to 763mA with this membrane) and membrane breakdown occurs at 450mA/cm² (equivalent to 1150mA with this membrane).

If membrane “cleaning” is performed before the membrane resistance has increased dramatically, the application of a current density equivalent to the maximum found to allow stable operation (around 750mA in this case) should not require a voltage high enough to cause excessive YSZ decomposition. It is proposed that future work should concentrate on evaluating the long-term operation of the membrane at 850°C with a voltage of 1V or less, but with short periods of high current density of around 300mA/cm² in an attempt to reduce the membrane resistance to a pre-SO₂ exposure level.

8.7.4 Conclusions

This experiment has shown that the external potential applied to the YSZ membrane affects the current/permeate oxygen concentration profile upon addition of SO₂ to the feed side. At an applied voltage of 2.00V the initial decline in current flowing was followed by a recovery period not seen at 1.00V. The subsequent decline was also slower until the circuit was opened for 2 minutes, at which point there was a step decline in current. The performance profile at 2V without opening the circuit should be investigated in order to determine the membrane longevity over longer timescales. During the second half of the SO₂ exposure time, a voltage of 1.50V was applied. There was also a step decline in current during the open circuit periods at 1.50V. Ap-

plication of 3.00V for two minutes caused an increase in performance. A potential mode of operation could therefore be to use a relatively low constant voltage with brief periods of higher voltage in order to recover the membrane's performance.

8.8 Overall conclusions of experimental programme

YSZ pellets, with platinum electrodes, conduct oxygen when subjected to an applied voltage in the range 1.00-2.00V, temperatures of 700 – 900°C, a feed of 30% SO₂, 10% O₂ and 60% He at atmospheric pressure and a pure helium sweep gas. A YSZ pellet with gold electrodes was also shown to conduct oxygen under similar conditions but at 800°C only.

Within 5 minutes of adding SO₂ to the feed gas a rapid decline in O₂ permeation flux began. Under an applied voltage of 1.00V the rapid decline was followed after a few minutes by a slower, slowing decline in performance until the change in permeate O₂ concentration approached steady state. A test at 2.00V showed a different response, with a shorter initial decline followed by a partial recovery and very slow decline following this. A short period at 3.00V appeared to partially recover the O₂ permeation performance.

Two types of platinum ink were used for applying the membrane electrodes, a bismuth fritted ink and a fuel cell grade ink containing no bismuth frit. Permeation results were very similar for membranes using each type of ink, therefore the presence of bismuth frit was discounted as a reason for the decrease in O₂ permeation.

XPS analysis showed the presence of sulphur on the surface of the membrane following SO₂ exposure. Since bismuth did not appear to affect the membrane performance, and in the light of new literature, it is thought that SO₂ adsorption on to the platinum and YSZ surface causes the performance reduction and that the application of higher voltages than 1.00V causes O₂ adsorption to be preferred over SO₂ adsorption on to the platinum surface. Brief periods of high current density, caused by increasing the applied voltage, may therefore recover the performance of the membrane during extended periods of operation.

Chapter 9

Overall conclusions and future work

The majority of hydrogen is currently produced by reforming fossil fuels. This is not a sustainable technology for massive scale hydrogen production for a “hydrogen economy” where transportation such as buses and private cars use fuel cells for motive power, since it creates significant amounts of CO_2 .

The high temperature thermal decomposition of sulphuric acid is a process common to a number of thermochemical cycles that are candidates for more sustainable massive scale hydrogen production. They use only water, heat and possibly electricity to produce hydrogen, with no waste streams. Equilibrium calculations have shown that very high temperatures are required to achieve high SO_2 yields in this endothermic process (Section 2.8). This currently limits the process to utilising concentrated solar heat. It is proposed that incorporating a membrane separation into the process could increase the SO_2 yield at a given temperature above the equilibrium value. This would enable the use of heat sources with lower maximum temperatures and allow throughput to be increased with very high temperature high sources.

Porous membranes are not suitable for this process, as the similar molecular diameters of SO_3 and SO_2 make separation difficult and selectivities would therefore be low. Although porous membranes can separate SO_2 and O_2 , it was anticipated that dense membranes could do so with higher selectivities.

Metal oxide stability calculations showed that the majority of metals used to fabricate dense oxygen separation membranes would not be stable under the process conditions required here. However, yttria-stabilised zirconia (YSZ) and platinum (for the electrodes) should be stable. YSZ is primarily an ion-conductor and requires an ex-

ternal electron conduction path.

The experiments carried out in this work on platinum electroded YSZ pellets showed that the oxygen permeation achievable with an $\text{SO}_2/\text{O}_2/\text{He}$ feed (30% SO_2) is lower than that achievable with an O_2/He feed, when an external potential of 1.00V is applied and at operating temperatures in the range 800-900°C. A steep initial decline in oxygen permeation was observed in the first few minutes upon adding SO_2 to the feed, with a more gradual decline following.

The decrease in membrane performance was attributed to SO_2 adsorption on to the platinum and YSZ surfaces. Literature indicated that SO_2 adsorption may be reduced or eliminated through variation of the applied potential across the membrane. A final experiment carried out to investigate this concluded that applying a higher potential (e.g. 2.00V) across the membrane can reduce the effect that SO_2 has on the oxygen permeation. Brief periods of even higher potential (in this case 3.00V) caused a recovery in membrane performance and this should be investigated as a potential future mode of operation.

9.1 Future work

It has been shown that Pt/YSZ membranes can be made to conduct oxygen from a feed of SO_2 , O_2 and He with varying degrees of degradation. Now that the basic feasibility of the process has been demonstrated, further work is required to stabilise and increase the performance of the membrane.

9.1.1 Membrane performance recovery

The final experiment indicated that the degradation at 850°C with an applied potential of 2.00V was slower than that at 1.00V. Opening the electrical circuit during SO_2 exposure at 2.00V caused a step change in O_2 permeation capability upon reconnection of the circuit. It is believed that the higher potential at the electrode retards the adsorption of SO_2 on to the surface and removing this voltage, albeit briefly, allows significant SO_2 adsorption on to the surface, increasing the mass transfer resistance and reducing performance. A full-length experiment, similar to those carried out at 1.00V, should be carried out at 2.00V in order to document the rate of decrease of oxygen permeate concentration compared to that observed at 1.00V. These experiments should be carried out without the hourly open circuit periods, in order to remove the effect these may have on the rate of SO_2 adsorption on to the platinum surface. The

oxygen analyser reading prior to beginning the initial hour-long period of He–O₂ application should be used for concentration correction purposes.

Similarly, during the experimental SO₂ exposure at 1.50V, it was observed that a brief period at 3.00V caused an apparent step increase in membrane oxygen flux upon returning to the lower voltage. Coming at the end of a test run that had investigated several factors, this performance increase can only be considered qualitatively. Given that the electrical power applied to this process increases the power requirements of the whole cycle and hence decreases overall efficiency, the ability to use brief periods of increased voltage to recover membrane performance and hence allow operation with a relatively low continuous applied voltage would be advantageous. This has been discussed in Section 8.7.3, with the conclusion that the short high voltage periods should use the voltage required to attain a specified current density at which stable operation is known to be possible. A run should be performed at 850°C with the same feeds as used previously and an applied voltage of 1.00V, with short periods of high current density (300mA/cm², around 750mA for the membranes being used here). The length of the high current periods could start relatively long (e.g. 2 minutes in every 15) and, if successful, be shortened to find the minimum length of time required to maintain the membrane performance. As a follow-on from this, the run could be repeated with lower standard voltages, since the lower the standard voltage the lower the power requirements of the process.

An extension of this principle is passive operation, as discussed earlier in this thesis. It may be possible, with an adequate oxygen concentration gradient, to transfer oxygen into the permeate stream without an externally applied voltage (see Section 7.3). This could be investigated using the existing apparatus by removing the power supply. As the potential induced across the membrane during passive operation would be small, it is expected that the SO₂ adsorption problems already covered would apply under this mode of operation. Once short-term passive operation has been demonstrated, it may be possible to recover the membrane using short periods of applied potential. If this can be shown to be effective, this could be an energy efficient method of performing oxygen separation using a YSZ electrolyte.

9.1.2 Progression from pure gas feeds to in-situ acid decomposition

Following the investigations into membrane recovery through voltage variation, the operation of the membrane in the presence of acid decomposition products should be determined. This would require the substitution of the pure gas feeds to the membrane feed side with the stream produced by passing aqueous sulphuric acid through

a heterogeneous catalyst bed.

Detailed design of such a rig is beyond the scope of this work, but the basic arrangement is demonstrated in Figure 9.1. The amount of concentrated (98wt%) sulphuric

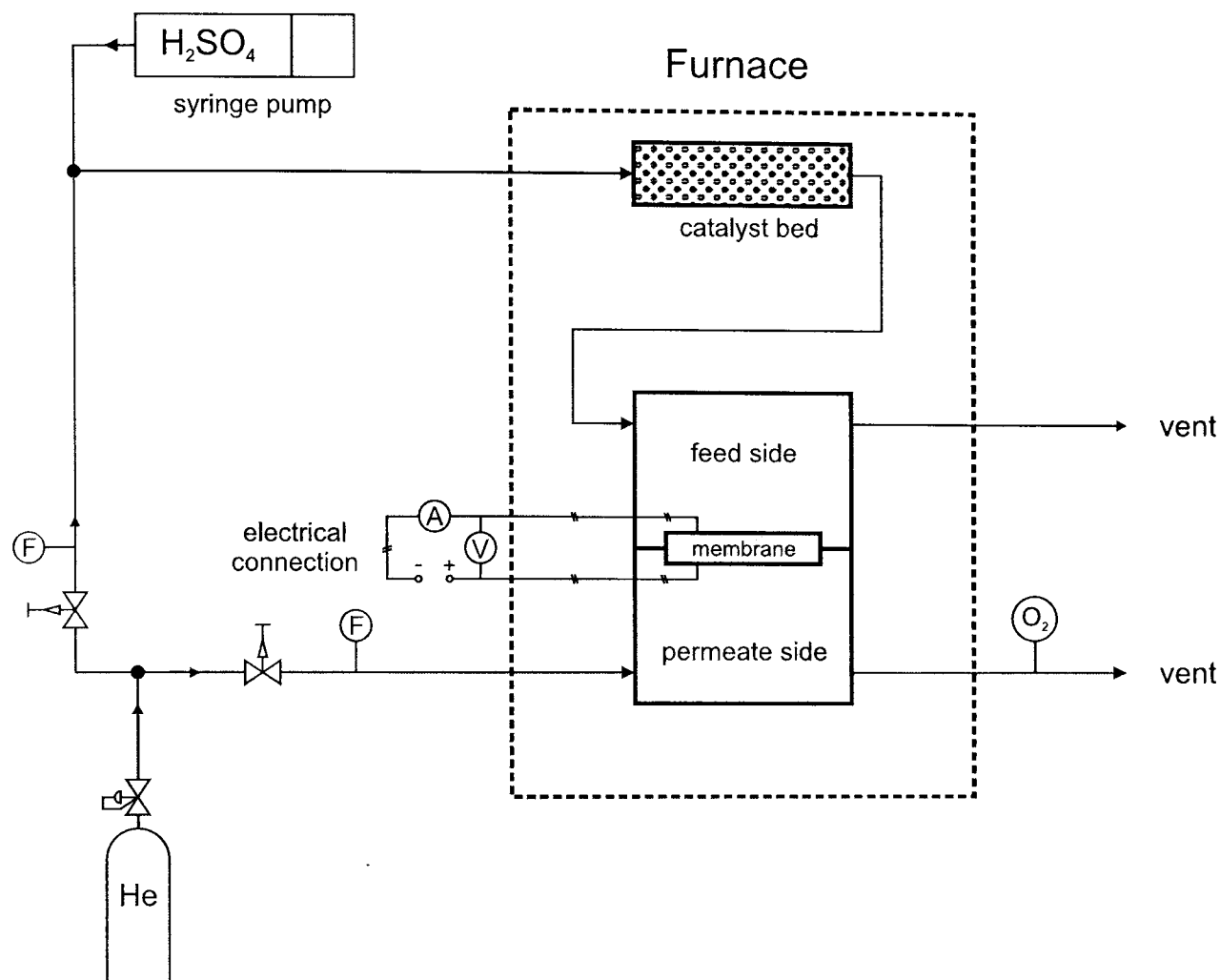


Figure 9.1: Schematic of experimental rig extension to include in-situ acid decomposition

acid required to achieve equivalent SO₂ flow to that used in the pure gas experiments has been calculated. Assuming that the equivalent of 15ml/min SO₂ at RTP is required, and 80% SO₂ yield is achieved (the approximate yield at 1 atm pressure and 850°C temperature), 2.546 ml/hr of 98wt% H₂SO₄ would be required to be fed to the catalyst bed.

A syringe pump would be well suited to delivering such a low liquid flowrate to the catalyst bed. An alternative would be a diaphragm pump being fed from a storage bottle of acid. Whilst previous work investigating H₂SO₄ decomposition catalysts has tended to use an inert carrier gas, this should not be used here as it would artificially dilute the flow to a concentration below that seen in fabricated acid decomposition processes.

In order to estimate the catalyst volume required, the gas flow rate through the bed was calculated. It was assumed, for flow rate purposes, that the H_2SO_4 supplied to the process was fully decomposed. The 2.546 ml/hr of 98wt% H_2SO_4 equates to a gas flow rate of 184.5 ml/min through the catalyst bed at operating temperature and pressure.

The amount of catalyst that should be used, or the volume it should occupy, can now be estimated based on values from the literature. Barbarossa et al. (2006) used excess catalyst in order to attain as close to equilibrium conversion as practicable. The residence time in the catalyst bed was seven seconds. Duplicating that residence time for this rig would require a catalyst bed volume of 21.5 cm^3 . Ginosar et al. (2007) deliberately used a high space velocity in order that effects would not be masked by excess catalyst. Since equilibrium conversion is desired here, the data from that paper cannot be applied here. Tagawa & Endo (1989) used a space velocity of 4300 (ml/hr NTP gas per cm^3 catalyst). The gas contained 4 mol% SO_3 . If this space velocity translates to 172 (ml/hr H_2SO_4) per cm^3 catalyst, 6.54 cm^3 catalyst would be required for this rig. Taking the larger value for safety, a quartz tube with a catalyst-packed zone of at least 21.5 cm^3 should be used.

Repeating the tests carried out with pure gases would give a strong indication of whether the membranes under investigation are indeed suitable for use with the sulphuric acid decomposition process. If the relatively short repeated tests proved positive, the next stage would be to assess the membrane's performance under long term use.

9.1.3 Thin supported membranes

The experiments carried out thus far have involved the application of an external potential to drive the oxygen pumping effect across the membrane. The system was not optimised for maximum efficiency. The use of thick YSZ pellets meant that the resistance of the electrolyte was high. The use of thinner pellets, or thin YSZ films supported on a porous material such as silica, should increase the oxygen flux by reducing that resistance. If Pt/YSZ proves to be a viable oxygen separation membrane combination, then the next logical step in its development would be to reduce the membrane thickness to increase the oxygen permeate flux. This would decrease the membrane area for a given oxygen removal duty, reducing the size and cost of the system.

References

- Abanades, S., Charvin, P., Flamant, G. & Neveu, P. (2006), 'Screening of water-splitting thermochemical cycles potentially attractive for hydrogen production by concentrated solar energy', *Energy* **31**(14), 2805–2822.
- Adler, S. B. (2004), 'Factors governing oxygen reduction in solid oxide fuel cell cathodes', *Chemical Reviews* **104**(10), 4791–4843.
- Agoudjil, N., Benmouhoub, N. & Larbot, A. (2005), 'Synthesis and characterization of inorganic membranes and applications', *Desalination* **184**(1-3), 65–69.
- Agrawal, R., Offutt, M. & Ramage, M. P. (2005), 'Hydrogen economy - an opportunity for chemical engineers?', *AIChE Journal* **51**(6), 1582–1589.
- Ailleret, F. (2004), Comparison of energy systems using life cycle assessment, Technical report, World Energy Council.
- Arima, T., Fukuyo, K., Idemitsu, K. & Inagaki, Y. (2004), 'Molecular dynamics simulation of yttria-stabilized zirconia between 300 and 2000K', *Journal Of Molecular Liquids* **113**(1-3), 67–73.
- Armor, J. N. (1998), 'Applications of catalytic inorganic membrane reactors to refinery products', *Journal Of Membrane Science* **147**(2), 217–233.
- Badwal, S. P. S. & Ciacchi, F. T. (2001), 'Ceramic membrane technologies for oxygen separation', *Advanced Materials* **13**(12-13), 993–996.
- Barbarossa, V., Brutti, S., Diamanti, M., Sau, S. & De Maria, G. (2006), 'Catalytic thermal decomposition of sulphuric acid in Sulphur-Iodine cycle for hydrogen production', *International Journal of Hydrogen Energy* **31**, 883–890.
- Bischoff, B. L., Forsberg, C., Wilson, D. F., Trowbridge, L. D. & Mansur, L. K. (2005), Applicability of inorganic membranes for improving the sulfur-iodine process

- for the production of hydrogen using nuclear energy, in 'AIChE Spring National Meeting', American Institute of Chemical Engineers, Atlanta, GA, United States.
- Brittain, R. D. & Hildenbrand, D. L. (1983), 'Catalytic decomposition of gaseous SO_3 ', *Journal Of Physical Chemistry* **87**(19), 3713–3717.
- Brutti, S., De Maria, G., Cerri, G., Giovannelli, A., Brunetti, B., Cafarelli, P., Semprin, E., Barbarossa, V. & Ceroli, A. (2007), 'Decomposition of H_2SO_4 by direct solar radiation', *Industrial and Engineering Chemistry Research* **46**(20), 6393–6400.
- Buckingham, B. (2009), Personal communication.
- Chen, F., Mourhatch, R., Tsotsis, T. T. & Sahimi, M. (2008), 'Experimental studies and computer simulation of the preparation of nanoporous silicon-carbide membranes by chemical-vapor infiltration/chemical-vapor deposition techniques', *Chemical Engineering Science* **63**(6), 1460–1470.
- Ciacchi, F. T., Badwal, S. P. S. & Zelizko, V. (2002), 'Tubular zirconia-yttria electrolyte membrane technology for oxygen separation', *Solid State Ionics* **152**, 763–768.
- Coen Porisini, F. (1983), 'Long-term corrosion tests of materials for thermal decomposition of sulphuric acid', *International Journal of Hydrogen Energy* **8**(10), 819–828.
- Coen Porisini, F. (1985), 'Corrosion resistance of Si-containing Ni-Fe-Cr alloys used as materials for the thermal decomposition of sulphuric acid', *International Journal of Hydrogen Energy* **10**(4), 255–262.
- Coen Porisini, F. (1989), 'Selection and evaluation of materials for the construction of a pre-pilot plant for thermal decomposition of sulfuric acid', *International Journal Of Hydrogen Energy* **14**(4), 267–274.
- Coulson, J., Richardson, J., Backhurst, J. & Harker, J. (1999), *Chemical Engineering*, Vol. 1, 6th edn, Butterworth-Heinemann, Oxford.
- Cutler, R. A. & Meixner, D. L. (2003), 'Ceria - lanthanum strontium manganite composites for use in oxygen generation systems', *Solid State Ionics* **159**(1-2), 9–19.
- de Vos, R. M., Maier, W. F. & Verweij, H. (1999), 'Hydrophobic silica membranes for gas separation', *Journal Of Membrane Science* **158**(1-2), 277–288.
- Dean, J. (1999), *Lange's Handbook of Chemistry*, 15th edn, McGraw-Hill.
- Dong, X. L., Zhang, C., Chang, X. F., Jin, W. Q. & Xu, N. P. (2008), 'A self-catalytic membrane reactor based on a supported mixed-conducting membrane', *Aiche Journal* **54**(6), 1678–1680.

- Drioli, E., Basile, A. & Criscuoli, A. (2000), 'High temperature membrane reactors for clean productions', *Clean Products and Processes* **2**(3), 179.
- El-Bousiffi, M. A. & Gunn, D. J. (2007), 'A dynamic study of steam-methane reforming', *International Journal of Heat and Mass Transfer* **50**(3-4), 723.
- Elder, R. & Allen, R. (2009), 'Nuclear heat for hydrogen production: Coupling a very high/high temperature reactor to a hydrogen production plant', *Progress In Nuclear Energy* **51**(3), 500–525.
- Elyassi, B., Sahimi, M. & Tsotsis, T. T. (2008), 'A novel sacrificial interlayer-based method for the preparation of silicon carbide membranes', *Journal Of Membrane Science* **316**(1-2), 73–79.
- Ewan, B. C. R. & Allen, R. W. K. (2005), 'A figure of merit assessment of the routes to hydrogen', *International Journal of Hydrogen Energy* **30**(8), 809.
- Forsberg, C. W. (2003a), 'Hydrogen, nuclear energy, and the advanced high-temperature reactor', *International Journal of Hydrogen Energy* **28**(10), 1073.
- Forsberg, C. W. (2003b), A lower temperature Iodine-Westinghouse-Ispra Sulfur process for thermochemical production of hydrogen, in 'American Nuclear Society Winter Meeting', Oak Ridge National Laboratory, New Orleans, Louisiana, USA.
- Forsberg, C. W., Trowbridge, L., Bischoff, B. & Mansur, L. K. (2004), Sulfur thermochemical processes with inorganic membranes to produce hydrogen, in 'AIChE Spring National Meeting', Oak Ridge National Laboratory, New Orleans, Louisiana, USA.
- Fu, J., Hou, M., Du, C., Shao, Z. G. & Yi, B. L. (2009), 'Potential dependence of sulfur dioxide poisoning and oxidation at the cathode of proton exchange membrane fuel cells', *Journal Of Power Sources* **187**(1), 32–38.
- Fukushima, M., Zhou, Y., Yoshizawa, Y. C. & Hirao, K. (2008), 'Water vapor corrosion behavior of porous silicon carbide membrane support', *Journal Of The European Ceramic Society* **28**(5), 1043–1048.
- Funk, J. E. (2001), 'Thermochemical hydrogen production: past and present', *International Journal of Hydrogen Energy* **26**(3), 185–190.
- Gilron, J. & Soffer, A. (2002), 'Knudsen diffusion in microporous carbon membranes with molecular sieving character', *Journal Of Membrane Science* **209**(2), 339–352.

- Ginosar, D. M., Glenn, A. W. & Petkovic, L. M. (2005), Stability of sulfuric acid decomposition catalysts for thermochemical water splitting, in 'AIChE Spring National Meeting', Idaho National Laboratory, Cincinnati.
- Ginosar, D. M., Petkovic, L. M., Glenn, A. W. & Burch, K. C. (2007), 'Stability of supported platinum sulfuric acid decomposition catalysts for use in thermochemical water splitting cycles', *International Journal of Hydrogen Energy* 32(4), 482.
- Gland, J. L., Sexton, B. A. & Fisher, G. B. (1980), 'Oxygen interactions with the Pt(111) surface', *Surface Science* 95(2-3), 587.
- Goldstein, S., Borgard, J. M. & Vitart, X. (2005), 'Upper bound and best estimate of the efficiency of the Iodine-Sulphur cycle', *International Journal Of Hydrogen Energy* 30(6), 619–626.
- Goldstein, S., Vitart, X. & Borgard, J. M. (2004), 'General comments about the efficiency of the Iodine-Sulphur cycle coupled to a high temperature gas cooled reactor', *International Scientific Journal for Alternative Energy and Ecology* 3(11), 20–27.
- He, T., Lu, Z., Huang, Y., Guan, P., Liu, J. & Su, W. (2002), 'Characterization of YSZ electrolyte membrane tubes prepared by a vacuum casting method', *Journal of Alloys and Compounds* 337(1-2), 231.
- Herle, J., McEvoy, A. J. & Thampi, K. R. (1994), 'Conductivity measurements of various yttria-stabilized zirconia samples', *Journal of Materials Science* 29(14), 3691.
- Hildebrand, J. H. (1976), 'Viscosity of dilute gases and vapors', *Proceedings of the National Academy of Sciences* 73(12), 4302–4303.
- Hirschfelder, J. O., Curtiss, C. F. & Bird, R. B. (1954), *Molecular Theory of Gases and Liquids*, corrected 1st edn, Wiley, New York.
- Huang, C. & T-Raissi, A. (2005), 'Analysis of Sulfur-Iodine thermochemical cycle for solar hydrogen production. Part I: Decomposition of sulfuric acid', *Solar Energy* 78(5), 632–646.
- Hwang, G. J., Kim, J. W., Choi, H. S. & Onuki, K. (2003), 'Stability of a silica membrane prepared by CVD using gamma- and alpha-alumina tube as the support tube in the HI-H₂O gaseous mixture', *Journal Of Membrane Science* 215(1-2), 293–302.
- Ishihara, T., Matsuda, H. & Takita, Y. (1994), 'Doped LaGaO₃ perovskite-type oxide as a new oxide ionic conductor', *Journal Of The American Chemical Society* 116(9), 3801–3803.

- Janek, J. & Korte, C. (1999), 'Electrochemical blackening of yttria-stabilized zirconia - morphological instability of the moving reaction front', *Solid State Ionics* **116**(3-4), 181-195.
- Jeong, Y. H. & Kazimi, M. S. (2007), 'Optimization of the Hybrid Sulfur cycle for nuclear hydrogen generation', *Nuclear Technology* **159**(2), 147-157.
- Joo, J. H. & Choi, G. M. (2008), 'Thick-film electrolyte (thickness < 20 μ m)-supported solid oxide fuel cells', *Journal of Power Sources* **180**(1), 195.
- Julbe, A., Farrusseng, D. & Guizard, C. (2001), 'Porous ceramic membranes for catalytic reactors - overview and new ideas', *Journal Of Membrane Science* **181**(1), 3-20.
- Kale, G. M., Wang, L. & Hong, Y. R. (2003), 'Planar SO_x sensor incorporating a bi-electrolyte couple', *Solid State Ionics* **161**(1-2), 155-163.
- Kharton, V. V., Viskup, A. P., Marozau, I. P. & Naumovich, E. N. (2003), 'Oxygen permeability of perovskite-type Sr_{0.7}Ce_{0.3}MnO_{3- δ} ', *Materials Letters* **57**(20), 3017-3021.
- Kim, J., Chang, J., Park, B. H., Shin, Y., Lee, K., Lee, W. & Chang, J. (2008), 'A study on the dynamic behavior of a sulfur trioxide decomposer for a nuclear hydrogen production', *International Journal Of Hydrogen Energy* **33**(24), 7361-7370.
- Kodama, T. & Gokon, N. (2007), 'Thermochemical cycles for high-temperature solar hydrogen production', *Chemical Reviews* **107**(10), 4048-4077.
- Komine, S. & Munakata, F. (2005), 'Dielectric relaxation analysis for 8 mol% YSZ single crystal', *Journal of Materials Science* **40**(15), 3887.
- Koster, A., Matzner, H. D. & Nicholisi, D. R. (2003), 'PBMR design for the future', *Nuclear Engineering And Design* **222**(2-3), 231-245.
- Kubo, S., Kasahara, S., Okuda, H., Terada, A., Tanaka, N., Inaba, Y., Ohashi, H., Inagaki, Y., Onuki, K. & Hino, R. (2004), 'A pilot test plan of the thermochemical water-splitting iodine-sulfur process', *Nuclear Engineering And Design* **233**(1-3), 355-362.
- Kuchi, G., Ponyavin, V., Chen, Y. T., Sherman, S. & Hechanova, A. (2008), 'Numerical modeling of high-temperature shell-and-tube heat exchanger and chemical decomposer for hydrogen production', *International Journal Of Hydrogen Energy* **33**(20), 5460-5468.

- Lau, K. C., Turner, C. H. & Dunlap, B. I. (2008), 'Kinetic Monte Carlo simulation of the yttria stabilized zirconia (YSZ) fuel cell cathode', *Solid State Ionics* **179**(33-34), 1912–1920.
- Lee, D. & Oyama, S. T. (2002), 'Gas permeation characteristics of a hydrogen selective supported silica membrane', *Journal Of Membrane Science* **210**(2), 291–306.
- Lin, X., Schneider, W. F. & Trout, B. L. (2004), 'Chemistry of sulfur oxides on transition metals. II. Thermodynamics of sulfur oxides on platinum(111)', *Journal Of Physical Chemistry B* **108**(1), 250–264.
- Lin, Y. S. (2001), 'Microporous and dense inorganic membranes: current status and prospective', *Separation And Purification Technology* **25**(1-3), 39–55.
- Liufu, S. C., Chen, L. D., Yao, Q. & Wang, C. F. (2006), 'Bismuth sulfide thin films with low resistivity on self-assembled monolayers', *Journal Of Physical Chemistry B* **110**(47), 24054–24061.
- Luo, T. & Gorte, R. J. (2004), 'Characterization of SO₂-poisoned ceria-zirconia mixed oxides', *Applied Catalysis B-Environmental* **53**(2), 77–85.
- Marozau, I. P., Kharton, V. V., Viskup, A. P., Frade, J. R. & Samakhval, V. V. (2006), 'Electronic conductivity, oxygen permeability and thermal expansion of Sr_{0.7}Ce_{0.3}Mn_{1-x}Al_xO_{3-δ}', *Journal Of The European Ceramic Society* **26**(8), 1371–1378.
- McLeary, E. E. & Jansen, J. C. (2004), 'Basic views on the preparation of porous ceramic membrane layers - a comparison between amorphous and crystalline layers, leading to a new method for the preparation of microporous continuous layers', *Topics In Catalysis* **29**(1-2), 85–92.
- Mitterdorfer, A. & Gauckler, L. J. (1999), 'Identification of the reaction mechanism of the Pt, O_(g)⁻² | yttria-stabilized zirconia system - Part I: General framework, modelling, and structural investigation', *Solid State Ionics* **117**(3-4), 187–202.
- Mizusaki, J., Narita, H., Tagawa, H., Katou, M. & Hirano, K. (1992), Anomalous oxygen evolution from zirconia cells at the transient state, in S. P. S. Badwal, M. J. Bannister & R. H. J. Hannink, eds, 'Science and Technology of Zirconia V', Technomic, Melbourne, Australia.
- Mohtadi, R., Lee, W. K. & Van Zee, J. W. (2004), 'Assessing durability of cathodes exposed to common air impurities', *Journal Of Power Sources* **138**(1-2), 216–225.

- Momirlan, M. & Veziroglu, T. N. (2002), 'Current status of hydrogen energy', *Renewable and Sustainable Energy Reviews* 6(1-2), 141–179.
- Moulson, A. J. & Herbert, J. M. (1990), *Electroceramics: Materials, properties and applications*, Chapman and Hall.
- Nagarajan, V., Ponyauin, V., Chen, Y. T., Vernon, M. E., Pickard, P. & Hechanova, A. E. (2008), 'Numerical study of sulfur trioxide decomposition in bayonet type heat exchanger and chemical decomposer with porous media zone and different packed bed designs', *International Journal Of Hydrogen Energy* 33(22), 6445–6455.
- National Research Council (2004), *The hydrogen economy: opportunities, costs, barriers, and R+D needs*, National Academies Press, Washington, DC.
- Oyama, S. T., Zhang, X. M., Lu, J. Q., Gu, Y. F. & Fujitani, T. (2008), 'Epoxidation of propylene with H₂ and O₂ in the explosive regime in a packed-bed catalytic membrane reactor', *Journal Of Catalysis* 257(1), 1–4.
- Ozturk, I. T., Hammache, A. & Bilgen, E. (1995), 'An improved process for H₂SO₄ decomposition step of the Sulfur-Iodine cycle', *Energy Conversion and Management* 36(1), 11–21.
- Perkins, C. & Weimer, A. W. (2004), 'Likely near-term solar-thermal water splitting technologies', *International Journal Of Hydrogen Energy* 29(15), 1587–1599.
- Perry, R. H. & Green, D. W. (1998), *Perry's Chemical Engineers' Handbook*, 7th edn, McGraw-Hill, New York.
- Petkovic, L. M., Ginosar, D. M., Rollins, H. W., Burch, K. C., Pinhero, P. J. & Farrell, H. H. (2008), 'Pt/TiO₂ (rutile) catalysts for sulfuric acid decomposition in sulfur-based thermochemical water-splitting cycles', *Applied Catalysis A: General* 338(1-2), 27.
- Pham, A. Q. & Glass, R. S. (1998), 'Oxygen pumping characteristics of yttria-stabilized-zirconia', *Electrochimica Acta* 43(18), 2699–2708.
- Ponyavin, V., Chen, Y., Mohamed, T., Trabia, M., Hechanova, A. E. & Wilson, M. (2008), 'Parametric study of sulfuric acid decomposer for hydrogen production', *Progress In Nuclear Energy* 50(2-6), 427–433.
- Rivera, D. (2005), In situ monitoring of sulfuric acid decomposition by Fourier Transform Infrared (FT-IR) spectroscopy in the sulfur-iodine thermochemical reaction for the production of hydrogen, in 'Sensors for Harsh Environments II', SPIE, Boston, MA, USA.

- Rosenbloom, A. J., Sipe, D. M., Shishkin, Y., Ke, Y., Devaty, R. P. & Choyke, W. J. (2004), 'Nanoporous SiC: A candidate semi-permeable material for biomedical applications', *Biomedical Microdevices* 6(4), 261–267.
- Rotureau, D., Viricelle, J. P., Pijolat, C., Caillol, N. & Pijolat, M. (2005), 'Development of a planar SOFC device using screen-printing technology', *Journal of the European Ceramic Society* 25(12), 2633.
- Russ, B. E., Sweet, W., Moore, R., Naranjo, G., Helie, M. & Pons, N. (2008), Status of the I-NERI Sulfur-Iodine Integrated-Loop Experiment, in 'AIChE Annual Meeting', Philadelphia, USA.
- Sakaba, N., Kasahara, S., Onuki, K. & Kunitomi, K. (2007), 'Conceptual design of hydrogen production system with thermochemical water-splitting iodine-sulphur process utilizing heat from the high-temperature gas-cooled reactor HTTR', *International Journal Of Hydrogen Energy* 32(17), 4160–4169.
- Saracco, G., Versteeg, G. F. & Vanswaaij, W. P. M. (1994), 'Current hurdles to the success of high-temperature membrane reactors', *Journal Of Membrane Science* 95(2), 105–123.
- Savitsky, E., Arskaya, E., Lazarev, E. & Korotkov, N. (1982), 'Investigation of corrosion resistance of materials in the presence of sulphuric acid and its decomposition products applied in the thermochemical cycle of hydrogen production', *International Journal of Hydrogen Energy* 7(5), 393–396.
- Shuk, P., Wiemhofer, H. D., Guth, U., Gopel, W. & Greenblatt, M. (1996), 'Oxide ion conducting solid electrolytes based on Bi_2O_3 ', *Solid State Ionics* 89(3-4), 179–196.
- Song, C. S. (2006), 'Global challenges and strategies for control, conversion and utilization of CO_2 for sustainable development involving energy, catalysis, adsorption and chemical processing', *Catalysis Today* 115(1-4), 2–32.
- Steenberghen, T. & Lopez, E. (2008), 'Overcoming barriers to the implementation of alternative fuels for road transport in Europe', *Journal Of Cleaner Production* 16(5), 577–590.
- Stojic, D. L., Marceta, M. P., Sovilj, S. P. & Miljanic, S. S. (2003), 'Hydrogen generation from water electrolysis - possibilities of energy saving', *Journal Of Power Sources* 118(1-2), 315–319.
- Suwanmethanond, V., Goo, E., Liu, P. K. T., Johnston, G., Sahimi, M. & Tsotsis, T. T. (2000), 'Porous silicon carbide sintered substrates for high-temperature membranes', *Industrial and Engineering Chemistry Research* 39(9), 3264–3271.

- Tagawa, H. & Endo, T. (1989), 'Catalytic decomposition of sulfuric acid using metal oxides as the oxygen generating reaction in thermochemical water splitting process', *International Journal of Hydrogen Energy* **14**(1), 11.
- Takebe, H., Sakamoto, D., Ohtaka, O., Fukui, H., Yoshiasa, A., Yamanaka, T., Ota, K. & Kikegawa, T. (2002), 'Ionic conductivity measurements of zirconia under pressure using impedance spectroscopy', *Journal Of Physics-Condensed Matter* **14**(44), 11507–11510.
- Tang, H. R., Van der Ven, A. & Trout, B. L. (2004), 'Phase diagram of oxygen adsorbed on platinum (111) by first-principles investigation', *Physical Review B* **70**(4).
- Teraoka, Y., Honbe, Y., Ishii, J., Furukawa, H. & Moriguchi, I. (2002), 'Catalytic effects in oxygen permeation through mixed-conductive LSCF perovskite membranes', *Solid State Ionics* **152**, 681–687.
- Tsai, C. Y., Tam, S. Y., Lu, Y. F. & Brinker, C. J. (2000), 'Dual-layer asymmetric microporous silica membranes', *Journal Of Membrane Science* **169**(2), 255–268.
- Tu, R. & Goto, T. (2003), 'Corrosion behavior of ceramics-coated Hastelloy-XR alloy in an Ar-SO₂ atmosphere', *Materials Transactions* **44**(5), 962–967.
- Weil, K. S., Hardy, J. S., Rice, J. P. & Kim, J. Y. (2006), 'Brazing as a means of sealing ceramic membranes for use in advanced coal gasification processes', *Fuel* **85**(2), 156–162.
- Weppner, W. (1977), 'Formation of intermetallic Pt-Zr compounds between Pt electrodes and ZrO₂-based electrolytes, and decomposition voltage of yttria-doped ZrO₂', *Journal Of Electroanalytical Chemistry* **84**(2), 339–350.
- West, A. R. (1999), *Basic Solid State Chemistry*, 2nd edn, Wiley.
- Wilson, K., Hardacre, C., Baddeley, C. J., Ludecke, J., Woodruff, D. P. & Lambert, R. M. (1997), 'A spectroscopic study of the chemistry and reactivity of SO₂ on Pt(111): Reactions with O₂, CO and C₃H₆', *Surface Science* **372**(1-3), 279–288.
- Wu, X. & Onuki, K. (2005), 'Thermochemical water splitting for hydrogen production utilizing nuclear heat from an HTGR', *Tsinghua Science and Technology* **10**(2), 270.
- Xomeritakis, G., Naik, S., Braunbarth, C. M., Cornelius, C. J., Pardey, R. & Brinker, C. J. (2003), 'Organic-templated silica membranes - I. Gas and vapor transport properties', *Journal Of Membrane Science* **215**(1-2), 225–233.

- Yamamura, Y., Ihara, C., Kawasaki, S., Sakai, H., Suzuki, K., Takami, S., Kubo, M. & Miyamoto, A. (2003), 'Materials design of perovskite-based oxygen ion conductor by molecular dynamics method', *Solid State Ionics* **160**(1-2), 93–101.
- Zaman, J. & Chakma, A. (1994), 'Inorganic membrane reactors', *Journal Of Membrane Science* **92**(1), 1–28.
- Zhang, W. X., Smit, J., Annaland, M. V. & Kuipers, J. A. M. (2007), 'Feasibility study of a novel membrane reactor for syngas production Part 1: Experimental study of O₂ permeation through perovskite membranes under reducing and non-reducing atmospheres', *Journal Of Membrane Science* **291**(1-2), 19–32.

Appendix A

Process simulation tables

The tables in this appendix present the results obtained from the *ProSimPlus* process simulations described in Section 3.6.

Separation factor w.r.t. O ₂	Temperature (K)	2 stages Pressure (bara)				4 stages Pressure (bara)				6 stages Pressure (bara)				8 stages Pressure (bara)			
		1.013	10	20	30	1.013	10	20	30	1.013	10	20	30	1.013	10	20	30
knudsen	900	39.68	20.97	16.53	14.15	40.86	21.83	17.30	14.87	40.97	21.92	17.38	14.95	40.98	21.93	17.39	14.96
knudsen	1000	66.44	42.57	35.74	31.93	67.54	43.79	36.90	33.05	67.61	43.90	37.01	33.16	67.62	43.91	37.02	33.17
knudsen	1100	84.33	64.74	57.43	53.04	84.95	65.87	58.65	54.28	84.97	65.94	58.74	54.38	84.98	65.95	58.75	54.39
knudsen	1200	92.87	80.66	74.97	71.24	93.15	81.40	75.88	72.24	93.15	81.44	75.94	72.31	93.15	81.44	75.94	72.31
knudsen	1300	96.55	89.67	86.00	83.41	96.67	90.08	86.55	84.06	96.67	90.09	86.57	84.09	96.67	90.09	86.57	84.09
10	900	47.48	25.47	19.91	16.88	56.61	31.82	25.13	21.42	60.53	34.93	27.75	23.74	62.61	36.74	29.31	25.13
10	1000	75.28	50.57	42.77	38.29	83.06	59.84	51.55	46.61	85.55	63.73	55.44	50.40	86.63	65.76	57.56	52.51
10	1100	90.67	73.62	66.35	61.77	94.53	81.67	75.26	70.99	95.39	84.30	78.47	74.48	95.70	85.47	79.98	76.18
10	1200	96.55	87.78	83.00	79.67	98.11	92.60	89.16	86.60	98.36	93.78	90.86	88.66	98.44	94.22	91.54	89.51
10	1300	98.60	94.49	91.90	89.94	99.23	96.92	95.32	94.06	99.31	97.37	96.05	95.00	99.33	97.52	96.30	95.34
100	900	48.60	26.15	20.45	17.35	60.06	34.14	27.02	23.07	66.03	38.89	31.03	26.60	69.88	42.25	33.92	29.17
100	1000	76.58	51.74	43.81	39.25	86.31	61.93	54.84	49.70	90.08	69.30	60.78	55.49	92.08	73.05	64.70	59.39
100	1100	91.62	74.92	67.65	63.05	96.44	84.99	78.82	74.61	97.74	89.00	83.71	79.93	98.31	91.15	86.50	83.07
100	1200	97.12	88.85	84.19	80.92	99.06	94.85	91.88	89.58	99.44	96.64	94.47	92.70	99.58	97.46	95.72	94.28
100	1300	98.93	95.23	92.80	90.93	99.71	98.25	97.06	96.06	99.83	98.93	98.16	97.48	99.87	99.21	98.62	98.11
1000	900	48.72	26.22	20.51	17.40	60.42	34.38	27.22	23.24	66.64	39.33	31.39	26.92	70.72	42.89	34.46	29.65
1000	1000	76.70	51.85	43.92	39.35	86.65	63.74	55.18	50.02	90.58	69.91	61.37	56.06	92.69	73.89	65.52	60.19
1000	1100	91.72	75.05	67.78	63.18	96.63	85.34	79.19	74.99	97.99	89.51	84.28	80.53	98.59	91.79	87.24	83.86
1000	1200	97.18	88.96	84.31	81.04	99.15	95.09	92.17	89.90	99.55	96.95	94.86	93.14	99.70	97.81	96.19	94.81
1000	1300	98.96	95.31	92.88	91.03	99.76	98.38	97.24	96.26	99.88	99.10	98.38	97.75	99.92	99.39	98.88	98.41
10000	900	48.73	26.22	20.51	17.40	60.46	34.40	27.24	23.26	66.70	39.37	31.43	26.95	70.80	42.95	34.51	29.70
10000	1000	76.72	51.87	43.93	39.36	86.68	63.78	55.22	50.06	90.63	69.97	61.43	56.11	92.75	73.98	65.61	60.27
10000	1100	91.73	75.07	67.80	63.19	96.65	85.37	79.23	75.02	98.02	89.56	84.34	80.59	98.62	91.85	87.31	83.94
10000	1200	97.19	88.97	84.33	81.05	99.16	95.11	92.20	89.93	99.56	96.98	94.90	93.19	99.71	97.85	96.24	94.86
10000	1300	98.97	95.32	92.89	91.04	99.76	98.40	97.25	96.28	99.89	99.12	98.41	97.77	99.93	99.41	98.90	98.44

Table A.1: CMR process simulation results from ProSimPlus. Stages represent number of theoretical equilibrium/separation stages employed by the CMR.

Separation factor w.r.t. O ₂	Temperature (K)	25% membrane efficiency				50% membrane efficiency				75% membrane efficiency				100% membrane efficiency			
		Pressure (bara)				Pressure (bara)				Pressure (bara)				Pressure (bara)			
		1.013	10	20	30	1.013	10	20	30	1.013	10	20	30	1.013	10	20	30
knudsen	900	36.35	18.71	14.51	12.26	36.41	18.77	14.57	12.33	36.47	18.82	14.63	12.38	36.83	19.04	14.80	12.52
knudsen	1000	62.41	39.00	32.44	28.79	62.48	39.07	32.51	28.87	62.54	39.14	32.58	28.94	62.92	39.51	32.91	29.24
knudsen	1100	81.14	60.67	53.37	49.03	81.18	60.73	53.44	49.10	81.22	60.80	53.51	49.18	81.48	61.19	53.91	49.57
knudsen	1200	90.85	77.15	71.13	67.25	90.87	77.20	71.18	67.31	90.89	77.25	71.24	67.37	91.04	77.54	71.58	67.73
knudsen	1300	95.34	87.11	82.96	80.11	95.35	87.14	83.01	80.16	95.37	87.18	83.05	80.21	95.45	87.37	83.29	80.48
10	900	36.75	18.94	17.19	12.40	37.17	19.21	14.90	12.59	37.58	19.47	15.11	12.77	37.96	19.72	15.31	12.94
10	1000	62.84	39.40	37.26	29.11	63.29	39.84	33.19	29.48	63.72	40.26	33.58	29.84	64.12	40.66	33.94	30.17
10	1100	81.43	61.09	58.91	49.45	81.73	61.55	54.27	49.93	82.02	61.99	54.72	50.37	82.29	62.40	55.14	50.79
10	1200	91.01	77.48	75.74	67.64	91.18	77.83	71.90	68.07	91.34	78.15	72.28	68.48	91.48	78.46	72.64	68.86
10	1300	95.43	87.33	86.15	80.41	95.52	87.55	83.51	80.73	95.61	87.77	83.78	81.03	95.69	87.97	84.03	81.31
100	900	36.79	18.97	14.70	12.42	37.27	19.27	14.95	12.63	37.72	19.56	15.18	12.83	38.16	19.84	15.41	13.02
100	1000	62.89	39.45	32.84	29.15	63.39	39.94	33.28	29.57	63.87	40.41	33.71	29.96	64.32	40.86	34.12	30.34
100	1100	81.46	61.14	53.85	49.51	81.80	61.66	54.38	50.03	82.12	62.14	54.88	50.53	82.42	62.60	55.35	51.00
100	1200	91.03	77.52	71.55	67.69	91.21	77.90	71.99	68.17	91.39	78.27	72.42	68.62	91.56	78.62	72.81	69.04
100	1300	95.44	87.35	83.26	80.45	95.54	87.60	83.58	80.80	95.64	87.84	83.87	81.13	95.72	88.06	84.15	81.44
1000	900	36.80	18.97	14.71	12.42	37.28	19.28	14.95	12.63	37.74	19.57	15.19	12.84	38.17	19.85	15.42	13.03
1000	1000	62.89	39.46	32.84	29.16	63.40	39.95	33.29	29.57	63.88	40.42	33.72	29.97	64.34	40.88	34.13	30.36
1000	1100	81.46	61.15	53.86	49.51	81.81	61.67	54.39	50.04	82.13	62.15	54.89	50.54	82.44	62.62	55.37	51.02
1000	1200	91.03	77.52	71.55	67.69	91.22	77.91	72.00	68.18	91.40	78.28	72.43	68.63	91.56	78.63	72.83	69.06
1000	1300	95.44	87.35	83.27	80.45	95.54	87.61	83.58	80.81	95.64	87.85	83.88	81.14	95.73	88.07	84.16	81.46
10000	900	36.80	18.97	14.71	12.42	37.28	19.28	14.95	12.63	37.74	19.57	15.19	12.84	38.18	19.85	15.42	13.03
10000	1000	62.89	39.46	32.84	29.16	63.40	39.95	33.29	29.57	63.89	40.43	33.72	29.98	64.34	40.88	34.14	30.36
10000	1100	81.47	61.15	53.86	49.51	81.81	61.67	54.39	50.04	82.13	62.16	54.89	50.54	82.44	62.62	55.37	51.02
10000	1200	91.03	77.52	71.55	67.70	91.22	77.91	72.00	68.18	91.40	78.28	72.43	68.63	91.56	78.63	72.83	69.06
10000	1300	95.44	87.35	83.27	80.45	95.54	87.61	83.58	80.81	95.64	87.85	83.88	81.14	95.73	88.07	84.17	81.46

Table A.2: Downstream separation process simulation results from ProSimPlus (20% recycle)

Separation factor w.r.t. O ₂	Temperature (K)	25% membrane efficiency				50% membrane efficiency				75% membrane efficiency				100% membrane efficiency			
		Pressure (bara)				Pressure (bara)				Pressure (bara)				Pressure (bara)			
		1.013	10	20	30	1.013	10	20	30	1.013	10	20	30	1.013	10	20	30
knudsen	900	36.45	18.80	14.61	12.37	36.61	18.94	14.75	12.51	36.76	19.07	14.88	12.64	37.45	19.48	15.19	12.90
knudsen	1000	62.52	39.12	32.56	28.92	62.68	39.30	32.74	29.10	62.83	39.46	32.90	29.27	63.57	40.16	33.53	29.84
knudsen	1100	81.21	60.78	53.49	49.15	81.32	60.95	53.67	49.35	81.42	61.11	53.84	49.52	81.92	61.85	54.60	50.27
knudsen	1200	90.89	77.23	71.22	67.35	90.95	77.35	71.37	67.51	91.00	77.48	71.51	67.66	91.28	78.04	72.16	68.35
knudsen	1300	95.36	87.17	83.03	80.19	95.40	87.25	83.13	80.31	95.43	87.32	83.23	80.42	95.57	87.69	83.69	80.93
10	900	37.45	19.38	15.04	12.71	38.45	20.03	15.56	13.16	39.34	20.60	16.03	13.56	40.13	21.12	16.45	13.93
10	1000	63.58	40.13	33.45	29.72	64.63	41.16	34.39	30.60	65.54	42.07	35.23	31.38	66.33	42.88	35.98	32.08
10	1100	81.93	61.85	54.57	50.23	82.62	62.91	55.67	51.32	83.22	63.83	56.63	52.28	83.74	64.64	57.48	53.13
10	1200	91.28	78.05	72.16	68.34	91.67	78.85	73.08	69.33	91.99	79.53	73.88	70.18	92.27	80.13	74.57	70.93
10	1300	95.58	87.70	83.70	80.93	95.78	88.21	84.34	81.65	95.96	88.65	84.89	82.27	96.11	89.03	85.36	82.81
100	900	37.57	19.47	15.11	12.76	38.70	20.19	15.70	13.27	39.72	20.86	16.23	13.74	40.64	21.46	16.73	14.17
100	1000	63.71	40.26	33.57	29.83	64.89	41.42	34.63	30.82	65.93	42.47	35.59	31.72	66.85	43.41	36.46	32.53
100	1100	82.02	61.98	54.71	50.36	82.80	63.18	55.95	51.60	83.47	64.23	57.04	52.70	84.06	65.17	58.03	53.69
100	1200	91.33	78.15	72.28	68.47	91.76	79.05	73.31	69.58	92.13	79.82	74.22	70.55	92.45	80.51	75.02	71.41
100	1300	95.60	87.76	83.78	81.02	95.83	88.34	84.50	81.83	96.03	88.83	85.12	82.54	96.20	89.27	85.67	83.15
1000	900	37.59	19.47	15.11	12.77	38.73	20.21	15.71	13.29	39.76	20.88	16.25	13.76	40.70	21.50	16.76	14.19
1000	1000	63.73	40.27	33.58	29.84	64.92	41.45	34.66	30.85	65.97	42.51	35.63	31.75	66.90	43.47	36.52	32.58
1000	1100	82.03	61.99	54.73	50.38	82.81	63.20	55.98	51.63	83.50	64.27	57.09	52.74	84.10	65.22	58.08	53.74
1000	1200	91.34	78.16	72.29	68.48	91.77	79.07	73.34	69.60	92.14	79.85	74.25	70.59	92.46	80.55	75.07	71.46
1000	1300	95.61	87.77	83.79	81.03	95.84	88.35	84.52	81.85	96.04	88.85	85.15	82.56	96.21	89.29	85.70	83.19
10000	900	37.59	19.47	15.11	12.77	38.73	20.21	15.71	13.29	39.76	20.88	16.26	13.76	40.70	21.50	16.76	14.19
10000	1000	63.73	40.27	33.58	29.84	64.92	41.45	34.66	30.85	65.97	42.51	35.63	31.76	66.91	43.47	36.52	32.59
10000	1100	82.03	62.00	54.73	50.38	82.82	63.21	55.98	51.63	83.50	64.27	57.09	52.74	84.10	65.22	58.09	53.75
10000	1200	91.34	78.16	72.29	68.48	91.77	79.07	73.34	69.61	92.14	79.86	74.26	70.59	92.47	80.55	75.07	71.46
10000	1300	95.61	87.77	83.79	81.04	95.84	88.35	84.52	81.85	96.04	88.85	85.15	82.57	96.21	89.29	85.70	83.19

Table A.3: Downstream separation process simulation results from ProSimPlus (40% recycle)

Separation factor w.r.t. O ₂	Temperature (K)	25% membrane efficiency Pressure (bara)				50% membrane efficiency Pressure (bara)				75% membrane efficiency Pressure (bara)				100% membrane efficiency Pressure (bara)			
		1.013	10	20	30	1.013	10	20	30	1.013	10	20	30	1.013	10	20	30
knudsen	900	36.65	18.98	14.79	12.54	36.96	19.23	15.04	12.80	37.20	19.43	15.23	12.98	38.17	20.01	15.66	13.34
knudsen	1000	62.72	39.34	32.78	29.14	63.04	39.68	33.12	29.48	63.29	39.94	33.38	29.74	64.30	40.92	34.25	30.53
knudsen	1100	81.35	60.99	53.72	49.39	81.56	61.32	54.07	49.75	81.72	61.58	54.34	50.04	82.40	62.60	55.39	51.07
knudsen	1200	90.96	77.39	71.41	67.55	91.08	77.63	71.69	67.86	91.17	77.82	71.92	68.10	91.54	78.60	72.81	69.05
knudsen	1300	95.40	87.27	83.16	80.34	95.47	87.42	83.36	80.56	95.52	87.55	83.51	80.73	95.72	88.05	84.14	81.43
10	900	38.68	20.18	15.68	13.26	40.49	21.36	16.65	14.10	41.93	22.32	17.43	14.78	43.12	23.13	18.09	15.35
10	1000	64.87	41.40	34.61	30.80	66.70	43.26	36.32	32.40	68.11	44.73	37.69	33.68	69.25	45.95	38.82	34.75
10	1100	82.78	63.15	55.92	51.57	83.97	65.01	57.87	53.52	84.86	66.45	59.38	55.06	85.56	67.61	60.61	56.30
10	1200	91.74	79.03	73.29	69.56	92.39	80.40	74.89	71.27	92.87	81.43	76.11	72.58	93.24	82.25	77.08	73.64
10	1300	95.83	88.33	84.48	81.82	96.17	89.19	85.58	83.05	96.42	89.84	86.40	83.98	96.62	90.35	87.05	84.72
100	900	38.97	20.37	15.83	13.39	41.07	21.75	16.96	14.37	42.81	22.92	17.91	15.20	44.28	23.93	18.75	15.92
100	1000	65.16	41.69	34.88	31.06	67.27	43.85	36.87	32.92	68.95	45.63	38.52	34.47	70.33	47.13	39.93	35.80
100	1100	82.98	63.45	56.24	51.89	84.33	65.60	58.48	54.14	85.38	67.31	60.29	55.98	86.22	68.72	61.80	57.51
100	1200	91.85	79.25	73.55	69.83	92.58	80.82	75.39	71.81	93.14	82.04	76.83	73.36	93.58	83.02	78.00	74.64
100	1300	95.89	88.47	84.66	82.02	96.27	89.46	85.92	83.43	96.57	90.22	86.88	84.53	96.80	90.82	87.65	85.41
1000	900	39.00	20.38	15.85	13.41	41.13	21.79	16.99	14.40	42.90	22.98	17.97	15.24	44.41	24.02	18.82	15.98
1000	1000	65.19	41.72	34.91	31.08	67.33	43.91	36.93	32.97	69.04	45.72	38.61	34.55	70.45	47.26	40.05	35.91
1000	1100	83.00	63.48	56.27	51.92	84.37	65.66	58.55	54.21	85.44	67.40	60.39	56.07	86.29	68.84	61.93	57.64
1000	1200	91.86	79.27	73.58	69.86	92.60	80.86	75.44	71.86	93.17	82.10	76.90	73.44	93.62	83.11	78.10	74.74
1000	1300	95.89	88.48	84.68	82.04	96.28	89.49	85.95	83.47	96.58	90.26	86.93	84.58	96.82	90.87	87.71	85.48
10000	900	39.00	20.39	15.85	13.41	41.14	21.79	17.00	14.40	42.91	22.98	17.97	15.25	44.42	24.02	18.83	15.99
10000	1000	65.19	41.73	34.91	31.08	67.34	43.92	36.94	32.98	69.05	45.73	38.62	34.56	70.46	47.27	40.07	35.92
10000	1100	83.00	63.48	56.27	51.92	84.38	65.67	58.55	54.22	85.44	67.41	60.40	56.08	86.30	68.85	61.94	57.65
10000	1200	91.86	79.28	73.58	69.86	92.61	80.87	75.45	71.87	93.18	82.11	76.91	73.45	93.62	83.11	78.11	74.75
10000	1300	95.89	88.49	84.68	82.04	96.28	89.49	85.95	83.48	96.58	90.26	86.93	84.59	96.82	90.88	87.72	85.49

Table A.4: Downstream separation process simulation results from ProSimPlus (60% recycle)

Separation factor w.r.t. O ₂	Temperature (K)	25% membrane efficiency				50% membrane efficiency				75% membrane efficiency				100% membrane efficiency			
		Pressure (bara)				Pressure (bara)				Pressure (bara)				Pressure (bara)			
		1.013	10	20	30	1.013	10	20	30	1.013	10	20	30	1.013	10	20	30
knudsen	900	37.13	19.37	15.17	12.93	37.60	19.74	15.52	13.27	37.88	19.95	15.73	13.47	39.02	20.62	16.22	13.86
knudsen	1000	63.21	39.86	33.30	29.66	63.69	40.37	33.79	30.15	63.97	40.66	34.08	30.43	65.15	41.81	35.10	31.35
knudsen	1100	81.67	61.50	54.25	49.95	81.99	61.99	54.78	50.49	82.17	62.28	55.09	50.80	82.95	63.47	56.31	52.01
knudsen	1200	91.14	77.76	71.85	68.03	91.31	78.13	72.27	68.49	91.41	78.34	72.52	68.76	91.84	79.24	73.56	69.86
knudsen	1300	95.50	87.51	83.46	80.68	95.59	87.74	83.76	81.01	95.65	87.88	83.93	81.20	95.88	88.45	84.65	82.01
10	900	41.48	22.02	17.19	14.56	44.42	24.02	18.83	15.99	46.39	25.41	19.97	16.99	47.83	26.44	20.83	17.74
10	1000	67.68	44.27	37.26	33.28	70.46	47.27	40.07	35.92	72.23	49.28	41.96	37.72	73.48	50.73	43.35	39.04
10	1100	84.59	66.01	58.91	54.58	86.30	68.85	61.94	57.65	87.35	70.67	63.90	59.66	88.07	71.96	65.30	61.11
10	1200	92.73	81.12	75.74	72.18	93.62	83.12	78.11	74.76	94.16	84.35	79.59	76.38	94.53	85.20	80.63	77.52
10	1300	96.35	89.65	86.15	83.71	96.82	90.88	87.72	85.49	97.10	91.62	88.68	86.59	97.29	92.13	89.34	87.34
100	900	42.26	22.55	17.61	14.93	45.96	25.10	19.72	16.77	48.64	27.04	21.32	18.17	50.73	28.59	22.63	19.32
100	1000	68.42	45.07	38.00	33.98	71.85	48.84	41.54	37.32	74.17	51.55	44.14	39.80	75.89	53.66	46.18	41.76
100	1100	85.07	66.78	59.72	55.40	87.13	70.28	63.48	59.23	88.46	72.67	66.09	61.91	89.42	74.44	68.05	63.96
100	1200	92.97	81.67	76.38	72.88	94.05	84.09	79.28	76.03	94.73	85.67	81.19	78.14	95.20	86.81	82.59	79.69
100	1300	96.48	89.99	86.59	84.20	97.03	91.46	88.48	86.35	97.39	92.40	89.69	87.75	97.64	93.07	90.56	88.76
1000	900	42.34	22.60	17.66	14.97	46.13	25.22	19.82	16.85	48.90	27.23	21.48	18.31	51.08	28.86	22.85	19.52
1000	1000	68.50	45.15	38.08	34.05	72.00	49.01	41.71	37.48	74.39	51.81	44.39	40.04	76.17	54.01	46.52	42.08
1000	1100	85.12	66.86	59.81	55.49	87.22	70.43	63.65	59.40	88.58	72.89	66.33	62.17	89.57	74.73	68.37	64.30
1000	1200	93.00	81.73	76.45	72.95	94.10	84.19	79.40	76.17	94.79	85.81	81.37	78.34	95.28	86.99	82.82	79.94
1000	1300	96.49	90.02	86.64	84.25	97.06	91.53	88.56	86.45	97.42	92.49	89.80	87.88	97.67	93.17	90.70	88.91
10000	900	42.35	22.61	17.66	14.98	46.15	25.24	19.83	16.86	48.93	27.25	21.50	18.33	51.12	28.89	22.87	19.54
10000	1000	68.51	45.16	38.09	34.06	72.02	49.03	41.72	37.49	74.41	51.84	44.41	40.06	76.20	54.04	46.55	42.12
10000	1100	85.12	66.87	59.82	55.50	87.23	70.45	63.66	59.42	88.60	72.91	66.36	62.20	89.58	74.76	68.41	64.33
10000	1200	93.00	81.74	76.46	72.96	94.10	84.20	79.41	76.18	94.79	85.83	81.39	78.36	95.29	87.01	82.84	79.97
10000	1300	96.50	90.02	86.64	84.26	97.06	91.53	88.57	86.45	97.43	92.50	89.82	87.89	97.68	93.18	90.71	88.93

Table A.5: Downstream separation process simulation results from ProSimPlus (80% recycle)

Appendix B

Metal oxide/sulphate equilibrium calculations

This appendix contains the full results of the *HSC Chemistry* equilibrium calculations described in Section 5.3. The equilibria were calculated at 1 and 20 bara for a solid phase, initially consisting of 1 kmol of the metal oxide, in the presence of a gaseous phase initially consisting of 100 kmol $\text{H}_2\text{SO}_4(\text{g})$. The other species present in the gaseous phase upon establishment of the equilibrium composition are SO_3 , SO_2 , O_2 and H_2O . The solid phase contains the metal oxide and all of the solid phase species present in the *HSC Chemistry* database that contain the appropriate metal and one or more of oxygen, sulphur and hydrogen. Tables B.1, B.2 and B.3 at the end of this appendix give the full list of species used for the set of simulations.

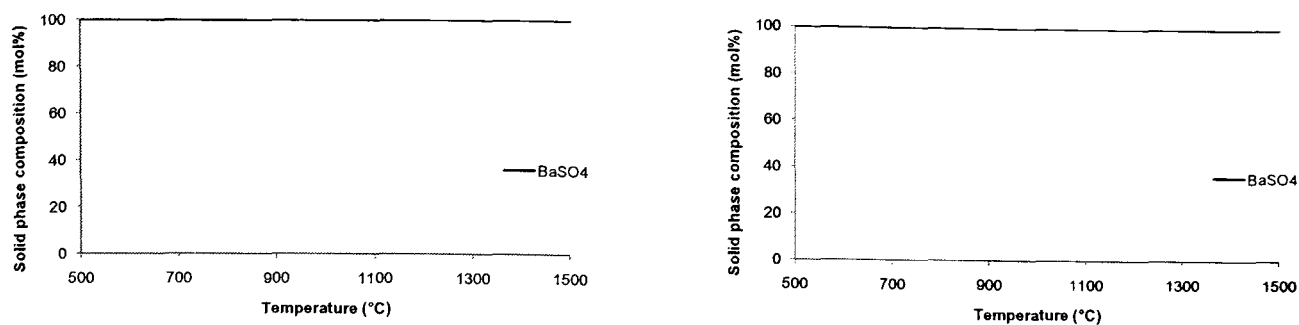


Figure B.1: Equilibrium calculation of BaO_2 stability at 1 bara (left) and 20 bara (right), with gaseous phase of H_2SO_4 equilibrium decomposition products in large excess. Calculations carried out by Gibbs minimisation in HSC Chemistry.

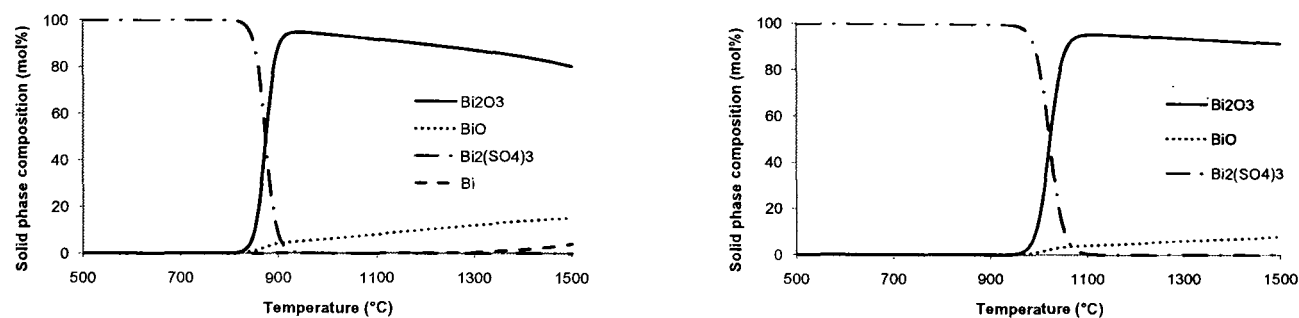


Figure B.2: Equilibrium calculation of Bi_2O_3 stability at 1 bara (left) and 20 bara (right), with gaseous phase of H_2SO_4 equilibrium decomposition products in large excess. Calculations carried out by Gibbs minimisation in HSC Chemistry.

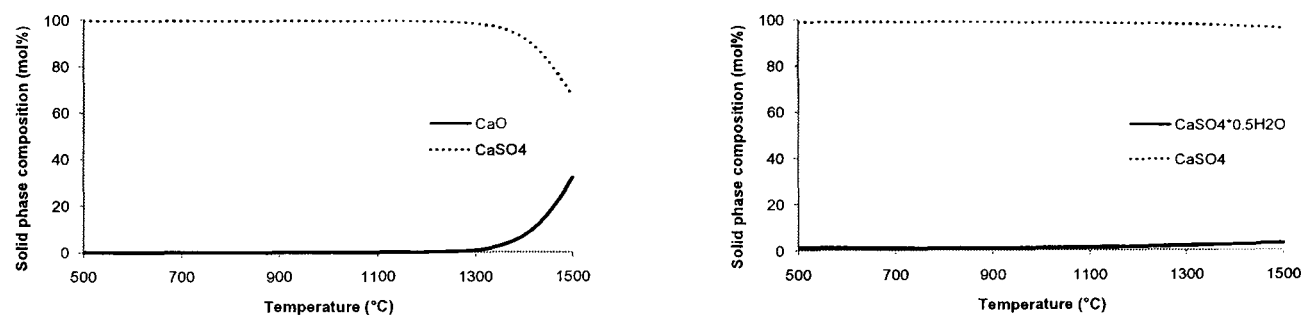


Figure B.3: Equilibrium calculation of CaO stability at 1 bara (left) and 20 bara (right), with gaseous phase of H_2SO_4 equilibrium decomposition products in large excess. Calculations carried out by Gibbs minimisation in HSC Chemistry.

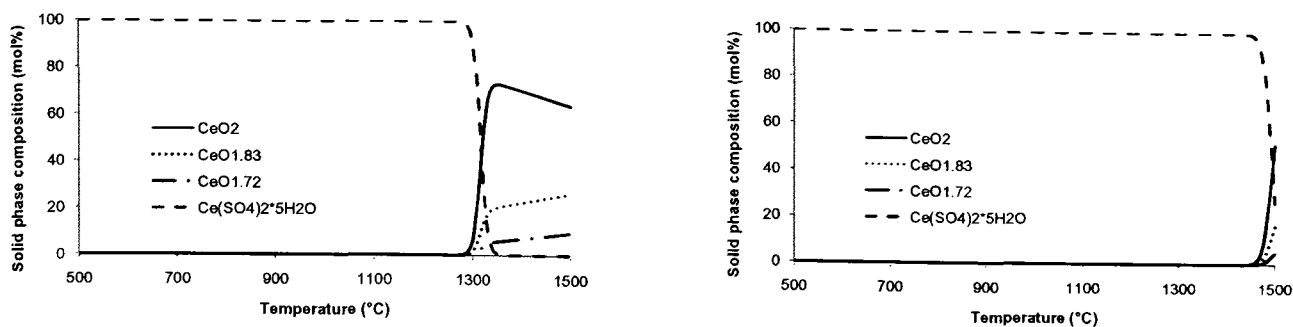


Figure B.4: Equilibrium calculation of CeO_2 stability at 1 bara (left) and 20 bara (right), with gaseous phase of H_2SO_4 equilibrium decomposition products in large excess. Calculations carried out by Gibbs minimisation in HSC Chemistry.

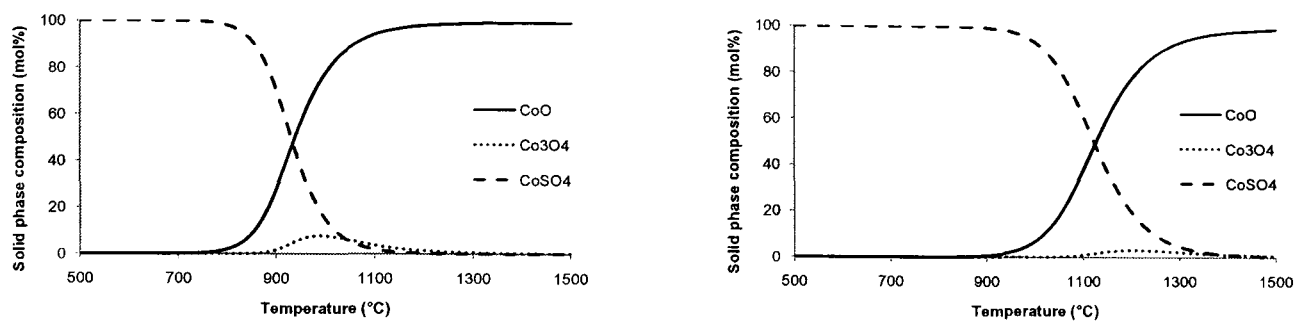


Figure B.5: Equilibrium calculation of CoO stability at 1 bara (left) and 20 bara (right), with gaseous phase of H_2SO_4 equilibrium decomposition products in large excess. Calculations carried out by Gibbs minimisation in HSC Chemistry.

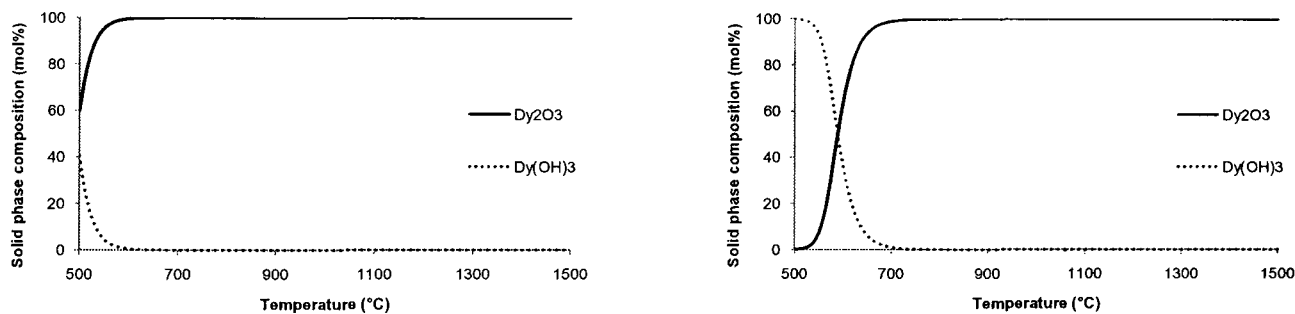


Figure B.6: Equilibrium calculation of Dy_2O_3 stability at 1 bara (left) and 20 bara (right), with gaseous phase of H_2SO_4 equilibrium decomposition products in large excess. Calculations carried out by Gibbs minimisation in HSC Chemistry.

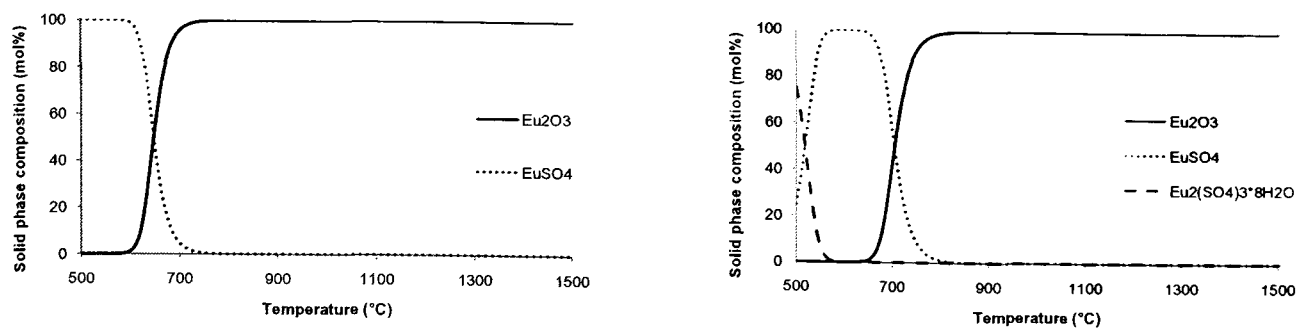


Figure B.7: Equilibrium calculation of Eu_2O_3 stability at 1 bara (left) and 20 bara (right), with gaseous phase of H_2SO_4 equilibrium decomposition products in large excess. Calculations carried out by Gibbs minimisation in HSC Chemistry.

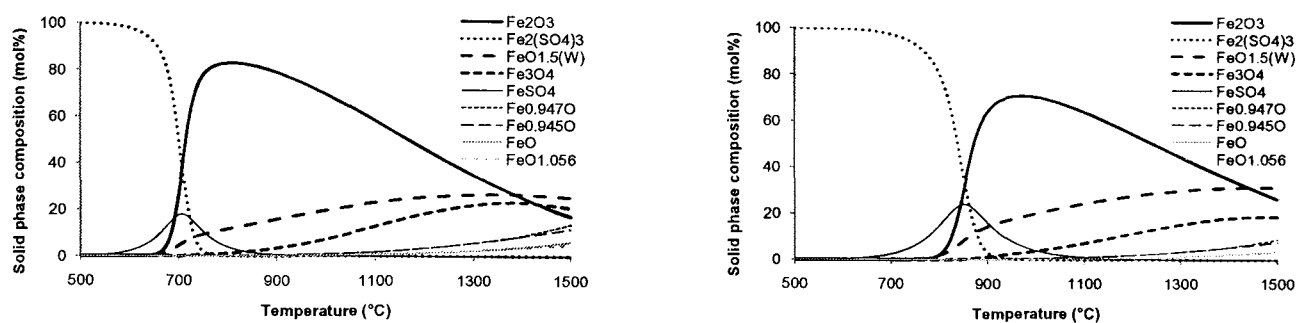


Figure B.8: Equilibrium calculation of Fe_2O_3 stability at 1 bara (left) and 20 bara (right), with gaseous phase of H_2SO_4 equilibrium decomposition products in large excess. Calculations carried out by Gibbs minimisation in HSC Chemistry.

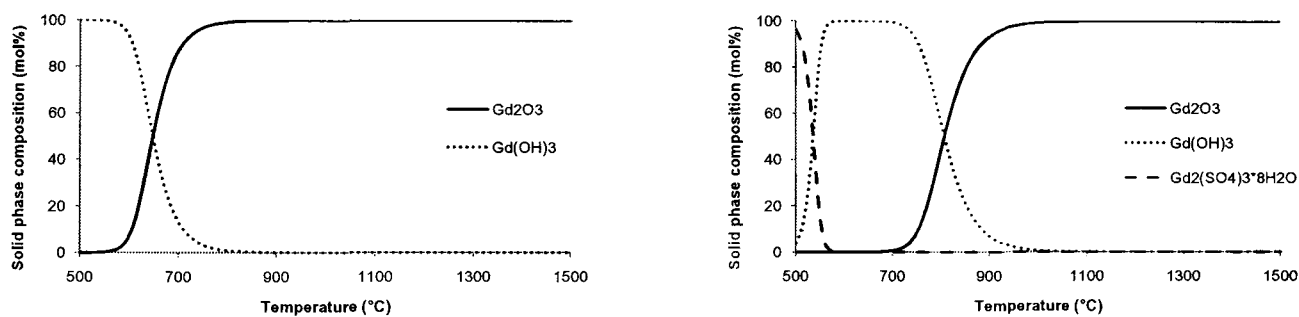


Figure B.9: Equilibrium calculation of Gd_2O_3 stability at 1 bara (left) and 20 bara (right), with gaseous phase of H_2SO_4 equilibrium decomposition products in large excess. Calculations carried out by Gibbs minimisation in HSC Chemistry.

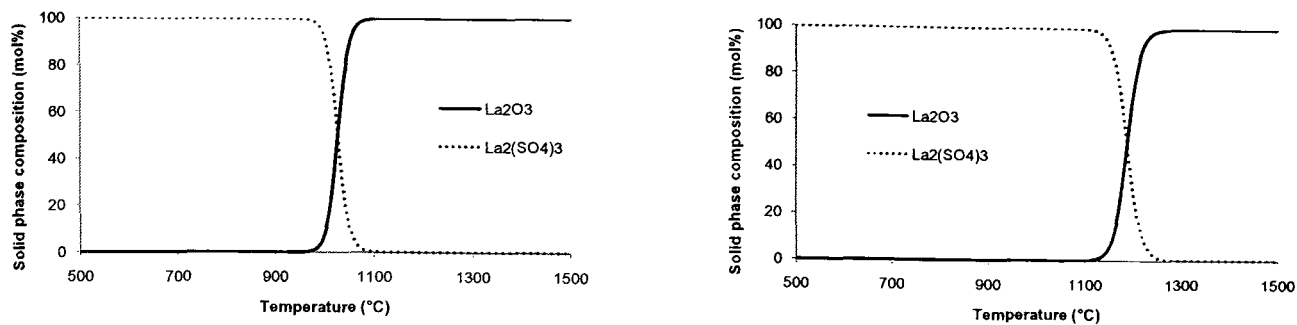


Figure B.10: Equilibrium calculation of La_2O_3 stability at 1 bara (left) and 20 bara (right), with gaseous phase of H_2SO_4 equilibrium decomposition products in large excess. Calculations carried out by Gibbs minimisation in HSC Chemistry.

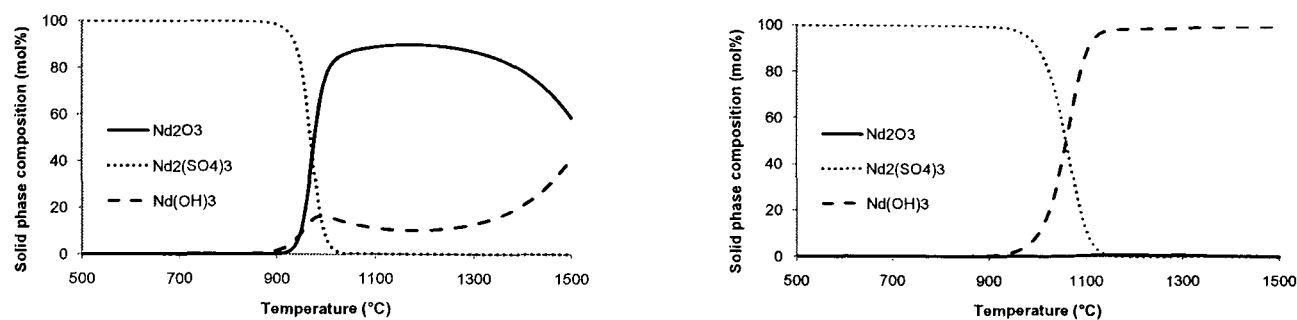


Figure B.11: Equilibrium calculation of Nd_2O_3 stability at 1 bara (left) and 20 bara (right), with gaseous phase of H_2SO_4 equilibrium decomposition products in large excess. Calculations carried out by Gibbs minimisation in HSC Chemistry.

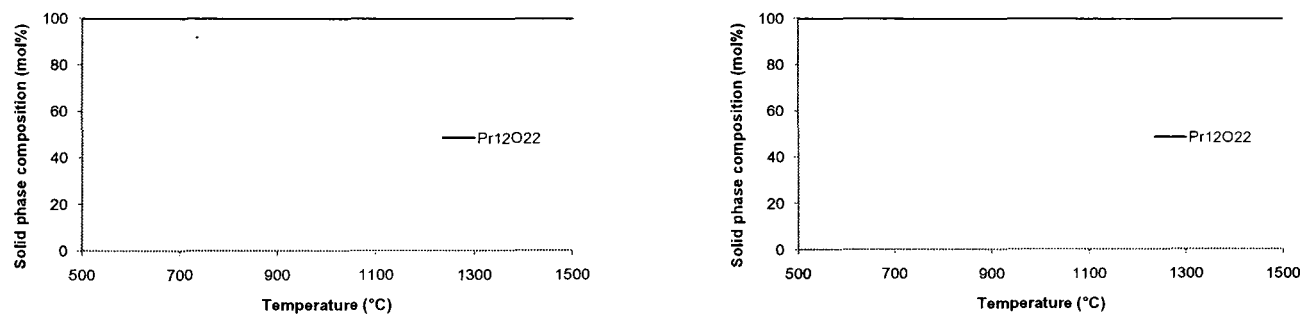


Figure B.12: Equilibrium calculation of Pr_2O_3 stability at 1 bara (left) and 20 bara (right), with gaseous phase of H_2SO_4 equilibrium decomposition products in large excess. Calculations carried out by Gibbs minimisation in HSC Chemistry.

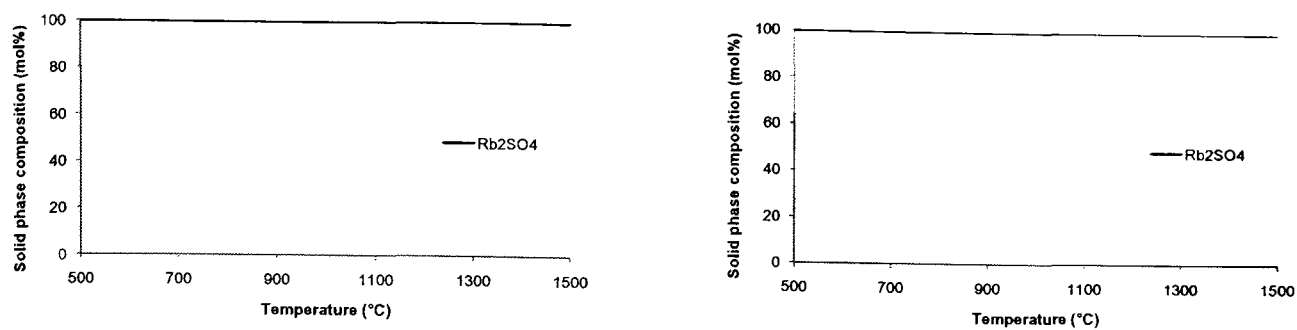


Figure B.13: Equilibrium calculation of Rb_2O_3 stability at 1 bara (left) and 20 bara (right), with gaseous phase of H_2SO_4 equilibrium decomposition products in large excess. Calculations carried out by Gibbs minimisation in HSC Chemistry.

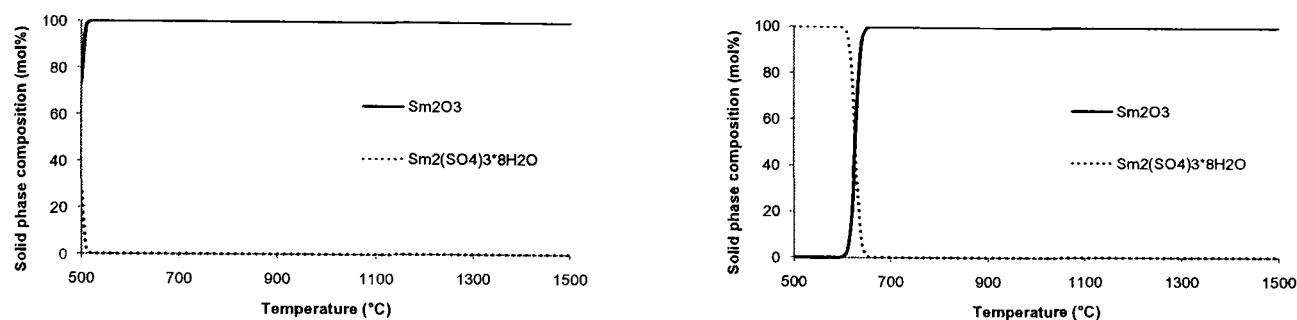


Figure B.14: Equilibrium calculation of Sm_2O_3 stability at 1 bara (left) and 20 bara (right), with gaseous phase of H_2SO_4 equilibrium decomposition products in large excess. Calculations carried out by Gibbs minimisation in HSC Chemistry.

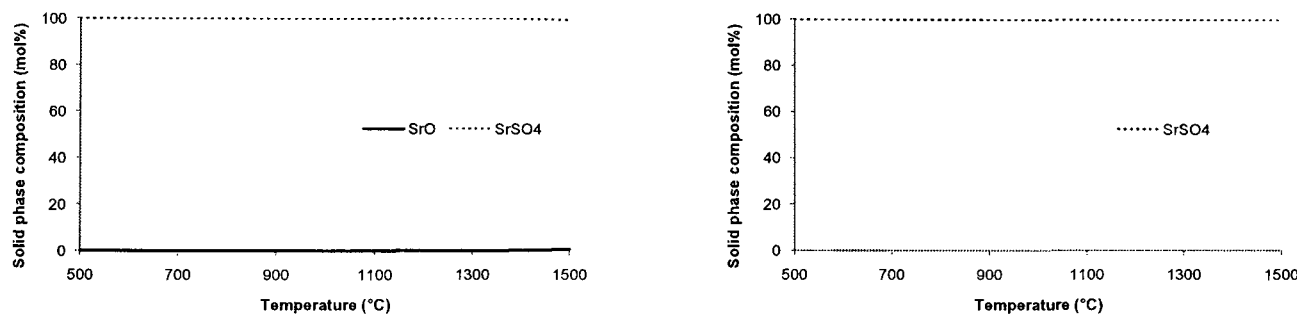


Figure B.15: Equilibrium calculation of SrO stability at 1 bara (left) and 20 bara (right), with gaseous phase of H_2SO_4 equilibrium decomposition products in large excess. Calculations carried out by Gibbs minimisation in HSC Chemistry.

AlO	BaO	BiO	CaO	CeO _{1.67}	CoO	DyO
Al ₂ O ₃	BaO ₂	Bi ₂ O ₃	CaO ₂	CeO _{1.72}	Co ₃ O ₄	Dy ₂ O ₃
Al(OH) ₃	Ba ₂ O	Bi(OH) ₃	Ca(OH) ₂	CeO _{1.78}	Co(OH) ₂	Dy(OH) ₃
Al ₂ O ₃ · H ₂ O	Ba(OH) ₂	Bi ₂ (SO ₄) ₃	CaSO ₃	CeO _{1.81}	Co(OH) ₃	Dy ₂ (SO ₄) ₃ · 8 H ₂ O
Al ₂ O ₃ · 3 H ₂ O	Ba(OH) ₂ · H ₂ O	Bi ₂ S ₃	CaSO ₄	CeO _{1.83}	CoSO ₄	DyS
Al ₂ (SO ₄) ₃	Ba(OH) ₂ · 3 H ₂ O	Bi	CaSO ₃ · 0.5H ₂ O	CeO ₂	CoSO ₄ · 6 H ₂ O	Dy ₂ S ₃
Al ₂ (SO ₄) ₃ · 6 H ₂ O	Ba(OH) ₂ · 8 H ₂ O	S	CaSO ₃ · 2 H ₂ O	Ce ₂ O ₃	CoSO ₄ · 7 H ₂ O	Dy
Al ₂ S ₃	BaSO ₄		CaSO ₄ · 0.5H ₂ O	Ce ₂ O ₂ S	CoS _{0.89}	S
Al	BaS		CaSO ₄ · 2 H ₂ O	Ce(SO ₄) ₂	CoS	
AlH ₃	Ba		CaS	Ce ₂ (SO ₄) ₃	CoS _{1.333}	
S	BaH ₂		Ca	Ce(SO ₄) ₂ · 5 H ₂ O	CoS ₂	
	S		CaH ₂	CeS	Co ₃ S ₄	
			S	CeS ₂	Co ₉ S ₈	
				Ce ₂ S ₃	Co	
				Ce ₃ S ₄	S	
				Ce		
				CeH ₂		
				S		

Table B.1: Species used for HSC Chemistry metal oxide stability calculations: Al - Dy

EuO	Fe _{0.945} O	Gd ₂ O ₃	La ₂ O ₃	Nd ₂ O ₃	PrO _{1.72}	PtO
Eu ₂ O ₃	Fe _{0.947} O	Gd(OH) ₃	La(OH) ₃	Nd(OH) ₃	PrO _{1.833}	PtO ₂
Eu ₃ O ₄	· FeO	Gd ₂ (SO ₄) ₃ · 8 H ₂ O	La ₂ (SO ₄) ₃	Nd ₂ (SO ₄) ₃	PrO ₂	Pt ₃ O ₄
Eu(OH) ₃	FeO _{1.056}	GdS	La ₂ (SO ₄) ₃ · 9 H ₂ O	Nd ₂ (SO ₄) ₃ · 8 H ₂ O	Pr ₂ O ₃	Pt(OH) ₂
EuSO ₄	FeO _{1.5}	Gd ₂ S ₃	LaS	NdS	Pr ₆ O ₁₁	PtS
Eu ₂ (SO ₄) ₃ · 8 H ₂ O	Fe ₂ O ₃	Gd	LaS ₂	Nd ₂ S ₃	Pr ₇ O ₁₂	PtS ₂
EuS	Fe ₃ O ₄	S	La ₂ S ₃	Nd	Pr ₁₂ O ₂₂	Pt
Eu ₃ S ₄	Fe(OH) ₂		La	NdH ₂	Pr(OH) ₃	S
Eu	Fe(OH) ₃		LaH ₂	S	Pr ₂ (SO ₄) ₃ · 8 H ₂ O	
S	Fe ₂ O ₃ · H ₂ O		S		PrS	
	FeO · OH				Pr ₂ S ₃	
	FeSO ₄				Pr ₃ S ₄	
	Fe ₂ (SO ₄) ₃				Pr	
	FeSO ₄ · H ₂ O				PrH ₂	
	FeSO ₄ · 4 H ₂ O				S	
	FeSO ₄ · 7 H ₂ O					
	Fe _{0.877} S					
	FeS					
	FeS ₂					
	Fe ₂ S ₃					
	Fe ₇ S ₈					
	Fe					
	S					

Table B.2: Species used for HSC Chemistry metal oxide stability calculations: Eu - Pt

RbO ₂	H ₂ O ₃ Si	Sm ₂ O ₃	SrO	Y ₂ O ₃	ZrO ₂
Rb ₂ O	H ₄ O ₄ Si	Sm ₂ (SO ₄) ₃ · 8 H ₂ O	SrO ₂	Y(OH) ₃	Zr(OH) ₄
Rb ₂ O ₂	H ₂ SiO ₃	SmS	Sr(OH) ₂	Y ₂ (SO ₄) ₃ · 8 H ₂ O	ZrO(OH) ₂
Rb ₂ O ₃	H ₂ Si ₂ O ₅	Sm ₂ S ₃	SrSO ₄	YS	Zr(SO ₄) ₂
RbOH	SiO ₂	S	SrS	Y ₂ S ₃	ZrS _{1.5}
Rb ₂ SO ₄	SiO ₂ · H ₂ O	Sm	S	S	ZrS ₂
Rb ₂ S	SiS		Sr	Y	ZrS ₃
Rb	SiS ₂		SrH ₂	YH ₂	Zr ₂ S ₃
RbH	S			YH ₃	S
S	Si				Zr
	Si ₂ H ₆				ZrH ₂

Table B.3: Species used for HSC Chemistry metal oxide stability calculations: Rb - Zr